Science

The Hunt for Money
in Biomedicine

CONTENTS

CONTENTS continued **>>**

page 22

page 46

ON THE WEB THIS WEEK

>> *Science* Podcast
On this week's show: life under rapid funding
change and a news roundup with David Grimm.

>> Find More Online
Check out *Science Express*, the weekly podcast,
videos, daily news, our research journals, and
Science Careers at **www.sciencemag.org.**

COVER

A lone scientist considers the state of biomedical funding in the
United States. As researchers adapt to new constraints, they are
reconsidering their strategy and their science, and trying to find
a road forward. See pages 9, 24, and 41.
Illustration: Mark Smith, MarkSmithIllustration.com

DEPARTMENTS

pages 48 & 97

page 65

Designer Chromosome

One of the ultimate aims of synthetic biology is to build designer organisms from the ground up. Rapid advances in DNA synthesis has allowed the assembly of complete bacterial genomes. Eukaryotic organisms, with their generally much larger and more complex genomes, present an additional challenge to synthetic biologists. **Annaluru et al.** (p. 55, published online 27 March) designed a synthetic eukaryotic chromosome based on yeast chromosome III. The designer chromosome, shorn of destabilizing transfer RNA genes and transposons, is ~14% smaller than its wild-type template and is fully functional with every gene tagged for easy removal.

Designer Embryo

Numerous signaling pathways have been implicated in controlling early vertebrate embryogenesis. **P.-F. Xu et al.** (p. 87) identify the minimal set of factors necessary to get uncommitted cells to organize a complete embryo. Two opposing gradients of the growth factors Nodal and Bone Morphogenetic Protein were sufficient to instruct zebrafish embryonic pluripotent cells to organize a complete embryo, not only in vivo but also in vitro. These findings may provide guidance for regenerative medicine studies aimed at constructing tissues and organs in vitro from cultured pluripotent cells.
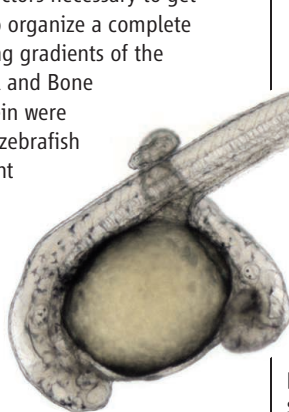
Deep, Driving Temperatures

Convection in Earth's mantle is largely controlled by the physical properties of the mantle such as density and viscosity. Because these factors are influenced by both temperature and composition, it has been difficult to ascribe one as the primary control over mantle convection or explain the long-wavelength features associated with mid-ocean ridges. Examining correlations between a global seismic velocity model with constraints on the depth and geochemical signature of mid-ocean ridges, **Dalton et al.** (p. 80; see the Perspective by **Kelley**) suggest that large temperature variations extending into the upper mantle explain most of the geophysical

Wearable Monitors >>

Advances in microelectronics have yielded high-quality devices that allow for intensive signal collection or transmission. **S. Xu et al.** (p. 70) show how to make a soft wearable system that is constructed like a stretchable circuit board, where the electronic components are bridged electrically by thin, meandering conducting traces that float in a highly visco-elastic polymer. A complete soft circuit capable of multisignal physiological sensing on skin was created, with potential for use in health monitoring or neonatal care.

and geochemical observations. Moreover, the analysis provides support for deeply rooted mantle plumes as the source of hot spot volcanism.

Engineering Larger DNA Structures

Several approaches now exist for the self-assembly of DNA into nanostructures. For example, three-arm DNA tripods can be assembled into larger wireframe polyhedra, but for the most complicated shapes, assembly yields can be low, apparently because the flexibility of smaller tripods allows for misassembly. **Iinuma et al.** (p. 65, published online 13 March) now show that larger, stiffer tripods that have controlled arm lengths and interarm angles can be designed to form a wide variety of open wireframe polyhedra—including tetrahedra, cubes, and hexagonal prisms, with edges 100 nanometers in length.

Inside Enceladus

Saturn's moon Enceladus has often been the focus of flybys of the Cassini spacecraft. Although small—Enceladus is roughly 10 times smaller than Saturn's largest moon, Titan—Enceladus has shown hints of having a complex internal structure rich in liquid water. **Iess et al.** (p. 78) used long-range data collected by the Cassini spacecraft to construct a gravity model of Enceladus. The resulting gravity field indicates the presence of a large mass anomaly at its south pole. Calculations of the moment of inertia and hydrostatic equilibrium from the gravity data suggest the presence of a large, regional subsurface ocean 30 to 40 km deep.

Constructed for Deconstruction

Lignin provides strength to wood but also impedes efficient degradation when wood is used as biofuel. **Wilkerson et al.** (p. 90) engineered poplar to produce lignin that is more amenable to degradation. From a handful of plants that contain more digestible lignin monomers, *Angelica sinensis* was selected and its monolignol transferase activities analyzed. The enzyme involved, coniferyl ferulate feruloyl-CoA monolignol transferase, was then expressed in poplar. The resulting poplar trees showed no difference in growth habit under greenhouse conditions, but their lignin showed improved digestibility.

Optogenetics Applied to Motorneuron Control

Nerves damaged by disease or injury do not always regenerate. In such cases, therapies involving transplanted stem cells show some promise. However, the new neurons derived from transplanted cells cannot communicate with the central control systems that would normally regulate movement. To avoid the need for such communication, in a proof-of-principle study, **Bryson et al.** (p. 94; see the Perspective by **Iyer and Delp**) added optogenetic control to differentiation and transplantation of motor neurons. In the mouse, these engineered neurons were able to reestablish connections within a damaged sciatic nerve and, when activated by localized light stimulation, could drive muscle contractions.

Additional summaries

Migration Monitor

Seasonal migrations move large numbers of animals across often vast distances. Such movement shifts large amounts of biomass

from one region to another, but, perhaps more importantly, moves animals that eat, excrete, and sometimes die in multiple remote systems. Such movements impact the communities, trophic structure, and function of these ecosystems in often underappreciated ways. **Bauer and Hoye** (p. 54) review migrations across taxa to identify the key ecological roles these long-distance movements play, and the unique threats the animals face in our increasingly modified world.

Completing the Set

G protein–coupled receptors (GPCRs) are membrane proteins that transduce extracellular signals to activate diverse signaling pathways. Significant insight into GPCR function has come from structures of three of four classes of GPCRs—A, B, and Frizzled. **Wu et al.** (p. 58, published online 6 March) complete the picture by

reporting the structure of metabotropic glutamate receptor 1, a class C GPCR. The structure shows differences in the seven-transmembrane (7TM) domain between class C and other classes; however, the overall fold is preserved. Class C GPCRs are known to form dimers through their extracellular domains; however, the structure suggests additional interactions between the 7TM domains mediated by cholesterol.

Cyanide Hitches a Ride

Cyanide is a by-product of the biosynthesis of ethylene in plants and it has been somewhat puzzling how the ion is safely removed before it can shut down enzymatic pathways by coordination to catalytic iron centers. A proposed mechanism has implicated the cyanoformate ion—essentially, a weak adduct of cyanide and carbon dioxide—as the initial product, although its lifetime was uncertain. **Murphy et al.** (p. 75; see the Perspective by **Alabugin and Mohamed**) crystallized this previously elusive adduct and found that its solution-phase stability varies inversely with the dielectric properties of the medium. The results bolster a picture in which the adduct shuttles the cyanide away from the hydrophobic confines of the enzyme before releasing the cyanide into the more polar aqueous surroundings.

Old Gradients

The surface ocean temperature gradient between the warmer Western Equatorial Pacific and the cooler Eastern Equatorial Pacific is smaller during El Niño episodes than during neutral periods or during La Niñas. Some reconstructions of Pacific Ocean sea surface temperatures (SST) covering periods before ~3 million years ago have suggested a permanent El Niño–like state. **Zhang et al.** (p. 84; see the Perspective by **Lea**) present data from a biomarker-derived proxy for SST that indicate a sizable east-west gradient has existed for the past 12 million years, contradicting the concept of a permanent El Niño–like state existed.

Backward or Forward

Although land animals generally walk forward, they readily switch to walking backward if they sense an obstruction or danger in the path ahead. Such a switch is likely to involve a neural signal sent from the brain down to local motor circuits, instructing these motor circuits to alter the phase at which specific leg muscles are activated. **Bidaye et al.** (p. 97; see the Perspective by **Mann**) identified such a neuron in *Drosophila*, which they call MDN (moonwalker descending neuron). Blocking synaptic transmission from MDN inhibited backward walking, and conversely artificially activating MDN caused flies to walk backward.

Dissecting SRP

In the secretory pathway, inserting transmembrane and secretory proteins into and through hydrophobic cell membranes is facilitated by a highly conserved RNA and protein-containing molecular machine, the signal recognition particle (SRP). **Grotwinkel et al.** (p. 101) determined the x-ray crystal structures of human SRP RNA (7SL RNA) bound to the RNA-binding domain (RBD) of the protein SRP subunit SRP68, both in the presence and absence of the SRP19 subunit. The 7SL RNA is remodeled by the SRP68-RBD, which bends one domain of the RNA and remodels a loop, exposing two nucleotides, which allow direct interaction with the ribosome. The findings explain how the SRP RNA drives translation elongation arrest, which is required for membrane insertion.

The New Patrons of Research

THE NEWS IS NOT ALL BAD ON THE SCIENCE FUNDING FRONT. DESPITE THE FACT THAT MANY U.S. researchers face increasing competition in chasing after federal support that has not kept pace with inflation (see the News special section on p. 24), private support is on the rise. Of course, such investments are not a new phenomenon: Nobel, Carnegie, and many others attached their names to major gifts to science more than a century ago. Today, a growing number of billionaires are likewise investing in scientific research as their personal philanthropy, choosing areas that reflect their deeply held passions. These patrons of science bring a refreshing new perspective to the projects they support, because they are typically unafraid to take risks, abhor bureaucracy, and nimbly cross disciplinary boundaries. Many are directly involved in the foundations they support, putting their personal imprimatur on the direction and operation of the ventures that bear their names. With all of this good news, it is somewhat surprising that this influx of private money has been viewed with some skepticism.*

One of the biggest concerns is that private funding for science could be viewed as a replacement for federal funding. However, unlike the federal portfolio, private support is not coordinated. Without adequate federal support, gaps of all kinds can develop—in the balance of exploratory, basic, applied, and translational research; in the support of scientific talent at different levels of training; and in the support of different types of institutions. For example, there are very different long-term impacts on science between a private investment in an institution devoted to basic research and a private investment targeted to globally eradicating a disease, although both are worthy endeavors. Even with new foundations entering the funding scene, the private share remains a small fraction overall and cannot compensate for substantial losses in federal dollars. For these reasons, it is important that scientists and philanthropists make the case to political leadership that private funding does not replace public support for research.

Another drawback is that some private foundations do not honor the federally negotiated overhead rates for academic institutions, because they want all of their funding to go "directly to science." The result is that only institutions with other sources of private support (such as unrestricted gifts and/or an endowment) that can cover the utilities, maintenance, etc., can accept awards that are restricted to research alone. The upshot is that well-endowed institutions can benefit from private research dollars, whereas those without flexible funds cannot, thus placing even more emphasis on the importance of large capital campaigns. But even well-endowed institutions may have a difficult time soliciting gifts to support the indirect costs of another donor's program. Scientists who serve on advisory bodies for these foundations can help by making the case that indirect costs are also legitimate costs of doing research.

A potentially sticky issue is that private funders want to set their own rules, and given the general frustration all around with the number and inflexibility of rules associated with federal funding, private funders generally choose to be more lenient. Following the more lax rules can be acceptable except when issues such as safety or scientific integrity are involved. For example, scientists should follow the standards of their field in terms of data sharing and other aspects of being a responsible citizen, even if not specifically spelled out by the supporting agent.

Private funding is, and always has been, a huge boon to the scientific enterprise. Universities and researchers have a long history of successfully merging public and private support to profit from the advantages of each funding source, accelerate scientific discovery, and benefit humanity. Given the many causes that could engage the attention of these philanthropists, we are fortunate that so many have chosen to give back to society through science.

–Marcia McNutt

Marcia McNutt is Editor-in-Chief of *Science*.

---

*W. J. Broad, "Billionaires with big ideas are privatizing American science," *New York Times*, 16 March 2014, p. A1.
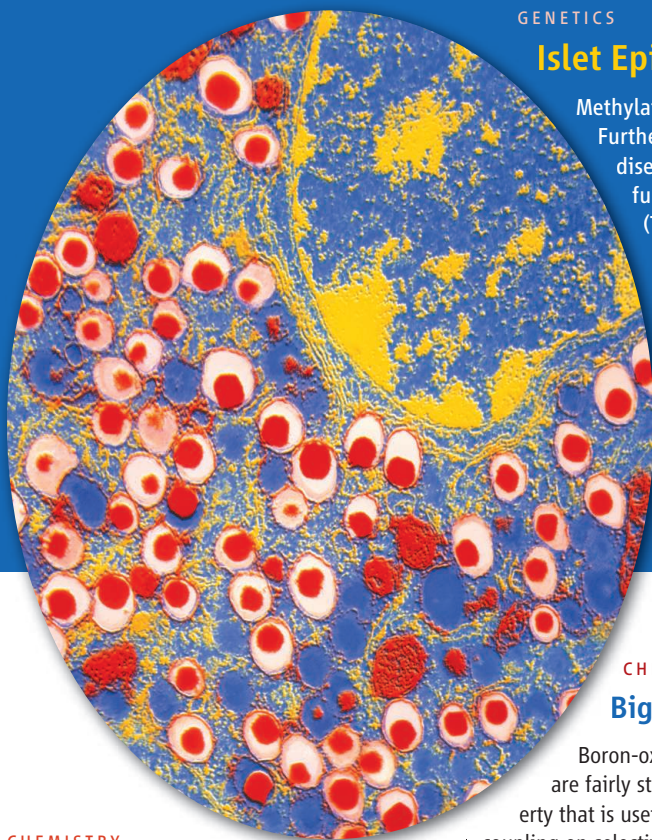
GENETICS

Islet Epigenetics

Methylation is a form of epigenetic regulation that can influence gene expression. Furthermore, methylation has been postulated to underlie some complex traits and diseases, especially those for which genetic factors have been poorly identified or functionally understood. In order to investigate the epigenetics of type 2 diabetes (T2D), Dayeh *et al.* examined the genome-wide DNA methylation patterns in pancreatic islets in both diabetics and nondiabetics. They found that the degree of methylation was correlated with transcription, although overall levels of methylation did not differ between diabetics and nondiabetics. Differentially methylated regions between individuals with and without T2D were identified. Of the more than 800 genes exhibiting differential methylation, 102 showed differential mRNA expression, including 17 candidate T2D genes expressed in islets. Furthermore, functional analyses provided support that these observed methylation differences may underlie differences in gene expression and potentially link the complex phenotype of T2D with epigenetic modifications. — LMZ

PLOS Genet. **10**, e1004160 (2014).

CHEMISTRY

Printable Hydrogels

Hydrogels consist of highly water-swollen cross-linked polymer networks, which make them of interest as materials for storing and delivering cells. However, because they are soft and squishy, it is difficult to shape or form the hydrogels in the way that you might construct pieces from more solid materials. One hydrogel system used for tissue engineering is based on gelatine, a low-immune-response, enzymatically degradable protein, which is cross-linked with methacrylamide groups. Through the addition of gellan gum, an FDA-approved food additive, Melchels *et al.* show that the gelatin-methacrylamide can be made stiff enough to be used in additive printing processes for making complex shapes. The chains in gellan gum bind through ionic bonding, so by adjusting the salt concentration, it is possible to tune the rheological properties to allow for shear thinning and yield stress, which are necessary for depositing material at controlled places. The salt concentrations, however, were lower than those found in physiological conditions, so the authors replaced some of the phosphate-buffered saline with the sugar mannose to provide a controlled osmotic-pressure environment to allow for the inclusion of cells within the gel material. — MSL

J. Mater. Chem. B 10.1039/c3tb21280g (2014).

CHEMISTRY

Big Break for Boron

Boron-oxygen (B-O) bonds generally are fairly strong and unreactive, a property that is useful in the reliance of Suzuki coupling on selective reactivity of the B-C bonds in boronate esters. Hirner *et al.* have devised a catalyst that formally cleaves B-O bonds through their intramolecular addition across an alkyne. Reasoning that direct insertion of a metal into the bond would face too high an energy barrier, the authors implemented a dual activation strategy, targeting a mechanism in which gold coordination enhances the reactivity of the C-C
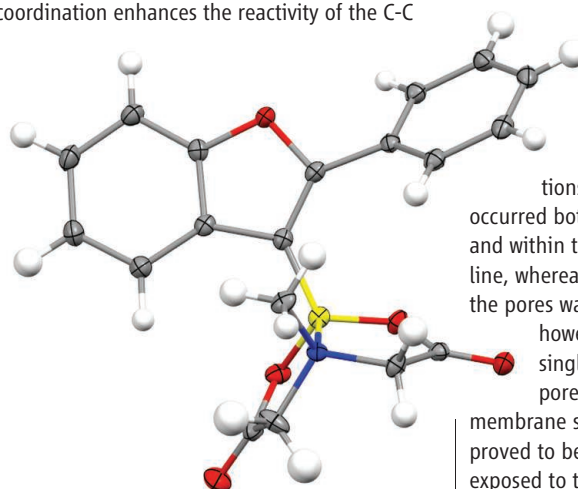
triple bond while trifluoroacetate coordination to B stimulates transfer of the adjacent O group. The protocol furnished a diverse array of benzo-furan products with a B substituent conveniently poised for further reactivity via Suzuki coupling

or other elaborations. Moreover, the reaction is broadly tolerant of groups such as halogens, esters, and nitriles, and it manifests complementary site-selectivity to arene C-H borylation reactions. — JSY

J. Am. Chem. Soc. **135**, 10.1021/ja500463p (2014).

MATERIALS SCIENCE

Confined Stability

Of the three polymorphs of calcium carbonate, vaterite is less stable than either calcite or aragonite and is difficult to obtain in single-crystal form without the use of additives. It is generally not seen in geologic materials, but there are a few cases where it appears as a biomineral. Schenk *et al.* synthesized $CaCO_3$ crystals inside track-etched coated polycarbonate membranes under a range of conditions. Under high concentrations of Ca^{2+}, precipitation of vaterite occurred both on the surface of the membranes and within the pores, but it was polycrystalline, whereas at low Ca^{2+}, little infiltration of the pores was observed. At intermediate values, however, the authors observed primarily single-crystal rods of vaterite within the pores and predominately calcite on the membrane surfaces. The vaterite crystals also proved to be stable for several days, even when exposed to the reaction solutions. The results are somewhat complicated, because vaterite crystallization was not observed in the pores of similarly treated membranes from a different supplier. The authors speculate that there probably are subtle differences in the microenviroments of the pores in the two different membranes

and, in particular, that the vaterite- growing membranes possess a surface coating that better collects and organizes the Ca^{2+} ions, thus stabilizing the formation of vaterite. — MSL

Chem. Commun. 10.1039/C4CC01093K (2014).

ECOLOGY

Data Driven Decision-Making

A combination of remote sensing and ecological modeling can increase the efficacy of the reintroduction of endangered plant species, a study in a Hawaiian dryland habitat shows. Reintroductions and habitat restoration are important components of conservation, but with often-limited resources, it can be important to maximize the chances of success. Questad *et al.* used LiDAR (airborne light detection and ranging) data to determine the optimum topographic features. LiDAR enables mapping of topography at a scale that is relevant to the establishment of individual plants — in this case the shrub *Dodonaea viscosa* and its associated native plant species. The topographic mapping was used to model the optimization of water and nutrient availability and hence to determine

sites that were most promising for restoration. Experimental plantings showed better establishment and growth in the sites that LiDAR identified as suitable. This suite of techniques indicates promise for restoring vegetation and species of conservation concern in a wider range of degraded and disturbed habitats. — AMS

Ecol. Appl. **24**, 385 (2014).

BIOMEDICINE

Rheumatoid Rescue?

MHC class II molecules can rescue endoplasmic reticulum–localized misfolded proteins from protein degradation and transport them to the cell surface intact by associating with the misfolded protein. MHC class II allelic polymorphisms are associated with susceptibility to many autoimmune diseases. Jin *et al.* have now found that cellular misfolded autoantigens rescued and complexed with MHC class II molecules can become targets for autoantibodies in patients with rheumatoid arthritis (RA). By analyzing sera from some RA patients in which autoantibodies against correctly folded intact proteins were not detectable, autoantibodies specific to misfolded proteins complexed with MHC class II molecules of disease-susceptible alleles but not disease-resistant MHC class II alleles were observed. This suggested that misfolded proteins complexed with MHC class II molecules are natural autoantigens for autoantibodies. Autoantibody binding to misfolded proteins transported by MHC class II molecules was strongly correlated with susceptibility to RA. Thus, misfolded proteins, which normally would not be exposed to the immune system, can be targets for autoantibodies when they avoid protein degradation. — SMH

Proc. Natl. Acad. Sci. U.S.A. **111**, 3787 (2014).

GENETICS

Regulating DNA Repair

Chromosomes carry the intricate code that makes and organizes cells and organisms. But chromosomes can break, causing a serious potential threat to cell and organismal survival. Repairing such breaks is vital, but repair can come with its own dangers, as certain repair pathways are necessarily error-prone—restoring chromosome integrity at the cost of introducing mutations into the genome. Microhomology-mediated end joining (MMEJ) is an error-prone form of repair that relies on very small (~5 to 25 base pairs) fortuitous homologies near the broken ends of chromosomes, which allow them to come together and be rejoined. A micro-homology signature is often seen in breakpoints in chromosome arrangements in cancers and other diseases, suggesting that MMEJ is commonly involved in such genome derangement. Deng *et al.* investigated MMEJ in the budding yeast *Saccharomyces cerevisiae*. They find that although resection [the trimming back of one of the DNA stands to generate a single-stranded DNA (ssDNA) tail] at the ends of the breaks is important to expose regions of microhomology internal to the break, it is not rate-limiting for repair. On the other hand, replication protein A, which binds ssDNA, actively prevents spontaneous annealing between the microhomologies and suppresses MMEJ. — GR

Nat. Struct. Mol. Biol. 10.1038/nsmb.2786 (2014).

CREDIT: USDA FOREST SERVICE
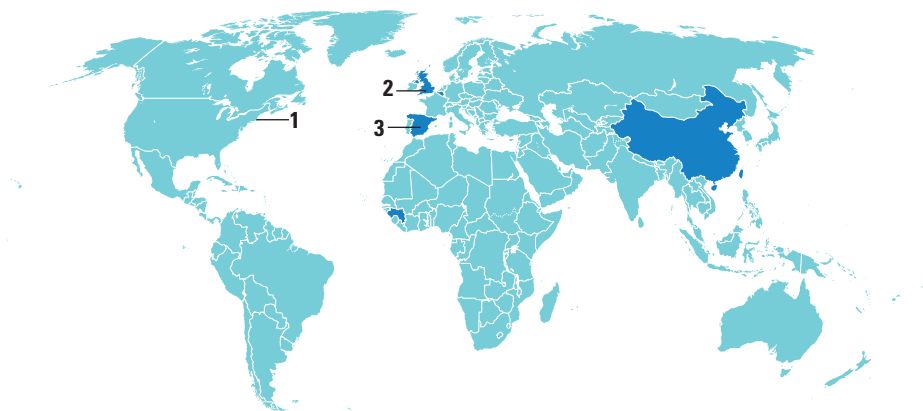
Woods Hole, Massachusetts 1

Iconic Sub Returns to the Deep

After a 3-year rebuild, the *Alvin* deep-sea submersible is returning to scientific service. The $42 million overhaul by the Woods Hole Oceanographic Institution in Massachusetts involved forging a titanium "personnel sphere," changing the imaging, lighting, and data systems, and upgrading its manipulator arms. In January, the Navy cleared *Alvin* for use at a diving depth of 3800 meters, and scientific trials of the
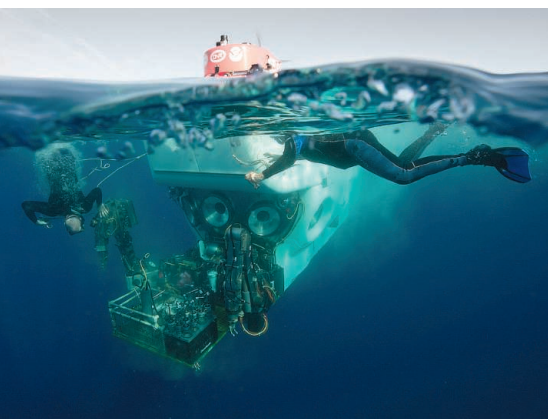
Upgrade. Divers recover *Alvin* after a test mission.

revamped sub were completed 26 March. A second stage of upgrades includes developing new batteries that will allow the sub to descend to 6500 meters.

First launched in 1964, the craft is the world's longest operating deep ocean submersible, responsible for many iconic discoveries—including the first hydrothermal vents, in 1977, and its explorations of the sunken *Titanic*—in its 50-year life. The improvements are meant to allow *Alvin* to explore the deep ocean for another 5 decades.

Swindon, U.K. 2

Funding Fears Dominate Physics Report

Physics research in the United Kingdom faces irreversible damage if it doesn't get a funding boost, an expert panel warns in a report to the United Kingdom's Science & Technology Facilities Council (STFC). In its Programmatic Review 2013, released 26 March, STFC argues that failure to increase physics funding would have catastrophic consequences: "The UK would lose leadership and credibility as an international partner on the world's scientific stage."

As the United Kingdom's main funding body for nuclear physics, particle physics, and astronomy, the council is struggling under the constraints of the 2015 to 2016 budget, unveiled in February. The government didn't cut STFC funding, but it froze it at the current levels through March 2016. That amounts to a cut after considering inflation, says Jonathan Butterworth, a physics professor at University College London and one of the authors of the report. "If it continues, the number of Ph.D. students, the amount of science, and the economic benefits, will all decrease," he says.

Madrid 3

Scientists Warn Against Vulture-Killing Drug

Researchers are urging the Spanish government to rescind approval of a drug that could threaten Europe's wild vulture populations. In a letter published online on 27 March in *Conservation Biology*, five scientists from Spanish and Swiss universities point to the devastating effects of diclofenac, an anti-inflammatory commonly used to treat pain in livestock, on vultures in India.

In 2003, researchers discovered that the drug was causing kidney failure in birds who ingested it while feeding on carcasses. It was banned for veterinary use in India, Nepal, Pakistan, and Bangladesh, but not before it wiped out most of India's vultures and left an ecological hole filled by feral dogs that help spread rabies.

Diclofenac is currently approved for human and veterinary use in many countries and is the active ingredient in more than 100 trade-named medications. Since the Spanish Agency for Medicines and Health Products approved it in March 2013, advocates have petitioned the government to reverse the move. So far, there has been no government response. **http://scim.ag/_vulture**

NEWSMAKERS

March of Dimes Prize Honors Neuroscientist's Genetic Quest

The nonprofit foundation March of Dimes has bestowed its annual developmental biology prize on neuroscientist **Huda Zoghbi** of Baylor College of Medicine in Houston,

NOTED

>The University of Konstanz in Germany has **broken off negotiations with scientific publisher Elsevier** over the price of a new site licensing agreement. In a statement last week, university Rector Ulrich Rüdiger condemned the Dutch publishing giant, which puts out more than 2500 titles, for its "aggressive pricing policy." To view 2014 articles, University of Konstanz researchers will now rely on interlibrary loans and Elsevier's pay-per-view arrangement. **http://scim.ag/Elsev**

Texas, for helping demystify Rett syndrome and other neurological disorders through more than a decade of genetic sleuthing. Zoghbi calls her career "a winding road," leading from medical school in Lebanon, which she fled in 1976 amid civil war, to becoming an authority in the genetics of neuropsychiatric disease.

Zoghbi's fascination with Rett syndrome began during a residency at Baylor, where she saw two young girls with previously normal development gradually stripped of motor coordination and cognitive abilities. It would take more than a decade to identify the responsible mutation, but the 1999 discovery and subsequent research linking the gene methyl CpG-binding protein 2 (*MECP2*) to functions from feeding behavior to social skills "influences the entire field of autism and other neuropsychiatric disorders," said Joe Leigh Simpson of March of Dimes' Research and Global Programs in a statement announcing the winner of the $250,000 prize this week.

Dynamical Systems Dynamo Nabs Abel Prize

Mathematician **Yakov Sinai** of Princeton University has won the Norwegian Academy of Science and Letters' million-dollar Abel Prize in mathematics for his work on dynamical systems— mathematical descriptions of the way physical systems change over time, from the rhythmic swings of a pendulum to turbulence in the oceans and atmosphere. The 78-year-old mathematician, also a senior researcher at the Landau Institute for Theoretical Physics of the Russian Academy of Sciences, focused on ergodic theory, an aspect of dynamical systems that averages a system's behavior over space or time. Such averages are often provably simple, even when the underlying dynamics are chaotic.

Sinai is famous for one such system, the "Sinai billiard," which mimics the behavior of electrons in metals. (See http://www.dynamical-systems.org/sinai/ for a headache-inducing demonstration.) His

Random Sample

NASA's Virtual Fashion Show

NASA engineers are adding a touch of flair to the next generation of space suits. In collaboration with the Philadelphia University Kanbar College of Design, Engineering and Commerce, the engineers dreamed up outlandish designs for the new Z-2 suits and are holding an online poll to decide which will become a prototype, set to be built by November.

The Z-2 offers handy new features such as 3D-printed hardware tailored for better mobility and a hard upper torso that can attach to the hull of a spacecraft or rover for exit and reentry. But the style of the prototype will depend on which of three designs—on display at http://jscfeatures.jsc.nasa.gov/z2/—gets the most votes by 15 April. The ocean-inspired "Biomimicry" model sports a squiggle-coated torso that glows in low light. Even more vibrant are the glowing teal patches on "Technology"—a retro-chic "homage to spacesuit achievements of the past," notes NASA's Z-2 website. And "Trends in Society" evokes future street clothing in the apparently to-be-trendy colors purple and neon green.

Alas, these styles will never leave Earth. They are just "cover layers" designed to protect the nuts and bolts of the suits while NASA tests them in vacuum chambers and its giant indoor pool. The final version will be plain white, NASA advanced suit team lead Amy Ross told an online commenter in a 26 March Reddit Q&A. In other words, space walks after Labor Day will continue to be déclassé.

work "has changed our understanding of change," said David Vogan, president of the American Mathematical Society, in a statement. Sinai will receive the award, given annually since 2003, at a ceremony in May.

Livermore Veteran Ascends To Director

William Goldstein, a theoretical physicist, is the new director of Lawrence Livermore National Laboratory in California, one of three national labs run by the Department of Energy's National Nuclear Security Administration. A 29-year Livermore veteran, Goldstein most recently served as the lab's deputy director for science and technology.

With more than 6300 employees and an annual budget of more than $1.5 billion, Livermore works primarily to ensure the reliability and safety of the United States' nuclear arsenal. It's also home to the National Ignition Facility, a gigantic battery of lasers that is used to test nuclear materials but has also been used to try to achieve nuclear fusion as a potential energy source. Goldstein himself helped develop the lab's smaller Jupiter Laser Facility. He trained as a particle theorist at Columbia University. Goldstein started on 31 March, replacing Parney Albright, who stepped down in November, and Bret Knapp, who led the lab in the interim.

THEY SAID IT

"**We have been in a really quiet time. It can't stay that way.**"

—U.S. Geological Survey seismologist Lucy Jones to the Associated Press after a magnitude-5.1 earthquake shook Los Angeles last week.

Mass destruction. Geology and heavy rains conspired to make the Oso landslide flow much farther than other slides of similar size, experts say.

OSO DISASTER

Even for Slide-Prone Region, Landslide Was Off the Chart

If Richard Iverson had been driving along state Route 530 in northwest Washington on 22 March and happened to witness the scarp of a hill disintegrate at 10:37 that morning, he would have felt safe pulling over to snap photos. Iverson, a landslide specialist with the U.S. Geological Survey (USGS) in Vancouver, Washington, would have expected the slide to end near the North Fork Stillaguamish River, well before it reached the highway a half kilometer on the other side. Instead, the wall of mud and rock barreled on. It swept across the river, burying more than a kilometer of Route 530 on the far side and engulfing an adjacent neighborhood.

As *Science* went to press, 27 people in that community of Oso, an hour's drive north of Seattle, were confirmed dead and 22 were still listed as missing. Although a flurry of critical media accounts have cited expert predictions of landslides for the area that were seemingly ignored, Iverson contends that the distance traveled by the Oso landslide was far beyond the norm for slides of its size falling from less than 200 meters. "I would not have anticipated this," he says. In the annals of landslide science, he says, last week's catastrophe was "an extreme event."

For now, probing the causes of the slide is less urgent than ensuring the safety of recovery teams in the face of quicksandlike conditions and continued rain showers that could trigger fresh landslides. "We are offering the best science we can in urgent and exclusive support of the recovery mission," says Chris Magirl, a geomorphologist with USGS's Washington Water Science Center in Tacoma. He and colleagues are also sizing up a new threat: water pooling behind a debris dam formed when the landslide blocked the North Fork Stillaguamish River. Collapse of the dam could unleash a wall of water from the 1.3-square-kilometer barrier lake on communities downstream.

The rugged terrain inland of Seattle is prone to landslides; logging can exacerbate the risk. The largest ever recorded occurred in 1980, when nearby Mount St. Helens collapsed as it erupted, sending 2.5 billion cubic meters of debris hurtling 23 kilometers down the North Fork Toutle River. Smaller slides are common near Oso, where a more than 100-meter-thick deposit of sand and gravel "outwash," left as glaciers retreated 14,000 years ago, is prone to collapse in

"I would not have anticipated this."
—RICHARD IVERSON, USGS

wet weather. Yet the latest Oso landslide stands out as an anomaly. USGS maintains a database of slides that includes data such as debris volume, height of the hillside that produced the slide, and length of runout. Last week, Iverson crunched the numbers for the Oso slide, which had an estimated volume of 8 million cubic meters and flowed about 1.13 kilometers from the toe of the slope. "It ran out three times longer than would have been expected by looking at other slides of this height and volume," Iverson says. If the landslide had been in the normal range, it would have blocked the river and possibly destroyed a few houses, he says. "But nothing like what happened."

Iverson suspects that geology and bad weather conspired to create conditions for the monster slide. The scarp that gave way on 22 March surrounds the site of a landslide in 2006 and other smaller slides. The debris from those slides, Iverson says, was "probably even more porous" than normal glacier outwash. Heavy rains over the past 2 months saturated the soil and the debris from the previous slide; when the scarp disintegrated last week, the debris squeezed soil as it fell. "This likely caused a dramatic increase in water pressure in the soil," reducing the friction between soil particles, Iverson says. The liquefied soil, he says, flowed across the valley much as would a wave of water. It even began to flow up the other side, he says, like water sloshing up the side of a bathtub.

Iverson compares the Oso event to a similarly sized landslide in Elm, Switzerland, in 1881 that killed 115 people. Eyewitness accounts described that slide, too, as a fast-moving flow—but the Oso landslide, Iverson says, was "nearly three times more mobile." Jonathan Godt, a USGS geologist in Denver, says he finds that scenario plausible, and adds that the floodplain the landslide rumbled across was wet at the time, also reducing friction. "You can speculate on a whole variety of mechanisms," he says. "It will take some careful studies to sort that all out."

As the search for victims at Oso has moved to a grim recovery phase, an overriding priority for scientists is detecting new slides in the area as early as possible

to warn the recovery crews. Earlier this week, USGS scientists were planning to use helicopters to reach the crown of the hill above the landslide scar and deploy tripod-mounted GPS instruments called spiders that measure ground displacement. If the spiders sense the ground shifting, signaling a new slide, searchers might have at least a few minutes to pull back.

A big wild card, meanwhile, is the water pooling behind the debris dam. USGS last week placed gages in the North Fork Stillaguamish River, upstream and downstream of the blockage, to better monitor flow. As *Science* went to press, USGS and state researchers were planning to deploy buoys in the barrier lake—thought to be up to 10 meters deep in spots—to augment depths calculated from 2013 topography measurements and observed shoreline positions. Data from a downstream gage in place before the landslide indicated that in the first day after the slide, about 2 million cubic meters of water piled up behind the dam. However, the river has since cut a new channel through the debris, alleviating pressure; new gage data shows that after peaking on 29 March, the barrier lake's elevation had ebbed nearly a meter by 1 April. "The risk of a flood seems to be abating," says Ralph Haugerud, a USGS geologist in Seattle. But as the painstaking work of recovering victims continues, scientists cannot afford to drop their guard.

**–RICHARD STONE AND ROBERT F. SERVICE**

PLANETARY SCIENCE

Cassini Plumbs the Depths of the Enceladus Sea

Suspicions that Saturn's icy moon Enceladus harbors an internal ocean—one that could host life—have hardened into near certainty with exquisitely precise observations from the Cassini spacecraft, reported in this week's issue of *Science*.

Orbiting Saturn, Cassini had "tasted" the plume of salty water that spews from Enceladus's south polar region. Geochemists concluded that the plume was most likely seawater from an ocean beneath tens of kilometers of crustal ice rather than some dry decomposition of icy deposits (*Science*, 10 June 2011, p. 1259). Now, team members analyzing Cassini's observations of the moon's gravity field present strong, independent evidence that liquid water underlies at least the southernmost part of the 500-kilometer body.

The newly reported observations rely on a high-tech variant of the familiar Doppler effect, in which the pitch of a train's whistle rises as the train approaches and then falls as it recedes. Big Earth-based antennas picked up similar—but much smaller—shifts in the signals from the spacecraft's 81-watt radio as Cassini flew within 100 kilometers of the moon's icy surface.

Cassini slowed and sped up by several millimeters—yes, millimeters—per second as it skimmed Enceladus, in part because of a fluctuating gravity field due to variations in the mass beneath the passing spacecraft. To isolate that gravity signature, scientists had to filter out other effects that could mimic the tiny signal, such as the pressure on the spacecraft from sunlight, the nudge from the heat radiating from its electrical generator, and—largest by far—the drag of the "wind" as Cassini plunged through the tenuous south polar plumes.
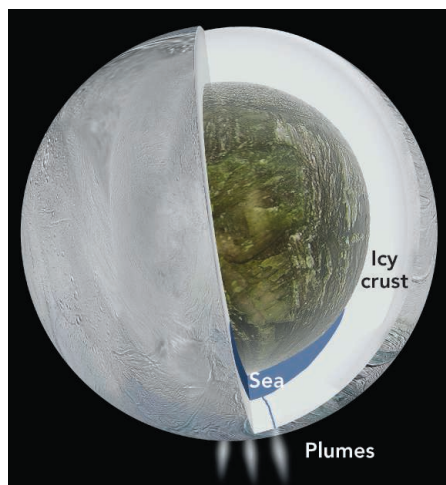
Inner waters. Gravity data from Cassini strongly suggest that a sea feeds the plumes of Enceladus.

As planetary scientist Luciano Iess of the Sapienza University of Rome and his colleagues report on page 78, the Cassini gravity data from three close flybys support earlier inferences that liquid water lurks within Enceladus. "I think the case for an ocean is quite strong," says Iess's co-author planetary physicist David Stevenson of the California Institute of Technology in Pasadena. "It's very hard to avoid the interpretation that you have water there." The presence of liquid water remains unexplained, but Saturn's powerful gravity probably played a role, by tidally kneading the moon and heating its interior.

The shape of Enceladus's gravity field, the authors write, strongly indicates that a roughly 10-kilometer-thick layer of liquid water lies beneath 30 to 40 kilometers of crustal ice at the south pole. Planetary physicist William McKinnon of Washington University in St. Louis tends to agree. "You could create a model [of the interior] without water, but people wouldn't find it satisfying," he says. The water layer could wrap around the moon to form a global ocean like the one on Jupiter's moon Europa. But the Cassini authors say a subcrustal sea confined to far southern latitudes would better explain the gravity data, the broad topographic depression Cassini scientists had mapped across the south pole, and the way so much of Enceladus's heat loss comes from the surface grooves spewing the plumes.

Such strong support for a sea beneath the spouting plumes of Enceladus should encourage scientists, mostly Cassini team members, who want NASA to send a new mission to Enceladus to explore for life. But Jupiter's Europa still looks to have too long a lead. The U.S. Congress added money to the president's fiscal year 2014 budget request for a study of a possible Europa mission; the administration joined in with a request for Europa money in fiscal year 2015. And in December, astronomers reported seeing what looked like a brief puff of water vapor coming from Europa's south pole. If true, the observation would show that Europa's deep, perhaps life-laden waters could be just as accessible as those inside Enceladus.

With the chance of a dedicated Enceladus mission receding, prospects for more insights into the Enceladus sea are bleak. Currently, Cassini is slated for "disposal" by incineration in Saturn's atmosphere no later than 2017. Even if scientists win a 3-year extension for the mission, it will make only three more flybys of Enceladus, none of which will be able to take gravity data. So decades may pass before humanity gets a closer look at Enceladus. **–RICHARD A. KERR**

Ancient presence. This citadel at the center of Erbil highlights the city's deep history.

ARCHAEOLOGY

Kurdistan Offers an Open Window on The Ancient Fertile Crescent

At the center of Erbil—one of the largest cities in northern Iraq and the capital of the autonomous region of Iraqi Kurdistan—is a reminder of its roots: an ancient citadel on an imposing mound containing a layer cake of ruins from millennia of occupation. Pottery fragments found on the slopes of this mound, or tell, show that continuous settlement stretches back at least 7500 years. Even Erbil's name has endured: Tablets from about 2200 B.C.E. mention the city of Irbilum.

This week, archaeologists from around the world will gather in Erbil to discuss the long history of the city and the wider region—and the promising future for archaeological research in Iraqi Kurdistan. Even as nearby countries such as Syria and Turkey curtail archaeological efforts, this once off-limits area within Iraq has begun welcoming outside scientists eager to probe its past. At the meeting, for example, several groups will describe how landscape surveys and digs are already painting a new picture of the Assyrian empire, which expanded from northern Iraq about 3000 years ago. Their findings suggest that northern Iraq, once the core of the Assyrian empire, had a dense population and an elaborate infrastructure, likely constructed by conquered populations resettled there.

Iraqi Kurdistan is at the heart of the Fertile Crescent, the region where farming and settlement first arose, stretching from the Mediterranean across modern-day Turkey and through Iraq to the Persian Gulf. Some of history's greatest civilizations—not just the Assyrians but also the Babylonians, Sumerians, and Hurrians—reigned over the rolling hills and valleys of Iraqi Kurdistan. "It's a crossroads of cultures in all periods," says Jessica Giraud, head of the French Institute in the Near East's mission in Erbil. "It's vital to answering all kinds of questions, from the domestication of plants and sedentarization to the birth of civilization."

Due to Iraq's tumultuous recent past, though, this part of the Fertile Crescent is practically a blank slate. Decades of war with Iran and a guerrilla uprising against Saddam Hussein's regime devastated the region and kept out archaeologists. "This is really virgin territory. It's never been thoroughly studied," says John MacGinnis, an archaeologist at the University of Cambridge in the United Kingdom.

The region has been relatively peaceful and stable since the American-led invasion of Iraq in 2003, and the Kurdistan Regional Government (KRG) has gained a high degree of autonomy from the central government in Baghdad. Abubakir Zainadin, head of KRG's General Directorate of Antiquities and a former guerrilla fighter, has actively encouraged an influx of researchers to help identify and preserve the region's heritage. "Since 2007, we have opened the gates for all foreign archaeologists," he says. Iraqi Kurdistan has signed contracts with 30 foreign universities and made contact with 15 more. Just since 2012, more than a dozen excavation missions led by foreign scientists have begun.

At the same time, conditions for research in other parts of ancient Mesopotamia have deteriorated (*Science*, 18 May 2012, p. 796). Civil war has forced archaeologists to abandon long-running projects in Syria. In Turkey, red tape and an increasing reluctance to give permits to foreigners has led many to look elsewhere. Nowadays, says Raija Mattila, director of the Finnish Institute in the Middle East and a conference co-organizer, "Kurdistan is pretty much the only possibility."

The region still poses many challenges, from uncleared minefields left over from the Iran-Iraq War to labor costs inflated by an oil boom economy. Archaeologists must also artfully negotiate their excavation contracts—typically signing an agreement with KRG officials and getting oral confirmation from the antiquities ministry in Baghdad. "Without that, people who want to go on working in southern Iraq would have problems later," says Konstantinos Kopanias, of the University of Athens, who organized a conference looking at archaeology all across Iraqi Kurdistan in November.

In Erbil this week, Harvard University archaeologist Jason Ur, who works with Giraud, will describe preliminary results from a survey of the countryside around the city. After identifying promising spots using satellite imagery—some of it taken by U.S. spy satellites in the 1960s—Ur and colleagues have started going into the field to identify ancient settlement sites. They're on the trail of the Assyrians, who often relocated vanquished populations back into the empire's core. "200,150 people, great and small, male and female, horses, mules, asses, camels, cattle and sheep without number, I brought away … and counted as spoil," Assyrian
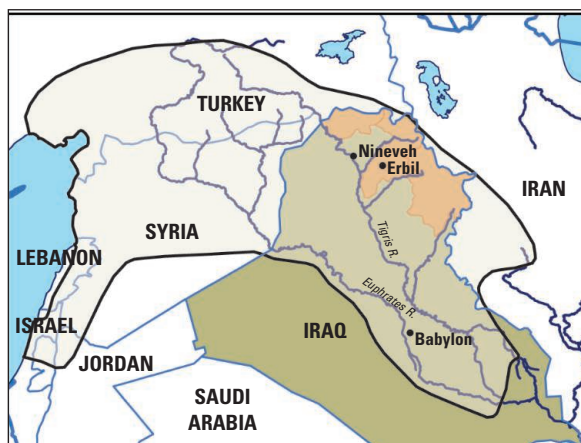
Northern roots. In the Iraq provinces overseen by the Kurdistan Regional Government (orange), archaeologists are rushing in to uncover signs of ancient Assyrians, who had a vast empire nearly 3000 years ago (black outline).

CREDITS: JASON UR/HARVARD UNIVERSITY (2)

Spy eye. Landscape discolorations in this satellite photo led archaeologists to begin excavating a tell and possible ancient town.

emperor Sennacherib boasted in an inscription from the 7th century B.C.E.

Ur thinks the Assyrians forcibly resettled this "spoil" in the arid plains around Erbil, building networks of irrigation canals to support the new settlements. In some of the areas that Ur's group surveyed, there were signs of habitation every square kilometer. "It's an extraordinarily high density of archaeological remains, the densest archaeological landscape documented yet in Iraq," he says.

Neighboring surveys support the idea of an empire expanding north with ambitious urban engineering. The Land of Nineveh Archaeological Project, focusing west of Erbil and run by Daniele Morandi Bonacossi at the University of Udine in Italy, has identified major canals—one 80 meters wide and 20 meters deep—and five early aqueducts in Kurdistan, all apparently built by the Assyrians.

Morandi Bonacossi's team also found hundreds of previously uncharted settlements, with pottery dates all starting in the Assyrian period. "They're tiny rural villages, or even farmsteads," he says. "It makes sense only if the landscape was highly engineered and cultivated with local irrigation. It was all meant to transform Nineveh's countryside into a densely populated area."

Other excavators are targeting smaller, older sites, such as Kani Shaie, a 2-hectare tell not far from Suleimaniyeh. In September and October, a Portuguese-U.S. team uncovered what may be a Sumerian colony. One find is an elaborately decorated clay tablet, roughly 5300 years old, covered with a complex seal impression and a numerical mark, possibly evidence for an elaborate administrative system.

Archaeologists are not only revealing the past, but also helping local authorities assess how best to protect it, especially from new construction projects. The research boom, however, sometimes stretches the local infrastructure: With archaeologists uncovering tons of potsherds each summer, there's still no place to properly store them. "We don't have good museums to accept and store objects," says Dlshad Marf, an archaeologist from Iraqi Kurdistan now studying at Leiden University in the Netherlands. "Right now, it's too much activity—we're not ready for all this."

As surveys chart the landscape of northern Iraq, adding hundreds of sites each season to the list of known settlements and paving the way for future excavations, archaeologists are anxious to dig deeper. "What's happening now is really basic exploration," MacGinnis says. "It's clear this wave of exploration is going to lead to new understandings of complex civilization."

–ANDREW CURRY

Andrew Curry is a writer based in Berlin.

THEORETICAL PHYSICS

The Morning After, Inflation Result Causes Headaches

Two weeks ago, when cosmologists announced that they had traced ripples in space and time from the universe's first instant, many of their peers hailed the result as a "smoking gun" for a wild theory called inflation. That theory says that in the first 10^{-32} seconds the universe expanded exponentially, stretching subatomic distances to cosmic lengths in a flash (*Science*, 21 March, p. 1296). Yet, as the smoke clears, the finding raises puzzles of its own.

Cosmologists still say that the observation from Background Imaging of Cosmic Extragalactic Polarization (BICEP), a specialized telescope at the South Pole, jibes with the simplest model of inflation and lays waste to more complicated ones. Ironically, however, the now-dead models are the ones most theorists favored. The simplest model and ones like it suffer from a conceptual problem that may render them internally inconsistent, researchers say.

"It's remarkable," says Scott Dodelson, a cosmologist at Fermi National Accelerator Laboratory in Batavia, Illinois. "On one hand, the first thing you write down works. But then when you think about it, the first thing you write down doesn't make any sense." To solve the puzzle, scientists may have to resort to speculative quantum theories of gravity such as string theory, which assumes that particles such as the photon and the electron are infinitesimal strings vibrating in different ways. "People will have to learn about string cosmology," predicts Uros Seljak of the University of California, Berkeley.

According to inflation, the newborn universe contained one thing: a quantum field a bit like an electric field. Like the air in a balloon, that "inflaton field" blew up space before decaying away into particles of matter and radiation. The field also roiled with infinitesimal quantum fluctuations that inflation magnified enormously, creating variations in the density of the cosmos that eventually seeded the formation of galaxies. Even as the inflaton field fluctuated, so

did the fabric of spacetime itself. Inflation magnified that thrumming into gargantuan gravitational waves, which stirred a particular churning motion in the early universe. That motion left its imprint on the afterglow of the big bang, the cosmic microwave background (CMB). When mapped across the sky, the arrowlike polarization of the microwaves should form faint pinwheel-like swirls. The BICEP team spotted those swirls, bolstering this scenario.

But what was the inflaton field? In 1982, Andrei Linde, an inflation pioneer at Stanford University in California, assumed that the field was a generic quantum field whose defining feature is that it interacts with itself so that the energy stored in it depends on the square of its amplitude. Given that dependence, the field's amplitude will change to reduce the stored energy, just as a marble on a hill lowers its stored energy by rolling downward. But whereas the marble merely converts stored energy into speed, the inflaton field's stored energy goes

into blowing up space. The field's amplitude eases slowly down the energy landscape, or potential, to the bottom (see diagram, below). There, the field oscillates, like a marble rattling the bottom of a bowl, as it decays away.

Linde's model explains both what drove inflation and—just as important—how inflation *stopped*. It also jibes with the BICEP result. The strength of the swirls that BICEP saw reveals the universe's energy density during inflation, which matches the starting energy required by Linde's model.

But there's a rub, says Michael Turner, a cosmologist at the University of Chicago in Illinois. To make inflation persist long enough to stretch the universe as flat as it is, Linde's energy hillside must be shallow and long. If so, the amplitude of the inflaton field must have changed immensely—by several times the amount needed for gravity to start showing weird quantum effects,

That's where string theory comes in. For 30 years, it has been physicists' best shot at a theory that melds quantum mechanics with Einstein's general theory of relativity, which states that gravity arises when energy and mass warp spacetime. String theory assumes the universe has 10 dimensions, six of them wound up in tiny loops, and some critics have dismissed it as an ultracomplicated "theory of anything"—so flexible that there is no conceivable way to test it empirically.

However, in the past 6 years, Eva Silverstein, a theorist at Stanford University, and colleagues have shown that string theory might resolve the problem with large-field inflation, preventing quantum corrections to the inflaton energy from blowing up. The models themselves are extremely complex, but the general idea is fairly simple, Silverstein says. The inflaton field still changes by a huge amount. But

string theory to a long-awaited test. "Certainly mechanisms and methods within it are being tested by this kind of data in a pretty serious way," she says. In coming years, many teams of observers hope to measure the spectrum of larger and smaller polarization swirls in the CMB. From that spectrum, researchers might be able to trace the inflaton potential and test string models. For example, Silverstein's models predict the potential might have a slight telltale wiggle in it.

Ultimately, Chicago's Turner says, theorists hope to connect inflation to the rest of particle theory. Scenarios like Linde's are just "toy models," he says; a real model would integrate inflation into some elaboration of physicists' standard model, which describes with exquisite precision particles such as photons, electrons, quarks, and the famed Higgs boson. "Here's one that we know doesn't work, but wouldn't
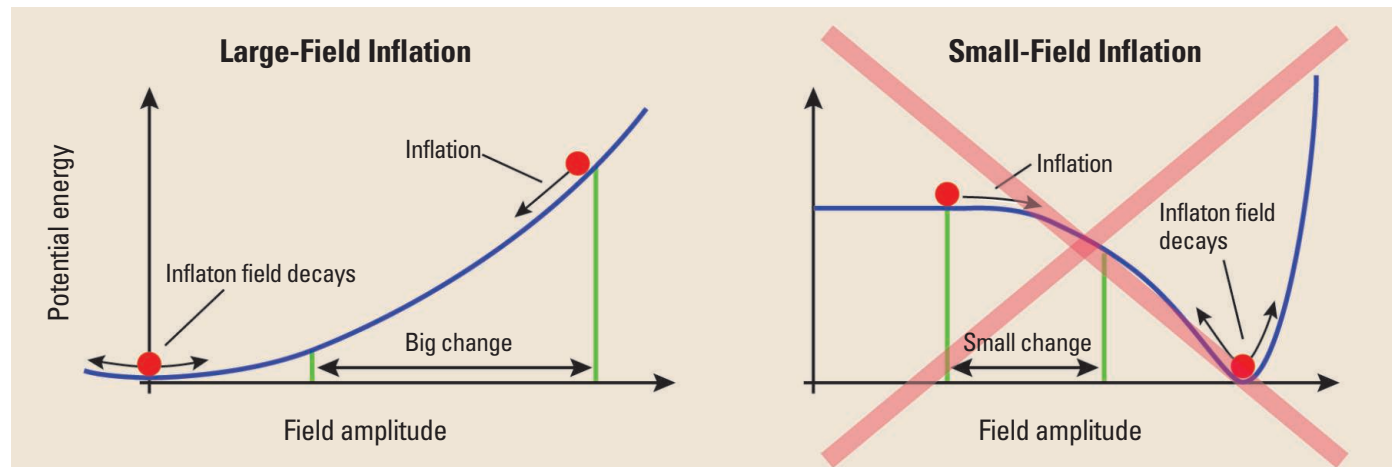
Paradox. Data support only models in which the field that drove inflation changed so much that the models go haywire (*left*).

a quantity called the Planck mass. In that case, additional interactions of the field with itself should swing out of control, and such "quantum corrections" should obliterate the smooth hillside on which the model depends.

To avoid that problem, many theorists have focused on so-called small-field inflation models. In those models, the inflaton field typically starts at a lower energy and rolls a shorter distance. Because the field's amplitude changes less, the nettlesome quantum corrections remain small and leave the potential smooth. However, small-field models also predict much weaker swirls than BICEP saw. So they're now dead.

That means theorists must confront head-on the problem with so-called large-field models like Linde's. To make such models workable, some are searching for some factor that keeps the quantum corrections in check.

naturally occurring interactions in string theory ensure that the quantum corrections have a regularity, repeating every time the field's amplitude changes by a certain amount. That "shift symmetry" limits the corrections. It's as if instead of rolling down a hill, the field rolls down a spiral chute and faces similar quantum corrections with each turn, Silverstein says.

Given the myriad versions of string theory and their flexibility, theorists probably won't be able to pin down one exact string-theory model of inflation, says Emil Martinec, a string theorist at the University of Chicago. Rather he says, their goal is to develop "a toolbox of mechanisms" that show how it's possible to construct a consistent theory of inflation.

Silverstein agrees but says the BICEP results still raise the prospect of putting

it be great if the inflaton were the Higgs?" he says. So far, such Higgs models produce small-field inflation.

Of course, such worries will be moot if the BICEP result doesn't hold up. That's a possibility, says William Jones, a cosmologist at Princeton University. Jones works on a balloon-borne experiment called SPIDER that will fly next year and should measure the CMB polarization more precisely than the BICEP2 instrument did. The BICEP team has taken a "bold gamble" in claiming its signal cannot come from something more mundane than primordial gravitational waves, he says. "I would not have made anywhere near as strong a claim," he says. If the BICEP results prove spurious, the less problematic models of inflation might come back to life.

–ADRIAN CHO

Be prepared. Researchers say governments should be doing more to prepare for climate impacts, such as this 2011 coastal flooding in Scotland.

CLIMATE SCIENCE

In New Report, IPCC Gets More Specific About Warming Risks

The latest report on climate impacts from the Intergovernmental Panel on Climate Change (IPCC) sounds a familiar warning: Climate change is already stressing human communities, agriculture, and natural ecosystems, and the effects are likely to increase in the future. But unlike the last edition, issued in 2007, this year's report is meant to be a practical guide to action. It goes out of its way to highlight the greatest risks, and draws on an emerging body of social science to suggest how policymakers might take practical steps to help communities adapt.

"The reframing of the report in terms of managing risk is a very good one," says geographer Susan Cutter, an expert on disasters at the University of South Carolina, Columbia, who reviewed part of the report, unveiled by the IPCC's Working Group II on 31 March. "I don't know of any other previous effort to rank the risks of climate change," says IPCC lead author Michael Oppenheimer of Princeton University. "We hope that will help policymakers make

investment decisions on adaptation."

The hefty report is the second of three volumes on climate change. The first, on physical effects, appeared this past September (*Science*, 4 October 2013, p. 23); a third, on ways to reduce or mitigate it, will be published later this month. This installment details how the buildup of carbon dioxide in Earth's atmosphere is affecting thousands of species, reducing farm yields, and threatening marine ecosystems with ocean acidification. For the future, the report says projections indicate "many more negative impacts than positive impacts." And for the first time, the IPCC attempts to

rank the threats. A shorter 44-page summary for policymakers, for instance, highlights eight especially pressing "key risks" (see box). These risks may have "potentially severe consequences for humans and social-ecological systems," the report says.

The new report also offers solutions, devoting four chapters to current efforts and potential strategies to adapt to a changing climate. On fisheries, for example, the document lays out how maintaining coastal vegetation or protecting reefs from fishing equipment or coral harvesters could help "maximize resilience" of coastal ecosystems to shifting ocean temperatures and chemistry. Some coastal communities are already incorporating rising sea levels into their zoning and planning efforts, it notes, but more could do the same. The biggest single barrier to improving societal resilience to the vagaries of climate? Poverty, the report says, and it devotes an entire chapter to the intersection of poverty and climate.

Such material comes as a direct response to policymakers, many of whom have begged scientists to make their climate work more meaningful for decision-making. IPCC participants say the new approach was born in 2011, during the preparation of an influential report on extreme events, known as SREX. That effort partnered climatologists with risk management scholars and other social scientists more closely than ever before. "[We] all had to be together in the same room," Cutter says. The National Science Foundation helped pave the way for similar collaborations by providing funding. Now, Cutter hopes the IPCC report will gain as much currency as the SREX study, which is being cited heavily in international fora on disaster preparation.

As climate impacts increasingly hit home, however, it is investment dollars for adaptation that will matter, not lip service, say the IPCC authors. Costs of global adaptation have been estimated between $70 billion and $100 billion per year by 2050, although the IPCC found low confidence in those numbers. But the report says that "the projected global needs [are] orders of magnitude greater than current investment levels particularly in developing countries."

–ELI KINTISCH

Eight Major Climate Risks

1. Death or harm from coastal flooding
2. Harm or economic losses from inland flooding
3. Extreme weather disrupting electrical, emergency, or other systems
4. Extreme heat, especially for the urban and rural poor
5. Food insecurity linked to warming, drought, or flooding
6. Water shortages causing agricultural or economic losses
7. Loss of marine ecosystems essential to fishing and other communities
8. Loss of terrestrial and inland water ecosystems

Not for science. Minke whales being processed aboard a Japanese whaling vessel.

ENVIRONMENTAL POLICY

Court Slams Japan's Scientific Whaling

Last week science made an unusual appearance in the United Nations' highest court, as judges ordered Japan to halt its controversial scientific whale hunt in the Antarctic. The 31 March ruling that the killing is not "for purposes of scientific research" delighted Australia, which pressed the case, and its antiwhaling allies.

"This is a clear victory for whales and for the integrity of science," says conservation geneticist C. Scott Baker of Oregon State University, Corvallis, who serves on the International Whaling Commission's (IWC's) Scientific Committee. "The court's ruling recognizes what many of us [on the committee] have argued for 20 years—that Japan's scientific whaling is simply a thinly veiled commercial whaling program."

The decision by the International Court of Justice in The Hague, the Netherlands, may not deter Japan from continuing its decades-old pursuit of whales in the name of research, however. Although Japanese officials say they are disappointed by the ruling, they have vowed to abide by it. But the order applies only to one program, analysts note, and does not address future programs or Japan's similar existing hunt in the North Pacific. "It is not obvious what Japan will do next," says physiologist Lars Walløe of the University of Oslo, who heads the Norwegian delegation to

the IWC and testified as a witness for Japan.

Australia's suit against Japan was rooted in the IWC's 1982 decision to ban commercial whaling (which Japan signed). After the ban, Japan claimed the right to kill whales for scientific purposes under provisions of the 1946 International Convention for the Regulation of Whaling. The limited hunts were needed, it argued, to understand whale populations and ecosystem dynamics (*Science*, 27 April 2007, p. 532). In 1995, for example, Japanese biologists calculated they needed to kill 400 minke whales from the Southern Ocean each year to estimate populations and understand the whale's role in the ecosystem.

That Antarctic hunt, known as JARPA (for Japanese Whale Research Program under Special Permit in the Antarctic) ended in 2005, but was immediately succeeded by JARPA II, a bigger hunt. It called for killing up to 850 minke whales, 50 humpback whales, and 50 fin whales per year. But Japan has never taken the humpbacks, and harassment of whaling ships by antiwhaling activists has reduced the minke kills in recent years (see box). In its complaint, Australia charged that JARPA II was designed to "cloak … commercial whaling in the lab coat of science," and offered "nothing more than the collection of data, a heap

of stones," rather than testable hypotheses. It urged the court to examine the meaning of scientific inquiry and whether JARPA II constituted real science. Japan, meanwhile, argued that it was following the IWC's rules and that Australia had "politicized science" in an attempt "to impose Australian values on Japan."

In their 73-page ruling, the court's 16-member judicial panel focused on legal issues, but they also evaluated Japan's claim that it is practicing science. By a 12 to four vote, they found that although JARPA II could "broadly be characterized as scientific research," it violated a number of IWC requirements. Japanese scientists did not seriously consider using nonlethal research methods, for instance, and used an opaque technique to calculate the sample size, or the number of whales needed to achieve meaningful results.

Ironically, it was Japan's own expert witness, Walløe, who appears to have driven home that point. The officials who wrote the 1946 scientific whaling rules did not intend for them to be used to take hundreds of whales, he testified—just "less than ten," the number of specimens generally required to describe a new species. And Walløe agreed that the methods Japan used to calculate sample size were "not transparent" and in some cases "worthless."

The court also questioned Japan's decision to enlarge the hunt under JARPA II, suggesting it was "largely, if not entirely, a function of political and logistical considerations." It faulted Japan for neglecting to peer-review JARPA before launching JARPA II and noted that JARPA II has produced just two peer-reviewed papers to date.

The decision marked "a good day for international law as well as for science," says law professor Alison Rieser of the University of Hawaii, Manoa. The court's narrow but deep technical ruling, she says, showed "that there are objective means of judging scientific research." The decision could help strengthen the hand of science review panels at other natural resource management bodies, she adds, such as fisheries commissions.

Phil Clapham, a marine biologist with the Alaska Fisheries Science Center in Seattle, Washington, echoed that view. The ruling, he says, backs "unequivocally what many at the IWC's scientific committee have been saying for years: The emperor truly has no clothes."

–VIRGINIA MORELL

Japan's Antarctic Whale Hunt (Number killed)		
Year	Minke	Fin
2006	508	0
2007	551	0
2008	680	1
2009	507	1
2010	171	2
2011	266	1

CREDIT: CORBIS

22

STEM CELL RESEARCH

RIKEN Panel Finds Misconduct in Controversial Paper

TOKYO—The spectacular claim of a new, easy way to make stem cells is continuing to unravel. Earlier this week, a Japanese investigating committee said it had found evidence of research misconduct in the work underlying recent *Nature* papers describing the method. The committee stopped short of calling for a retraction and will leave disciplinary decisions to a separate committee, but RIKEN President Ryoji Noyori said he favors retraction of one of the papers if the committee's findings are upheld on appeal.

The report deals another blow to lead author Haruko Obokata of the RIKEN Center for Developmental Biology (RIKEN CDB) in Kobe, Japan; the committee concluded that she "sorely lacks, not only a sense of research ethics, but also integrity and humility as a scientific researcher." But Obokata continues to stand by her research, and says she will appeal the conclusions. "I am filled with feelings of indignation and surprise," she said in a statement released after the report was made public at a press conference here on Tuesday.

The controversy centers on a surprisingly simple method for creating a new type of stem cells, called STAP (stimulus-triggered acquisition of pluripotency), published in a research paper and an accompanying letter online on 29 January by Obokata and colleagues at RIKEN CDB, along with other institutions in Japan and at Harvard Medical School in Boston. They reported briefly bathing blood cells from newborn mice in an acidic solution and then tweaking culture conditions to produce stem cells. The method would be far simpler than any other yet proven for deriving stem cells, seen as a key material for regenerative medicine (*Science*, 31 January, p. 469).

Doubts about the papers surfaced almost immediately after they were published. On 17 February, after a preliminary investigation, RIKEN assembled a six-person panel chaired by Shunsuke Ishii, a RIKEN molecular geneticist, to investigate six specific allegations. The committee's 14 March interim report found problems but stopped short of calling them misconduct (*Science*,

21 March, p. 1299). Its final report, however, identified two instances of misconduct.

One of these involves splicing together parts of two photos of electrophoresis gels into figure 1i of the paper, an act of "falsification," according to the report. The other instance was reusing images apparently originating from Obokata's doctoral thesis in the paper, even though the experimental conditions differed significantly. The images, in figures 2d and 2e of the paper, constitute "fabrication," the report states. The committee also said that the experiments are so poorly documented "that it will be extremely difficult for anyone else to accurately trace or understand her experiments."

Obokata rejected the findings. Regarding figure 1i, "[t]he idea was to present an easy-to-view photo," she wrote in her statement; the changes "did not change the obtained results." Problems with figures 2d and 2e were the result of a simple mix-up that the team had spotted on its own, she wrote, adding that they have submitted a correction to *Nature*. "At this stage, considering the STAP cell discovery itself to be fabricated is a misunderstanding; I cannot possibly accept this," her statement said.

Apologies. At a 1 April press conference, RIKEN President Ryoji Noyori said he recommends retracting the main STAP paper if misconduct findings are upheld.

Obokata was the only team member found guilty of misconduct, but the report notes the "heavy responsibility" of co-authors Teruhiko Wakayama, a former RIKEN researcher now at the University of Yamanashi in Kofu, and Yoshiki Sasai, of RIKEN CDB. Both offered apologies. The report does not mention the non-Japanese co-authors.

At the press conference, Ishii emphasized that the panel focused solely on the six issues that were raised at the outset of the investigation and did not address the overall validity of the papers, whether they should be retracted, or if STAP cells really exist. That's a missed opportunity, some scientists say. "They should have considered all the problems that have been raised with the papers, not just the six," says Robert Geller, a University of Tokyo geophysicist who has written about the structural problems afflicting Japan's research. Geller thinks that Obokata's co-authors should not have gotten off so lightly and says Obokata's response to the committee findings suggests a failure to teach young scientists about the importance of accurate notes, full and accurate citations, and image-handling practices.

Meanwhile, it remains unclear whether a simple acid bath might really have the powerful effects the team claimed. Many groups appear to have tried, but there have been no reports of success. Hitoshi Niwa, another RIKEN CDB co-author, said this week that experiments are still under way at his lab. Niwa "is one of the world experts when it comes to pluripotency," says Hans Schöler, a stem cell biologist at the Max Planck Institute for Molecular Biomedicine in Münster, Germany. "If he states that he or a member of his lab independently reproduced the findings, then we will continue trying ourselves," he says.

The fate of the two papers is still uncertain as well. A representative for *Nature* says the journal will study the new report and continue its own investigation. Noyori said he will recommend retraction of the main paper, which contains most of the problems identified by the committee, if the misconduct is confirmed in an appeals process. "Further," he said, reading from a written statement, "strict but fair disciplinary action will be taken on the basis of recommendations by a disciplinary committee set up for this purpose."

–DENNIS NORMILE

With reporting by Gretchen Vogel.

CHASING the MONEY

As constraints take hold in biomedicine, scientists are forced to adapt

MONEY. IT IS WHAT FUELS RESEARCH, AND these days, it's almost all biomedical scientists in the United States can talk about.

They've been buffeted by funding swings at the National Institutes of Health (NIH), their field's primary benefactor. And now they're anxious about the future, as Congress tries to rein in debt by slowing government spending.

One result: Morale is as low and uncertainty as high as she's ever seen it, says molecular biologist Shirley Tilghman, president emerita of Princeton University. "The image that comes into my head is a seesaw," she says. "The highs are higher and the lows are lower."

Not everyone is teetering. Some researchers and universities are raking in record-setting sums, in part by aggressively diversifying their funding sources (*Science*, 21 June 2013, p. 1394). But the triumphs only underscore a dominant theme: The

U.S. funding landscape is shifting. And with change comes adaptation.

For this special package, *Science* explored how biomedical research at U.S. universities—a $32 billion enterprise that involves hundreds of thousands of people— is reshaping itself. We found a complex mosaic, captured in the profiles that follow. To put them in context, it helps to examine what the hard data can—and can't—tell us about what's really happening on the ground.

What we know

Over the past 20 years, federal investment in R&D as a share of the gross domestic product has fluctuated above and below 1%, and now stands a bit under it. Biology has long been a favored child of funders, its allure growing with time. Today, roughly two-thirds of federal R&D money at universities goes to the life sciences, about 10% more than in the early 1970s. Industry spending

also increased in the 1980s and 1990s, and now provides about 7% of the R&D dollars that flow to universities.

At the same time, NIH's budget has sustained wild swings that many economists say make for an inefficient research enterprise. Between 1998 and 2003, the agency's budget doubled, from less than $14 billion to more than $27 billion. For the next 5 years it stayed largely flat. Then came an infusion of $10.4 billion in 2009, part of the federal stimulus plan to fight the recession—followed by a sizable bump downward in 2013, a 5% across-the-board cut from the sequester.

Universities responded predictably to the budget doubling: They expanded, adding new buildings and filling them with staff members and trainees, who needed money of their own to thrive. In 2002, a commentary in *Science* suggested that biomedical researchers had become dependent on annual budget increases of at least 6% (24 May, p. 1401). But

that didn't happen. "[T]he fundamental problems are structural in nature," concluded Michael Teitelbaum of the Alfred P. Sloan Foundation in New York City 6 years later (*Science*, 1 August 2008, p. 644). "[B]iomedical research funding is both erratic and subject to positive-feedback loops that together drive the system ineluctably toward damaging instability."

That instability is now on vivid display. On the one hand, the future looks a tad brighter: NIH's 2014 budget increased 3.5%, to $30 billion. But that will likely not be enough to sustain the community as it hopes. NIH's grant approval rate dropped below 17% last year, compared with about 30% in the late 1990s, and the average size of standard research grants fell for the first time in recent memory.
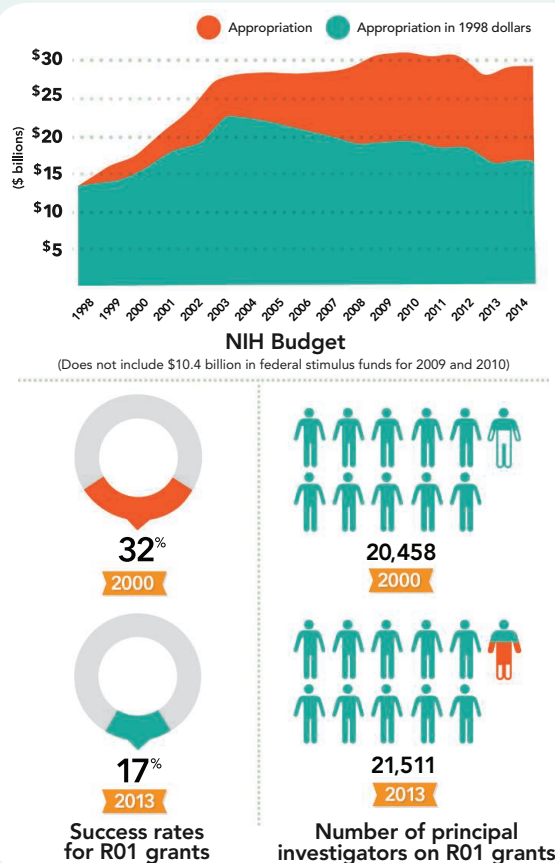
What it all means

Some say the endless complaints about money are a bit much: After all, NIH is still the biggest funder of biomedical research in the world. Universities and other institutions kick in another $7 billion from various sources to support their biology researchers.

But inflation is taking a bite. In 2013, the NIH budget of $29.15 billion was, when adjusted for inflation, almost $5 billion less than the $27.17 billion available in 2003. And some economists argue the losses are even greater, because the cost of gene sequencers, supercomputers, and even mice usually rise faster than the general rate of inflation.

The funding swings have also exposed a mismatch between how the government supports biomedical research—one fiscal year at a time—and how science is practiced—incrementally, with progress measured in years or even decades. Because NIH now approves less than one in five grant applications, scientists say they are spending more of their time submitting proposals—leaving less for the research needed to win grants in the first place.

What we don't know

It's "appalling how little is known" about how the community is adjusting to these pressures, says Julia Lane, an economist at the American Institutes for Research in Washington, D.C. Are young investigators suffering more than established ones? Are smaller labs contracting more than larger ones? Which fields of research are most affected? "You have these major adjustments, and it's shocking that there is no method of understanding what the impacts are," Lane adds. "The science agencies are charged with building, identifying, and funding the best science. They don't have as their mandate to answer these questions." Dark rumors abound, fueling the sense of unease.

For NIH, the knowledge gap can hamper its decision-making. The agency makes it easier for new investigators to get funding, for example, but it doesn't know how they fare 5 years out, when their first big grant is up for renewal. "We want to make sure we're not setting them up for failure," says Sally Rockey, NIH's deputy director for extramural research. The agency plans to start tracking these people, to gauge whether they're headed for dire straits.

Also hotly debated is whether NIH should scale back support for the 1600 or so "millionaires," the principal investigators who boast more than $1.5 million a year in grant money. NIH gives their proposals extra review, but in most cases offers additional support with peer reviewers' bless-ings, "because," Rockey says, "we're a meritocracy." Jeremy Berg, a former NIH institute director who's now at the University of Pittsburgh, recently found that more than 80% of those who already receive about $650,000 a year in direct support from the Howard Hughes Medical Institute also get money from NIH—an average of two grants each, or roughly another $400,000 a year. (This funding does not include so-called indirect costs, which allows the institution to cover overhead.) "Should we be supporting a smaller number of investigators but at a very rich rate," Tilghman wonders, "or should we be letting 100 flowers bloom?"

Economists are trying to answer some of these questions (see Policy Forum, p. 41). At the University of North Carolina, Chapel Hill, Maryann Feldman is poring over records from nine universities to understand how the support that labs receive influences publications, patents, and researcher characteristics. Feldman is also studying "venture philanthropy," which applies businesslike goals to charity work, to see how academics are relying on it and whether it redirects their research. At Ohio State University, Columbus, economist Bruce Weinberg is exploring how the structure of a lab and its funding shape the training of graduate students and postdocs and their professional future. "Hopefully the data will be built" to show how the community is adjusting, Weinberg says. "But it's not there yet."

Some suggest a rethinking of the entire enterprise. "I think for a long time people in biomedical science bought into what you hear in industry, which is, 'If you don't grow, you die,'" Tilghman says. "And it's not true, it's absolutely not true." Maybe, she suggests, scientists and their institutions should question whether they are well served by ever-expanding labs, flanked by construction cranes building still more facilities.

The end result for some senior scientists right now is caution: Play it safe, tighten your belt. That could have a trickle-down effect to the mouths they help feed. "I cannot take a grad student and make a 5- to 6-year commitment," says Arturo Casadevall, a microbiologist and immunologist at Albert Einstein College of Medicine in the Bronx, New York. "I don't know where we're going to be in 5 or 6 years."

–JENNIFER COUZIN-FRANKEL

NIH Budget
(Does not include $10.4 billion in federal stimulus funds for 2009 and 2010)

Appropriation — Appropriation in 1998 dollars

32% — 2000
17% — 2013
Success rates for R01 grants

20,458 — 2000
21,511 — 2013
Number of principal investigators on R01 grants

Online
sciencemag.org

Podcast interview with author Jennifer Couzin-Frankel (http://scim.ag/pod_6179).

The Vulnerable: Talene Yacoubian

Talene Yacoubian is exactly the kind of researcher the federal government says we need more of: a Duke- and Harvard-trained physician-scientist, a neurologist who balances her care for Parkinson's patients with a hunt for treatments that slow the disease. But at 43, Yacoubian's career has been one long slog, and she sometimes wonders if she should just give up on academic research.

M.D.-Ph.D. program at Duke University, she moved back to Boston and to a neurology residency through a joint program of the Harvard-affiliated Massachusetts General and Brigham and Women's hospitals—where she fell in love with the idea of combining bench research with patient care.

In the summer of 2007, Yacoubian settled into her own lab space at the University

the automatic reductions in federal spending known as the sequester. In March 2013, after the White House and Congress failed to reach a compromise, the sequester hit. Yacoubian became a casualty, and her proposal was turned down.

What followed was a flurry of grant applications and mounting stress. A new R01 proposal failed, too: NIH's Center for Scientific

Age at first research grant

36
1980

42
2013

Once upon a time, scientists her age would be well on their way—with their own blossoming lab, their own stable funding. Instead, Yacoubian, an assistant professor at the University of Alabama, Birmingham, has spent the past 3 years churning out grant proposals and struggling to win her first R01, the basic research grant from the National Institutes of Health (NIH) that is the ticket to an independent research career. Around her, scientists she admires are shuttering their labs.

"This is what I've spent all these years wanting to do," she says. "But it just may not be feasible with everything changing in science." Her dilemma illustrates one of the biomedical research community's biggest worries: that it is losing a generation of young scientists.

Yacoubian grew up in Chattanooga, Tennessee; though her first language was her parents' Armenian, she now speaks with a trace of a Southern accent. As a freshman at Harvard University, she took a neurobiology course and was hooked. After an

of Alabama. She had a career development award from NIH, and a fellowship from the American Parkinson Disease Association to study proteins that protect against cell death. The tenure clock was ticking: She had 10 years before it was up and would need an R01 to be considered.

But that clock was competing with another, the age at which the average Ph.D. receives his or her first R01—36 in 1980 and 42 today. (It is 44 for M.D.-Ph.D.s like Yacoubian.) To support this vulnerable group, many NIH institutes have a more lenient cutoff for grant applications from those who finished graduate school or medical residency within the last 10 years. It's not clear that the policy is working, however; so far, the average age for a first R01 has not budged, according to the agency.

In fall 2011, Yacoubian sent off her first R01 application. She didn't make the cut, so she revised and resubmitted the proposal for a second and last shot. A year earlier, her score would likely have meant success. But NIH was bracing for a 5% funding cut from
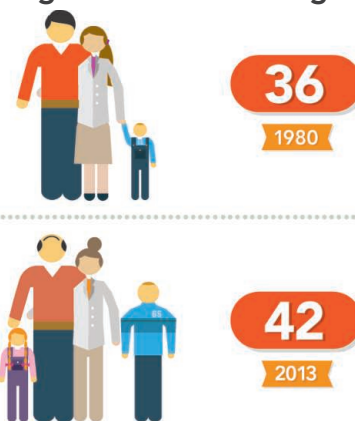
Review deemed it too similar to her previous application, making it ineligible. "I spent the summer really frustrated and trying to figure out what direction I needed to go," Yacoubian says.

To wow reviewers with a brand-new topic, she generated data for yet another R01, on how a misfolded protein spreads through the brain in Parkinson's. She opted not to replace a departing postdoc, graduate student, and technician, so her staff dropped from six to three. Small foundation grants and bridge funding from her department kept her afloat, barely. In February, after ice storms closed her 4- and 7-year-olds' schools for 6 days, Yacoubian hit a low point. "I've seen folks I've known who've been very successful in science just finally say, 'It's just not worth it,'" she says.

Last month, as winter thawed into spring, Yacoubian finally got some good news. Nearly 7 years after she finished her training, she learned that her latest R01 submission scored well within the funding window for early stage investigators. Just one step remains—approval by an NIH council in May. "A weight is off my shoulders," she says. But she won't relax until she has the award letter in her hand. After so much time struggling to make it, she's still not sure she has.

–JOCELYN KAISER
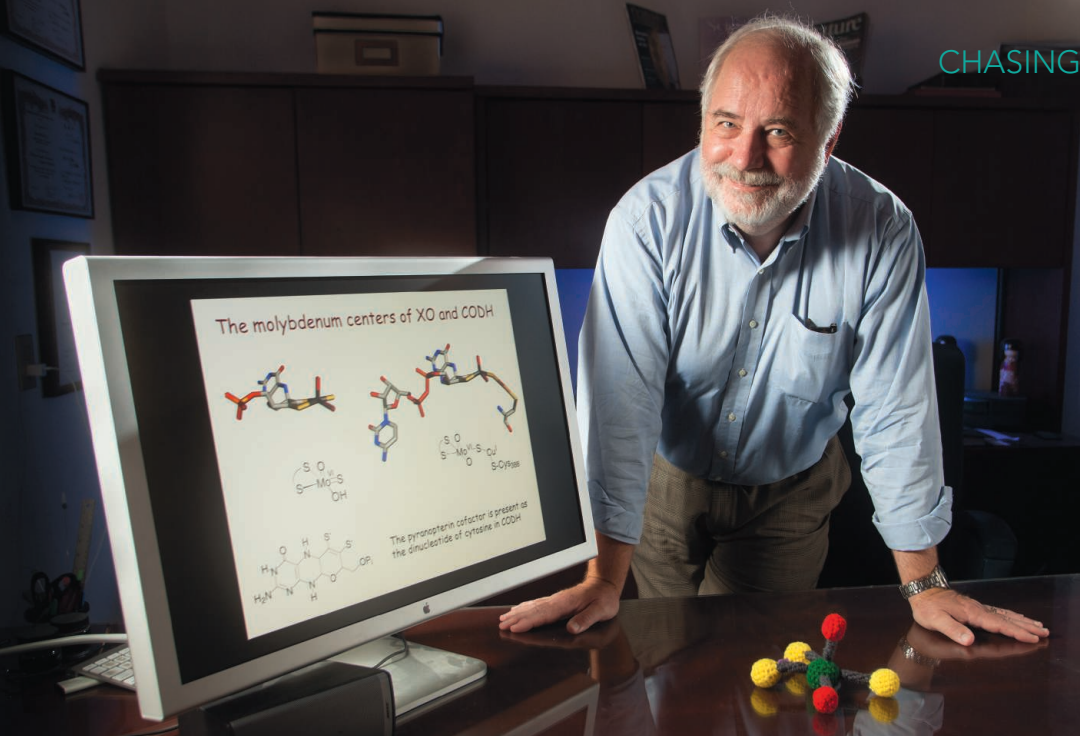
The Veteran: Russ Hille

Russ Hille was smitten with science back in high school. But it wasn't until he took a biochemistry course in college in the 1970s that, he says, "the angels started singing." The infatuation led to an illustrious career—a Ph.D. in biochemistry in 1979, research awards from the Alexander von Humboldt Foundation in 2003 and 2011, honors from two universities for his work in enzymology, and international recognition from his peers. But in 2012 at the University of California (UC), Riverside, he hit a wall. His longtime patron—the National Institutes of Health (NIH)—told him it was cutting him off.

The news came as a shock, Hille says—as astonishing as the act of generosity that launched his lab more than 3 decades ago. Back in the 1980s, he was a postdoc with renowned biochemist Vincent Massey at the University of Michigan, Ann Arbor. The science was about as basic as it gets: They studied an essential enzyme called xanthine oxidase that, among many roles, helps make uric acid that is excreted in urine. As he dug into the project, Hille became fascinated by an active site in xanthine oxidase that contains the trace metal molybdenum. He decided to focus on the class of molybdenum-containing enzymes. Massey agreed. More than that, he let Hille keep half of the National Science Foundation (NSF) grant on which they were co-investigators; Hille later took it to a new job at Ohio State University, Columbus.

Now 62, bearded, and congenial, Hille, like many older scientists, says he has no plans to retire anytime soon. He speaks with irony about his money problem—not his first. In the mid-1980s, after NSF declined to continue its support, he turned to NIH and won two grants worth a total of $1 million per year.

At regular intervals, NIH readily renewed his grants, sustaining his group of about 10 researchers. In 2007, he moved from Ohio to sunny UC Riverside to head its biochemistry department. His colleague and friend at Riverside, Thomas Baldwin, the former dean of the university's College of Natural and Agricultural Sciences, recalls that Hille's NIH portfolio seemed like a "phenomenal amount of money."

No more. In 2011 and 2012, for the first time in nearly a quarter-century, Hille's grants from two NIH institutes were not renewed. Stunned, he appealed. His merit scores remained below the fundable level, and he was out.

A shrinking NIH budget likely forced Hille's research to the sidelines. For more than 20 years, his proposals had won merit rankings near the top 10% of grants considered. He says that such rankings are no longer a guarantee of success: "It's clear that for the foreseeable future a score in the teens will not get you funded. You've got to be in single digits."

One reviewer's evaluation, Hille says, "dinged" his grant for not being "innovative." Hille disagrees. Furthermore, he argues, "innovativeness" is a subjective measure, one that he thinks NIH favors more now than in the past.
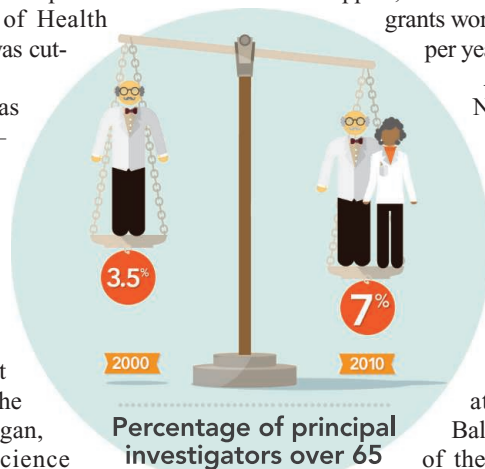
Even after decades of devotion, Hille concedes that molybdenum enzyme research is "an unsexy area." But, he insists, it is important. The enzymes modulate oxidation and reduction reactions that are critical to life. "Very bad things happen to humans when they are not able to utilize molybdenum properly," Hille says. Mutations in the four known human molybdenum enzymes can lead to toxicity and death. A 1988 Nobel Prize celebrated work in which molybdenum enzymes were critical, including the discovery that the anticancer drug 6-mercaptopurine can stop leukemia if given with a molybdenum enzyme inhibitor. But Hille doesn't focus on medicines, just the biology.

Richard Holm, former chair of Harvard University's chemistry department and now a professor emeritus there, calls Hille "one of the most important if not the most important molybdenum biochemist of the last 40 years." But he also intimates that the field has lost its fizz. Holm was fascinated by these enzymes 2 decades ago, but now he says, "from my point of view, the most interesting questions have been answered."

Without NIH's support, Hille's lab has shrunk. Now it's just him, an associate to manage the research, and three grad students. This slimmed-down team found a new patron last summer. The Department of Energy awarded Hille a $480,000, 3-year grant, backing his plan to study an exotic enzyme with a unique active center that contains both molybdenum and copper. It's found in bacteria that consume carbon monoxide; Hille argued it might prove useful in bioenergy production.

"I'm still in the saddle," Hille insists. Before long, he aims to take another run at NIH. **–ELIOT MARSHALL**

The molybdenum centers of XO and CODH

The pyranopterin cofactor is present as the dinucleotide of cytosine in CODH

Percentage of principal investigators over 65

3.5% 2000

7% 2010

The Adapter: Rachel Brewster

Rachel Brewster is 46, an explorer of brain development with a dogged determination. "Maybe you talk to me 5 years from now, and I tell you I fought the battle and I caved in," she says. For now, "I refuse to accept that."

Brewster is tenured at the University of Maryland, Baltimore County (UMBC), and she's scrambling to remake her lab and her science as her first major research grant expires this month. She is letting her postdoctoral fellows go; a frantic search to secure them alternate employment has met with partial success. She's on the cusp of winning a small grant from the National Institutes of Health (NIH) and is preparing to manage her lab on $50,000 a year, down from about $200,000. In 2 years, that shoestring budget itself will run dry.

Brewster landed at UMBC in 2003, after marrying a biologist she met at New York University (NYU) who accepted a job at Johns Hopkins University in Baltimore. Since securing tenure, she aspired to create a different culture from the one she experienced during her postdoc, in a prestigious lab at NYU's Skirball Institute of Biomolecular Medicine. "I do not want to have the kind of cutthroat lab where people feel the pressure to work Saturday, Sunday, 16 hours a day," she says. "But then there's of course a price to pay," she admits. "The price to pay is in productivity."

Her lab uses zebrafish to disentangle how the early brain is shaped, and Brewster has also made it a priority to support women and students from minority groups. In part that reflects her own background—she grew up in Switzerland, the child of a Jamaican mother and a British Guyanese father who worked for the United Nations. She's fiercely proud of UMBC, a state school that graduates a remarkable 40% or so of its students, many of them minorities, from science-based majors, well above the national average of 25%. "A lot of our students are daughters and sons of recent immigrants, people who still believe in the American dream and who are investing every penny and dime they have to get their kids an education," she says.

Brewster's funding fortunes have tracked biomedicine's budget gyrations. In early 2009, just as she was up for tenure—and just as her training grant from the National Science Foundation was about to run out—she received a congratulatory phone call from NIH. Her application for an R01, the individual research grant that's manna to many scientists, had been funded on the first try.

37,008 2000   **61,013** 2013

Grant applications

12,245 2000   **11,199** 2013

Grant awards

Relief mingled with surprise. Brewster had received strong but not stellar reviews, scoring in the 23rd percentile, below the official cutoff for funding. But timing was on her side: President Barack Obama's stimulus package to combat the national recession had begun a $10.4 billion, one-time infusion into NIH. Brewster became a beneficiary. For the next 5 years, she was safe.

Taking nothing for granted, she immediately began thinking ahead. Within a year, Brewster had submitted a new proposal to the nonprofit March of Dimes, to study a protein that unexpectedly guides neural tube development. It was rejected. She turned to NIH, and there received a review score in the 14th percentile—her highest ever—but it wasn't enough. Back to the March of Dimes, which turned her down again. Then finally last fall, Brewster logged on to her computer, shaking, to learn how she'd fared in a second and final attempt at NIH. The news was exceptionally good: She'd hit the 2nd percentile and was nearly guaranteed to receive $100,000 over 2 years.

Still, things were looking grim for her lab. Productivity lagged, in part because she and her postdocs had been busy churning out more than a dozen grant applications. Brewster hadn't published since 2011 and decided not to even bother trying to renew her R01 yet, certain her lack of papers all but assured rejection.

As this spring closed in, Brewster knew her postdocs had to go. She was paying for them out of the expiring grant. Unlike fellows at top research schools who often secure their own funding, those at UMBC are less likely to do so. Brewster describes one as "totally brilliant" but unlikely to progress on an academic track. The other, a Johns Hopkins Ph.D., had a strong desire to teach and had joined Brewster's lab to keep her options open.

Meanwhile, Brewster constantly considers how to stretch the dollars she has. One challenge is finding cheap labor. A dozen undergraduates now rotate through her lab. She recruited a woman she knows, who never completed her Ph.D. and is home with her three children, to spend 2 months training lab members to perform cell transplants on zebrafish. Brewster shares a technician with a colleague. Her four graduate students are supported by teaching assistantships. And Brewster herself, who receives a 9-month stipend from UMBC but relies on grants to cover the summer months, is taking no money to cover the 3-month gap, a substantial salary cut.

Brewster sees her future in sharp relief: To survive, she believes, she must remake her science and her funding strategy. It may be years, if ever, before she applies

again for an R01 as a solo scientist, and she is in discussion with a colleague in Washington, D.C., about a joint application. She's weighing a high-risk, high-payoff NIH grant, for a study with colleagues on the effects of low oxygen in the zebrafish brain, and considering seeking money from the Department of Defense or the American Heart Association.

Brewster recognizes that her small lab, with students and trainees who may need extra nurturing, isn't a powerhouse on par with the Harvards and Stanfords of the world. "But if the measure is what am I contributing by training the next generation of scientists, I am doing more" than colleagues at far more prestigious universities, she contends. Furthermore,

"creativity can come from anywhere, good critical thinking, innovative thinking, can come from anywhere," she says. She points to the movie business, which includes big-budget films along with tiny independent ones. Both have a contribution to make. In science, she asks, "do you want to have a world with nothing but blockbusters?"

–JENNIFER COUZIN-FRANKEL

The Administrator: Jay Walsh

Jay Walsh's spacious second-floor office suite may be tucked away in a drab, concrete building in Evanston, Illinois, but it sits at the heart of Northwestern University's vibrant research enterprise. Walsh is all about the big picture. At 54, after 2 decades at Northwestern as a faculty member, he has risen to be vice president for research. There, he sees the disconnect between the upbeat view from 10,000 feet and the strain playing out in individual labs.

Walsh's days focus on money: helping his staff navigate the rules required to bring in state dollars, traveling to meetings with funding agencies and local and state officials, and courting donors whose checkbooks he's keen to crack open. In many ways, life these days is good for Walsh—and Northwestern. The university celebrated an 8% rise in overall research funding in 2013, to $550 million dollars. Its support from the National Institutes of Health (NIH) has soared 90% in the last 13 years, far faster than NIH's budget. Like other institutions, Northwestern suffered under the sequester that knocked 5% off NIH's 2013 budget. But while its own NIH funding dipped 4%, it was able to compensate with money from other government agencies, nonprofits, and industry.

Walsh, who worked on developing laser ablation and optics as medical tools before stepping into his current post in 2007, credits several factors for the university's financial success. There are medical school alliances with local hospitals and research partnerships with the Department of Energy's nearby Argonne and Fermi national laboratories, on whose boards he serves. Northwestern is drawing on the annual payout from its roughly $8 billion endowment to help it fund startup packages for new faculty in renewable energy, biomedical sciences, nanosci-

Increase Between 2000 and 2013

ence, and other areas. With Northwestern Medicine, the university's medical school in Chicago is embarking on a $1 billion expansion. A new building is slated to break ground next year.

The school's growth backs a common perception among biomedical scientists: that the rich are getting richer, while universities with more modest resources are shrinking. But on a big scale, that perception is simply incorrect, says Sally Rockey, NIH's deputy director for extramural research. "Over a 25-year period we've hardly seen a difference in which are our top 100 institutions," says Rockey, who notes she likes to "blow up urban myths." She adds, "we don't see growth, we don't see decline" in how institutions are faring relative to one another.

Northwestern, however, is an exception: Its ranking among NIH-funded institutions has climbed from 36th to 22nd from 2002 to 2012. But while Walsh savors the numbers, his scientists struggle to maintain them. One center director told Walsh that he now submits nine proposals to win a couple of grants, rather than the five he used to. Even if the money still flows into the center director's bank account in the end—which so far it has—securing the dollars remains fraught with uncertainty.

One way the university has tried to ease this burden is by embedding staff within departments to handle the administrative portions of grants, such as budgets and faculty biosketches. Last year, a donor chipped in to create a dedicated bridge fund, available to faculty whose applications score within striking distance of the funding cutoff. But only eight, including seven of about 540 principal investigators in the medical school, are relying on formal bridge money now.

Others are making do in different ways—for example, by tapping unused grant funds they'd previously stashed away. This cohort is largely invisible, and Walsh doesn't know how many apparently secure scientists belong to it.
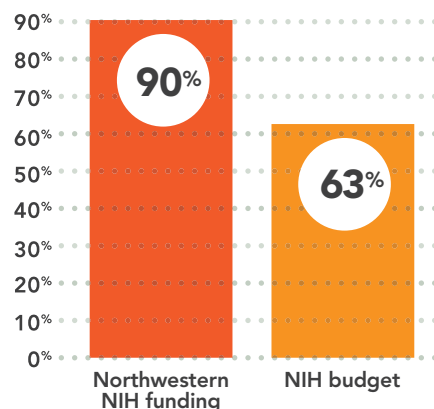
–JOCELYN KAISER

The Well-Heeled: Donald Bowden

Donald Bowden likes to say that his field favors "the most adaptable, or the best adapted." And in the Darwinian environment of biomedical research, the 63-year-old geneticist is undeniably well adapted. Last year, his lab at Wake Forest University in Winston-Salem, North Carolina, received more than $2.8 million from the National Institutes of Health (NIH), all of it research project grants known as R01s. In 2010, he ranked in the top 2% of about 26,000 project grant recipients. Bowden's success reflects a mix of factors—a hot area of research, good timing, strong collaborations. And, most likely, a healthy dose of luck.

"It isn't like my career was this can't-miss, success-is-obvious kind of career," Bowden maintains. But his research focus—the genetic underpinnings of type 2 diabetes and its complications in African-Americans—is attracting more and more attention and concern. Using funding that first trickled in from foundations, then gushed from NIH when the

Bowden says. As a young Ph.D. student in molecular biology at the University of California, Berkeley, he was drawn to clinical questions while many around him championed basic research. After finishing a postdoc in 1981, he spent 9 years at a now-defunct Massachusetts biotechnology company, exploring the genetic underpinnings of endocrine diseases. In 1989, he made the jump to Wake Forest, bringing with him a modest NIH grant for diabetes genetics.

In Winston-Salem, Bowden found himself at the heart of a large African-American community deeply affected by the disease and its complications. He soon teamed up with a young Wake Forest nephrologist named Barry Freedman, and the two began recruiting volunteers to examine the genetic basis of kidney disease. Bowden was most interested in the disease as a complication of diabetes, but remained open to other questions, too. "He didn't have tunnel vision," Freedman says. "He very early on recognized the value of

Bowden's database now contains more than 15,000 DNA samples, 2000 CT scans, and MRIs and cognitive testing outcomes on hundreds of volunteers. His network includes dozens of clinicians, geneticists, statisticians, and epidemiologists. He has created a resource that continues to entice those with deep pockets.

One reason for that, Bowden believes, is his work's obvious clinical implications. He suspects tighter budgetary times are "driving things to be more translatable, which I actually don't think is bad." His current projects—he has seven active R01s, plus modest support from individual donors—aim to pinpoint genetic loci for diabetes risk and

6% of senior scientists have $1.5 million or more in grants, and they consume 28% of all research projects grant funding.
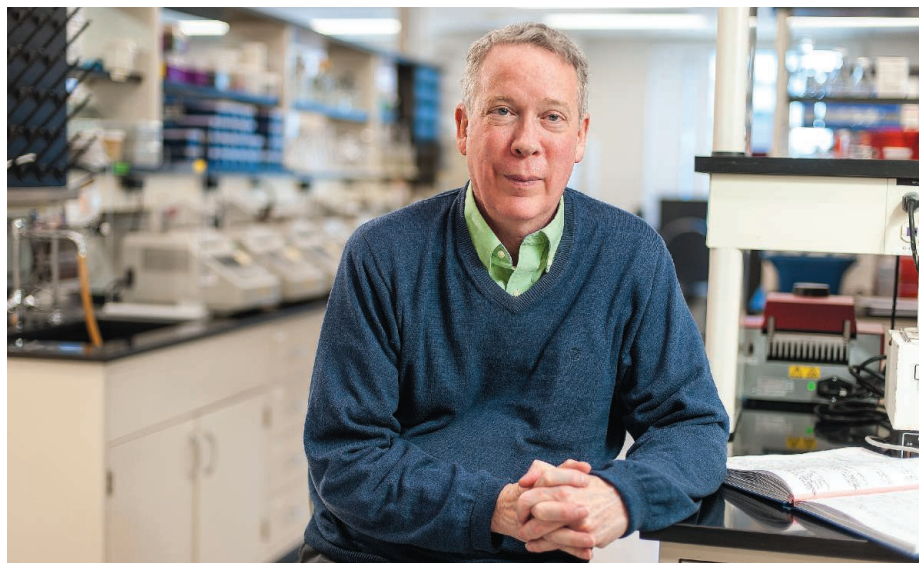
agency was at its most generous, Bowden drew on nearby neighborhoods to build a large genetic database. It continues to fuel new research questions and attract new grants.

Meanwhile, he found collaborators in other Wake Forest investigators, who offered both a scientific sounding board and a financial safety net. When one lab's funding runs thin, a colleague's money keeps projects chugging forward. The research network, with Bowden's 16-person genomics lab at its core, is prospering and extending support to more vulnerable young scientists.

"The threads all go back quite a long way,"

what a genome center could do."

Still, Bowden says the early '90s were "anxious times" financially. When NIH didn't come through, an aging center at Wake Forest offered him a small pilot grant to collect heart CT scans on diabetic patients. The preliminary data convinced the American Diabetes Association to kick in more cash.

As the database of scans and DNA samples grew, NIH took notice. In 2001, in the midst of the agency's celebrated budget doubling, its National Heart, Lung, and Blood Institute offered Bowden and his collaborators roughly $1 million a year for 3 years.
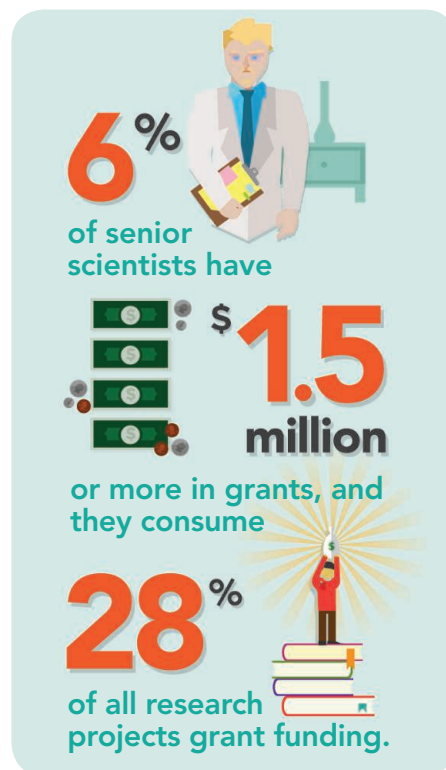
diabetic kidney disease in African-Americans, and find rare gene variants that contribute to risk of cardiovascular disease in both African-Americans and Hispanics.

Bowden's advice to fledgling researchers: Seek shelter with a well-funded lab and join an existing study, then steer toward independence—one step at a time. His career, Bowden acknowledges, hasn't been marked by dramatic breakthroughs. "Everybody hopes to have a really big hit, which I don't think I've really gotten yet," he says. But after a "slow and painful" climb, he's enjoying the payoff. **–KELLY SERVICK**

The Crowd-Funder: Heidi Moretti

27 January 2014: 35 days remaining, $0 raised—Heidi Moretti's plea for $4350 has gone live. The nutritionist was halfway through a 40-patient clinical trial examining whether vitamin D can help people with heart problems when some of her small grants and institutional support ran out. "With your help," Moretti writes on the website Experiment.com, "we can complete our study, publish our findings and influence the care of chronic heart failure for the better."

A clinician at St. Patrick Hospital in Missoula, Montana, Moretti, 40, had discovered the website a few months earlier as she pondered how to raise some extra cash. Like many other biomedical researchers, Moretti is hunting for money beyond traditional sources such as the National Institutes of Health. Some have tapped private foundations, wealthy individuals, and businesses. "Crowd funding" has opened yet another avenue, demonstrating that small donors can pile up millions of dollars for projects such as movies, smarter phones, and even a better backyard telescope. Now, a few science-focused groups, including the websites Experiment, SciFund Challenge, and Petridish, want to replicate that success.

Acting on a tip from a staffer at the Vitamin D Council, a California-based nonprofit, Moretti was soon polishing punchy graphics and prose for her 35-day campaign. But she wondered: "Could it really work?"

33 days remaining, $1000 raised—The first donations roll in, including some from friends and family in Moretti's hometown of Valier, Montana, population 509. To spread the word, she spends evenings on e-mails, Facebook updates, and testing her wings on Twitter. "Vitamin D research for heart failure patients in progress," she tweets. "Please help or retweet!"

Thinking about how to attract $10 or $100 at a time was a "very creative and exciting process," Moretti says. It took about 10 days to prepare her plea— relatively painless compared with the grind of assembling a formal proposal to a big government funder or foundation. But the yield is almost certain to be much lower, too.

7 days remaining, $2100 raised—"The deadline was getting closer, and I was stuck at about 50%," Moretti says. "But they warn you to expect most donations at the beginning and the end. So I just kept reaching out." Each week, she got a small surge after the Vitamin D Council featured her project in its e-mail newsletter.

Moretti knew it was all or nothing. Like many crowd funding sites, Experiment takes a cut of successful campaigns—5% in this case. But if the goal isn't met, neither the site nor the researcher get anything, and donors aren't charged. Active social networking can tip the scales, says Experiment.com staffer Oscar Jasklowski, a former bioengineering doctoral student. It was especially critical for Moretti, whose hope of $4350, as modest as it sounds, placed her in a danger zone. About 70% of those who ask for less than $3000 have met their goal, but the success rate dips for bigger asks. Overall, as of the end of March, about 39% of the site's 298 completed projects had raised what they'd sought. The 117 successful projects raised some $732,000; the two largest about $25,000 each.
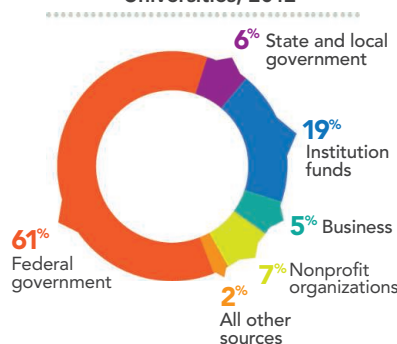
5 days remaining, $4300 raised— The Internet's global reach is suddenly on vivid display. "Out of nowhere, from someone I didn't know" comes a gift of $2000, Moretti says. The donor, who lives in Turkey, finds her through a mention in the Vitamin D Council newsletter.

Although generous, $2000 is a drop in the bucket for most biomedical researchers. Private dollars aren't about to replace government funding: In 2012, for instance, 7.25% of the estimated $37.2 billion spent on life sciences research at U.S. universities came from philanthropic sources, according to the National Science Foundation. Still, for scientists like Moretti operating on shoestrings, this money-raising tactic offers a chance to stay in the game.

0 days remaining, $4510 raised—Elated and relieved to have surpassed her goal, Moretti says she "wouldn't hesitate" to crowd fund again. The final tally: 37 gifts, an average of $122 each. "With grants, there is waiting and waiting," she says. "This way, you get a pretty immediate response from people you know care about the research."

–**DAVID MALAKOFF**

Life Sciences Research Funding at U.S. Universities, 2012

- **6%** State and local government
- **19%** Institution funds
- **5%** Business
- **7%** Nonprofit organizations
- **2%** All other sources
- **61%** Federal government

Anatomy of a Grant:
Michael Imperiale

Every year, about $16 billion flow from the coffers of the National Institutes of Health (NIH) to labs lucky enough to have won an individual research grant. From there, the money buys microscopes and gene sequencers, pays for graduate student stipends, supports travel, keeps the lab lights lit and the bathrooms stocked with toilet paper, and serves a myriad of other purposes. *Science* wanted to track this spending, following where exactly grant money goes.

So we asked some researchers if they would open their books for us. The answer was usually no: Scientists told us they worried about inviting an audit from their funding agency. One who agreed was Michael Imperiale, a microbiologist at the University of Michigan, Ann Arbor. He shared details for a 5-year R01 grant, the individual research award from NIH on which many scientists rely. Imperiale won his R01 in 2010, to study the molecular biology of BK polyomavirus, which causes urinary tract infections in childhood and can cause life-threatening illness in recipients of kidney and bone marrow transplants. Like many scientists, he balances essentials like salaries with supplies—all the while paying a heavy overhead charge to his university.

–YUDHIJIT BHATTACHARJEE
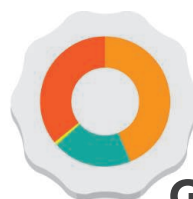
GRANT TOTAL
$1,150,979

So far, this is how much NIH has paid out. And here is where the money went, from the time Imperiale was awarded funding in 2010 until January 2014.

SALARIES + BENEFITS
$504,184 / 43.8%

Paying for the people doing the research takes a huge bite. For Imperiale, that includes support for a postdoc, a research technician, and two part-time undergrads. Unlike some researchers in this era of "soft money," Imperiale isn't relying on the grant to pay most of his salary. His R01 provides for a quarter of the roughly $220,000 a year that supports him and his family. In addition, Imperiale gives a cut to the university for tuition for one graduate student; so far, that's amounted to $46,640.

"Until about 3 years ago, I had a second grant," Imperiale says. "When it didn't get renewed, I had to shut that project down and cut back on personnel." Fortunately, the affected lab members were already transitioning elsewhere.

SUPPLIES
$225,971 / 19.6%

The antibodies Imperiale uses to determine whether the virus is replicating "cost a ton of money," Imperiale says: between $300 and $500 dollars for 200 micrograms, which typically covers a batch of 1000 slides. "We also use primary cells, which are expensive to buy and culture." It doesn't help that the cost of supplies Imperiale buys keeps going up.

And he is not alone. The Biomedical Research and Development Price Index, which goes by the catchy acronym BRDPI (pronounced "bird pie"), has for decades tracked biomedical inflation and how it compares with inflation in the general economy. Since 1980, BRDPI has outpaced economic inflation in every year but one.

When funding is tight, the lab tries to cut costs in every way possible: by rationing supplies, for example.

TRAVEL
$10,024 / 0.87%

Airplane tickets and hotels are expensive, but Imperiale and two to three lab members attend two conferences every year: the American Society for Virology's annual gathering and the smaller DNA Tumour Virus Meeting. There, they catch up with colleagues from around the world, swap ideas for experiments, and showcase their work.

Imperiale's grant doesn't cover all the meeting costs—just registering for the virology meeting costs $500 for a member of the society and $400 for each graduate student. He draws on discretionary funds from the university to close the gap. Even in the age of Skype and other video-conferencing technologies, meetings remain immensely popular and a huge moneymaker for dozens of scientific societies.

INDIRECT COSTS
$410,800 / 35.7%

The University of Michigan—like all institutions—charges the federal government a fee for providing the infrastructure needed to carry out federally funded research projects. So far, it has collected $410,800 from NIH to host Imperiale's grant, a fairly typical rate. This amount works out to a little more than a third of the total funding that NIH is shelling out for his R01.

Where does this money go? It pays for maintenance of the 120-square-meter space that Imperiale's lab occupies—everything from electricity and heating to janitorial services. Accountants and other employees on campus who manage the grant take a cut. The university must maintain biosafety and chemical safety, and keep Imperiale's lab in compliance with an ever increasing list of federal regulations. The upshot is that this portion of the overall grant never reaches Imperiale.
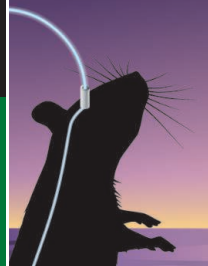
LETTERS

edited by Jennifer Sills

NextGenVOICES

Results: Science Advocacy

If you had 5 extra hours per week to devote to advocacy for science, how would you use that time? In January, we asked young scientists to send us their ideas. We heard from almost 300 readers. Many felt that their time would be best spent inspiring schoolchildren; creating accessible articles, blogs, and media to explain science; and reaching out to the public through workshops and talks. A sample of the responses can be found below. To allow for as many voices as possible, in some cases we have printed excerpts of longer submissions (indicated by ellipses) and lightly copyedited original text for clarity. To read the complete versions, as well as many more, go to http://scim.ag/NextGen10Results.
Follow *Science*'s NextGen VOICES survey on Twitter with the hashtag #NextGenSci.

Submit Now: Science Ethics

Add your voice to *Science*! Our new NextGen VOICES survey is now open:

What is the most challenging ethical question facing young investigators in your field? How should it be addressed?

To submit, go to http://scim.ag/NextGen11

Deadline for submissions is 16 May. A selection of the best responses will be published in the 4 July issue of *Science*. Submissions should be 250 words or less. Anonymous submissions will not be considered. Please submit only once.

NextGen Speaks

I WOULD GO TO MIDdle schools and high schools and give presentations to students demonstrating what real science is.... I believe that they need to be shown that science isn't the endless stream of words and formulas that they find in textbooks. To me, the phrases "wow," "no way," and "really?" should represent what students think of science, instead of "I hope I don't fail."

HANI I. NAGA

Vagelos Scholars Program in the Molecular Life Sciences, University of Pennsylvania, Philadelphia, PA 19104, USA. E-mail: haninaga@sas.upenn.edu

...I WOULD ORGANIZE AND CARRY OUT teacher hikes where we would discuss current science topics/debates.... We don't learn to appreciate the world around us from textbooks, nor do we become enthusiastic about meetings with Powerpoint slides. However, most of us enjoy informative conversation, and most of us could use a bit of exercise in the outdoors. Teachers (of all kinds, not only STEM teachers) exert tremendous influence over our next generation of citizens.... When a teacher is interested, the students become interested. Teachers are the most effective advocates for science. Carl Sagan stated, "Science is a way of thinking much more than it is a body of knowledge," and it is the teachers who will change the way of thinking.
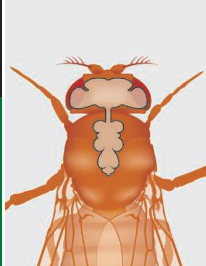
HELEN PETACH

AAAS Science and Technology Policy Fellow, U.S. Agency for International Development, Washington, DC 20523, USA. E-mail: helen.petach@gmail.com

I WOULD VOLUNTEER MY EXTRA TIME AND resources toward sharing my passion for science with younger students in underprivileged schools. As a former middle school science teacher, I have witnessed the unfortunately low emphasis on science at younger ages, especially in low-income schools, yet I have also seen it excite and change the mindset of the way young students interact with the world. If we want to change the understanding gap between academics and the public, then we need to share our passions with younger generations in order that they may understand the problems, policies, and choices that they will face in the future.

KEN LUZYNSKI

Department of Integrative Biology and Evolution, Konrad Lorenz Institute of Ethology, University of Veterinary Medicine, Vienna, 1160, Austria. E-mail: kenny.luzynski@gmail.com

I WOULD GIVE LECtures to school pupils and students about science and how it serves society and improves lives. I would also write newspaper articles about harnessing science for the betterment of communities.

OTHUSITSE RICKY MADIBELA

Department of Animal Science and Production, Botswana College of Agriculture, Gaborone, 6, Botswana. E-mail: omadibel@bca.bw

...I WOULD LIKE TO help the students in the poor mountainous areas in Western China to learn the latest scientific advances. ...Computers and Internet are not avail-

a model with whom they can identify. The long-term objective is to stimulate scientific vocation. When asked the question "What would you like to do as a job?," young children would answer not only "doctor, teacher, pirate, or princess," but also "scientist."….

MATHILDE LAURENT-BROCQ

Institut de Chimie et des Matériaux Paris-Est, CNRS UMR 7182, Equipe Métaux et Céramiques à Microstructures Contrôlées, 94320, Thiais, France. E-mail laurent-brocq@icmpe.cnrs.fr

able for many primary and secondary schools there, and the teachers may be "village teachers" who have not received higher education. Consequently, the students there lack understanding of the outside world. Therefore, if I had 5 extra hours per week, I would…take my computer and the most recent scientific knowledge I have learned, and I would teach them. For example, I would teach them about cloud computing, the Internet of Things, and Big Data. I think learning the latest interesting scientific knowledge would broaden their horizons and stimulate their passion for science.…

KAILE ZHOU

School of Management, Hefei University of Technology, Hefei, Anhui, 230009, China and Key Laboratory of Process Optimization and Intelligent Decision-Making, Ministry of Education, Hefei, Anhui, 230009, China. E-mail: kailezhou@gmail.com

I WOULD TRAIN TO BECOME A MAGICIAN. Then, once I have honed my skills, I would go to a school and fascinate all the kids. When I have their full attention, I will reveal all the tricks. But before they lose interest or become deluded, I'll bewitch them with more sophisticated illusions. Then I'll explain that the green rabbit I pulled out of the hat is glowing by expressing green fluorescent protein, that the fog is solid carbon dioxide that sublimates at atmospheric conditions, and that I pulled the right card out of the deck by using a mathematical algorithm. And I will say to the kids that if they study science, they will touch that magic.…
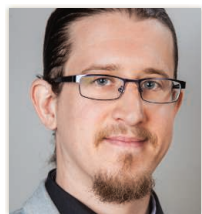
CORRADO NAI

Department 4, Materials and Environment, BAM Federal Institute for Materials Research and Testing, 12205, Berlin, Germany and Department of Microbiology, Free University of Berlin, 14195, Berlin, Germany. E-mail: corrado.nai@gmail.com

VISUAL SPAM IS EVERYWHERE. …MANY TIMES I find myself wondering, "What if it were as easy to find out about new science discoveries as it is to learn about brand new models of cars, drinks, or women's clothing?" Maybe if we had a little information about the mysteries of nature, we would be inspired to pursue a branch of science…. If I had 5 hours a week to spare, I would start placing posters on my college walls. They would begin with "Did you know...?" and then provide text about interesting scientific facts. I would include related unsolved questions and end with the phrase "Would you help spread the word?" **NICOLÁS A. CAPITELLI**

Departamento de Matemática, Facultad de Ciencias Exactas y Naturales, Universidad de Buenos Aires, Buenos Aires, 1428, Argentina. E-mail: ncapitel@dm.uba.ar

I WILL CREATE A CARTOON WHOSE HEROES ARE children (boys and girls) who solve the world's problem thanks to science. Each science specialty (physics, chemistry, mathematics, biology, computer science, and so on) would be represented by one character. Those children would be the new "scientific superheroes." The "bad guys" would be a society of grown-ups who are against change and sharing of knowledge. The idea is to give to children

MAYBE IT'S TIME TO LET SCIENCE ADVOCATE for itself. Science has come to acquire solemnity, whereas it should be about curiosity and amazement. …I believe in taking science into the everyday world of as many people as possible, 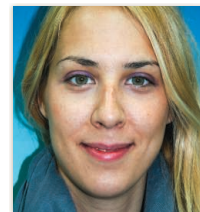trying to get the scientist into real-life scenarios. Schools and kindergartens should be able to visit research labs, but also scientists should be able to spend a few hours a week in educational institutions, and not only that, but every cultural space available. We need more likable science geeks and more socially adequate Ph.D.s who are able to not only educate but entertain. I'd use my time trying to bring the sexy back to science, or at least making sure to make someone laugh and learn something while trying. **PABLO ADRIÁN GONZÁLEZ**

Laboratorio de Agrobiotecnología, Departamento de Fisiología y Biología Molecular y Celular, Universidad de Buenos Aires, Buenos Aires, Argentina and El Gato y La Caja (elgatoylacaja.com). E-mail: pablo201083@gmail.com

THE GOAL OF THE ADVOCACY IS TO MAKE science available and interesting to a much broader audience than the scientific community…. To reach the general public and send an effective message, science should exploit the power of social and mainstream media. However, bringing media and science together represents a challenge and requires various 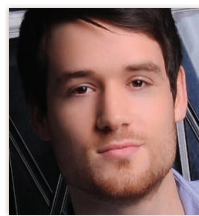skills, from understanding scientific literature to being able to market and communicate it further to broader audience. Thus, for fruitful advocacy, at the beginning, I would devote 5 hours per week to learn from the experts what and how people want to hear from us. Afterward, I would use this time to engage in tweeting interesting results from articles I read, posting about new achievements on a widely used

Web portals, or finding ways to participate in TV/radio shows and give thought-provoking talks. If we learn how to use all these social media tools, possibilities are endless…. In the end, if we as scientists don't speak loudly, how will others know and understand the importance of science?　**MARJANA BRKIC**

Department of Neurobiology, Institute for Biological Research, University of Belgrade, 11000, Belgrade, Serbia. E-mail: marjana.brkic@ibiss.bg.ac.rs

…I WOULD CREATE A BLOG THAT WOULD emphasize the potential practical applications of "useless" research. It would elucidate connections between findings in different fields and potential applications, and crowdsource opinions to stimulate interdisciplinary collaboration and debate the most urgent direction for the translation of breakthroughs. ….　**JAVIER ELKIN**

Institute of Neurology, University College London, London, WC1N 3AR, UK. E-mail: javier.elkin.10@ucl.ac.uk

…HAVING AN EXTRA 5 HOURS, AS A YOUNG woman scientist, I would take a leadership role in the advancement of diversity in scientific fields. There is a dire need to support diversity in both the academic and corporate scientific workplace. Part of diversity could be achieved by developing a structured program on mentoring and encouraging young girls to pursue careers in science, engineering, and technology. The extra time could be used to hold regular meetings and address issues affecting young women in science without interfering with one's academic or social activities.…　**REGINA MAPHANGA**

Materials Modelling Centre, University of Limpopo, Sovenga, Polokwane, Limpopo, 0727, South Africa. E-mail: maphangarr@yahoo.com

I WOULD DEVOTE THAT TIME TO DEVELOPING the presence of science on media outlets like YouTube. The new generation of scientists is accustomed to instant gratification; information is at their fingertips in short phrases on a single Web page. YouTube channels dedicated to STEM topics, such as SciShow, have videos with hundreds of thousands of views. Using animated diagrams to describe a cell process or writing out a mathematical concept on a digital screen allows inquisitive young minds to digest the content more easily. Narrated by a witty voice-over in 10 minutes or less, these videos teach a concept without scaring away a student like lengthy journals or hour-long lectures tend to do.　**MEGAN NOLL**

Department of Biochemistry, University of Pennsylvania, Philadelphia, PA 19104, USA. E-mail: megnoll@sas.upenn.edu

…I WOULD SPEND THOSE HOURS AT THE HOSpital, sitting alongside family members of patients. A 5-minute talk with the physician about the health status of their relative is often all the information they receive. I believe that those people deserve a better understanding of the current scientific knowledge about the disorder affecting their relative. In return for giving them a better understanding, I would try to convince them that the impact of nonscientists will be crucial in the next two decades of science. To reach the next level in science, we will need the entire community to support us with ideas and technology share (such as computer power and electricity sharing). With 39 million hospitalizations in the United States every year (according to 2007 data), this group forms a highly accessible and motivated source of scientific supporters. Only in times of crisis do we realize the threats of disease that wait ahead of us in life, and I believe this is the perfect moment to activate this group of people to contribute to science in the next decades.…　**ELIAS ADRIAENSSENS**

Department of Pharmacology, University of Oxford, Mansfield Road, Oxford OX1 3QT, UK. E-mail: elias.adriaenssens@pharm.ox.ac.uk

…I WOULD CREATE A CONSORTIUM OF CONcerned young scientists advocating for legislative action on climate change, with a thrust toward scientists in red states. Our major objective would be to write state and national representatives, imploring that they make the hard decision and look long instead of short, valuing societal over personal gain, and enact a price on carbon dioxide and other greenhouse gases that would put renewable technologies on an equal playing field with fossil fuels. The only chance for action in Washington is a ground-up movement of voters demanding responsibility, and what better place to start than with those who understand the implications of climate change the best?　**DAVID GARFIELD**

Department of Chemistry, University of California, Berkeley, Berkeley, CA 94702, USA. E-mail: david.garfield@berkeley.edu

…A CONSIDERABLE AMOUNT OF TIME AND funding must be spent to repeat the same experiments and find the details of optimized conditions. By creation of some comprehensive online databases, these parameters could be organized and shared with others. This would help various research groups to focus only on their main cutting-edge project goals and save their time and financial resources.…If I have several extra hours per week to advocate science, I will help to generate such databases, at least in my own field of expertise.　**HAMED ARAMI**

Department of Materials Science and Engineering, University of Washington, Seattle, WA 98195, USA. E-mail: arami@uw.edu

…WITH 5 EXTRA HOURS TO DEDICATE TO ADVOcacy, I would want to sit down for lunches with all the congressmen and senators and tell them what science means to me, the next generation of scientists, and most importantly, our country. Maybe if I tell them that it takes an insane amount of love and passion for science to live on $20,000 a year as graduate students and dive headfirst into the unknown that is our current R&D situation, then they will see that funding science means funding dedicated, brilliant people who advance our country's well-being behind the scenes, on old and scratched-up lab benches. I'd round up all the hungry graduate students who will excitedly talk about their projects and remind the congressmen that science is an unstoppable driving force behind innovation. I just hope they will pay for lunch.　**IRINA TIPER**

Department of Microbiology and Immunology, University of Maryland, Baltimore, MD 21201, USA. E-mail: itiper@umaryland.edu

I WILL USE THE TIME TO INITIATE THE CHINESE Scientist Oral History Project, which will document the history of science through interviews with leading Chinese scientists....This unique collection of interviews will offer fresh insights into science and scientists in China. I will...carefully survey the backgrounds of leading scientists in each field and select the best candidate willing to share his or her stories, especially autobiographical anecdotes about both career successes and failures. ...I will allow each scientist to talk candidly about his or her motivation, career path, frustrations, and triumphs, as well as family and childhood. Finally, I will make the interview video and transcripts free online....
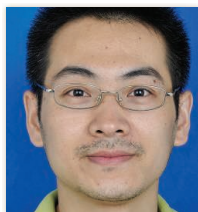
FENGBO LI

Zhejiang Academy of Agricultural Sciences, Hangzhou, Zhejiang, 310021, China. E-mail: fengboli@gmail.com

FIRST, I WOULD TURN OFF MY COMPUTER, smartphone, television, iPad, and all other electronics. I would round up a group of children from my neighborhood, the local school, the skate park, or the mall. I would take them outside to a city park, a lake, a creek, a garden. I would bring binoculars and set up a spotting scope and encourage them to look up, look down, look all around, and let their imagination run wild about how what they see got there, how it functions, and how many more questions still need to be answered. In short, I would try as hard as I could to connect young kids to the natural world around them, instilling an interest in science without a single text, tweet, or blog post. **ELIZABETH M. PHILLIPS**

School of Aquatic and Fishery Sciences, University of Washington, Seattle, WA 98195–5020, USA. E-mail: emp11@uw.edu

IF I HAD 5 EXTRA HOURS PER WEEK TO ADVOcate for science, I would use that time actually DOING science! In my opinion, the best way to advocate for science is to do science and generate exciting results that demonstrate the value of science to society. However, because of the risk of losing funding to support my position, I am instead spending those 5 hours (or more!) submitting proposal after proposal to funding agencies that can fund less than 10% of the applications that they receive....

MICHAEL G. KEMP

Department of Biochemistry and Biophysics, University of North Carolina School of Medicine, Chapel Hill, NC 27599, USA. E-mail: michael_kemp@med.unc.edu

Letters to the Editor

Letters (~300 words) discuss material published in *Science* in the past 3 months or matters of general interest. Letters are not acknowledged upon receipt. Whether published in full or in part, Letters are subject to editing for clarity and space. Letters submitted, published, or posted elsewhere, in print or online, will be disqualified. To submit a Letter, go to www.submit2science.org.

HISTORY OF SCIENCE

Complex Interplay of Islam and Science

B. Harun Küçük

Marwa Elshakry's *Reading Darwin in Arabic* is not so much about Darwin in Arabic as it is about reading the Arabic intellectual life of the late 19th and early 20th centuries through Darwin. But, above all, the book is about words, about historical semantics. It will come as no surprise to those familiar with Elshakry's previous work that she offers exceptionally nuanced readings of key concepts such as science, progress, materialism, evolution, socialism, education, nation, and the common good in Arabic. She uses words to cut through many preconceptions about Islam and modernity, most notably the very idea that science and Islam were two separate domains of meaning.

Through a careful reading of words, Elshakry (a historian of science at Columbia University) articulates the fluid transitions between epistemic, religious, and political authority. The Sultan, Muslim scholiasts, Western-educated professionals, public intellectuals, missionaries, imperial powers, nationalists, pan-Islamists, Ottomanists, and socialists vied for the public's attention and consent through a proxy battle of words waged on the high-acid paper of the industrial era. For almost all of the contenders, the stakes were no less than the very survival of Islam. But just what was the best way to serve one's religion? Here, too, we encounter a veritable list of characters. Some believed that Islam stood in need of internal reform and revival, while others tried to accommodate modern scientific ideas through Koranic exegesis and rhetoric. Some were sympathetic toward the colonial rule, while others believed in evolutionary or revolutionary socialism. Some looked up to the Ottoman Sultan, while others pleaded their case before a broad public. To some, Darwin was the harbinger of a liberating cosmology. To others, he was the embodiment of all that was wrong with the modern age.

Many of these threads merge into a knot in the pivotal chapter of the book, "Darwin and the Mufti." The protagonist of this densely footnoted chapter is the famous reformist

grand mufti of Egypt, Muhammad 'Abduh (1849–1905). His predicament, I thought, was the most interesting—no offense to the Syrian physician Shibli Shumayyil (1850–1917), a secularist who occupies much of Elshakry's attention in the earlier chapters—because it clearly illustrates just how complicated was the task of defining and defending innovation, renewal, and reform in a polarized society.

Elshakry fills *Darwin in Arabic* with careful contextualization. Nonetheless, the book demonstrates to anyone familiar with 19th-century science that—contrary to the testimonies of the French historian Ernest Renan (1823–1892) and nearly all of his contemporary orientalists—the Islamic world was not so different from Europe after all. As Elshakry notes, "Darwin's Muslim readers—like many of his global

Spreading the word about science. The cover of the widely distributed popular-science monthly *Al-Muqtataf* (The Digest). Established (1876) by editors at the Syrian Protestant College in Beirut, it moved to Cairo in 1885 and was published there until shortly after the army officers' coup of 1952.

readers more generally—did not so much view his ideas as an unprecedented novelty as see them as part and parcel of more long-standing and more familiar cosmological or metaphysical arguments, from which vantage point they were either selectively appropriated or discounted."

Arguably, the main element that distinguished the Muslim lands from Europe was the reinvigorated Arabic intellectual tradition that served as a portolan to locate novel scientific ideas in ancient philosophical waters. She identifies this long-standing heritage, which had witnessed a revival during the *Al-Nahda* (the Arabic cultural renaissance of the 19th century), as a contested resource that Darwinists and anti-Darwinists tried to enroll in their ranks. Her evidence goes so far as to suggest, I believe rightly, that tradition and scientific innovation were co-constructed as the debates raged on for nearly a century in popular journals and mass-printed books.

As familiar as the discursive elements and the intellectual positions in Elshakry's book will be to historians of 19th-century science, one cannot also help but notice the absence from the narrative of a certain sense of science: the methodical production of new knowledge about the natural world. In other words, we lack knowledge about the scientific practices of this period's Arabs. Elshakry clearly documents that they said as Francis Galton said. But did they also do as Galton did? This was, in a way, the question raised by the Ottoman mathematician and historian of science Salih Zeki (1864–1921) in his 1910 essay "İskolastik" ("Scholastic"), where he criticized the *ulama*'s propensity to reason away without considering the facts at each step of the argument. Science, he argued, was about producing and using empirical evidence, not about the ability to overcome an opponent in debate. Reading Elshakry's account, one wonders whether the Muslim discussions of the 19th century turned Darwin into a type of scholiast or whether scientific practices also had a role to play.

The question of practice notwithstanding, Elshakry's book is a remarkable feat of scholarship that builds on an impressive base of sources. Some readers will be drawn to the thick, satisfying narrative, while others will profitably mine the bibliography for their own research. I believe *Reading Darwin in Arabic* will serve as a beacon of insight and inspiration for scholars of the Middle East and historians of modern science.
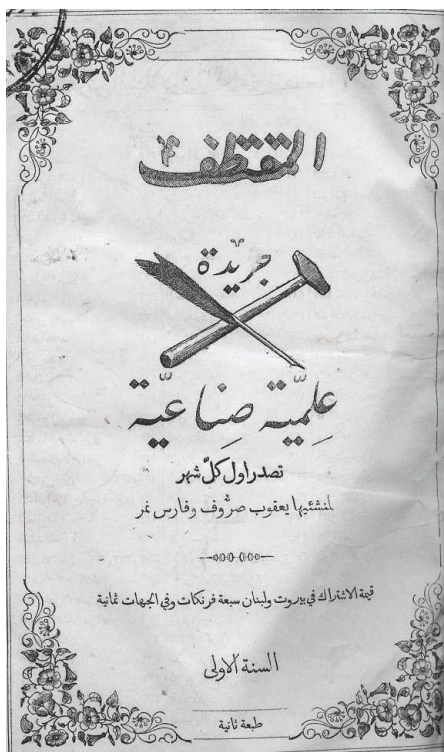
The reviewer is at the Max Planck Institute for the History of Science, Boltzmannstrasse 22, 14195 Berlin, Germany. E-mail: hkucuk@mpiwg-berlin.mpg.de

EXHIBITION

Feeding the Raven

Camels are not orthodox transport for Vikings. Yet to trade Newfoundland walrus ivory for silk with the Caliphate of Baghdad, some Norsemen must have been familiar enough with them. An exhibition currently at the British Museum attempts to improve the Vikings' reputation by using objects amassed from sites ranging from the Atlantic to the Caspian to demonstrate what cosmopolitan traders Vikings really were. But the objects that have survived the intervening millennium—mostly bones, swords, and silver—tend to reinforce the Vikings' image as bloodthirsty and greedy berserkrs. And although evidence from place names, language, and literature also attests to a better cultural legacy for the Vikings, the exhibition includes the 10th-century Arab diplomat Ibn Fadlan's comment that "They are the filthiest of God's creatures…. They are like wandering asses."

It appears that a technological change that revolutionized boat design opened the door for the Viking diaspora around 800 CE. The new lightweight, shallow-drafted, and large ships (with capacities of up to 100 men) were fit not only for coasting but also for longer sea crossings at speed, powered by wind and oarsmen. Initial visits were fleeting and bloody, often targeting monasteries in northern and eastern Britain known to have gold and silver items. Although in Skaldic verse ships are called "iron-studded dragons" (and there are plenty of iron nails on display), the exhibits do not tell us enough about boat building given how important it was to Viking expansion—the basic ship design was even inverted into houses. We do learn how many sheep were required to supply wool for the sails and how many horses were needed for the hair ropes, and it is thought that woodworking was done on such a scale as to cause the deforestation of Iceland. But Viking craftsmen were buried with their metal-working tools, so why don't we learn more about their methods? Likewise, how did the seafarers navigate? Criss-crossing the north Atlantic
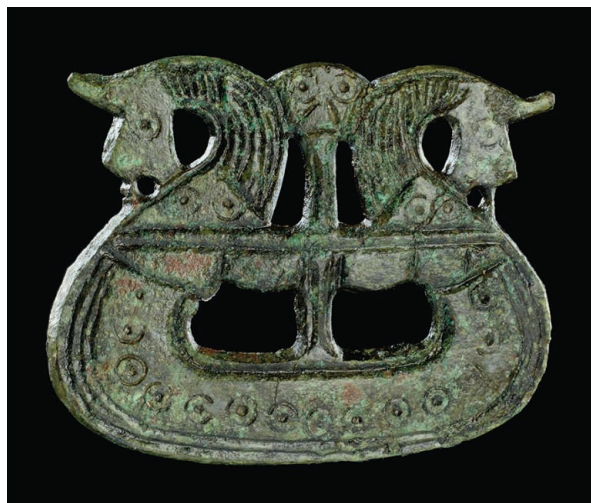
Ship-shaped brooch (Denmark, 800–1050).

was not trivial, but it was regular and possibly frequent: Icelandic wives came from Ireland, and in the Sagas we learn that Icelanders went raiding annually.

What motivated the initial spirit for overseas raiding in a farming culture remains a matter for conjecture. One notion is that bride prices had inflated to the extent that Viking oligarchs had to travel increasing distances to find the wherewithal to purchase a wife.

The Cuerdale and Vale of York hoards are of hack silver or gold (i.e., cut up for easy transport and smelting). Loot was not always melted down, and pieces of British ecclesiastical ornament modified into women's jewelry have been found in Scandinavian burials. When at one point the battered English attempted appeasement by buying off the pirates, this only stoked more raiding.

Contact seems to have been mostly restricted to one to three ships at a time. Occasional evidence (e.g., a mass grave of decapitated men from around 1000 CE discovered on the south coast of England in 2009) indicates that despite the Vikings' fearsome reputation, single boatloads did not always prevail. Hence, there must have been substantial pressure to adapt to local mores and customs, as without extended supply lines and reinforcement, such irregular landings of so few men would not have given rise to settlement. That adaptation did occur is documented in various churchyard orna-

ments in Britain and Scandinavia that simultaneously depict Ragnarok and crucifixion. Over a century or so, emigrant Vikings adopted local organized religions and resumed their ancestral land-based lifestyles. It seems later immigration brought a more benign energy, which in England facilitated urbanization and industrialization. New Viking cities developed into modern Derby, Nottingham, Leicester, and, most notably, York (Jorvic), where continuing excavations have unearthed a huge wealth of Viking relics.

Such cities needed trade to sustain their populations, industry, and commerce. Here again Viking ship-building technology triumphed. The shallow-draft boats allowed expansion across the Baltic and Mediterranean Seas into Central Asia, because they could travel Europe's long, broad rivers. The presence in hack silver hoards of coins from as far away as Afghanistan documents the range of Viking influence. Certainly, the Vikings had contact with Byzantium, where they traded for cloth for garments, and with the Rhineland, where the prized Ulfberht sword blades were made from steel obtained from India. Ships transported a profusion of amber beads from the Baltic and pottery from muddy England. Furthermore, it seems incontrovertible that the Vikings reached North America.

The exhibition might have further engaged visitors with considerations of the Vikings' genetic legacy in modern Europeans—recent research confirms the spread of "nordmen" genes into eastern Europe [e.g., (1)]. (For instance, were the early raiders from the same populations as the later migrants?) It would also have been enriched by including additional details about how things were done or made along with the wider context of surrounding populations and their interactions with the Vikings. And a bit more labeling of display objects would make those more informative.

Ultimately, the exhibition persuades us that there was more to the Vikings than bloodletting. Nonetheless, their society still comes across as pretty cutthroat.

—**Caroline Ash**

References
1. G. Hellenthal *et al.*, *Science* **343**, 747 (2014).

RESEARCH FUNDING

Science Funding and Short-Term Economic Activity

Expenditures from grant funds support many different types of workers and vendors across the nation.

Bruce A. Weinberg,[1,2,3] Jason Owen-Smith,[4] Rebecca F. Rosen,[5] Lou Schwarz,[6] Barbara McFadden Allen,[7] Roy E. Weiss,[8] Julia Lane[5,9,10,11]*

There is considerable interest among policy-makers in documenting short-term effects of science funding. A multiyear scientific journey that leads to long-term fruits of research, such as a moon landing, is more tangible if there is visible nearer-term activity, such as the presence of astronauts. Yet systematic data on such activities have not heretofore existed. The only source of information for describing the production of most science is surveys that have been called "a rough estimate, frequently based on unexamined assumptions that originated years earlier" (1).

But although science is complicated, it is not magic. It is productive work. Scientific endeavors employ people. They use capital inputs. Related economic activity occurs immediately. Data characterizing these activities can be directly captured through the financial and payroll records of research organizations and have been used in other arenas, such as labor policy. Our data provide the first detailed information about initial inputs to the publicly funded scientific enterprise and lay the foundation to trace subsequent results (2).

These new data were initially generated in response to the mandate put in place by the 2009 American Recovery and Reinvestment Act, also known as the stimulus package, which required that recipients of stimulus funds document the resulting jobs created and retained. In response, almost 100 U.S. universities and five federal agencies, with the support of the Federal Demonstration Partnership, established the STAR METRICS data program. The goal of the program was to document not just short-term, but also longer-term, results of scientific activity and to use

automated approaches to do so (2). The first tranche of rich data are drawn directly from university personnel and financial administrative records that track actual expenditures of all active federal projects. These data provide project-level information about the occupations of the part-time and full-time workforce paid on each funded grant and about the purchases made from vendors who supply scientific researchers. Neither of these types of information have reliably been available before (3, 4).

The results reported in this paper represent an analysis of 2012 expenditure data from nine Committee on Institutional Cooperation (CIC) universities participating in the emerging UMETRICS initiative—Michigan, Wisconsin, Minnesota (Twin Cities), Ohio State, Northwestern, Purdue, Michigan State, Chicago, and Indiana [see supplementary material (SM) for full details on data and analyses]. These universities received about $7 billion in research and development (R&D) funding from all sources in 2012; 56% of that came from federal government sources (5). In the

aggregate, the 15 institutions that make up the CIC receive 8 to 10% of all federal research dollars. The majority of these institutions are large, Midwestern public universities. Hence, they are not representative of all recipients of federal funds. However, it is unlikely that the type of science that is conducted with those funds is markedly different from that conducted at many other major research universities, and they provide a window into a large portion of federal research activity in the era of tightening federal budgets. Moreover, the 2012 data we analyzed reflect expenditures from federal funds obligated over multiple prior years. These data thus offer a different, and possibly smoother, picture than is apparent in the often volatile annual federal-funding cycle.
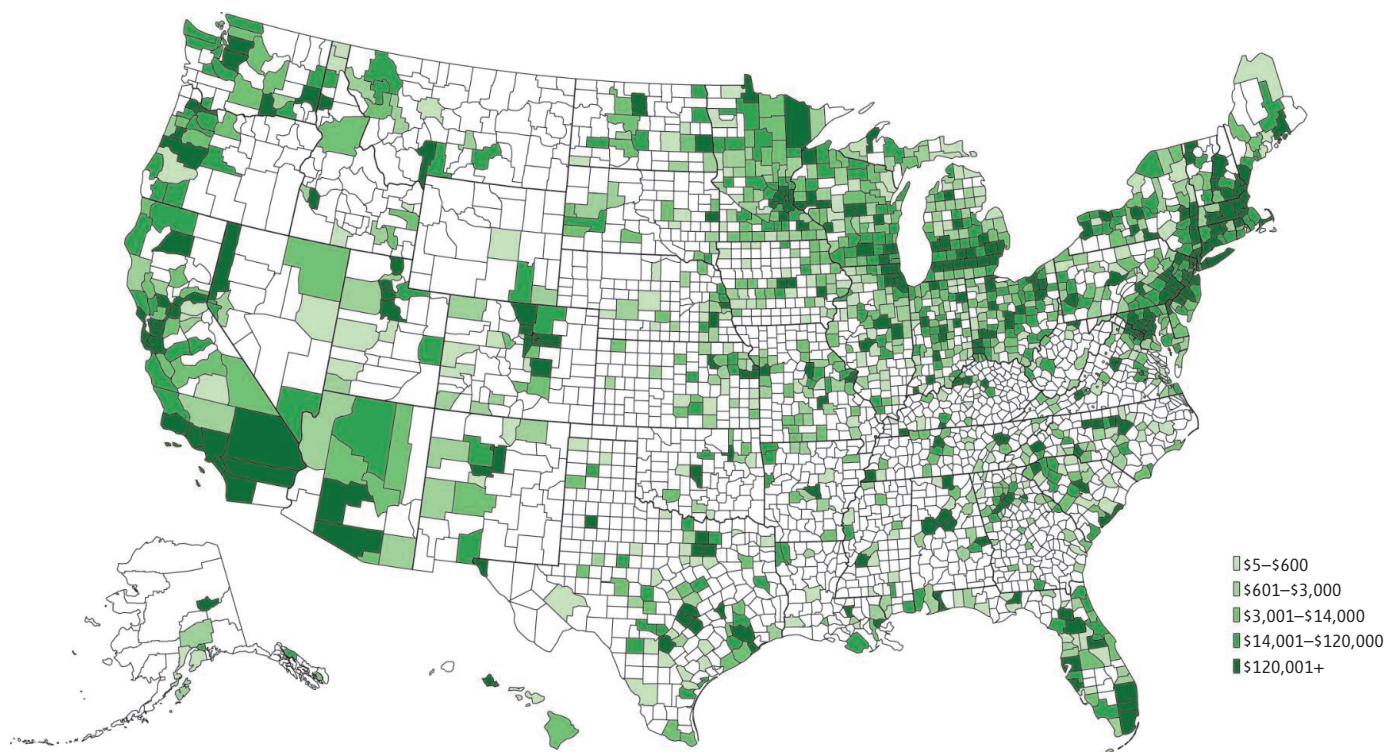
Our initial analysis of all expenditures supported by federal funding to these nine CIC institutions—monies from some 30 agencies—shows that the production of science is complex but eminently traceable. We document reliance on a wide variety of inputs, including a heterogeneous mix of skills

[1]Ohio State University, Columbus, OH 43210, USA. [2]Institute for the Study of Labor (IZA), 53113 Bonn, Germany. [3]National Bureau of Economic Research, Cambridge, MA 02138, USA. [4]University of Michigan, Ann Arbor, MI 48109, USA. [5]American Institutes for Research, Washington, DC 20007, USA. [6]Factor 21, Arlington, VA 22201, USA. [7]Committee on Institutional Cooperation, Champaign, IL 61820, USA. [8]University of Chicago, Chicago, IL 60637, USA. [9]Observatoire des Sciences et des Techniques, 75015 Paris, France. [10]Bureau d'Economie Théorique et Appliquée (BETA) University of Strasbourg CNRS, 6700 Strasbourg, France. [11]University of Melbourne, Victoria 3010, Australia.

*Corresponding author: jlane@air.org

Differences in workforce composition in projects funded by NSF divisions and NIH institutes. NIA, National Institute on Aging; NINDS, National Institute of Neurological Disorders and Stroke; NIMH, National Institute of Mental Health; NIDDK, National Institute of Diabetes and Digestive and Kidney Diseases; NICHD, Eunice Kennedy Shriver National Institute of Child Health and Human Development; NIAID, National Institute of Allergy and Infectious Diseases; NHLBI, National Heart, Lung, and Blood Institute. (See SM.)

The geographic distribution of vendor and subaward expenditures. (See SM.)

Legend:
- $5–$600
- $601–$3,000
- $3,001–$14,000
- $14,001–$120,000
- $120,001+

(embodied in numerous students, postdocs, and research staff), as well as diverse goods and services purchased locally, within the institution's home state, and nationally. More detailed analysis of projects supported by two major science agencies [National Institutes of Health (NIH) and National Science Foundation (NSF)] reveals the need for extensive research at the levels of the individual grant and research group. That work will yield better knowledge about the process of scientific production while illuminating short-term consequences of changes in funding.

Of course, science funding is not primarily a jobs or economic stimulus program. The full public value of federal R&D rests on its long-term contributions to human knowledge and economic growth. The short-term activity that we document here results from the process of scientific work and should not be confused with the long-term benefits generated by the products of research.

Characterizing the Scientific Workforce

Although the question of whether federal research grants represent a form of public assistance for unproductive professors is beyond our purview, at least part of the claim (6) that federal funding primarily supports faculty "welfare queens in white lab coats" finds little support in these data. The people employed to conduct research on these campuses bring diverse types of skills to a wide range of jobs. Many are students learning the trade of science. Faculty researchers account for fewer than one in five of the individuals supported by federal funding. About one in three workers is either a graduate or an undergraduate student. One in 3 is either research staff or a staff scientist, and about 1 in 10 is a postdoctoral fellow.

Composition of the workforce on projects supported with funds from different sources can vary dramatically. Support from the NIH is substantial: The agency funds, in whole or in part, almost 40% of the individuals working on federally funded research projects we examined. The NSF supports just over 21%, whereas the Department of Education supports under 10%. Those numbers mask disparate workforce effects. NIH grants touch more than 50% of federally funded postdoctoral fellows, but only 24% of graduate students and 22% of undergraduates. By contrast, NSF dollars pay wages to over 35% of federally funded graduate students, 22% of undergraduates and fewer than 20% of postdoctoral fellows. It is not surprising that almost 25% of the undergraduates we observed work in some capacity on research grants funded by the Department of Education. One possible source of heterogeneity in the composition of the scientific workforce and in the mix of research and training could be differences in the missions of funders (7).

Another source of heterogeneity is the substantial variability in workforce composition across scientific areas (see the chart). Grants funded by NIH Institutes like the National Cancer Institute (NCI), which typically require the use of high-technology equipment, are more likely to rely on research staff. In contrast, grants from the National Institute of General Medical Sciences (NIGMS)—nearly 15% of which are training grants—rely more on graduate students and postdocs. Grants to chemists rely more on graduate students; those to mathematicians reach more faculty.

Untangling the reasons for empirical variations in the nature of the science, the type of the equipment that is used, and the size of the grants that each lab receives requires attention to the technical demands of different research areas, the orientations and rules of particular funders, and the strategies investigators deploy to fund and pursue their intellectual agendas. These variations seem likely to have substantial effects on research, training, and the social outcomes of science. Although these results may be intuitively obvious to scientists and students of science, this new evidence provides a systematic basis to quantify that intuition can rigorously inform policy-makers on the processes of science.

For example, empirical analyses of these rich data could help inform training policy. Recent reports suggest that graduate students' ability to complete their degrees and

move into a permanent position depends on federal support. We also know that increases in training time are likely to have a chilling effect on the next cohort of scientists as greater opportunity costs reduce the numbers of people willing to embark on and complete scientific training (*3*). Empirical analyses that systematically link modes of training support to completion time and future matriculations can inform more effective policies to develop the scientific workforce. Empirical analyses could also inform policy decisions about different funding structures. Changes in funding to support disciplinary rather than interdisciplinary research or shifts from lab-based to center-based mechanisms are likely to change the type of workforce that is funded, as well as the mix of subsequent outcomes. Investing in building empirical evidence about the contribution of each of these factors would provide important evidence for policy-makers as they ponder the appropriate level and structure of federal support for science.

National Economic Reach

These data also shed light into the amount spent on goods and services from those subcontractors and vendors that provide inputs into the production of science. In 2012, the nine CIC institutions spent almost $1 billion of research expenditures on goods and services from U.S. vendors and subcontractors. Of those expenditures, more than 16% went to vendors in the university's home county, over 16% more in the rest of the home state, and the balance to vendors across the United States (see the map).

Both common sense and careful research dictate that science requires tangible and intangible inputs produced by organizations in a wide range of industries—grants buy mice and telescopes, reagents and computers (*4*). When we examined the vendors for many grants, we expected to see purchases from well-known large firms, and we did. But we were struck by two new sets of facts as we examined the Web sites of some of the tens of thousands of vendors which supplied research inputs. First, we were surprised by how many were small, niche high-technology companies. The important role of small, specialized companies in the scientific ecosystem is important and easy to miss as the presence of small businesses in complicated national markets can go largely undetected. Second, vendor Web sites suggest that many small businesses leverage the capacity they develop in supporting federally funded science to build new products and services. The role that science funding plays in stimulating

innovation on the part of suppliers is also not well documented and understood.

More nuanced analyses of the effects federal grant purchases exert on the productivity of vendors represent a second, policy-relevant way that research using these data could shed light on both short-run and longer-term economic effects of federal R&D funding. If, as our analysis suggests, the process of scientific research supports organizations and jobs in many of the high skill sectors of our economy, rapid changes in funding could have substantial downstream consequences. In addition, the effects are likely to be national, rather than local (see the second figure).

The purchases can be substantial, but clearly depend on the nature of the research and probably the size and structure of the grant, as well as the rules of the funding agency. When we examined differences in spending within the research university's home state, we found different patterns depending on the source of funding. When scientists funded by NSF's mathematical sciences division purchase goods and services, they are much more likely to purchase within their home state; researchers funded by NCI tend to purchase materials from out of state, perhaps where specialized equipment vendors are located. The substantial variations across fields and funders are striking and merit much more study.

Although we currently lack (but expect these data to stimulate) the capacity to fully explain the sources and implications of these findings, our analysis indicates how scientific activity reverberates in unexpected ways through high-skill industries concentrated far away from a grant's recipient. A deeper analysis of expenditures of all institutions using, e.g., Census Bureau data, could be used by policy-makers to quantify how science funding drives innovation in suppliers of scientific equipment on the demand side.

Evidence Rather Than Anecdotes

Fortunately, the empirical foundations for science policy are being built by behavioral and social scientists across the world (*7, 8*). Universities as far apart as the University of Melbourne and the Universidad Complutense de Madrid are exploring similar systems. There is first-rate work being done using data to document the effects of different access policies on research and innovation (*9*), or of the variability of funding on scientific output (*10*).

Our data contribute to this burgeoning movement by documenting short-run scientific activity and by providing evidence about the multifaceted, widespread nature of that activity. In particular, our data indi-

cate the complexity of estimating the short-term effects of changes in scientific funding. It is important to note that any effort to rigorously quantify such effects requires information about how changes will be allocated across agencies and programs; estimates about how states, private funders, performers and researchers would respond; and assumptions about what would otherwise happen with science funds. The impact on competitiveness of vendors and subcontractors would also need to be taken into account. Based on our analysis of the grant funded workforce at these institutions, it seems clear that the consequences of funding cuts or the benefits of increases would fall disproportionately on trainees and staff segments of the scientific workforce who constitute much of our future capacity for cutting-edge R&D.

Decisions about the allocation of resources for research are made every year in every country. It is time the scientific community provided evidence rather than anecdotes so that policy-makers can assess the consequences of their decisions. The contribution of the UMETRICS initiative, and the database that underpins it, is to provide the foundations of such evidence that can be used not just in the United States but in other countries across the world.

References and Notes

1. National Research Council, *Data on Federal Research and Development Investments: A Pathway to Modernization* (National Academies Press, Washington, DC, 2010), p. 1.
2. J. Lane, S. Bertuzzi, *Science* **331**, 678 (2011).
3. National Institutes of Health, "Biomedical research workforce working group report," (NIH, Bethesda, MD, 2012); http://acd.od.nih.gov/biomedical_research_wgreport.pdf.
4. P. E. Stephan, *How Economics Shapes Science* (Harvard Univ. Press, Cambridge, MA, 2012).
5. NSF, Higher Education Research and Development Survey, (NSF, Arlington, VA, 2013); http://www.nsf.gov/statistics/herd/.
6. S. Begley, *Newsweek*, 14 January 1991, 44.
7. J. Lerner, S. Stern, Eds., *The Rate and Direction of Invented Activity Revisited* (Univ. of Chicago Press, Chicago, 2012).
8. Center for the Science of Science and Innovation Policy, "Empirical foundations of science and innovation policy," workshop summary, Paris, France, 16 and 17 September 2013 (CSSIP, Washington, DC, 2013); http://cssip.org/login/september-workshop.
9. J. L. Furman *et al.*, *Nature* **468**, 757 (2010).
10. J. Owen-Smith *et al.*, *J. Policy Anal. Manage.* **31**, 741 (2012).

Supplementary Materials
www.sciencemag.org/content/344/6179/41/suppl/DC1

NEUROSCIENCE

Optogenetic Regeneration

Shrivats M. Iyer[1] and Scott L. Delp[1,2]

Applying tools from optogenetics with ideas from regenerative medicine may herald a new era of translational optogenetics.

The first decade of optogenetics has seen many efforts to improve our understanding of normal and pathological neural circuitry (*1*). The great impact of these efforts has stemmed from an alliance between systems neuroscientists and protein engineers—the first group identifying neural circuits amenable to causal dissection, the second developing tools that enable unprecedented degrees of control over neural activity. The next decade of optogenetics is likely to see the development of a new alliance that may have similarly important implications–one between optogenetics and translational medicine. On page 94 of this issue, Bryson *et al.* describe one model for how such an alliance may proceed, applying tools from optogenetics in concert with ideas in regenerative medicine to restore muscle function in a mouse model of peripheral nerve injury (*2*).

The threshold question that all optogenetic experiments face is that of achieving stable expression of opsins in the desired cell population (*1*). Bryson *et al.* adopted an approach to solve this problem that has some precedent in the field (*3*). The authors genetically engineered mouse embryonic stem cells to stably express channelrhodopsin-2 (ChR2), a cation channel sensitive to blue light, and then differentiated these cells in vitro to obtain optogenetically activatable ChR2 motorneurons. Thus, shining blue light on these ChR2 motorneurons could robustly drive neuronal firing. They then grafted aggregates of stem cells (embryoid bodies) containing these ChR2 motorneurons into a mouse model of muscle denervation in which the sciatic nerve was ligated. The engrafted ChR2 motorneurons survived, matured, and grew to innervate the denervated muscles of the lower limb, allowing Bryson *et al.* to restore muscle function through illumination of the graft site in anesthetized mice with blue light.

For reasons that remain somewhat unclear but are the subject of active study through computational modeling (*4*), optogenetic stimulation of ChR2 motorneurons results in motor unit recruitment patterns that closely track physiological motor unit recruitment order (*5*), unlike electrical stimulation,
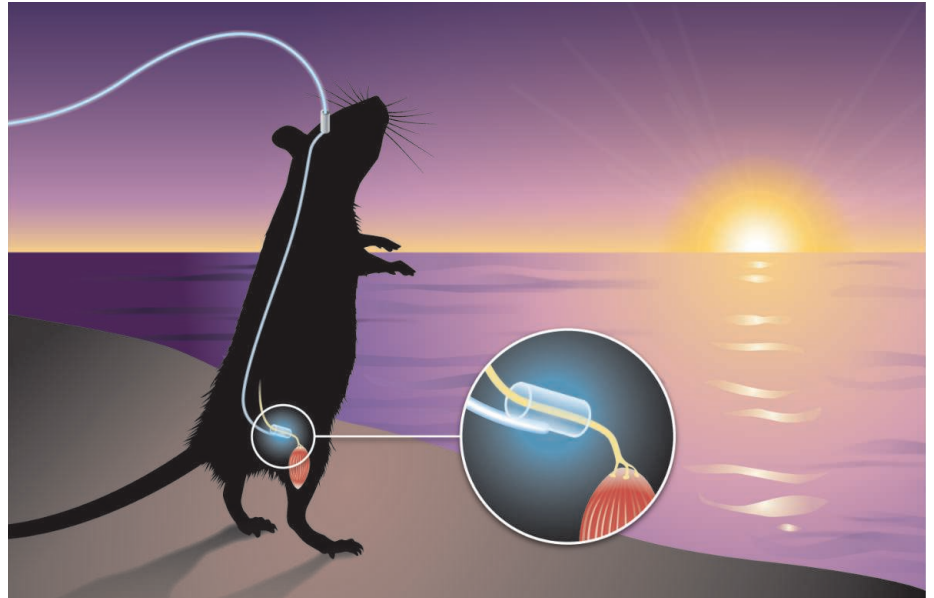
The dawn of translational optogenetics. Bryson *et al.* restored muscle function in a mouse model of peripheral nerve injury in an anesthetized animal. In the future, neural circuits in live animals might be controlled with robust light-emitting devices to restore physiological functions.

which produces a reverse or random recruitment order (*6*). Bryson *et al.* were therefore able to use their engrafted ChR2 motorneurons to achieve "orderly recruitment" of reinnervated muscles. These results confirm previous reports indicating that optogenetic stimulation activates muscles in a way that induces less fatigue than electrical stimulation, thus enabling optogenetically induced force to be sustained for long durations through preferential recruitment of fatigue-resistant motor units (*5*).

The capabilities that Bryson *et al.* demonstrate are likely to spur many subsequent studies. One critical question is whether the restoration of muscle function achieved can be extended to mice that are not under anesthesia. This will likely require the use of chronically implantable light-emitting nerve cuffs, which allow for optogenetic activation of peripheral nerves in freely moving animals. (*7*). Also of great interest will be the quality and persistence of the enabled control. Bryson *et al.* describe ChR2 motorneuron endplates (innervated regions of muscle) that are malformed, and hypothesize that this is due to initial in vivo inactivity of the transplanted ChR2 motorneurons. Chronic cuff implantation would allow for optoge-

netic activation of these neurons immediately after engraftment, which may help prevent such malformation. The long-term survival of engrafted ChR2 motorneurons is another major challenge that must be overcome.

The cell transplantation framework used by Bryson *et al.* may also have applicability in the treatment of other forms of nervous pathology. Stem cell grafts and electrochemical neuroprostheses may have potential use in the treatment of spinal cord injury (*8*, *9*). Combining these strategies with the stimulation specificity provided by the optogenetic approach of Bryson *et al.* may be a productive direction for future research efforts.

By demonstrating how results from regenerative medicine may be integrated with new techniques in muscle physiology to restore function, Bryson *et al.* exemplify the type of interdisciplinary synthesis that will be essential for developing translational optogenetics. Like Bryson *et al.*, others have identified neurons outside the brain as the likely first target for optogenetic translation (*10*). In addition to control over peripheral motorneurons (*2*, *5*, *7*), foundational work has been done in this area to demonstrate that optogenetics may be used to control retinal cells (*11*) and pain circuits (*12*, *13*).

[1]Department of Bioengineering, Stanford University, Stanford, CA 94305, USA. [2]Department of Mechanical Engineering, Stanford University, Stanford, CA 94305, USA. E-mail: delp@stanford.edu

CREDIT: H. MCDONALD/SCIENCE

However, several challenges remain to be overcome before the first successful optogenetic therapy is realized. Among these is the extension of optogenetic techniques beyond murine models to nonhuman primates (14), particularly in neural circuits outside the brain. Equivalently important is improved assessment of the long-term safety of opsin expression across a variety of delivery strategies, including both viral vectors (such as adeno-associated viruses), and cell transplants such as those used by Bryson *et al*. The development of robust light-emitting devices that are well tolerated upon implantation is also critical; these may potentially be wirelessly powered. And opsins will need to be developed that exhibit improved light sensitivity (particularly to red light) and a wide range of different temporal characteristics. These challenges notwithstanding, this study by Bryson *et al*. provides an elegant step along the path to optogenetic translation (see the figure).

References and Notes
1. K. M. Tye, K. Deisseroth, *Nat. Rev. Neurosci.* **13**, 251 (2012).
2. J. B. Bryson *et al.*, *Science* **344**, 94 (2014).
3. J. P. Weick *et al.*, *Stem Cells* **28**, 2008 (2010).
4. R. L. Arlow, T. J. Foutz, C. C. McIntyre, *Neuroscience* **248**, 541 (2013).
5. M. E. Llewellyn, K. R. Thompson, K. Deisseroth, S. L. Delp, *Nat. Med.* **16**, 1161 (2010).
6. C. S. Bickel, C. M. Gregory, J. C. Dean, *Eur. J. Appl. Physiol.* **111**, 2399 (2011).
7. C. Towne, K. L. Montgomery, S. M. Iyer, K. Deisseroth, S. L. Delp, *PLOS ONE* **8**, e72691 (2013).
8. P. Lu *et al.*, *Cell* **150**, 1264 (2012).
9. R. van den Brand *et al.*, *Science* **336**, 1182 (2012).
10. J. C. Williams, T. Denison, *Sci. Transl. Med.* **5**, 177ps6 (2013).
11. V. Busskamp, B. Roska, *Curr. Opin. Neurobiol.* **21**, 942 (2011).
12. S. M. Iyer *et al.*, *Nat. Biotechnol.* **32**, 274 (2014).
13. I. Daou *et al.*, *J. Neurosci.* **33**, 18631 (2013).
14. I. Diester *et al.*, *Nat. Neurosci.* **14**, 387 (2011).

CHEMISTRY

A CO₂ Cloak for the Cyanide Dagger

The fleeting stability of the cyanoformate ion formed from CO_2 and cyanide has implications for plant enzymology and CO_2 sequestration.

Igor Alabugin and Rana K. Mohamed

In the ever-expanding universe of compounds prepared to date, it is remarkable that a two-carbon ion with an apparently simple electronic structure could have eluded structural characterization until now. It is especially notable because this ion is formed from carbon dioxide (CO_2) and cyanide (CN^-), each with a rich chemical history. On page 75 of this issue, Murphy *et al.* (1) report trapping the elusive cyanoformate ion as a crystalline salt with a bulky and unreactive cation. Their crystallographic and spectroscopic analysis along with quantum-mechanical calculations reveal a seemingly ordinary carbon-carbon (C–C) bond with the length of ~1.5 Å, yet cyanoformate balances on the brink of fragmentation in nonpolar environments and its C–C bond breaks in more polar solvents.

On first glance, bonding of CO_2 and CN^- could be expected because the carbon atom in CN^- is nucleophilic (electron rich), whereas the carbon in CO_2 is electrophilic (electron poor) (see the figure, panel A). Every discussion on the chemistry of ketones, esters, and similar functional groups in an undergraduate organic chemistry class includes attack of the lone pair of electrons of a nucleophile at the carbonyl (the C=O group). In this process, a π bond is sacrificed to give a σ bond. Usually, σ bonds are stronger than π bonds, so the overall transformation is thermodynamically favorable. For example, interaction of cyanide with ketones and aldehydes (formation of cyano alcohols, also known as cyanohydrins) dates back to the classic 1850 work of Strecker (see the figure, panel B) (2).

Formation and decomposition of cyanonohydrins is commonly used by bacteria, plants, fungi, and a few animals (e.g., millipedes) as a way to store cyanide and release it on demand (cyanogenesis) (3). Rumor has it that this reaction offered protection from cyanide to Grigori Rasputin, a controversial figure of Russian history (4). One attempt to poison Rasputin failed because of his apparent immunity to cyanide. The theory is that his killers put the cyanides in sweet pastries, and the carbonyl functionality on the sugar molecules served as an antidote by reacting with the cyanide and forming cyanohydrins.

However, CO_2 is a much tougher nut to crack than a typical ketone, and its reaction with cyanide is considerably less favorable. Not only is the energy cost for distorting the linear CO_2 molecule into the bent sp² geometry (~75 kcal/mol) (5) comparable to the C–C bond energy, but π bonds at sp-hybridized carbons are stronger than π bonds at sp²-hybridized carbons (6, 7). The relatively small enthalpic preference for cyanoformate formation is wiped out by unfavorable entropy. The 133° O–C–O angle in cyanoformate suggests that CO_2 is poised, like a spring, for the escape to its relaxed linear geometry. The ephemeral nature of cyanoformate illustrates that C–C bonds can, under
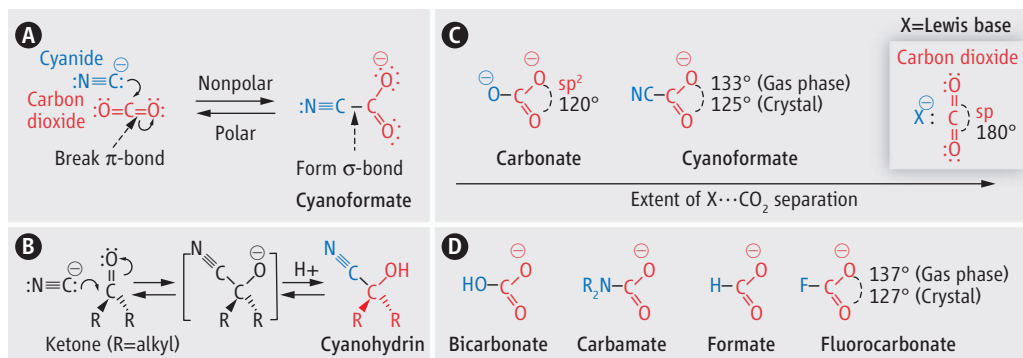
Traps for CO_2 and CN^-. (**A**) Traps for cyanide can be transient, such as capture in cyanoformate, where, as shown by Murphy *et al.*, stability depends on solvent polarity. (**B**) Long-term capture of cyanide in cyanohydrins. (**C**) CO_2 trapping can bend this linear molecule into the sp² geometry of carbonate ions or the intermediate structure of cyanoformate, depending on the degree of interaction. (**D**) Lewis bases can act as traps for CO_2.

Department of Chemistry and Biochemistry, Florida State University, Tallahassee, FL 32306, USA. E-mail: alabugin@chem.fsu.edu

the right circumstances, be broken without a penalty. Unraveling this fundamental puzzle has several practical implications.

Through the formation of cyanoformate, CO_2 can "cloak" cyanide and escort it away from its potential targets. This process may shed light on the mystery surrounding ethylene production from 1-aminocyclopropane-1-carboxylic acid (ACC) by ACC oxidase (also known as ethylene-forming enzyme, EFE) (8). Ethylene is a plant hormone that plays an important role in processes such as fruit ripening and seed germination. Along with ethylene, this enzymatic pathway forms the putative cyanoformate intermediate, (9) in close vicinity to the iron center of the enzyme active site. If cyanoformate were to decompose immediately, the iron-containing active site could be deactivated by the CN^-. For example, CN^- halts cellular respiration by inhibiting cytochrome c oxidase. Sacrificial metal ions, such as Fe(III) and Co(II), are used in antidotes for cyanide poisoning because of their ability to intercept CN^-.

Murphy et al. suggest that nature may use a more economical solution by employing CO_2 as a masking Lewis acid and that the transient stability of cyanoformate allows

sufficient time for CN^- to be shuttled away under the cloak provided by coordination with CO_2. The calculated energies for release of CN^- suggest that cyanoformate should be unstable in water but persist in the less polar enzyme active sites.

There is one more important implication of the fleeting stability of cyanoformate. Capture of CO_2 from the atmosphere or combustion streams is a crucial technological challenge for mitigating its effects as a greenhouse gas. A common approach uses the Lewis acidity of CO_2 in reactions with a suitable base, i.e., by scrubbing with amines (10) or by catalytically reducing CO_2 into formates, either enzymatically (11) or with metals (12, 13) (see the figure, panels C and D). The range of Lewis base–CO_2 interactions changes from covalent bonds to weak non-covalent interactions in amine-functionalized nanoporous solids (14). Reversibility of such processes is important because it allows regeneration of the sorbent. The work of Murphy et al. illustrates how CO_2 complexes with a Lewis base can be formed and broken on demand, depending on external conditions.

The story of cyanoformate illustrates that even simple molecules can unlock chemical

and biochemical mysteries. What lessons can we learn from this small ion on the brink of fragmentation? If plants need CO_2 to detoxify from cyanide, can we rely on cyanide to detoxify the atmosphere from CO_2? With the blanket of greenhouse gases around the world thickening year by year, now is the time to investigate.

References
1. L. J. Murphy et al., Science **344**, 75 (2014).
2. A. Strecker, Chem. Pharm. **75**, 27 (1850).
3. D. S. Seigler, Plant Secondary Metabolism (Kluwer Academic, New York, 1999).
4. E. Radzinsky, The Rasputin File (Doubleday, New York, 2000).
5. I. V. Alabugin, B. Gold, M. Shatruk, K. Kovnir, Science **330**, 1047 (2010).
6. I. V. Alabugin, B. Gold, J. Org. Chem. **78**, 7777 (2013).
7. A. Nicolaides, W. T. Borden, J. Am. Chem. Soc. **113**, 6750 (1991).
8. D. O. Adams, S. F. Yang Proc. Natl. Acad. Sci. U.S.A. **76**, 170 (1979).
9. M. C. Pirrung, Acc. Chem. Res. **32**, 711 (1999).
10. G. T. Rochelle, Science **325**, 1652 (2009).
11. K. Schuchmann, V. Müller, Science **342**, 1382 (2013).
12. J. F. Hull et al., Nat. Chem. **4**, 383 (2012).
13. M. S. Jeletic, M. T. Mock, A. M. Appel, J. C. Linehan, J. Am. Chem. Soc. **135**, 11533 (2013).
14. R. Vaidhyanathan et al., Science **330**, 650 (2010).

ECOLOGY

To Fence or Not to Fence

Fences must be used with care in biodiversity conservation to avoid unintended consequences.

Rosie Woodroffe,[1] Simon Hedges,[2] Sarah M. Durant[1,2]

Habitat fragmentation undermines the functioning of ecosystems, and so biodiversity conservation often entails maintaining or restoring landscape connections. However, conservationists also destroy connectivity by constructing wildlife fences. A recent debate about the use of fences to protect African lions (1–3) highlights a more general need to evaluate the role of fencing in conservation.

People and wildlife can be uneasy neighbors. Many wild species damage valuable livestock, crops, or infrastructure; some carry livestock diseases; and a few threaten human lives. At the same time, people kill wild animals for food, trade, or to defend lives or property, and human activities degrade wildlife habitat. Separating people and wildlife by fencing can appear a mutually beneficial way to avoid such detrimental effects.

While some fences may be last-ditch attempts to preserve wildlife areas already isolated by human development, others are constructed within relatively contiguous wildlife habitat. For example, in parts of southern Africa, fencing of individual land parcels secures wild animals as privately owned commodities in a wildlife economy centered on sport hunting. In North America, roads may be fenced to minimize collisions that can kill people and wildlife. Fences have been constructed in Australia to protect native marsupials from invasive species, and in Kenya to separate critically endangered hirola antelope from natural predators. Botswana is traversed by veterinary cordon fences intended to prevent disease transmission from wildlife to livestock, and fencing has also been considered as a way to halt the spread of infectious cancer among Tasmanian devils. In Africa, containing rhinos in small fenced areas makes them easier to protect from poachers.

Although fencing can have conservation benefits, it also has costs. When contiguous habitats are converted into islands, the resulting small and isolated populations are prone to extinction, and the ensuing loss of predators and other larger-bodied species alters interactions between other species in ways that cause further local extinctions, a process that has been termed ecological meltdown (4). Areas isolated by fencing are likely to experience similar consequences unless the wildlife populations they contain are intensively managed.

Fencing can lower not only the number but also the density of organisms that can be supported in a landscape. In highly variable environments, both wild herbivores and pastoral people move widely to track resources such as food and water. Constraining these movements by fencing lowers the carrying capacity of such environments. Just as settlement of formerly nomadic pastoralist people can lead to overgrazing and land degradation (5), so construction of fences

[1]Institute of Zoology, Regent's Park, London NW1 4RY, UK. [2]Wildlife Conservation Society, 2300 Southern Boulevard, Bronx, NY 10460, USA. E-mail: rosie.woodroffe@ioz.ac.uk

has been linked to vegetation changes (*6*) and marked declines in wild herbivores, even where fences were constructed for conservation purposes (*7*). Such impacts are likely to be especially severe where climate change increases the frequency and severity of extreme weather events (*5, 8*).

Fencing structures themselves can exacerbate pressures on wildlife. They offer a ready supply of wire, which can be used to fashion snares for poaching. Furthermore, predators such as wolves and African wild dogs (see the figure, panel A) can learn to improve their hunting success by chasing prey into fences (*9*). These impacts and the resulting fence damage in turn prompt hostility from managers, which can lead to deliberate predator removal. Less tangibly, fencing alters people's relationship with nature. Where policy changes have constrained the movements of formerly nomadic people, fences can be perceived as symbols of the policy, generating local hostility to wildlife conservation efforts (*10*).

In principle, these harmful effects of fencing on ecosystems might be countered by improved protection from human activities, as well as the societal benefits of protecting people from wildlife. However, the challenges of appropriate fence design, location, construction, and maintenance mean that fences often fail to deliver the anticipated benefits (see the figure, panel B). In Africa, fences are a negligible barrier to determined poachers, who need little more than a pair of pliers to gain access to valuable wildlife. For example, fencing has not prevented substantial illegal killing of rhinos in recent years. Although many fences provide effective barriers to wildlife, failures are commonplace. For example, a study of 37 fences in South India found that 49% failed to prevent passage of elephants,

mainly because of poor maintenance and deliberate breaches by local people seeking access to the fenced areas (*11*).

The balance between beneficial and detrimental effects of fencing wildlife was recently debated after a call to fence African parks to conserve lions, which reach higher densities (relative to estimated carrying capacity) inside fenced reserves than in unfenced areas (*1*). If fencing is effective in resolving human-wildlife conflict, it should reduce lion mortality from human predation (a top-down effect). However, herbivores may not benefit in the same way, because fencing constrains their ability to escape lions and other natural predators. At the same time, restricting herbivores' ability to exploit ephemeral food sources increases the likelihood of their populations being food-limited (bottom-up effects), and fencing has been repeatedly associated with herbivore declines (*7*). Changes in herbivory prompt cascading effects on vegetation (*6*) and are likely to influence many other ecosystem components. Although relatively high lion densities inside fenced areas have been portrayed as successful conservation of a key ecosystem process (*3*), they might indicate food webs profoundly altered by fencing.

Despite these concerns, fences are a powerful tool for conserving and restoring wildlife in landscapes that are highly modified by human activity. In New Zealand, where invasive species extirpated mainland populations of species such as the hihi, fencing of Maungatautari and other sites has facilitated the creation of "mainland islands" free of invasive species, allowing restoration of native fauna (*12*). Likewise, in South Africa more-or-less intact (albeit highly managed) assemblages of large mammals have been restored in fenced areas of former farmland at reserves such as Ithala and Pilanesberg,

Pros and cons of fencing. Fences may allow some species, such as lions, to reach high densities, but they also profoundly alter ecosystems. For example, for species like the African wild dog (**A**) and many of its ungulate prey, fencing may increase the risk of extinction and reduce their resilience in the face of climate change. Furthermore, in some cases fences may fail to prevent passage of wildlife, such as these elephants in Kenya (**B**).

and these areas are increasingly viewed as nuclei for more extensive restoration efforts entailing progressive removal of fencing.

Where wildlife habitat remains extensive, however, alternative approaches will usually be more appropriate than large-scale fencing. A variety of approaches—including traditional farming practices such as herding, planned grazing, and crop guarding, as well as wildlife-sensitive land-use planning—can help to mitigate conflicts between people and wildlife without the need for fencing (*13*). Likewise, a combination of testing, vaccination, and meat preparation can prevent transmission of foot-and-mouth disease without the need to separate cattle from wildlife by fencing (*14*). Rather than enclosing wildlife, fences may be used to enclose small areas of intense conflict such as settlements, wells, or grain stores. Where rhinos need to be contained for their own protection, special fences that allow passage of other species have proven effective. Likewise, in North America, livestock fences have been constructed that allow passage of pronghorn. Even virtual fences have been developed for particular species; for example, scent marks have been used to constrain African wild dogs in an otherwise unfenced reserve (*15*). The wider applicability of such costly and labor-intensive approaches is uncertain.

Reconciling the needs of people and wildlife is a perpetual challenge, and separating the two may be appealing. Too often,

however, fences are constructed without a realistic assessment of the costs and benefits. In the United States, growing populations of large carnivores and megaherbivores are conserved in unfenced reserves, showing that fencing is not a necessary condition for conservation of such species. As climate change increases the importance of wildlife mobility and landscape connectivity, fence removal may become an important form of climate change preparedness, and fencing of wildlife should become an action of last resort.

References

1. C. Packer *et al.*, *Ecol. Lett.* **16**, 635 (2013).
2. S. Creel *et al.*, *Ecol. Lett.* **16**, 1413 (2013).
3. C. Packer *et al.*, *Ecol. Lett.* **16**, 1414 (2013).
4. J. Terborgh *et al.*, *Science* **294**, 1923 (2001).
5. M. W. Næss, *Int. J. Sust. Dev. World Ecol.* **20**, 123 (2013).
6. L. Cassidy, R. Fynn, B. Sethebe, *Afr. J. Ecol.* **51**, 513 (2013).
7. R. Ben-Shahar, *J. Trop. Ecol.* **9**, 249 (1993).
8. A. M. Shrader, S. L. Pimm, R. J. van Aarde, *Biodivers. Conserv.* **19**, 2235 (2010).
9. H. T. Davies-Mostert, M. G. L. Mills, D. W. Macdonald, *J. Appl. Ecol.* **50**, 1358 (2013).
10. A. Hoole, F. Berkes, *Geoforum* **41**, 304 (2010).
11. C. D. Nath, R. Sukumar, *Elephant-Human Conflict in Kodagu, Southern India: Distribution Patterns, People's Perceptions and Mitigation Methods* (Asian Elephant Conservation Centre, Bangalore, 1998).
12. J. G. Ewen, K. A. Parker, K. Richardson, D. Armstrong, C. Smuts-Kennedy, *Conserv. Evidence* **8**, 58 (2011).
13. R. Woodroffe, S. Thirgood, A. R. Rabinowitz, *People and Wildlife: Conflict or Coexistence?* (Cambridge Univ. Press, Cambridge, 2005).
14. Southern African Development Community, "The Phakalane Declaration on Adoption of Non-Geographic Approaches for Management of Foot and Mouth Disease" (2012); www.rr-africa.oie.int/docspdf/en/2012/Phakalane_Declaration.pdf.
15. C. R. Jackson, J. W. McNutt, P. J. Apps, *Wildl. Res.* **39**, 31 (2012).

NEUROSCIENCE

The Michael Jackson Fly

A pair of neurons in the CNS of flies controls and coordinates their ability to walk backward.

Richard S. Mann

Although most of us are more comfortable walking forward, in part because we can see where we are going, people also have the capacity to walk, and even run, in a backward direction. This skill comes in handy when we get stuck in tight dead-end spaces and is even a trendy exercise routine for some (*1*). Perhaps most famously, Michael Jackson immortalized the move in his iconic moonwalker dance. Not surprisingly, the capacity for backward locomotion is not limited to humans and now, thanks to elegant experiments carried out in the fruit fly by Bidaye *et al.* and reported on page 97 of this issue (*2*), we have some understanding of how animals choose between forward and backward locomotion.

Experimental systems as diverse as mice, locusts, stick insects, and flies have taught us a lot about the kinematics and underlying neural control of forward walking (*3–7*). Each leg joint is controlled by motor neurons triggering contractions of opposing flexor and extensor muscles. The challenge for the nervous system, and perhaps more so for a six-legged fly compared to the two-legged Mr. Jackson, is to coordinate each of these joint bends, both within a leg (e.g., hip and knee) and between legs (e.g., left and right). Interneurons acting locally within the central nervous system (CNS), where the motor neuron cell bodies reside, somehow coordinate all of these limb movements, assisted by sensory neurons in the legs that report load and joint angle back to the CNS (*7*, *8*).

Walking backward is not a simple reversal of walking forward: For example, when we walk forward or backward, our knees bend the same way with each step, but the muscles in our hips that move our thighs work oppositely, depending on the direction (*9*). Such reversals in the movement of a proximal leg joint relative to more distal leg joints are also observed in backward-walking stick insects (*10*, *11*). In other words, when our brains tell our motor systems to change direction, they selectively modulate parts of the locomotor circuit. How do nervous systems manage to accomplish this?

To begin to answer this question, Bidaye *et al.* turned to the fruit fly to exploit its powerful genetic toolkit. They began by watching what happened to the locomotor behavior of flies in which different combinations of neurons were artificially activated. To execute this screen, the authors used the yeast transcription factor Gal4 and its cognate UAS binding site to drive the expression of the thermally activated cation channel TrpA1 in subsets of neurons. From about 3500 Gal4/UAS-TrpA1 transformed fly lines, each expressing TrpA1 in a stereotyped set of neurons, they found one line that caused flies to walk backward

Department of Biochemistry and Molecular Biophysics, Columbia University, New York, NY 10032, USA. E-mail: rsm10@columbia.edu
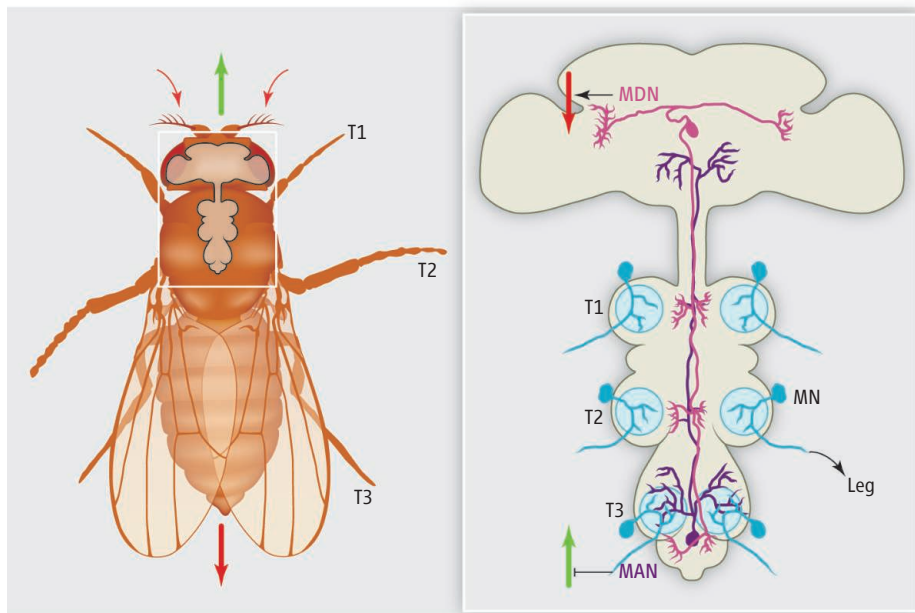
A neural circuit for moonwalking. Flies walk forward (green arrow) or backward (red arrow) in response to sensory cues (small red arrows). MDN and MAN are neurons that control walking direction, presumably by indirectly coordinating the activities of motor neurons (MN) via the leg neuropil (blue circles).

CREDIT: P. HUEY/SCIENCE

instead of forward, a phenotype they dubbed "moonwalker." Conversely, silencing these neurons greatly inhibited backward walking in situations, such as hitting a dead end, where wild-type flies normally choose to walk backward.

By expressing green fluorescent protein (GFP) under the control of Gal4/UAS instead of TrpA1, they found that the moonwalker line was active in seven morphologically distinct neurons. Subsequent experiments designed to identify which of the seven were important revealed that bilaterally activating only a specific pair of neurons was sufficient to make flies "do the moonwalk." While one of these neurons was located in the brain and sent its axon posteriorly into the ventral nerve cord (VNC), where motor neuron cell bodies reside, the second neuron had the opposite orientation: Its cell body resided in a posterior region of the VNC and sent its axon anteriorly, into the brain (see the figure). On the basis of these two distinct orientations, the authors named these neurons MDN and MAN, for "moonwalker descending neuron" and "moonwalker ascending neuron," respectively (see the figure).

Bidaye *et al*. then used more precise genetic tools to tease out the individual contributions of MDN and MAN in the control of walking direction. Activation of MDN alone was sufficient to induce a significant amount of backward walking, while activating MAN alone was not. However, activating either MDN or MAN was sufficient to interfere with forward walking; flies in which either neuron was activated still walked forward, but for shorter distances. Thus, it seems that whereas MDN activity triggers a switch from forward to backward walking, MAN activity contributes to the moonwalker phenotype mainly by inhibiting forward walking (see the figure). MDN, with its cell body in the brain, may receive sensory cues from, for example, the eyes or antennae, that inform the fly it is approaching a dead end. As such, MDN may be a "command neuron" analogous to command interneurons in *Caenorhabditis elegans* that promote backward crawling in response to touching the worm's head (*12–14*).

Although the findings of Bidaye *et al*. provide the first glimpse into how flies, and perhaps other legged animals, control walking direction, many questions remain. For one, none of the upstream or downstream neurons that make functional connections with MDN or MAN are known. Of particular interest is whether and how MDN and MAN selectively modify only parts of the locomotor circuit to induce flies to change direction. In *C. elegans*, forward and backward crawling require distinct motor neurons that receive information from different command interneurons (*13, 14*). To figure out whether something similar is happening in limbed locomotion, we need a better understanding of the circuitry that controls forward walking. Answers will no doubt come from a wide variety of approaches, including ones similar to those used by Bidaye *et al*., to provide cellular resolution to complex motor outputs such as walking.

References and Notes

1. L. Neporent, "No gain in backward exercise, experts say," New York Times, 13 October 1998; www.nytimes.com/1998/10/13/health/no-gain-in-backward-exercise-experts-say.html.
2. S. S. Bidaye, C. Machacek, Y. Wu, B. J. Dickson, *Science* **344**, 97 (2014).
3. O. Kiehn, *Curr. Opin. Neurobiol.* **21**, 100 (2011).
4. M. Goulding, *Nat. Rev. Neurosci.* **10**, 507 (2009).
5. A. Büschges, T. Akay, J. P. Gabriel, J. Schmidt, *Brain Res. Rev.* **57**, 162 (2008).
6. R. Strauss, *Curr. Opin. Neurobiol.* **12**, 633 (2002).
7. C. S. Mendes, I. Bartos, T. Akay, S. Márka, R. S. Mann, *Elife* **2**, e00231 (2013).
8. S. Zill, J. Schmitz, A. Büschges, *Arthropod Struct. Dev.* **33**, 273 (2004).
9. M. Lee, I. Kim, J. Son, Y. Kim, *Gait Posture* **38**, 674 (2013).
10. P. Rosenbaum, A. Wosnitza, A. Büschges, M. Gruhn, *J. Neurophysiol.* **104**, 1681 (2010).
11. T. Akay, B. Ch. Ludwar, M. L. Göritz, J. Schmitz, A. Büschges, *J. Neurosci.* **27**, 3285 (2007).
12. B. J. Piggott, J. Liu, Z. Feng, S. A. Wescott, X. Z. Xu, *Cell* **147**, 922 (2011).
13. S. R. Wicks, C. H. Rankin, *J. Neurosci.* **15**, 2434 (1995).
14. M. Chalfie *et al.*, *J. Neurosci.* **5**, 956 (1985).

IMMUNOLOGY

Immune Activation with HIV Vaccines

Future HIV vaccine research should consider the balance between responses that favor protection and those that lead to susceptibility to infection.

Anthony S. Fauci,[1] Mary A. Marovich,[1] Carl W. Dieffenbach,[1] Eric Hunter,[2] Susan P. Buchbinder[3]

The development of a safe and effective HIV vaccine is perhaps the most important and challenging goal remaining in HIV-AIDS research. Recent progress using a poxvirus vector prime and envelope protein boost strategy demonstrated a modest but statistically significant level of efficacy and established the concept that a vaccine could prevent HIV infection (*1*), and approaches to boost durability and efficacy are currently in the planning stages (*2*). But the results of two vaccine concepts based on recombinant adenovirus serotype-5 (rAd5) (*3–5*) pointed to a potential major problem—that such vaccines might increase susceptibility to HIV infection. This also raised the question of whether the problem extends to some or all of the other recombinant adenovirus vectors currently in development or to other vector-based vaccines.

Last year, the U.S. National Institute of Allergy and Infectious Diseases (NIAID) convened the Mini-Summit on Adenovirus Platforms for HIV Vaccines (*6*) to investigate this issue. Furthermore, the question was raised whether increased susceptibility might be seen with any HIV vaccine that activates the immune system rendering activated CD4^{+} T cells more susceptible to HIV infection, while at the same time inducing little or no protective effect against HIV acquisition (*6*).

Between 2005 and 2013, two rAd5 vaccines for HIV were assessed in three efficacy studies (*3–5*). The first study (Step), using three doses of the Merck rAd5 vaccine containing genes encoding three HIV-1 proteins (gag, pol, and nef), was stopped for futility. In addition, a statistically significant trend toward increased HIV infections in vaccine recipients was observed (*3, 7*). The group at highest risk was uncircumcised men who both had sex with men (MSM) and had high titers of preexisting antibodies against Ad5. The following Phambili trial of the same Merck rAd5 vaccine, conducted

[1]National Institute of Allergy and Infectious Diseases, Bethesda, MD 20892, USA. [2]Department of Pathology and Laboratory Medicine, Emory Vaccine Center at Yerkes National Primate Research Center, Emory University, Atlanta, GA 30322, USA. [3]San Francisco Department of Public Health, Department of Medicine, University of California, San Francisco, CA 94143, USA. E-mail: afauci@niaid.nih.gov

in South Africa, was closed and unblinded early during the enrollment period. Few participants received the planned three doses of vaccine. Analysis of the data showed no increased risk of HIV infection (5). However, data from the long-term unblinded follow-up of Phambili participants suggested an increased risk of infection in vaccinated men relative to unvaccinated controls (8).

In 2009, a different rAd5 vaccine was tested in the HIV Vaccine Trial Network (HVTN) 505 trial. It contained three doses of a DNA prime (a plasmid of non-HIV DNA and certain HIV genes) followed by a single boost of rAd5 expressing HIV envelope and viral structural antigens. The study restricted enrollment to circumcised MSM who lacked preexisting antibodies to Ad5, because no level of increased risk had been seen in this group in the Step trial (7). The HVTN 505 trial was halted prematurely because it met futility criteria; however, there was no evidence of increased risk of HIV infection in the vaccinated subjects (9).

Results of a Meta-Analysis

A meta-analysis of the Step, Phambili, and HVTN 505 trials was performed by statisticians from the HVTN Statistics and Data Management Center and from NIAID. Combining data from the three studies, there was an overall hazard ratio of 1.33 ($P < 0.01$) associated with vaccination. However, almost all of the increased risk of HIV acquisition was driven by the Merck vaccine (Step and Phambili: hazard ratio = 1.41, $P = 0.005$) with the Step trial contributing most infection endpoints. HVTN 505 considered alone did not show any trend toward infection risk (6, 10). It could not be determined whether the lack of increased susceptibility in the latter trial was due to population or regimen (inclusion of env, DNA prime, and single rAd5 boost with differences in vector backbone).

Other Ad-Based Vaccines

Alternative Ad vectors for use in tuberculosis or malaria vaccines have not been evaluated in trials in sufficient numbers of adults at risk for HIV infection to provide useful information about possible interactions with HIV. However, active-duty U.S. Army recruits have been vaccinated with Ad4/7 to prevent highly contagious respiratory illnesses in close quarters during training (11). From 1999 to 2011, the Army interrupted and then resumed vaccination with Ad4/7, creating three separate cohorts for comparison. The serologic data were reviewed retrospectively for these three cohorts, and no changes in HIV incidence were detected (6).

Potential Mechanisms for rAd5 Effects

In 2008, NIAID held an HIV Vaccine Summit, which fostered studies to understand the possible mechanisms of the effects seen in the Step study (12). Results revealed at the 2013 NIAID Mini-Summit included those from nonhuman primate studies of the Merck rAd5-gag/pol/nef vaccine constructs. The data showed an increase in activated CD4$^+$ T cells in the gastrointestinal mucosa after rAd vaccination and increased simian immunodeficiency virus (SIV) acquisition after rAd-SIV vaccination; the empty rAd vector did not increase SIV acquisition (13). Human gut biopsies of individuals vaccinated with the DNA prime and rAd5 boost as part of HVTN 204 (low risk) and HVTN 505 (high risk) revealed high numbers of activated Ad-specific CD4$^+$ T cells, with increased expres-

HIV vaccine–induced immune response interactions. Immune activation associated with HIV vaccination theoretically can lead to increased infection due to the activation of CD4$^+$ T cells during the immune response. The level of protection seen with a vaccine can be viewed as the balance between the responses to the vaccine that lead to susceptibility to infection and by the responses that favor protection.

sion of C-C chemokine receptor type 5 (the co-receptor for HIV), but no HIV-specific cells in multiple samples from the rectum and colon (6). Furthermore, the activated T cells were concentrated in unevenly distributed foci, making extensive sampling a necessity (14). Although there is no current evidence of increased risk of HIV acquisition for other Ad vectors, the presence of rAd5-activated T cells in tissue and the degree of shared epitopes between Ad serotypes that are recognized by CD4$^+$ T cells should be considered as a possible area of concern.

Ad serotype cross-reactivity can be attributed, in part, to recognition by CD4$^+$ T cells and CD8$^+$ T cells of highly conserved regions in Ad hexon protein across most human and primate Ad species (15–17). Therefore, this issue must at least be considered in the risk-benefit analysis of potential HIV vaccine trials using alternate Ad vectors. However, in a phase 1 study using a single rAd26-HIV env vaccination, a limited set of rectal biopsies showed no evidence for increased Ad-specific T cell activation in low-risk vol-

unteers and a different host gene activation signature from that in Ad5-vaccinated individuals (6). Nonetheless, a description of the rAd5 experience should be included in informed consents associated with HIV vaccine trials using alternate Ad vectors.

It is conceivable that increased risk of HIV infection could be associated with any vaccination strategy that activates T cells, especially at mucosal surfaces. If the balance between the stimulation of protective anti-HIV responses versus Ad-specific responses that activate CD4$^+$ T cells leans toward an anti-HIV response, then protection might be seen despite the presence of susceptible T cell targets. However, increased risk to infection may be seen if the anti-HIV response is weak and does not counterbalance the increased susceptibility of activated CD4$^+$ T cells; if the anti-HIV response wanes faster than the CD4$^+$ T cell activation; or if the Ad-induced response is maintained and boosted by reexposure to alternative adenoviruses. Furthermore, cellular immune responses against Ad5, regardless of Ad serostatus, diminished anti-HIV responses to rAd5-HIV vaccination in Step (15). Thus, the efficacy of an HIV vaccine may reflect a balance of two competing activities—anti-HIV responses and T cell activation.

Considerations for the Future

Given the increased risk and the lack of efficacy in trials using rAd5, further HIV vaccine studies testing rAd5 vectors are not appropriate. When considering HIV vaccines that are designed to elicit a component of T cell immunity, a risk-benefit analysis should consider the balance between anti-HIV responses and vector-directed responses that activate CD4$^+$ T cells (see the figure). This is particularly important when assessing viral vectors, including alternative Ad vectors. Future clinical testing of Ad-

based vaccines should evaluate the amounts and distribution of both vector and insert responses in target tissues where HIV acquisition is known to occur.

Other research activities could be pursued to help clarify the roles of antivector responses in overall HIV vaccine efficacy. For example, nonhuman primate studies using empty vectors or vectors with non-HIV inserts as placebo controls could define the levels of antivector immunity and evaluate the effect on virus acquisition of this vector-related activation of CD4$^+$ T cells independent of an anti-HIV response. Also, the field could benefit from additional nonhuman primate studies. For example, the identification of biomarkers in primates that indicate increased risk of acquisition (18) could be valuable to monitor for risk in early-phase human studies.

A better understanding of mucosal immune responses to HIV vaccination is also needed. The timing, location, and number of mucosal biopsies that define the vaccine-induced gut immune responses need clarification. Understanding the influence of the mucosal microbiome on vaccination (19) and the impact specifically of the virome will be important. Particularly for

Ad-based vectors, understanding components of risk related to the level of Ad exposure and persistence will be essential.

For non-HIV vaccine trials using vectors that induce strong T cell immunity that are conducted in regions with high HIV incidence, it may be important to monitor for HIV acquisition, depending on the target population. In such studies where the population may be at risk of HIV exposure, HIV incidence should be monitored at the end of the study and for an appropriate follow-up period.

The experience with rAd5-based HIV vaccines has shown that vaccine-induced protection likely reflects the balance between beneficial anti-HIV responses and deleterious effects of immune activation that increases the susceptibility of CD4$^+$ T cells to infection (see the figure). Among the spectrum of existing or planned vaccines, this phenomenon is likely unique for an HIV vaccine because the activated CD4$^+$ T cell is the very target for the virus. These observations should be taken into consideration in future HIV vaccine research endeavors and underscores the importance of maximizing the specific anti-HIV responses of such candidates.

References
1. S. Rerks-Ngarm et al., N. Engl. J. Med. 361, 2209 (2009).
2. M. L. Robb et al., Lancet Infect. Dis. 12, 531 (2012).
3. S. P. Buchbinder et al., Lancet 372, 1881 (2008).
4. M. J. McElrath et al., Lancet 372, 1894 (2008).
5. G. E. Gray et al., Lancet Infect. Dis. 11, 507 (2011).
6. National Institute of Allergy and Infectious Diseases Mini-Summit on Adenovirus Platforms for HIV Vaccines, 19 September 2013 (webcast available at www.niaid.nih.gov/topics/HIVAIDS/Research/vaccines/Pages/adenovirusPlatforms.aspx).
7. A. Duerr et al., J. Infect. Dis. 206, 258 (2012).
8. G. E. Gray et al., Lancet Infect. Dis. 10.1016/S1473-3099(14)70020-9 (2014).
9. S. M. Hammer et al., N. Engl. J. Med. 369, 2083 (2013).
10. S. Hammer et al., AIDS Res. Hum. Retroviruses 29 (11), abstract P04.38 LB (2013).
11. C. H. Hoke Jr., C. E. Snyder Jr., Vaccine 31, 1623 (2013).
12. A. S. Fauci et al., Science 321, 530 (2008).
13. H. Qureshi et al., J. Virol. 86, 2239 (2012).
14. J. McElrath, paper presented at The Collaboration for AIDS Vaccine Discovery Meeting, Seattle, WA, December 2013. Sponsored by the Bill and Melinda Gates Foundation.
15. N. Frahm et al., J. Clin. Invest. 122, 359 (2012).
16. N. A. Hutnick et al., Vaccine 28, 1932 (2010).
17. B. Heemskerk et al., J. Virol. 77, 6562 (2003).
18. E. Martinelli et al., J. Acquir. Immune Defic. Syndr. 64, 325 (2013).
19. W. B. Williams et al., AIDS Res. Hum. Retroviruses 29 (11), abstract OA03.04 (2013).

10.1126/science.1250672

Inside Earth Runs Hot and Cold

Mid-ocean ridge volcanoes sample a mantle that varies in temperature and composition.

Katherine A. Kelley

The global mid-ocean ridge system is an interconnected network of volcanoes that produces the oceanic crust, which covers 70% of Earth's surface. The physical and chemical attributes of mid-ocean ridges, such as the depth of the volcanic ridge axis below the sea surface, the thickness of the oceanic crust created there, the composition of the erupted lava, and the way seismic waves interact with the mantle beneath the ridge, collectively reflect the properties of the mantle that melts to form the oceanic crust. On page 80 of this issue, Dalton et al. (1) explore relationships between global seismic wave velocities in the mantle beneath mid-ocean ridges and a global data set of ridge depth and lava chemistry (2). They find strong correlations between these three factors, ultimately linking the trends to a global mantle temperature variation of ~250°C.

Lavas erupted at mid-ocean ridges form as the mantle moves upward in response to tectonic plate movements at the surface. As the mantle ascends, it melts at a depth controlled partly by its temperature (3), such that hotter mantle will start melting deeper and produce more magma, ultimately leading to a shallower ridge axis and a thicker oceanic
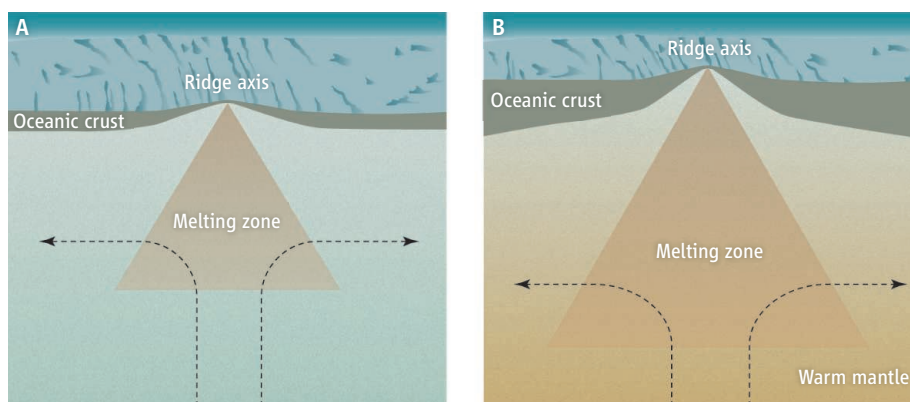
Creating oceanic crust at mid-ocean ridges. As the mantle moves upward beneath mid-ocean ridges, it melts and creates a volcanic chain (ridge axis) that constructs the oceanic crust. (**A**) At cooler temperature, less melting takes place, the ridge axis is deep, and the oceanic crust is thin. (**B**) Higher temperatures enable more melting, creating a shallower axis and thicker crust.

Graduate School of Oceanography, University of Rhode Island, Narragansett, RI 02882, USA. E-mail: kelley@gso.uri.edu

crust when compared with cooler mantle (see the figure). Hotter mantle also produces compositionally different lavas because it melts more, and seismic waves slow down when traversing hotter mantle. The seismic properties of the mantle beneath the ridge, the composition of the erupted lava, and the morphology of the ridge axis thus provide three independent sensors of mantle temperature. By compiling global-scale data sets, enabled through modern geoinformatics efforts (4, 5), Dalton et al. show that the parameters of axial depth, lava composition, and seismic wave velocity covary globally, as expected from variations in mantle temperature.

Yet, temperature is not the only factor that controls the physical and chemical attributes of mid-ocean ridges. Other recent assessments of global-scale data sets have challenged a primary role for temperature variations (6). By taking different approaches to constraining axial depth and correcting lava compositions for the effects of crystallization within the crust, such studies argue that variations in mantle composition are the main control on axial depth and lava chemistry, with minor temperature variations (<50°C) (6).

By including the mantle seismic properties in their analysis, Dalton et al. suggest that temperature is indeed the primary factor. Higher mantle temperatures are expected to produce shallower ridge axes, lavas with lower sodium concentrations, and lower seismic wave speeds. How mantle composition relates to axial depth, lava composition, and seismic velocity, on the other hand, depends

on how it is defined. For example, in (6) and (1), the mantle composition may vary globally as a function of how much it has melted previously, which influences its density and the composition and volume of magma it produces when melted but does not appreciably influence the speed of seismic waves that travel through it.

A key role, however, remains for mantle composition to determine the physical and chemical attributes of global mid-ocean ridges, because we know Earth's upper mantle is chemically heterogeneous. Compositionally distinct crustal materials from Earth's near-surface environment, such as marine sediments and oceanic crust, have been returned to the mantle through the subduction of tectonic plates at ocean trenches, enriching the mantle in elements such as volatiles (for example, H_2O and CO_2) that may influence mantle properties. The water content of the mantle affects the seismic velocities (7), as well as affecting the amount and composition of the crust produced by melting (8). A wetter mantle yields lower seismic velocities, thicker crust, and shallower ridge axes, similar to the effects of higher mantle temperature, but lava composition would define trends orthogonal to those found by Dalton et al. Similarly, trace quantities of carbon in the mantle could drive small amounts of melting at great depth beneath mid-ocean ridges (9), which may also influence seismic velocities and lava composition.

To what extent do water, carbon, and other compositional factors vary in Earth's mantle,

and over what length scales? How are these variations expressed in the physical and chemical structure of modern mid-ocean ridges and the oceanic crust? Two potential paths forward involve global and local scale studies of the ridge system. Progress in constraining global-scale variations of H_2O and CO_2 in mid-ocean ridge lavas, and their mantle sources, lags behind our understanding of other elements. As global data sets and models of volatile element distribution develop, we may more fully resolve the competing effects of temperature and composition on global-scale geophysical and geochemical characteristics of spreading ridges. Smaller length scales of compositional heterogeneity in the mantle may also be poorly resolved by globally averaged data sets (10), requiring focused, local studies of the ridge system to access smaller-scale features.

References
1. C. A. Dalton, C. H. Langmuir, A. Gale, *Science* **344**, 80 (2014).
2. A. Gale, C. A. Dalton, C. H. Langmuir, Y. Su, J.-G. Schilling, *Geochem. Geophys. Geosyst.* **14**, 489 (2013).
3. C. H. Langmuir, E. M. Klein, T. Plank, *Geophys. Monogr.* **71**, 183 (1992).
4. K. Lehnert, Y. Su, C. H. Langmuir, B. Sarbas, U. Nohl, *Geochem. Geophys. Geosyst.* **1**, 1 (2000).
5. W. B. F. Ryan et al., *Geochem. Geophys. Geosyst.* **10**, Q03014 (2009).
6. Y. Niu, M. J. O'Hara, *J. Pet.* **49**, 633 (2008).
7. S.-i. Karato, *Geophys. Monogr.* **138**, 135 (2003).
8. P. D. Asimow, C. H. Langmuir, *Nature* **421**, 815 (2003).
9. R. Dasgupta, M. M. Hirschmann, *Earth Planet. Sci. Lett.* **298**, 1 (2010).
10. L. Stixrude, C. Lithgow-Bertelloni, *Annu. Rev. Earth Planet. Sci.* **40**, 569 (2012).

OCEANS

Not So Permanent El Niño

Paleoclimate data point to a warm tropical ocean with a clear east-west temperature gradient during the warm climates of the Pliocene and Miocene.

David W. Lea

Knowledge of the behavior of the tropical oceans under different climate conditions is important for understanding not only past climate change but also present and future global warming, especially given the recent finding that the cool state of the equatorial Pacific might be the cause of the current global warming hiatus (1). On page 84 of this issue, Zhang et al. evaluate the long-term evolution of tropical Pacific sea surface temperatures (SSTs) since 12 million years ago (2). They conclude that the equatorial Pacific was warmer

during the Pliocene (5.3 to 2.6 million years ago) and late Miocene (12.0 to 5.3 million years ago) than it is today and that the temperature difference between the eastern and western tropical Pacific that is a fundamental characteristic of today's ocean was present (although somewhat smaller than it is today) during these warmer time intervals.

This view of the past tropical Pacific is strikingly different from the picture that has dominated paleoclimate thinking since 2005, when Wara et al. (3) argued that the tropical Pacific during the Pliocene was very different from that of today. In the present climate, the tropical Pacific is dominated by a distinct zonal gradient, with cool tem-

peratures in the east and warm temperatures in the west (see the figure, panel A). Wara et al. reported Mg/Ca data showing that this gradient was nearly absent during the warmer climate of the Pliocene (see the figure, panel B). Because the equatorial zonal gradient slackens during El Niño events, the researchers called the Pliocene configuration a "permanent El Niño–like condition."

Since then, scientists have sought to understand the cause of the change, and in particular the observation that the Pliocene warm pool was no warmer than in preindustrial times, despite inferred higher atmospheric carbon dioxide concentrations in the Pliocene (4). Yet the warm pool is known

Department of Earth Science, University of California, Santa Barbara, CA 93109–9630, USA. E-mail: lea@geol.ucsb.edu
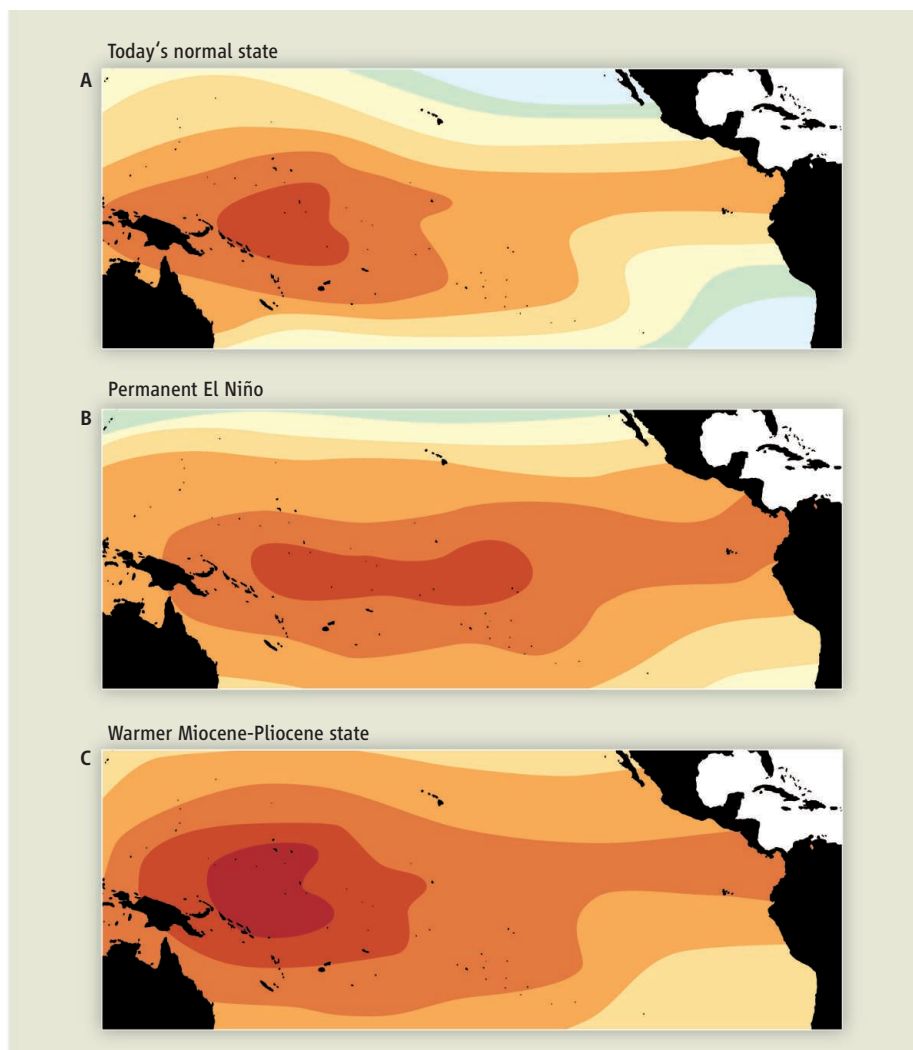
States of the Tropical Pacific. (**A**) The normal state for today's tropical Pacific. During El Niño events, the EEP warms by up to 5°C, while the WEP cools slightly; during La Niña events, the EEP cools by up to 3°C, while the WEP warms slightly. (**B**) Permanent El Niño–like state previously inferred for the Miocene-Pliocene (*4*), with a much warmer EEP and a similar or slightly cooler WEP. In this scenario, the zonal temperature gradient nearly vanishes. (**C**) In the warmer Miocene-Pliocene state inferred by Zhang *et al.*, both the EEP and WEP are warmer than they are today, as expected for the higher atmospheric CO_2 concentrations in the Miocene-Pliocene. The zonal gradient is only slightly smaller than in today's normal state.

et al. (*3*) based their inferences on magnesium-to-calcium ratio (Mg/Ca), a proxy that is recorded in foraminifera shells and is particularly good at recording surface conditions. But secondary factors influence shell Mg/Ca, and these influences, which include changes in seawater composition and variable shell preservation, are amplified on longer time scales (*9*). For TEX_{86}, a compound synthesized by marine archaea, there are large uncertainties associated with where in the water column the compounds are synthesized and which calibration is best (*10*). The $U_{37}^{K'}$ proxy, synthesized by a few species of haptophyte algae, is far better characterized; the observation from this proxy that all warm pool samples of Miocene age and older formed at an SST of ≥28°C bolsters the inferences from TEX_{86} (*2*). A full resolution of these different views, however, cannot be achieved without future research into the efficacy of the proxies on Miocene and Pliocene time scales.

If the view of the past tropical Pacific that emerges from Zhang *et al.*'s study proves correct, it has strong implications for a number of emerging challenges in climate science. It becomes far less likely that future global warming might lead to a permanent El Niño–like state, especially given that simulations of future global warming do not show such a response (*11*). Furthermore, the TEX_{86} data support previous evidence that the warm pool responds strongly to radiative forcing (*5*, *6*). Finally, Zhang *et al.*'s data support theoretical and modeling studies showing that there are no regulating mechanisms limiting tropical SSTs from increasing above 30°C in response to higher greenhouse gases, both in the past and the future (*12*).

References and Notes

1. Y. Kosaka, S.-P. Xie, *Nature* **501**, 403 (2013).
2. Y. G. Zhang, M. Pagani, Z. Liu, *Science* **344**, 84 (2014).
3. M. W. Wara, A. C. Ravelo, M. L. Delaney, *Science* **309**, 758 (2005).
4. A. V. Fedorov *et al.*, *Nature* **496**, 43 (2013).
5. K. Tachikawa *et al.*, *Quat. Sci. Rev.* **86**, 24 (2014).
6. H. Tokinaga, S.-P. Xie, C. Deser, Y. Kosaka, Y. M. Okumura, *Nature* **491**, 439 (2012).
7. D. J. Hill *et al.*, *Clim. Past* **10**, 79 (2014).
8. A. P. Ballantyne *et al.*, *Geology* **38**, 603 (2010).
9. M. Medina-Elizalde, D. W. Lea, *Paleoceanography* **25**, PA2208 (2010).
10. J. E. Tierney, M. P. Tingley, *Geochim. Cosmochim. Acta* **127**, 83 (2014).
11. P. N. DiNezio *et al.*, *J. Clim.* **22**, 4873 (2009).
12. I. N. Williams, R. T. Pierrehumbert, M. Huber, *Geophys. Res. Lett.* **36**, L21805 (2009).

to be sensitive to radiative forcing both in past (*5*) and modern climates (*6*), and therefore should warm with higher atmospheric greenhouse gas abundances. Fedorov *et al.* (*4*) have proposed some novel dynamical mechanisms to account for the lack of higher SSTs in the warm pool, but recent simulations show both warming of the warm pool and a tropical Pacific zonal gradient in the Pliocene (*7*). Overall, it is difficult to reconcile unchanged Pacific warm pool SSTs with higher atmospheric CO_2, smaller ice sheets, and much warmer conditions in the high-latitude Arctic (*8*).

Zhang *et al.*'s data may resolve this quandary. The authors use a relatively new paleo-temperature proxy, TEX_{86}, which can record SSTs above 28°C, the upper limit for the widely used organic geochemical proxy $U_{37}^{K'}$. That limit is critical to studies of the Pacific warm pool, where modern SSTs exceed 28°C. The TEX_{86} data record warmer SSTs than exist today in both the eastern equatorial Pacific (EEP) and western equatorial Pacific (WEP) during the Pliocene and Miocene (see the figure, panel C). Averaging all available TEX_{86} and $U_{37}^{K'}$ proxy SST data suggests a progressive cooling of both the WEP and EEP since the Miocene, with intensified cooling after 4 million years ago. The east-west gradient never approached zero, as implied for a permanent El Niño–like state.

How can we reconcile these disparate views? As in many problems in paleoclimate, the differences come down to the strengths and weaknesses of the various proxies. Wara

Migratory animals link resident communities across the globe.

Migratory Animals Couple Biodiversity and Ecosystem Functioning Worldwide

S. Bauer* and B. J. Hoye

Background: Every year, billions of migratory animals cross the planet in pursuit of increased foraging opportunities, improved safety, and higher reproductive output. In so doing, these migrants transport nutrients, energy, and other organisms (including seeds, mollusks, parasites, and pathogens) between disparate locations. Migrants also forage and are preyed upon throughout their journeys, thereby establishing transport and trophic interactions with resident communities. Migratory animals thus couple ecological communities across the globe and may mediate their diversity and stability. However, as yet, the influence of migrants and their services on these communities is often overlooked, and as a consequence of global changes, migrations are threatened worldwide.

Advances: We review several examples in which interactions between migratory animals and resident communities have been quantified, illustrating the processes by which migrants may uniquely alter energy flow, food-web topology and stability, trophic cascades, and the structure and dynamics of (meta-)communities. For example, the inputs of nutrients and energy originating from distant localities by migrants can dramatically increase resource availability, with rippling consequences for productivity at various trophic levels and the potential to drive the transition between alternative stable states. Migrant-mediated transport of propagules of other organisms can lead to the establishment of new or lost species, as well as influencing gene flow and genetic mixing among resident populations. Similarly, migrants can alter parasite transmission, diversity, and evolution by harboring a broader range of parasites than residents and by either facilitating or hindering the long-distance dispersal of parasites.

Foraging by migrants can also have profound effects on community processes and ecosystem functions. For instance, grazing by migratory animals can alter nutrient cycling, primary productivity, biomass of edible plants, competitive interactions between plant species, and ultimately, the composition and long-term persistence of the entire plant community. The most striking difference between migrant and resident consumers is, however, the pulsed nature of migrant utilization and the timing of their interactions. Together, these fundamentally define the relationship between migrant abundance and primary production (in the case of migrant herbivores) or the stability of food webs (in the case of migratory predators).

Outlook: Our Review demonstrates that the highly predictable, seasonally pulsed nature of animal migration, together with the spatial scales at which it operates and the immense number of individuals involved, not only set migration apart from other types of movement, but render it a uniquely potent, yet underappreciated, dimension of biodiversity that is intimately embedded within resident communities. Given the potential for migration to influence ecological networks worldwide, we suggest integrative network approaches, through which studies of community dynamics and ecosystem functioning may explicitly consider animal migrations, understand the ramifications of their declines, and assist in developing effective conservation measures.
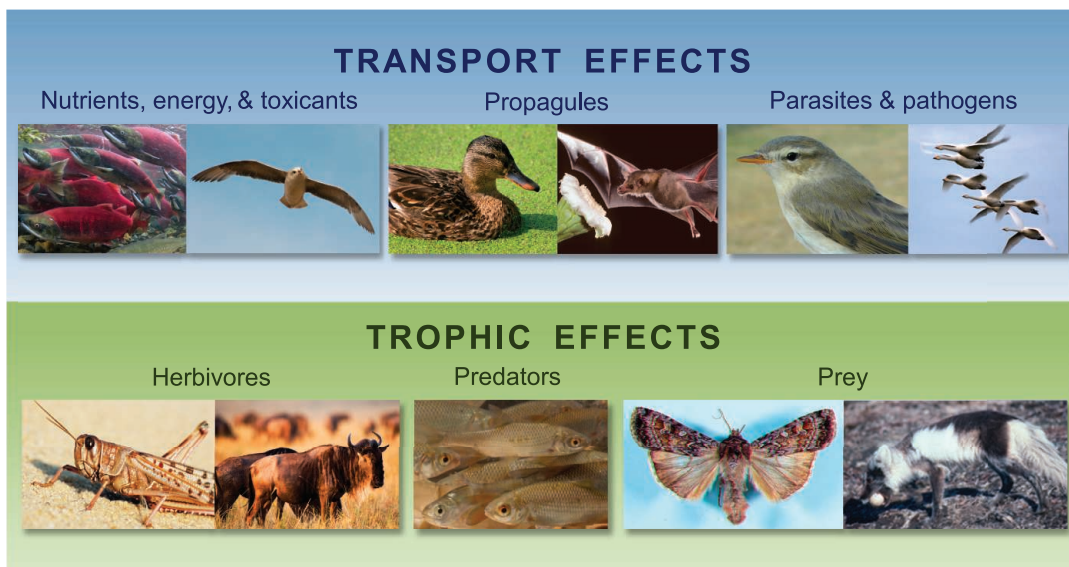
Migrants change communities and ecosystems. By transporting energy, nutrients, and other organisms, as well as foraging and becoming prey, migratory animals can substantially alter the dynamics of resident communities that they connect on their journeys across the globe. We illustrate key examples where migratory species profoundly alter food-web dynamics, community processes, and ecosystem functioning, indicating that migrants represent a unique, yet highly influential, component of biodiversity.

Migratory Animals Couple Biodiversity and Ecosystem Functioning Worldwide

S. Bauer[1,2]* and B. J. Hoye[3,4]

Animal migrations span the globe, involving immense numbers of individuals from a wide range of taxa. Migrants transport nutrients, energy, and other organisms as they forage and are preyed upon throughout their journeys. These highly predictable, pulsed movements across large spatial scales render migration a potentially powerful yet underappreciated dimension of biodiversity that is intimately embedded within resident communities. We review examples from across the animal kingdom to distill fundamental processes by which migratory animals influence communities and ecosystems, demonstrating that they can uniquely alter energy flow, food-web topology and stability, trophic cascades, and the structure of metacommunities. Given the potential for migration to alter ecological networks worldwide, we suggest an integrative framework through which community dynamics and ecosystem functioning may explicitly consider animal migrations.

Migration is the story of life on the move. Each year, billions of animals—from butterflies weighing less than a gram to 40-ton whales—fly, walk, or swim their way across the planet in pursuit of improved foraging conditions, safety, and reproductive opportunities (*1*, *2*). Migrations are persistent, directional movements from one destination to another, uninterrupted by intervening resources (*2*). The distances covered are often astounding, yet, the most extraordinary aspects of migration are perhaps the ubiquity of the phenomenon and the abundance of individuals involved. For instance, an estimated 1855 bird species (19% of extant species) are migratory (*3*). Of the avian species that use terrestrial and freshwater habitats, roughly 45% of those breeding in North America undergo seasonal migration (*4*), and over 30% breeding in the Palearctic migrate to sub-Saharan Africa (*4*), with many more migrating within Europe. Although accurate estimates of the number of individuals involved are scant, more than 2 billion passerine birds are found to migrate to sub-Saharan Africa (*5*), whereas upwards of 3 billion insects migrate over any 1-km stretch of countryside in southern England (*6*).

Historically, research on animal migration has focused on the migrants themselves: how, when, where, and why animals migrate (*7*). However, it is increasingly recognized that migration has ecological effects that pervade resident communities. The mere presence of migrants means that they will be preyed upon and forage and, in so doing, acquire nutrients, energy, and hitchhiking organisms that are subsequently transported to future destinations. Although migration patterns vary considerably across species, the large spatial scales traveled, together with their seasonality, which generate pulsed, highly predictable interactions, critically differentiate migration from other types of movement. Moreover, by integrating resource peaks or avoiding periods of heightened mortality risk over time and space, migrants may sustain considerably larger populations than otherwise similar resident species, often by an order of magnitude (*8*). Collectively, these features suggest that migratory animals have the potential to uniquely alter community structure, dynamics, and ecosystem function along their routes.

Notwithstanding recent research on spatial linkages between habitats and ecosystems (*9*), little work has been devoted specifically to the role of animal migration in ecological networks. This knowledge gap may, in part, stem from the inherent difficulty of the task, in addition to historical legacies within the disciplines of community ecology and migration ecology. Yet, neglecting migrants in community and ecosystem ecology restricts our understanding by reducing the number of species considered and failing to account for both spatial coupling and temporal dynamics.

Here, we review several case studies in order to define fundamental processes by which the transport and trophic effects of migratory animals influence ecological networks (Fig. 1). These examples illustrate the potential for migrants to uniquely alter energy flow, food-web topology and stability, trophic cascades, and the structure and dynamics of metacommunities (Fig. 2). In the hope of fostering integrative research that incorporates the regular, directed, mass movements of migrants in ecological networks, we synthesize key concepts from community ecology that may be readily adapted to incorporate migrant processes, particularly resource pulses and spatial subsidies. Looking to the future, we discuss novel network approaches for investigating the relative importance of migrants in maintaining ecosystem diversity, resilience, and stability that will also provide valuable insight into the consequences of rapid declines of animal migrations and the cascading effects of management actions along migratory routes.

Transport and Trophic Effects of Migrants
Transport Effects: Nutrients, Energy, and Toxicants

Upon arrival at a site, migrants deposit nutrients, energy, and other substances into resident communities and ecosystems via excreta (e.g., feces and urine), reproductive material (such as eggs), or the dead bodies of migrants themselves (Fig. 1). These allochthonous subsidies (resources that originate in one habitat but are moved into another) can result in a net inflow of energy and nutrients (*10*). Although allochthonous inputs are likely to occur in most (if not all) migratory systems, quantitative estimates of these subsidies—and their consequences—are primarily limited to the transport of nutrients and energy by oceanic migrants returning to coastal ecosystems (Fig. 2). For instance, the migration of Norwegian spring-spawning herring (*Clupea harengus*) constitutes the world's largest flux of energy effected by a single population, with the transfer of roughly 1.3×10^6 tons of biomass annually (*11*).

The migration of anadromous fishes, particularly salmon (Salmonidae), to their natal lakes and streams also constitutes a massive transfer of nutrients and energy from the ocean to freshwater ecosystems (*12*) and the surrounding terrestrial habitats (*13*). Salmon predictably increase both nitrogen and phosphorus in their spawning habitat, with estimates of 190% and 390% increases, respectively, in some streams (*12*). However, these inputs do not result in an increase in gross primary productivity; rather, migratory salmon increase ecosystem metabolism by up to threefold and, in so doing, force a switch from a net-autotrophic to a strongly net-heterotrophic metabolic state (*12*). Salmon also alter the physical properties of the stream, increasing air-water gas exchange by nearly 10-fold during peak spawning. Although nutrient transfer is not entirely unidirectional (as juveniles migrate to the ocean), an estimated 85% of the nutrients from carcasses or eggs are "stored" in the local food web (*14*), which alters the composition and structure of phytoplankton communities (*15*), riparian vegetation (including doubling the density of the overstory and halving the density of the understory) (*16*), and the phenology of stream insects (*17*).

Migratory seabirds also import vast quantities of nutrients to their terrestrial breeding colonies (*18*). Because these nutrients are accumulated over relatively small areas, they tend to result in relatively localized ecosystem changes (*19*). Seabirds may also introduce toxicants, such as organochlorines and heavy metals, which causes them to accumulate locally (*20*).

Because migratory populations may form enormous aggregations during certain periods, the allochthonous inputs of migrants can result in short pulses of high-intensity inputs (*21*) that can drive the transition between alternative stable states

[1]Department of Bird Migration, Swiss Ornithological Institute, 6204 Sempach, Switzerland. [2]Department of Animal Ecology, Netherlands Institute of Ecology (NIOO-KNAW), Post Office Box 50, 6700 AB Wageningen, Netherlands. [3]Department of Ecology and Evolutionary Biology, University of Colorado, Ramaley N122, Campus Box 334, Boulder, CO 80309, USA. [4]Centre for Integrative Ecology, School of Life and Environmental Sciences, Deakin University, Locked Bag 20000, Geelong, Victoria 3220, Australia.

*Corresponding author. E-mail: silke.s.bauer@gmail.com

(*12*). Migrants can also exert kinetic energy on a resident ecosystem through their grubbing, foraging, or breeding activities that may fundamentally alter the physical properties of their habitat (*22*).

Transport Effects: Propagule Dispersal

Migratory movements also represent a unique dispersal mechanism for seeds, spores, and (parts of) other organisms (collectively "propagules") across biogeographic barriers (*23*) (Fig. 2). In light of the importance of dispersal for population structure, adaptive capabilities, and evolutionary trajectories in theoretical studies (*24*), such long-distance dispersal events may be highly important for the (re-)colonization of unoccupied habitats, the recovery of lost populations, maintenance of gene flow, and gene mixing in metapopulations, even if they are relatively rare events (*25*). Yet, despite the potential importance of animal migrations and the wealth of information on local dispersal of propagules, migrant-mediated dispersal has been investigated in a surprisingly limited number of taxa, and rarely from the perspective of the recipient community.

A critical initial step in the dispersal process is the retention of viable propagules in or on migrants. Experimentally derived retention times, combined with field data on speeds of migratory movements, have been used to estimate the distances over which propagules could be transported, with estimates ranging from 200 to 1200 km for migratory water birds (*25*, *26*). However, retention times in free-living animals could be substantially altered by physiological changes during migration (*27*).

Although these studies reveal the potential for long-distance propagule dispersal by migratory animals, evidence for (or against) migrant-mediated dispersal is lacking. Notably, long-distance movements are typically confined to a limited time period, which must align with the flowering, fruiting, or reproductive time of the dispersed organism(s) for dispersal to take place (*28*). Moreover, the survival of propagules during passage in the digestive tract (*26*) and through deposition, germination, and competition in the resident community must also be assessed in order to quantify the consequences of this dispersal for community dynamics (*23*) (Fig. 3).

Migrants may also play an important role in propagule dispersal within resident communities. For instance, columnar cacti (Pachycereeae) are pollinated by numerous species migrating between western Mexico and southern Arizona, with Lesser long-nosed bats (*Leptonycteris yerbabuenae*) in particular shown to be responsible for up to 100% of cacti fruit-set, however their relative importance varies along their migratory route and between cacti species (*29*). Given that cacti represent crucial water and nutrient sources for a variety of desert animals (*29*), pollination services provided by these migrants facilitate the persistence of a large proportion of the ecosystem. In addition, migratory pollinators also mediate high levels of genetic diversity and gene flow between cacti populations (*30*).

Transport Effects: Parasite Dispersal

Although all animals can host a variety of parasites, migrants may play a unique role in parasite dynamics, both within and between resident communities [recently reviewed in (*31*)]. Migrations may facilitate the long-distance dispersal of parasites, as has been widely assumed for several zoonotic pathogens including Ebola virus (by migratory fruit bats), avian influenza viruses (by migratory water birds), and West Nile virus (by migratory songbirds), yet clearly documented examples are exceedingly rare (*31*). Migrants may also encounter a broader range of parasites than residents (*32*), which increases the likelihood of transmitting novel parasites to resident species (*31*). In addition, the intense physiological demands of migration (in some species) may trade off with immune responses, potentially rendering migrants more susceptible to infection. For instance, migratory birds (in captivity) show shifts in measures of innate immune responses during the migratory period (*33*). Although the link between these immune responses and susceptibility to primary infection is yet to be established, simulated migration can catalyze a relapse of prior infections (*34*). Many migrants also aggregate in groups many times larger than at other periods during the year at key refueling locations en route, which can enhance parasite transmission and result in prevalences that are as much as 17 times that in other locations (*35*).

The role of migrants in altering parasite transmission and diversity is, however, complicated by the infection process itself, particularly the timing of infection, the host's ability to tolerate infection, and the availability of susceptible hosts (Fig. 3). Animals must become infected before departure from a site, migrate successfully while infected, and remain infectious until arriving at a subsequent site. Yet, in one of the few examples
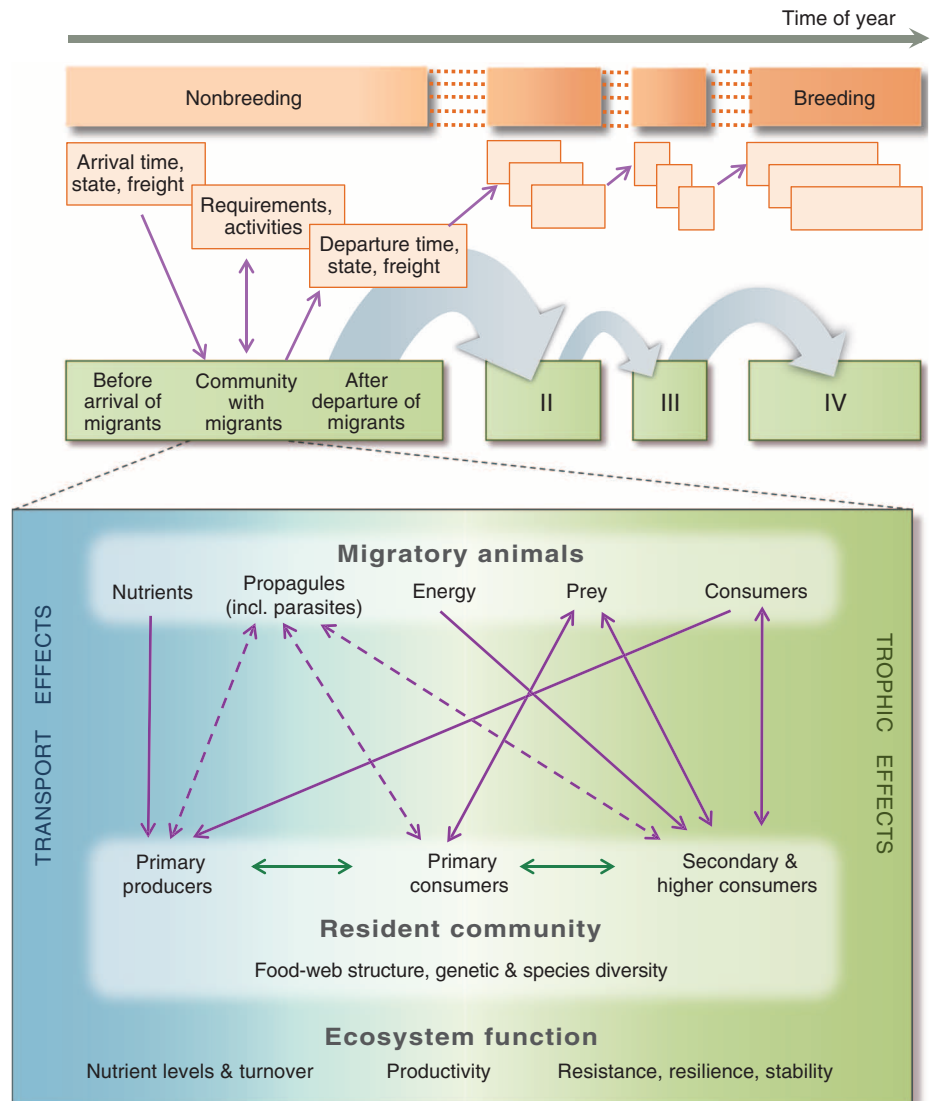
Fig. 1. Schematic overview of the interactions between migrants and the multiple resident communities they visit during their annual or life cycles (purple arrows). These may influence demographic rates of resident populations directly (solid arrows) and indirectly (dashed arrows) through interactions among residents (green arrows).
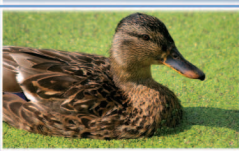
MIGRATORY SPECIES		EFFECT ON COMMUNITY
Pacific Salmon spp. (*Oncorhynchus spp.*) Migrate to north Pacific ocean as smolt; return as adults to spawn in natal rivers		Nutrient & energy input via carcasses & eggs, altering productivity at several trophic levels (*12,14*)
Northern fulmar (*Fulmarus glacialus*) Breed along Arctic coastlines in large colonies; migrate to more southerly waters outside breeding season		Fertilize otherwise nutrient-poor terrestrial systems (breeding sites) with vast quantities of marine-derived nutrients (*18,19*)
Mallard (*Anas platyrhynchos*) Partial migrants - northernmost breeding populations winter further south		Transport freshwater molluscs & plant seeds, internally & externally, over potentially considerable distances (*25 -27*)
Long-nosed bat (*Leptonycteris yerbabuenae*) Females migrate from central Mexico to southern USA in spring to raise young		Pollinate cactai along migratory route, altering reproductive success, gene flow, and resource availability for desert animals (*29, 30*)
Old-world songbirds (*Passeriformes*) Many species breed in northern Europe & return to sub-Saharan Africa in autumn		Migrants harbor haemosporidian parasites from breeding & wintering ranges, suggesting transmission with residents across migratory range (*32*)
Bewick's swan (*Cygnus columbianus bewickii*) Breed on tundra in Arctic Russia, return to western Europe in autumn		Avian influenza virus infection linked to foraging during autumn mighration; potentially increase terrestrial transmission in winter (*37*)
Desert locust (*Schistocerca gregaria*) Migrate 100s of km in search of food & favorable conditions		Consumes its own mass daily; when gregarious grazing may devastate agricultural crops (*40,41*)
Wildebeest spp. (*Connochaetes spp.*) Long distance migrations across the African savannah follow seasonal rainfall patterns		Migrants increase primary productivity, with the timing of grazing decoupled from the timing of plant growth (*39,45*)
Roach (*Rutilus rutilus*) Partial migrants; freshwater tributaries in winter, return to lakes in spring		Migration out of lakes allows rapid growth of zooplankton in spring, altering phytoplankton abundance & transition between turbid- & clear-water states (*48*)
Army cutworm (*Euxoa auxiliaris*) Adults summer in Rocky Mountains; mate & lay eggs on Great Plains in autumn		Important food source of Grizzly bears (*Ursus arctos*) occupying talus slopes during summer (*51*)
Greater snow goose (*Anser caerulescens atlanticus*) Breed in Arctic north America; migrate to mid-Atlantic coast of USA for winter		Geese and their eggs prey for Arctic fox (*Vulpes lagopus*) populations, altering fox abundance and predation pressure on alternate prey (*50*)

Vertical labels (left side): TRANSPORT EFFECTS — Nutrients, energy, toxins / Propagules / Parasites. TROPHIC EFFECTS — Herbivores / Predators / Prey.

Fig. 2. Key examples of migrant-induced changes to the dynamics of resident community processes. [Photo credits in order of appearance: J. B. Armstrong, B. J. Hoye, A. K. Glover, M. D. Tuttle (Bat Conservation International), J. Waldenström, B. J. Hoye, bikeriderlondon (shutterstock.com), S. Uryadnikov (shutterstock.com), J. Brodersen, D. White Jr., and J. Bêty].

to date, monarch butterflies (*Danaus plexippus*) infected with a protozoan parasite exhibited 19% shorter flight distances and 10 to 16% slower flight speeds, and lost proportionately more body mass (2.5% as compared with 1.6% of starting body mass) for the distance flown (*36*). Similarly, Bewick's swans (*Cygnus columbianus bewickii*) infected with low-pathogenic avian influenza virus delayed departure by up to 1 month and traveled shorter distances during the early stages of spring migration compared with uninfected individuals (*37*). Crucially, mechanistic models demonstrate that such infection-induced delays may result in spatial separation of infected and susceptible migrants, substantially dampening infection dynamics (*38*). Thus, although migrants may experience greater exposure to parasites and exhibit potential for long-distance dispersal, migration may also reduce infection risk (*31*).

Trophic Effects: Herbivory

The foraging of migrants en route establishes consumer-resource interactions across several sites. Similar to resident species, grazing by migratory animals has been shown to alter nutrient cycling, primary productivity, biomass of edible plants, competitive interactions between plant species, and ultimately, the composition and long-term persistence of the entire plant community (*22*, *39*) (Fig. 3). Perhaps the most pervasive migratory herbivores are insects, many of which are the world's major agricultural pests (*2*). For example, desert locusts (*Schistocerca gregaria*) can consume their own weight in vegetation each day, such that one swarm on the horn of Africa was estimated to have consumed, on a daily basis, enough vegetation to feed 400,000 people for an entire year (*40*). Although such onslaughts show little evidence for resource competition with nomadic livestock, individual localities can be completely devastated, with long-term socioeconomic ramifications in the human population (*41*).

The striking difference between migrant and resident herbivores, however, is the pulsed nature of migrant utilization, and consequently, the temporary carrying capacity of sites for migrants is larger than it would be for year-round residents (*8*, *10*). Moreover, the timing of grazing by migrants relative to the timing of growth of primary producers fundamentally defines the relation between grazing intensity and primary production (*39*). For example, herds of up to 1 million migratory wildebeest (*Connochaetes gnou*) use the highly nutritious forage of the short grass plains for calving during the wet season; outside of this period, the wildebeest migrate to woodlands where plants are less abundant and of lower nutritional quality (*42*). Theoretical studies demonstrate that year-round grazing of the plains by an equivalent number of residents would result in herbivory-limited plant growth, reduced standing biomass, and a loss of excess nitrogen from the system, resulting in a long-term reduction in aboveground net primary productivity (*39*). However, because the timing of grazing by migrants is decoupled from the timing of plant growth, increased grazing intensity from migrants results in substantially higher primary productivity than that in an ecosystem devoid of their presence (*39*).

In addition to interactions with primary producers, migratory herbivores interact with resident herbivores. The outcome of migrant-resident interactions may, however, substantially differ from standard theoretical predictions. For instance, if resident species are limited by seasonal variation in resources, then during the seasons of plenty, resources are conceivably available in excess of the capacity of residents to consume them. As a result, a migratory subordinate may be able to exploit resources shared with an otherwise competitively dominant resident species, as is the case for the migratory ungulates on the plains during the wet season (*10*). Conversely, grazers that reside
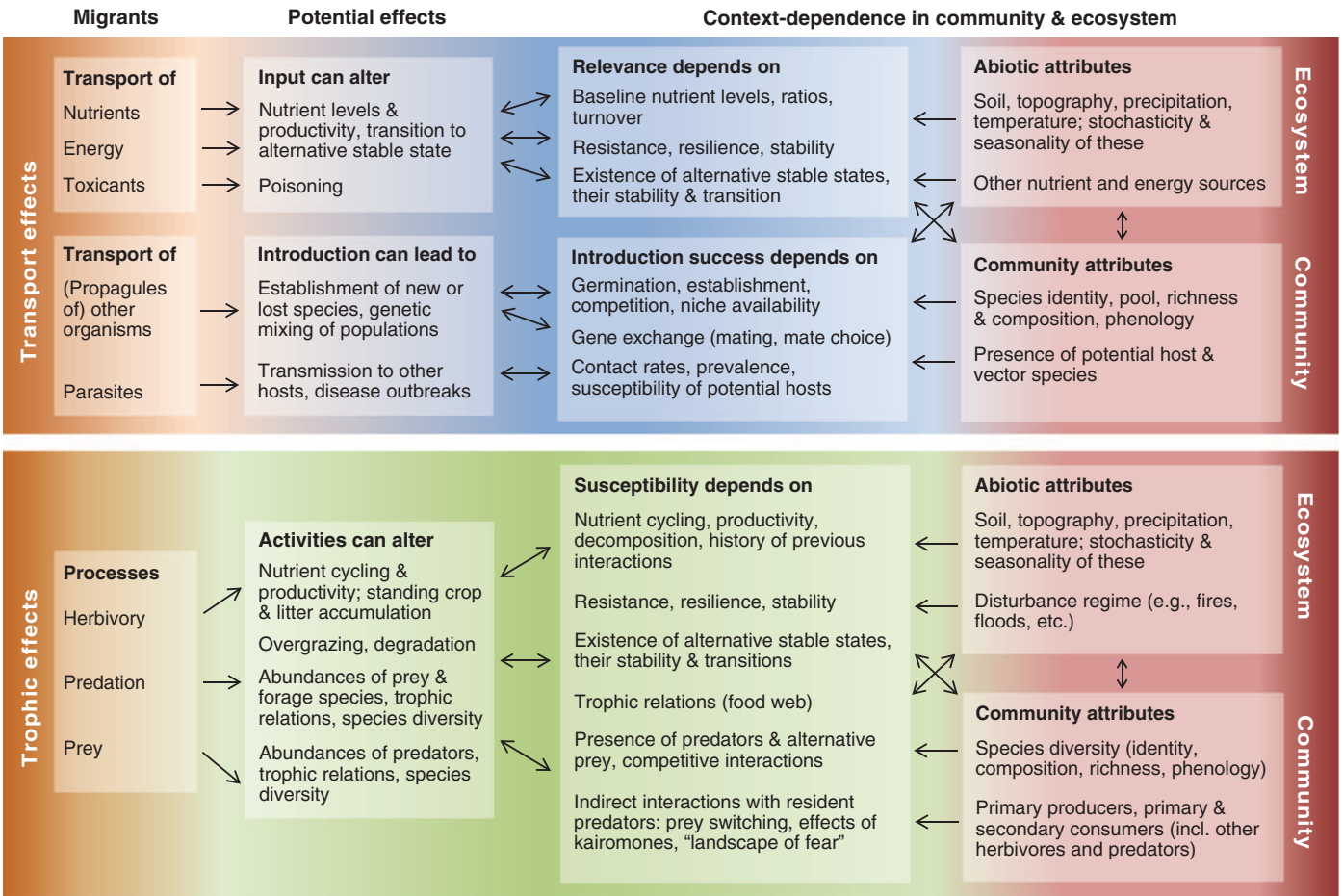
Fig. 3. The transport and trophic effects that migratory animals exert on resident communities critically depend on the attributes of communities and ecosystems.

year-round in the woodland interact with migrants during the period of food scarcity, and the influence of migratory competitors may have synergistic negative effects (*10*).

The annual migration of wildebeest not only typifies the concept of spatially coupled food webs (*43*, *44*) but illustrates coupling between communities whose dynamics operate at very different rates and with different energetic efficiencies (*45*). The short grass plains are ephemeral, boom-and-bust systems that occur for only a restricted period each year, despite providing the majority of the annual protein requirement of the migratory grazers (*45*). Thus, energy moves through the food web of the short grass plains at a "fast" pace. The woodlands show "slower" energy chains, with plant productivity less variable between seasons and, as a result, resident herbivores extending reproduction throughout a larger portion of the year (*46*). The migratory herds uniquely couple the fast resource chains of the plains to the slow resource chains of the woodlands (*45*).

Trophic Effects: Predation

Many seabirds, raptors, cephalopods, fish, and marine mammals are migratory predators, with the potential to exert top-down regulation on prey populations and resident communities through trophic cascades. For instance, numerous species of migratory birds and bats prey on insects, which reduces their local abundance and thereby limits insect outbreaks and damage to agricultural crops, as well as alters forest ecosystem dynamics (*41*, *47*). Interactions between migratory predators and community processes are, however, exemplified in studies of aquatic systems (Fig. 2).

In addition to the iconic salmonid and eel migrations, numerous cyprinid fish undertake seasonal migrations in north-temperate environments—

departing from lakes in autumn to spend the winter in streams and wetlands before returning in spring (*48*). When a large proportion of the fish population migrates, predation pressure on zooplankton is diminished, which facilitates rapid growth in the zooplankton population in spring and results in a high probability of a stabilized clear-water phase (*48*). Yet, without mass migration, predation pressure on zooplankton remains high during winter, which results in largely unrestricted phytoplankton growth in spring that can prevent the establishment of macrophytes and either destabilize the clear-water phase or catalyze a transition to a turbid state. Thus, these seasonal migrations may drive transitions between alternative stable states in lakes (*48*).

Migratory predators may also mediate indirect interactions between prey species in physically separated habitats, generating strong spatial patterns in trophic cascades (Figs. 1 and 3). For instance, the availability of prey in one location can, through its effect on predator abundance, indirectly influence the intensity of predation exerted at another location (*10*). Theoretical studies have demonstrated that the degree of spatial coupling, particularly by large mobile consumers, is overwhelmingly important to the stability of food webs (*49*). Weak to intermediate spatial coupling in particular—achieved when predators range over several scales of their prey and also switch prey preference in order to overcome spatial and temporal variation in prey abundance—can be potent stabilizers of food webs (*49*).

Trophic Effects: Migrants as Prey

Migrants not only use, but can also constitute resource peaks that may be exploited by resident predators along migration routes (*10*). For instance, migratory prey are an unmistakably im-

portant resource for lions (*Panthera leo*) in the Serengeti, who time their reproduction to coincide with wildebeest migration so faithfully that lions in the dry season range breed at a completely different time of year to lions in the wet season range (*10*) (Fig. 4). Similarly, reproduction in Eleonora's falcons (*Falco eleonorae*) in the Mediterranean is coincident with the autumn migration of song birds, and Arctic foxes (*Vulpes lagopus*) experience higher reproductive rates as a result of the highly predictable subsidies from migratory geese, such that the probability of fox reproduction declined by more than 70% for every 10 km between the fox den and a goose breeding site (*50*). Yet, migratory prey need not be large-bodied to have a significant influence on resident ecosystems. Larvae of army cutworm moths (*Euxoa auxiliaris*) hibernate on the Great Plains, then migrate to the Rocky Mountains as newly emerged adults in spring, where they have been shown to form a substantive food source for grizzly bears (*Ursus arctos horribilis*) inhabiting talus slopes, both in terms of proportion of prey items (>95% of their ingested volume) and energy density (*51*).

As migratory populations are larger than "equivalent" resident populations (*8*), they may represent a double-edged sword for resident species in terms of shared predators. Subsidized by migrants, resident predators may become more abundant than would otherwise be the case (*52*) and thus increase predation risk to residents when migrants are no longer present, as seen in lions and hyenas (*Crocuta crocuta*) that switch to resident species when the herds of migratory ungulates depart (*46*). Yet the presence of migrants may also provide residents with a temporal refuge from predation. The temporary presence of migrants, coupled with their influence on predator populations, therefore acts to sequentially

Fig. 4. Migratory herbivores furnish a smorgasbord for resident lions at both ends of their migratory range in the Serengeti. [©www.iStockphoto.com/GlobalP]

enhance then reduce indirect competition with similar resident species (*45*).

Synthesizing Migrant Influences on Ecological Processes

As the foregoing examples illustrate, migrations are not simply the movement of animals. They are ecological processes embedded in, and interacting with, a complex web of resident communities. Resident communities both shape migration routes and phenology (*1*) and are, in turn, modified by the presence of migrants, the carryover effects of previous sites on migrants, and the legacy effects of migrant-resident interactions that persist long after migrants have departed. Systems that play host to migratory species may, therefore, profoundly differ from those that do not because of at least three features: (i) the timing, frequency, and predictability of migrations; (ii) the intensity of interactions; and (iii) the spatial scales over which they connect communities and ecosystems.

The timing of migration relative to resident phenology is fundamental to the strength and direction of migrant-resident interactions (*53*). For instance, migrants can only be important pollinators if their visits coincide with peak flowering (*29*). Similarly, if parasite prevalence shows a marked seasonal dynamics, transmission may be restricted to sites where high prevalence and migrant visitation coincide (*54*). The synergy between migrant and resident phenologies also exists when visitation and resource growth are out of phase, as evidenced by increased primary productivity of savannah woodland habitats through the grazing of migratory ungulates in the dry season.

The frequency of migrations and the immense number of individuals involved often mean that migrant inputs constitute "resource pulses," defined as occasional, intense, brief episodes of increased resource availability that can profoundly alter demographic rates and abundances of interacting populations (*55*, *56*). In systems where the frequency of these events is longer than resident breeding cycles, resource pulses may result in a consumer population overshooting its carrying capacity once the resource pulse has finished, potentially leading to a population crash, and even (local) extinction (*55*). The effects of resource pulses can therefore persist long after the pulse itself is extinguished and may fundamentally alter community structure via extinction, invasion, or transition to alternative stable states (*55*). Critically, the effect of a resource pulse is intensified when the pulse is either more temporally concentrated or allochthonous in origin (*57*), both of which are expected for communities visited by migratory animals (Fig. 3). Moreover, migrations are often highly predictable events and of similar periodicity to resident breeding cycles, such that migrations could be expected to enhance the demographic rates of residents without the dramatic population crashes associated with resource pulses with a periodicity of multiple years [e.g., seed mast (*56*)]. However, such predictions have yet to be explicitly tested using the available theoretical frameworks.

The strength of interspecific interactions may be of paramount importance to the influence of migratory species on resident communities. In general, weak interspecies interactions (i.e., low instantaneous rate of per capita population change in one species as a result of changes in the other) have been shown to dampen oscillations in the abundance of resources and consumers, which makes them potent stabilizers in complex food webs (*43*, *58*). Several characteristics indicate that migrants may maintain many weak interactions. The presence of migrants in a resident community is pulsed, and although interactions may be of high intensity while migrants are present, their visits are both infrequent (usually once or twice per year) and short in duration (only a fraction of the annual cycle), such that they rarely constitute the sole consumers of local resources. Likewise, resident predators rarely rely solely on migrants as resource. Thus, not only are weak interactions generated between migrants and resident predators but, through prey-switching, there is a concomitant weakening of the interactions between resident predators and resident prey. It iis noteworthy that the strength of interactions maintained by migrants is likely to be predicated on both the migrants themselves (frequency and duration of

presence, resources consumed) and the recipient community, particularly the abundance and diversity of other, ecologically similar species (Fig. 3). On a global scale, the importance of migrants in resident communities may therefore be expected to increase with increasing latitude, altitude, and aridity.

Finally, animal migrations often span distances that are orders of magnitude greater than foraging or dispersal movements, such that interactions between several disparate communities may be mediated by migratory species. For instance, spatial nesting—in which resident primary producers are increasingly coupled across several spatial scales by large mobile consumers that adaptively follow resource asynchronies across spatially distinct regions—is thought to be central to the stability of complex food webs (*43*, *49*). This is particularly evident when the component resident systems operate at significantly different rates (i.e., coupling fast and slow energy chains) (*44*). Synchronized resource dynamics, on the other hand, would degenerate and possibly remove this spatial coupling. Although some aspects of spatial nesting are evident in the migration of ungulates across the African savannah and the migration of cyprinid fish between lakes and streams (*45*, *48*), many of the predators of these
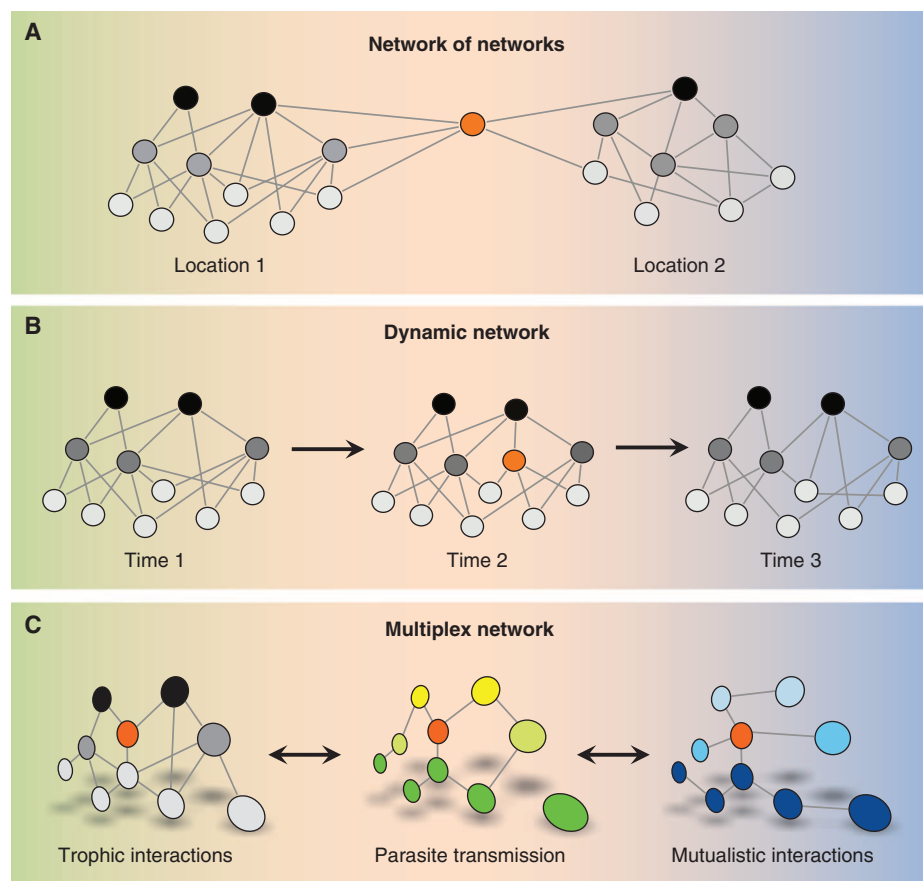
Fig. 5. Network approaches are ideally suited to investigating the role of migratory animals (orange nodes) and may assist in designing effective management actions. (**A**) Network-of-networks—several resident networks linked by migrants; (**B**) dynamic networks—nodes and edges change with the passage of migrants; (**C**) multiplex networks—nodes interact through several interdependent networks, e.g., trophic, mutualistic, and parasite transmission.

migrants remain resident year-round, in contrast to the increased mobility of predators that is anticipated in current food-web studies. Food-web theory may therefore benefit from explicit consideration of migratory movements in coupling asynchronous resource dynamics.

Such "mobile links" have also been shown to increase ecosystem resilience by providing sources for reorganization after disturbance [i.e., ecological memory (9)]. Indeed, it is well established that dispersal between heterogeneous sites can influence patterns of diversity in metacommunities (24). Although studies of metacommunity structure generally assume that dispersal is constant through time, recent theoretical consideration of stochasticity in dispersal rates suggests that punctuated dispersal events lead to increased heterogeneity among communities (59). The predictability of migration in space and time may therefore render migrant-mediated dispersal fundamental to both the structuring metacommunities and the maintenance of ecological memory.

Outlook and Future Challenges

The breadth of mechanisms outlined above, combined with the sheer abundance of migratory taxa worldwide, suggests that migrants may represent profound but as-yet-underappreciated dimensions of biodiversity that are intimately embedded within local communities. For the handful of species whose interactions have been quantified, it is evident that migrants may substantially alter community structure and ecosystem processes across broad spatial scales; however, it would be premature to assume that this is the case for all migrant-resident interactions. Several synthetic questions therefore pose exciting challenges for future research, including how the effects of migrants differ between sites along migratory routes; how traits of migrants (taxon, trophic position, mode of locomotion, and so on) influence their role in linking communities; and how community attributes (diversity, stability, phenology, resource availability, size, isolation, and so on) modify the relative importance of migrant effects. Collectively, these synthetic questions inform the crucial question: What are the global consequences of the rapid decline and disappearance of many animal migrations?

Across the globe, migration is an increasingly threatened phenomenon as a consequence of habitat destruction, creation of barriers, over-exploitation, and climate change (60). The loss of migrants and migratory behavior also entails the loss of their ecosystem services—the manifold transport and trophic effects outlined above. Management strategies must therefore be designed to conserve not only migratory species but also their ecosystem functions. Yet, the conservation of migrants poses exceptional scientific and societal challenges (60), as events at each stage of the migratory cycle affect behavior and demographic rates (61) and ecological interactions at other stages (Fig. 1). Management actions therefore require detailed understanding of the cascad-

ing influence of multiple stages across multiple locations.

A promising framework for understanding complex systems and developing effective conservation strategies comes from network theory (62). Network approaches detail the pattern of interactions ("edges") between entities ("nodes": species, populations, and individuals), and have been increasingly used to identify structural properties ("topology") that confer stability and resilience in ecological systems (63, 64). The majority of such network approaches have considered single (resident) communities, in static (time-aggregated) networks, focusing on a single interaction type (e.g., trophic or mutualistic interactions) (65). Given that animal migrations link several disparate ecological communities, introduce dynamics by their temporary presence, and interact through several simultaneous processes, three recent advances in network theory would greatly enhance our ability to assess the ecological importance of animal migrations, the consequences of their loss, and the effectiveness of potential management measures: networks-of-networks, dynamic networks, and multiplex networks (Fig. 5).

The conservation of migratory species is often inherently transnational, and as a result, targeted management actions that consider the entire migratory range and identify the optimal collaboration between jurisdictions are required. To this end, the analysis of network-of-networks (Fig. 5A), through explicit consideration of migrant-mediated interactions between resident networks, facilitates a mechanistic understanding of the cascading consequences of losing migrants, as well as identification of the nodes and edges most influenced by such a loss and those with the greatest influence on the persistence of migrants and their migrations. Networks-of-networks therefore allow detailed assessment of how perturbations and management actions in one resident network cascade through other resident networks. Furthermore, because the arrival and departure of migrants represents the addition and removal of nodes and edges in a network (Fig. 5B), standard time-aggregated networks may not accurately depict the gross topology (the arrangement of nodes and edges) and flow (how resources, information, and such are propagated between nodes) of the entire network, including properties related to network stability [reviewed by (65)]. By examining changes in network topology ("rewiring") and flow over time, and their mutually dependent feedbacks, using several time-ordered interaction matrices, dynamic network approaches are ideally suited to assessing the speed, extent, and magnitude of migrant-induced rewiring and, hence, the consequences of disappearing animal migrations for network flow and stability. Finally, migrants interact with resident communities through several processes simultaneously (Fig. 1), by forming a network of several interdependent networks (Fig. 5C) (66). So-called multiplex networks are increasingly recognized as vital to understanding the behavior and stability of complex systems be-

cause most systems are inherently comprised of coupled networks (67); the properties promoting stability and resilience can be vastly different from those identified for networks of single-interaction types (66); and multiplex networks are far more susceptible to catastrophic failure, which may even follow the removal of a single node (66, 67). Although multiplex networks are still rare in ecological studies (68, 69), coextinction cascades can be dramatically accelerated when feedbacks between multiple networks are included (68). Because each of these network approaches match scales of action to the scales of problem (70), the efficiency of various targeted interventions, in terms of diffusion through the entire network-of-networks, can be assessed (71).

Understanding the causes and consequences of community structure and dynamics remains a major frontier in ecology, particularly in light of the unprecedented rate of species extinctions facing the planet (43). Given the ubiquity of migrants and their potential to link disparate communities the world over, ecological processes in one location cannot be viewed in isolation. Greater understanding of how migratory patterns uniquely influence ecological networks is therefore of paramount importance to the conservation and management of migratory and resident species alike.

References and Notes

1. T. Alerstam, A. Hedenström, S. Åkesson, Long-distance migration: Evolution and determinants. *Oikos* **103**, 247–260 (2003). doi: 10.1034/j.1600-0706.2003.12559.x
2. H. Dingle, *Migration: The Biology of Life on the Move* (Oxford Univ. Press, Oxford, 1996).
3. J. S. Kirby et al., Key conservation issues for migratory land- and waterbird species on the world's major flyways. *Bird Conserv. Int.* **18** (suppl. 1), S49 (2008). doi: 10.1017/S0959270908000439
4. G. W. Cox, The evolution of avian migration systems between temperate and tropical regions of the New World. *Am. Nat.* **126**, 451 (1985). doi: 10.1086/284432
5. S. Hahn, S. Bauer, F. Liechti, The natural link between Europe and Africa— 2.1 billion birds on migration. *Oikos* **118**, 624–626 (2009). doi: 10.1111/j.1600-0706.2008.17309.x
6. J. W. Chapman, V. A. Drake, D. R. Reynolds, Recent insights from radar studies of insect flight. *Annu. Rev. Entomol.* **56**, 337–356 (2011). doi: 10.1146/annurev-ento-120709-144820; pmid: 21133761
7. M. S. Bowlin et al., Grand challenges in migration biology. *Integr. Comp. Biol.* **50**, 261–279 (2010). doi: 10.1093/icb/icq013; pmid: 21558203
8. J. M. Fryxell, J. Greever, A. R. E. Sinclair, Why are migratory ungulates so abundant? *Am. Nat.* **131**, 781 (1988). doi: 10.1086/284822
9. J. Lundberg, F. Moberg, Mobile link organisms and ecosystem functioning: Implications for ecosystem resilience and management. *Ecosystems (N.Y.)* **6**, 87 (2003). doi: 10.1007/s10021-002-0150-4
10. R. M. Holdo, R. D. Holt, A. R. E. Sinclair, B. J. Godley, S. Thirgood, in *Animal Migration: A Synthesis*, E. J. Milner-Gulland, J. M. Fryxell, A. R. E. Sinclair, Eds. (Oxford Univ. Press, Oxford, 2011), pp. 131–143.
11. O. Varpe, O. Fiksen, A. Slotte, Meta-ecosystems and biological energy transport from ocean to coast: The ecological importance of herring migration. *Oecologia* **146**, 443–451 (2005). doi: 10.1007/s00442-005-0219-9; pmid: 16195881
12. G. W. Holtgrieve, D. E. Schindler, Marine-derived nutrients, bioturbation, and ecosystem metabolism: Reconsidering the role of salmon in streams. *Ecology* **92**, 373–385 (2011). doi: 10.1890/09-1694.1; pmid: 21618917

13. G. J. Chen *et al.*, Long-term zooplankton responses to nutrient and consumer subsidies arising from migratory sockeye salmon (*Oncorhynchus nerka*). *Oikos* **120**, 1317–1326 (2011). doi: 10.1111/j.1600-0706.2011.19042.x

14. J. W. Moore, D. E. Schindler, Nutrient export from freshwater ecosystems by anadromous sockeye salmon (*Oncorhynchus nerka*). *Can. J. Fish. Aquat. Sci.* **61**, 1582–1589 (2004). doi: 10.1139/f04-103

15. G. J. Chen *et al.*, Salmon-derived nutrients drive diatom beta-diversity patterns. *Freshw. Biol.* **56**, 292–301 (2011). doi: 10.1111/j.1365-2427.2010.02496.x

16. K. K. Bartz, R. J. Naiman, Effects of salmon-borne nutrients on riparian soils and vegetation in southwest Alaska. *Ecosystems (N. Y.)* **8**, 529–545 (2005). doi: 10.1007/s10021-005-0064-z

17. J. W. Moore, D. E. Schindler, Spawning salmon and the phenology of emergence in stream insects. *Proc. Biol. Sci.* **277**, 1695–1703 (2010). doi: 10.1098/rspb.2009.2342; pmid: 20129980

18. N. Michelutti *et al.*, Seabird-driven shifts in Arctic pond ecosystems. *Proc. Biol. Sci.* **276**, 591–596 (2009). doi: 10.1098/rspb.2008.1103; pmid: 18945662

19. S. Caut *et al.*, Seabird modulations of isotopic nitrogen on islands. *PLOS ONE* **7**, e39125 (2012). doi: 10.1371/journal.pone.0039125; pmid: 22723945

20. S. K. Brimble *et al.*, High arctic ponds receiving biotransported nutrients from a nearby seabird colony are also subject to potentially toxic loadings of arsenic, cadmium, and zinc. *Environ. Toxicol. Chem.* **28**, 2426–2433 (2009). doi: 10.1897/09-235.1; pmid: 19604032

21. S. Hahn, S. Bauer, M. Klaassen, Quantification of allochthonous nutrient input into freshwater bodies by herbivorous waterbirds. *Freshw. Biol.* **53**, 181 (2008).

22. A. Zacheis, J. W. Hupp, R. W. Ruess, Effects of migratory geese on plant communities of an Alaskan salt marsh. *J. Ecol.* **89**, 57–71 (2001). doi: 10.1046/j.1365-2745.2001.00515.x

23. R. Nathan *et al.*, Mechanisms of long-distance seed dispersal. *Trends Ecol. Evol.* **23**, 638–647 (2008). doi: 10.1016/j.tree.2008.08.003; pmid: 18823680

24. M. A. Leibold *et al.*, The metacommunity concept: A framework for multi-scale community ecology. *Ecol. Lett.* **7**, 601–613 (2004). doi: 10.1111/j.1461-0248.2004.00608.x

25. D. S. Viana, L. Santamaría, T. C. Michot, J. Figuerola, Migratory strategies of waterbirds shape the continental-scale dispersal of aquatic organisms. *Ecography* **36**, 430–438 (2013). doi: 10.1111/j.1600-0587.2012.07588.x

26. C. A. van Leeuwen, G. van der Velde, J. M. van Groenendael, M. Klaassen, Gut travellers: Internal dispersal of aquatic organisms by waterfowl. *J. Biogeogr.* **39**, 2031–2040 (2012). doi: 10.1111/jbi.12004

27. C. H. van Leeuwen, M. L. Tollenaar, M. Klaassen, Vector activity and propagule size affect dispersal potential by vertebrates. *Oecologia* **170**, 101–109 (2012). doi: 10.1007/s00442-012-2293-0; pmid: 22419480

28. P. Clausen, B. A. Nolet, A. D. Fox, M. Klaassen, Long-distance endozoochorous dispersal of submerged macrophyte seeds by migratory waterbirds in northern Europe—a critical review of possibilities and limitations. *Acta Oecol.* **23**, 191–203 (2002). doi: 10.1016/S1146-609X(02)01150-5

29. G. Nabhan, Ed., *Conserving Migratory Pollinators and Nectar Corridors in Western North America* (Univ. of Arizona Press, Tucson, AZ, 2004).

30. J. Hamrick, J. Nason, T. Fleming, J. Nassar, in *Columnar Cacti and Their Mutualists: Evolution, Ecology, and Conservation,* T. Fleming, A. Valiente-Banuet, Eds. (Univ. of Arizona Press, Tucson, AZ, 2002), pp. 122–133.

31. S. Altizer, R. Bartel, B. A. Han, Animal migration and infectious disease risk. *Science* **331**, 296–302 (2011). http://www.ncbi.nlm.nih.gov/entrez/query.fcgi?cmd=Retrieve&db=PubMed&list_uids=21252339&dopt=Abstractdoi: 10.1126/science.1194694; pmid: 21252339

32. J. Waldenström, S. Bensch, S. Kiboi, D. Hasselquist, U. Ottosson, Cross-species infection of blood parasites between resident and migratory songbirds in Africa. *Mol. Ecol.* **11**, 1545–1554 (2002). doi: 10.1046/j.1365-294X.2002.01523.x; pmid: 12144673

33. D. M. Buehler, T. Piersma, K. Matson, B. I. Tieleman, Seasonal redistribution of immune function in a migrant shorebird: Annual-cycle effects override adjustments to thermal regime. *Am. Nat.* **172**, 783–796 (2008). doi: 10.1086/592865; pmid: 18999941

34. Å. Gylfe, S. Bergström, J. Lundström, B. Olsen, Reactivation of *Borrelia* infection in birds. *Nature* **403**, 724–725 (2000). doi: 10.1038/35001663; pmid: 10693792

35. S. Krauss *et al.*, Coincident ruddy turnstone migration and horseshoe crab spawning creates an ecological 'hot spot' for influenza viruses. *Proc. Biol. Sci.* **277**, 3373–3379 (2010). doi: 10.1098/rspb.2010.1090; pmid: 20630885

36. C. A. Bradley, S. Altizer, Parasites hinder monarch butterfly flight: Implications for disease spread in migratory hosts. *Ecol. Lett.* **8**, 290–300 (2005). doi: 10.1111/j.1461-0248.2005.00722.x

37. B. J. Hoye, thesis, Utrecht University (2011).

38. S. J. Galsworthy *et al.*, Effects of infection-induced migration delays on the epidemiology of avian influenza in wild mallard populations. *PLOS ONE* **6**, e26118 (2011). doi: 10.1371/journal.pone.0026118; pmid: 22028812

39. R. M. Holdo, R. D. Holt, M. B. Coughenour, M. E. Ritchie, Plant productivity and soil nitrogen as a function of grazing, migration and fire in an African savanna. *J. Ecol.* **95**, 115–128 (2007). doi: 10.1111/j.1365-2745.2006.01192.x

40. J. Roffey, in *The Movement and Dispersal of Agriculturally Important Biotic Agents*, D. R. MacKenzie *et al.*, Eds. (Claitor's Publishing, Baton Rouge, LA, 1985), pp. 533–540.

41. J. A. Sánchez-Zapata *et al.*, Desert locust outbreaks in the Sahel: Resource competition, predation and ecological effects of pest control. *J. Appl. Ecol.* **44**, 323–329 (2007). doi: 10.1111/j.1365-2664.2007.01279.x

42. A. R. E. Sinclair, H. Dublin, M. Borner, Population regulation of Serengeti wildebeeest: A test of the food hypothesis. *Oecologia* **65**, 266–268 (1985). doi: 10.1007/BF00379227

43. N. Rooney, K. S. McCann, Integrating food web diversity, structure and stability. *Trends Ecol. Evol.* **27**, 40–46 (2012). doi: 10.1016/j.tree.2011.09.001; pmid: 21944861

44. N. Rooney, K. S. McCann, J. C. Moore, A landscape theory for food web architecture. *Ecol. Lett.* **11**, 867–881 (2008). doi: 10.1111/j.1461-0248.2008.01193.x; pmid: 18445027

45. A. Dobson, Food-web structure and ecosystem services: Insights from the Serengeti. *Philos. Trans. R. Soc. London. B Biol. Sci.* **364**, 1665–1682 (2009). doi: 10.1098/rstb.2008.0287; pmid: 19451118

46. A. R. E. Sinclair, Mammal population regulation, keystone processes and ecosystem dynamics. *Philos. Trans. R. Soc. London B Biol. Sci.* **358**, 1729–1740 (2003). doi: 10.1098/rstb.2003.1359; pmid: 14561329

47. S. A. Van Bael *et al.*, Birds as predators in tropical agroforestry systems. *Ecology* **89**, 928 (2008). doi: 10.1890/06-1976.1; pmid: 18481517

48. C. Brönmark *et al.*, There and back again: Migration in freshwater fishes. *Can. J. Zool.* (2013). doi: 10.1139/cjz-2012-0277

49. K. S. McCann, J. B. Rasmussen, J. Umbanhowar, The dynamics of spatially coupled food webs. *Ecol. Lett.* **8**, 513–523 (2005). doi: 10.1111/j.1461-0248.2005.00742.x; pmid: 21352455

50. M. A. Giroux *et al.*, Benefiting from a migratory prey: Spatio-temporal patterns in allochthonous subsidization of an Arctic predator. *J. Anim. Ecol.* **81**, 533–542 (2012). doi: 10.1111/j.1365-2656.2011.01944.x; pmid: 22268371

51. J. D. White Jr., K. C. Kendall, H. D. Picton, Grizzly bear feeding activity at alpine army cutworm moth aggregation sites in northwest Montana. *Can. J. Zool.* **76**, 221–227 (1998). doi: 10.1139/z97-185

52. C. Packer, R. D. Holt, P. J. Hudson, K. D. Lafferty, A. P. Dobson, Keeping the herds healthy and alert: Implications of predator control for infectious disease. *Ecol. Lett.* **6**, 797–802 (2003). doi: 10.1046/j.1461-0248.2003.00500.x

53. L. H. Yang, V. H. W. Rudolf, Phenology, ontogeny and the effects of climate change on the timing of species interactions. *Ecol. Lett.* **13**, 1–10 (2010). doi: 10.1111/j.1461-0248.2009.01402.x; pmid: 19930396

54. B. J. Hoye *et al.*, Reconstructing an annual cycle of interaction: Natural infection and antibody dynamics to avian influenza along a migratory flyway. *Oikos* **120**, 748–755 (2011). doi: 10.1111/j.1600-0706.2010.18961.x

55. R. D. Holt, Theoretical perspectives on resource pulses. *Ecology* **89**, 671–681 (2008). doi: 10.1890/07-0348.1; pmid: 18459331

56. R. S. Ostfeld, F. Keesing, Pulsed resources and community dynamics of consumers in terrestrial ecosystems. *Trends Ecol. Evol.* **15**, 232–237 (2000). doi: 10.1016/S0169-5347(00)01862-0; pmid: 10802548

57. A. Hastings, Temporally varying resources amplify the importance of resource input in ecological populations. *Biol. Lett.* **8**, 1067–1069 (2012). doi: 10.1098/rsbl.2012.0669; pmid: 22915629

58. K. McCann, A. Hastings, G. R. Huxel, Weak trophic interactions and the balance of nature. *Nature* **395**, 794–798 (1998). doi: 10.1038/27427

59. M. G. Matias, N. Mouquet, J. M. Chase, Dispersal stochasticity mediates species richness in source-sink metacommunities. *Oikos* **122**, 395–402 (2013). doi: 10.1111/j.1600-0706.2012.20479.x

60. D. S. Wilcove, M. Wikelski, Going, going, gone: Is animal migration disappearing. *PLOS Biol.* **6**, e188 (2008). doi: 10.1371/journal.pbio.0060188; pmid: 18666834

61. X. A. Harrison, J. D. Blount, R. Inger, D. R. Norris, S. Bearhop, Carry-over effects as drivers of fitness differences in animals. *J. Anim. Ecol.* **80**, 4–18 (2011). doi: 10.1111/j.1365-2656.2010.01740.x; pmid: 20726924

62. M. E. Newman, The structure and function of complex networks. *SIAM Rev.* **45**, 167–256 (2003). doi: 10.1137/S003614450342480

63. A.-M. Neutel, J. A. P. Heesterbeek, P. C. De Ruiter, Stability in real food webs: Weak links in long loops. *Science* **296**, 1120–1123 (2002). http://www.ncbi.nlm.nih.gov/entrez/query.fcgi?cmd=Retrieve&db=PubMed&list_uids=12004131&dopt=Abstractdoi: 10.1126/science.1068326; pmid: 12004131

64. E. Thébault, C. Fontaine, Stability of ecological communities and the architecture of mutualistic and trophic networks. *Science* **329**, 853–856 (2010). http://www.ncbi.nlm.nih.gov/entrez/query.fcgi?cmd=Retrieve&db=PubMed&list_uids=20705861&dopt=Abstractdoi: 10.1126/science.1188321; pmid: 20705861

65. B. Blonder, T. W. Wey, A. Dornhaus, R. James, A. Sih, Temporal dynamics and network analysis. *Methods Ecol. Evol.* **3**, 958–972 (2012). doi: 10.1111/j.2041-210X.2012.00236.x

66. S. V. Buldyrev, R. Parshani, G. Paul, H. E. Stanley, S. Havlin, Catastrophic cascade of failures in interdependent networks. *Nature* **464**, 1025–1028 (2010). doi: 10.1038/nature08932; pmid: 20393559

67. D. Helbing, Globally networked risks and how to respond. *Nature* **497**, 51–59 (2013). doi: 10.1038/nature12047; pmid: 23636396

68. A. Valiente-Banuet, M. Verdu, Human impacts on multiple ecological networks act synergistically to drive ecosystem collapse. *Front. Ecol. Environ* **11**, 408–413 (2013). doi: 10.1890/130002

69. M. J. O. Pocock, D. M. Evans, J. Memmott, The robustness and restoration of a network of ecological networks. *Science* **335**, 973–977 (2012). http://www.ncbi.nlm.nih.gov/entrez/query.fcgi?cmd=Retrieve&db=PubMed&list_uids=223630098&dopt=Abstractdoi: 10.1126/science.1214915; pmid: 22363009

70. A. M. Guerrero, R. R. McAllister, J. Corcoran, K. A. Wilson, Scale mismatches, conservation planning, and the value of social-network analyses. *Conserv. Biol.* **27**, 35–44 (2013). doi: 10.1111/j.1523-1739.2012.01964.x; pmid: 23305381

71. T. W. Valente, Network interventions. *Science* **337**, 49–53 (2012). http://www.ncbi.nlm.nih.gov/entrez/query.fcgi?cmd=Retrieve&db=PubMed&list_uids=22767921&dopt=Abstractdoi: 10.1126/science.1217330; pmid: 22767921

RESEARCH ARTICLES

Total Synthesis of a Functional Designer Eukaryotic Chromosome

Narayana Annaluru,[1]* Héloïse Muller,[1,2,3,4]* Leslie A. Mitchell,[2,5] Sivaprakash Ramalingam,[1] Giovanni Stracquadanio,[2,6] Sarah M. Richardson,[6] Jessica S. Dymond,[2,7] Zheng Kuang,[2] Lisa Z. Scheifele,[2,8] Eric M. Cooper,[2] Yizhi Cai,[2,9] Karen Zeller,[2] Neta Agmon,[2,5] Jeffrey S. Han,[10] Michalis Hadjithomas,[11] Jennifer Tullman,[6] Katrina Caravelli,[2,12] Kimberly Cirelli,[1,12] Zheyuan Guo,[1,13] Viktoriya London,[1,13] Apurva Yeluru,[1,13] Sindurathy Murugan,[6] Karthikeyan Kandavelou,[1,14] Nicolas Agier,[15,16] Gilles Fischer,[15,16] Kun Yang,[2,6] J. Andrew Martin,[2,6] Murat Bilgel,[13] Pavlo Bohutskyi,[13] Kristin M. Boulier,[12] Brian J. Capaldo,[13] Joy Chang,[13] Kristie Charoen,[13] Woo Jin Choi,[13] Peter Deng,[11] James E. DiCarlo,[13] Judy Doong,[13] Jessilyn Dunn,[13] Jason I. Feinberg,[12] Christopher Fernandez,[12] Charlotte E. Floria,[12] David Gladowski,[12] Pasha Hadidi,[13] Isabel Ishizuka,[12] Javaneh Jabbari,[12] Calvin Y. L. Lau,[13] Pablo A. Lee,[13] Sean Li,[13] Denise Lin,[12] Matthias E. Linder,[12] Jonathan Ling,[13] Jaime Liu,[13] Jonathan Liu,[13] Mariya London,[12] Henry Ma,[13] Jessica Mao,[13] Jessica E. McDade,[13] Alexandra McMillan,[12] Aaron M. Moore,[12] Won Chan Oh,[13] Yu Ouyang,[13] Ruchi Patel,[13] Marina Paul,[12] Laura C. Paulsen,[13] Judy Qiu,[13] Alex Rhee,[13] Matthew G. Rubashkin,[13] Ina Y. Soh,[12] Nathaniel E. Sotuyo,[12] Venkatesh Srinivas,[13] Allison Suarez,[13] Andy Wong,[13] Remus Wong,[13] Wei Rose Xie,[12] Yijie Xu,[13] Allen T. Yu,[12] Romain Koszul,[3,4] Joel S. Bader,[2,6] Jef D. Boeke,[2,11,5]† Srinivasan Chandrasegaran[1]†

Rapid advances in DNA synthesis techniques have made it possible to engineer viruses, biochemical pathways and assemble bacterial genomes. Here, we report the synthesis of a functional 272,871–base pair designer eukaryotic chromosome, synIII, which is based on the 316,617–base pair native *Saccharomyces cerevisiae* chromosome III. Changes to synIII include TAG/TAA stop-codon replacements, deletion of subtelomeric regions, introns, transfer RNAs, transposons, and silent mating loci as well as insertion of loxPsym sites to enable genome scrambling. SynIII is functional in *S. cerevisiae*. Scrambling of the chromosome in a heterozygous diploid reveals a large increase in a-mater derivatives resulting from loss of the *MATα* allele on synIII. The complete design and synthesis of synIII establishes *S. cerevisiae* as the basis for designer eukaryotic genome biology.

*S*accharomyces cerevisiae has a genome size of ~12 Mb distributed among 16 chromosomes. The entire genome encodes ~6000 genes, of which ~5000 are individually nonessential (*1*). Which of these nonessential genes are simultaneously dispensable? Although a number of studies have successfully mapped pairwise "synthetic lethal" interactions between gene knockouts, those methods do not scale well to three or more gene combinations because the number of combinations rises exponentially. Our approach to address this question is to produce a synthetic yeast genome with all nonessential genes flanked by loxPsym sites to enable inducible evolution

and genome reduction (a process we refer to as SCRaMbLEing) in vivo (*2*, *3*). The availability of a fully synthetic *S. cerevisiae* genome will allow direct testing of evolutionary questions—such as the maximum number of nonessential genes that can be deleted without a catastrophic loss of fitness and the catalog of viable 3-gene, 4-gene, … *n*-gene deletions that survive under a given growth condition—that are not otherwise easily approachable in a systematic unbiased fashion. Engineering and synthesis of viral and bacterial genomes have been reported in the literature (*4–11*). An international group of scientists has embarked on constructing a designer eukaryotic genome, Sc2.0 (www.syntheticyeast.org), and here we report the total synthesis of a complete designer yeast chromosome.

Yeast chromosome III, the third smallest in *S. cerevisiae* [316,617 base pairs (bp)], contains the *MAT* locus determining mating type and was the first chromosome sequenced (*12*). We designed synIII according to fitness, genome stability, and genetic flexibility principles developed for the Sc2.0 genome (*2*). The native sequence was edited in silico by using a series of deletion, insertion, and base substitution changes to produce the desired "designer" sequence (Fig. 1, figs. S1 and S2, and supplementary text). The hierarchical wet-laboratory workflow used to construct synIII (Fig. 2) consisted of three major steps: (i) The 750-bp building blocks (BBs) were produced starting from overlapping 60- to 79-mer oligonucleotides and assembled by using standard polymerase chain reaction (PCR) methods (*13*, *14*) by undergraduate students in the Build-A-Genome class at JHU (Fig. 2A) (*15*). The arbitrary naming scheme for the differently sized DNA molecules used in the Sc2.0 project is explained in fig. S3. (ii) The 133 synIIIL (left of the centromere) BBs and 234 synIIIR BBs were assembled into 44 and 83 overlapping DNA minichunks of ~2 to 4 kb, respectively (table S1, Fig. 2B, and fig. S4) (*16*, *17*). (iii) All adjacent minichunks for synIII were designed to overlap one another by one BB to facilitate further assembly in vivo by homologous

[1]Department of Environmental Health Sciences, Johns Hopkins University (JHU) School of Public Health, Baltimore, MD 21205, USA. [2]High Throughput Biology Center, JHU School of Medicine, Baltimore, MD 21205, USA. [3]Group Spatial Regulation of Genomes, Department of Genomes Genetics, Institut Pasteur, F-75015 Paris, France. [4]CNRS, UMR 3525, F-75015 Paris, France. [5]New York University Langone Medical Center, New York, NY 10016, USA. [6]Department of Biomedical Engineering and Institute of Genetic Medicine, Whiting School of Engineering, JHU, Baltimore, MD 21218, USA. [7]Biological Sciences, Research and Exploratory Development Department, JHU Applied Physics Laboratory, Laurel, MD 20723, USA. [8]Department of Biology, Loyola University Maryland, Baltimore, MD 21210, USA. [9]University of Edinburgh, Edinburgh, Scotland, UK. [10]Carnegie Institution of Washington, Baltimore, MD 21218, USA. [11]Department of Biology, JHU, Baltimore, MD 21218, USA. [12]Krieger School of Arts and Sciences, JHU, Baltimore, MD 21218, USA. [13]Whiting School of Engineering, JHU, Baltimore, MD 21218, USA. [14]Pondicherry Biotech Private Limited, Pillaichavady, Puducherry 605014, India. [15]Sorbonne Universités, Université Pierre et Marie Curie, Univ Paris 06, UMR 7238, Génomique des Microorganismes, F-75005 Paris, France. [16]CNRS, UMR7238, Génomique des Microorganismes, F-75005 Paris, France.

*These authors contributed equally to this work.

†Corresponding author. E-mail: jef.boeke@nyumc.org (J.D.B.); schandra@jhsph.edu (S.C.)
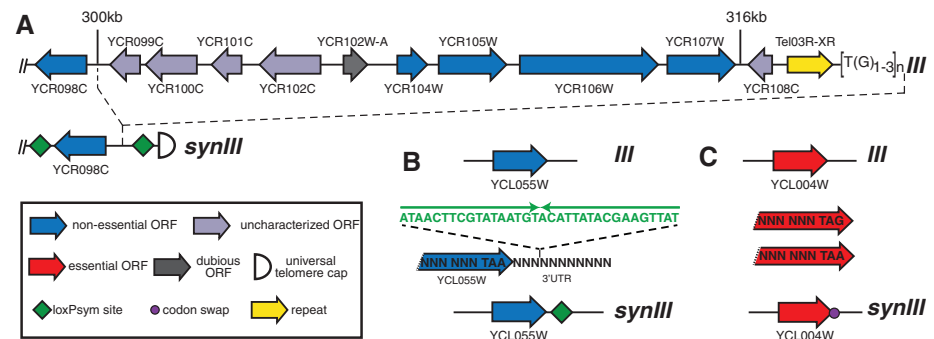
Fig. 1. SynIII design. Representative synIII design segments for loxPsym site insertion (**A** and **B**) and stop codon TAG to TAA editing (**C**) are shown. Green diamonds represent loxPsym sites embedded in the 3' untranslated region (UTR) of nonessential genes and at several other landmarks. Fuchsia circles indicate synthetic stop codons (TAG recoded to TAA). Complete maps of designed synIII chromosome with common and systematic open reading frame (ORF) names, respectively, are shown in figs. S1 and S2.

recombination in yeast (18, 19). By using an average of 12 minichunks and alternating selectable markers in each experiment, we systematically replaced the native sequence of *S. cerevisiae* III with its synIII counterpart in 11 successive rounds of transformation (Fig. 2C and table S2) (20, 21).

Genome Comparisons

PCRTag analysis (2) revealed the presence of synIII synthetic PCRTags and absence of native PCRTags (Fig. 3A; see supplementary text and figs. S5 to S7 for the complete set of PCRTag

analyses). The smaller size of synIII and intermediates in its full synthesis as compared with the native yeast chromosome was demonstrated by pulsed-field gel electrophoresis (Fig. 3B and fig. S8) (22). Analysis of the intermediate strains revealed that the starting strain had some unexpected rearrangements in at least two chromosomes and that an additional rearrangement occurred during the assembly process; these did not affect synIII (fig. S8). These abnormalities were eliminated through back-crossing the synIIIL intermediate strain to strain BY4742 (table S3), yielding a *MATα* strain

with an electrophoretic karyotype perfectly matching BY4742 but for the expected altered length III (compare lane 97 to 97* in fig. S8). Southern blot analyses using arm-specific radiolabeled probes further verified and validated the structure of the left- and right-arm telomere ends of synIII, which had been specified by the universal telomere cap (UTC) sequence (fig. S9). Restriction fragment sizes on Southern blots are compatible with the deletion of *HML*, *HMR*, and much of each subtelomere (fig. S9). This was further confirmed by complete genome sequencing of the synIII strain.

Fig. 2. SynIII construction. (**A**) BB synthesis. JHU students in the Build-A-Genome course synthesized 750-bp BBs (purple) from oligonucleotides. nt, nucleotides. (**B**) Assembly of minichunks. Two- to 4-kb minichunks (yellow) were assembled by homologous recombination in *S. cerevisiae* (table S1). Adjacent minichunks were designed to encode overlap of one BB to facilitate downstream assembly steps. Minichunks were flanked by a rare cutting restriction enzyme (RE) site, *Xma*I or *Not*I. (**C**) Direct replacement of native yeast chromosome III with pools of synthetic minichunks. Eleven iterative one-step assemblies and replacements of native genomic segments of yeast chromosome III were carried out by using pools of overlapping synthetic DNA minichunks (table S2), encoding alternating genetic markers (*LEU2* or *URA3*), which enabled complete replacement of native III with synIII in yeast.

A Step 1: Synthesize Building Blocks (BBs) from oligonucleotides
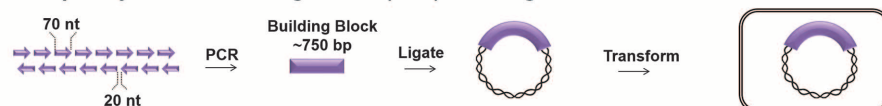
B Step 2: Assemble 2-4 kb minichunks
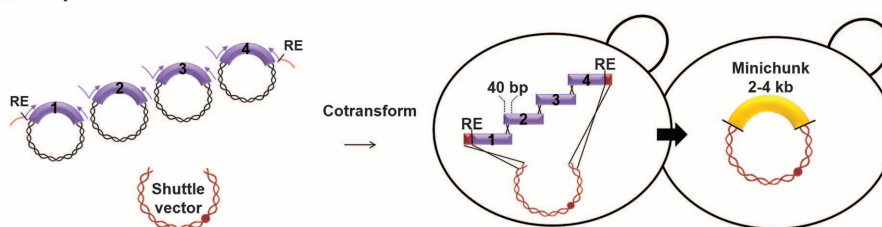
C Step 3: Replace native *III* with minichunks
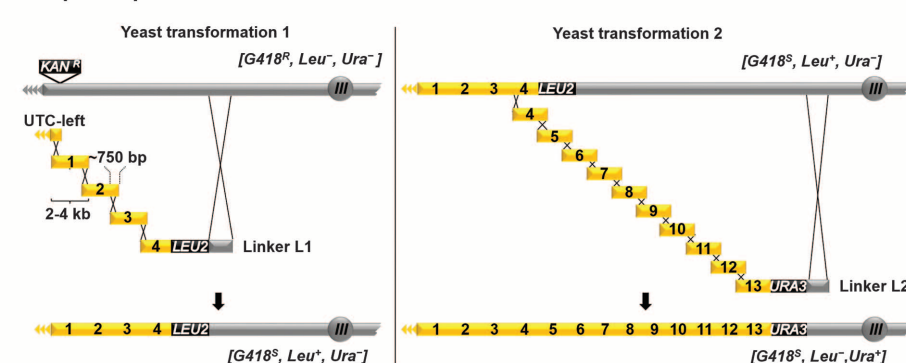
Fig. 3. Characterization and testing of synIII strain. (**A**) PCRTag analysis (one PCRTag per ~10 kb) of the left arm of synIII and WT yeast (BY4742) DNA is shown. Analysis of the complete set of PCRTags is shown in figs. S4 to S6. (**B**) Karyotypic analysis of synIII and synIIIL strains by pulsed-field gel electrophoresis revealed the size reduction of synIII and synIIIL compared with native III. Yeast chromosome numbers are indicated on the right side. SynIII (272,871 bp) and native chromosome VI (270,148 bp) comigrate in the gel. A karyotypic analysis of synIII and all intermediate strains is shown in fig. S8. (**C**) SynIII and synIIIL phenotyping on various types of media. Tenfold serial dilutions of saturated cultures of WT (BY4742), synIIIL, and synIII strains were plated on the indicated media and temperatures. YPD, yeast extract peptone dextrose; YPGE, yeast extract peptone glycerol ethanol; MMS, methyl methanosulfate. A complete set of synIII and synIIIL phenotyping under various conditions is shown in fig. S11.
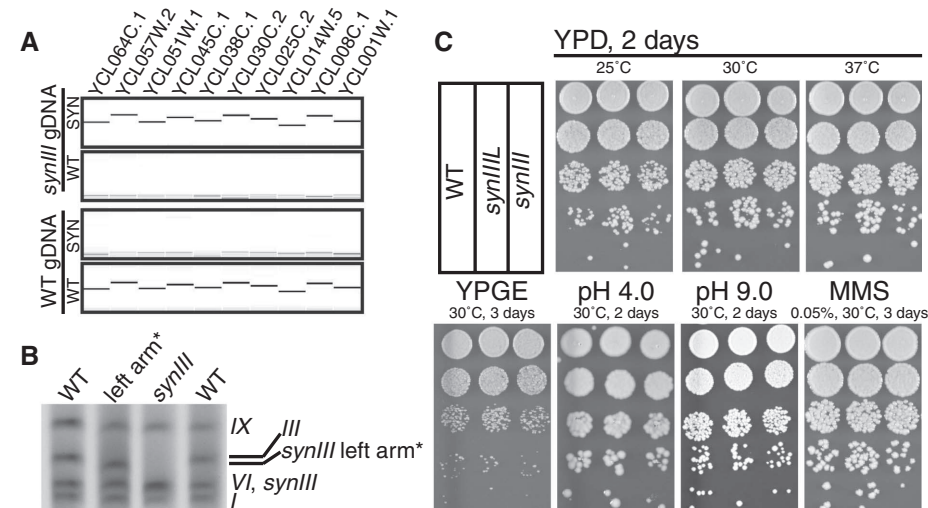
DNA sequencing of the synIII strain genome revealed sequence differences at 10 sites in synIII compared with our designed sequence (table S4). Nine of the changes are base substitutions or 1-bp insertions or deletions (indels). Three of the nine mutations correspond to preexisting but apparently innocuous mutations in the minichunks and BBs. Of the remainder, two correspond to the wild-type (WT) base at this position and thus may simply reflect inheritance of WT sequence. Because PCRTag analysis (table S5) was the method used to validate transformants during the 11 intermediate construction steps, the recombination events involved are patchy transformants, with tiny patches of native DNA instead of synthetic sequence that would have been missed during the PCRTag analysis. The remaining four mutations, which must have originated during the integration process, all occur in regions of overlap in the synIII minichunks, suggesting that the homologous recombination process may be somewhat error-prone relative to baseline error rates

(23). The tenth change is the absence of an expected loxPsym site.

To check for negative effects of modifications on fitness of synIII-containing strains from the WT (BY4742), we examined colony size, growth curves, and morphology under various conditions. A growth curve analysis established that synIII and the isogenic native strain had no detectable fitness difference (fig. S10). The strains were also indistinguishable from each other on colony-size tests (Fig. 3C), indicating that defects in fitness attributable to the synIIIL intermediate or synIII are very modest, with only 1 condition out of 21 (high sorbitol) showing a subtle fitness defect for synIII (fig. S11). Cell morphology of all intermediate strains was similar to that of WT (fig. S12) except that, during replacement round R3 (giving rise to strain 219 kb-synIII), a very low frequency (~1% of cells) of morphologically abnormal buds were observed (fig. S12). We performed transcript profiling to identify possible changes in gene expression across synIII or genome-wide re-

sulting from synonymous substitutions, introduction of loxPsym sites, and other changes. Although 10 loci are differentially expressed at genome-wide significance ($P < 7.4 \times 10^{-6}$ for 5% family-wise error rate based on 6756 loci with at least one mapped read and also corresponding to 1% false discovery rate), eight of these correspond to loci intentionally deleted from synIII. The remaining two loci are *HSP30* on synIII, ~16-fold down, and *PCL1* on native chromosome *XIV*, ~16-fold up (fig. S13).

The inclusion of hundreds of designed changes in the synthetic chromosome, including the removal of 11 transfer RNA (tRNA) genes said to be important sites of cohesin loading, might result in subtle or overt destabilizing effects on the synthetic chromosome; alternatively, removal of repetitive DNA sequences might increase stability by reducing the likelihood of "ectopic" recombination events involving two different repeat copies. Because of the 98 loxPsym sites added to synIII (and all the other changes), it was important to evaluate the genome integrity and the loss rate of the chromosome in the absence of Cre expression. PCRTag analysis revealed that synIII is stable over 125 mitotic generations in 30 independent lineages (Fig. 4A). To evaluate the loss rate of synIII, we used the a-like faker assay in which *MAT*α cells carrying synIII were monitored for acquiring the ability to mate as *MAT*a cells, a consequence of losing chromosome III (24). Despite the extensive chromosome engineering, the frequency of *MAT*α/synIII loss was not significantly different from that of the WT control (Fig. 4B).

It is not known whether cohesin accumulation at a tRNA gene region directly depends on the presence of the tRNA gene, nor is its effect on chromosome stability clear. We compared the map of cohesin binding sites on native chromosome III and synIII by using chromatin immunoprecipitation sequence (ChIP-seq) analysis (fig. S14). The overall cohesin binding pattern is similar between the two chromosomes. However, at three tRNA genes that show a prominent peak in the native chromosome, that peak is reduced or in one case [the glutamine tRNA gene tQ(UUG)C] completely absent from synIII (fig. S14). Thus, we conclude that tRNA genes and their documented interactions with both cohesin and condensin (25, 26) are dispensable for high levels of chromosome stability. We also compared the replication dynamics of synIII and native III (supplementary text, table S9, and fig. S15) and saw few dramatic changes in dynamics in spite of several autonomously replicating sequences having been deleted.

SCRaMbLEing in haploid strains containing chromosome synIII leads to lethality via essential gene loss (fig. S16). We looked for more subtle effects of SCRaMbLE in a heterozygous *MAT*a/α (mating incompetent) diploid strain with a synthetic *MAT*α chromosome and a native *MAT*a chromosome synIII/III; (fig. S17). We introduced the Cre-EBD plasmid into such strains, as well as into
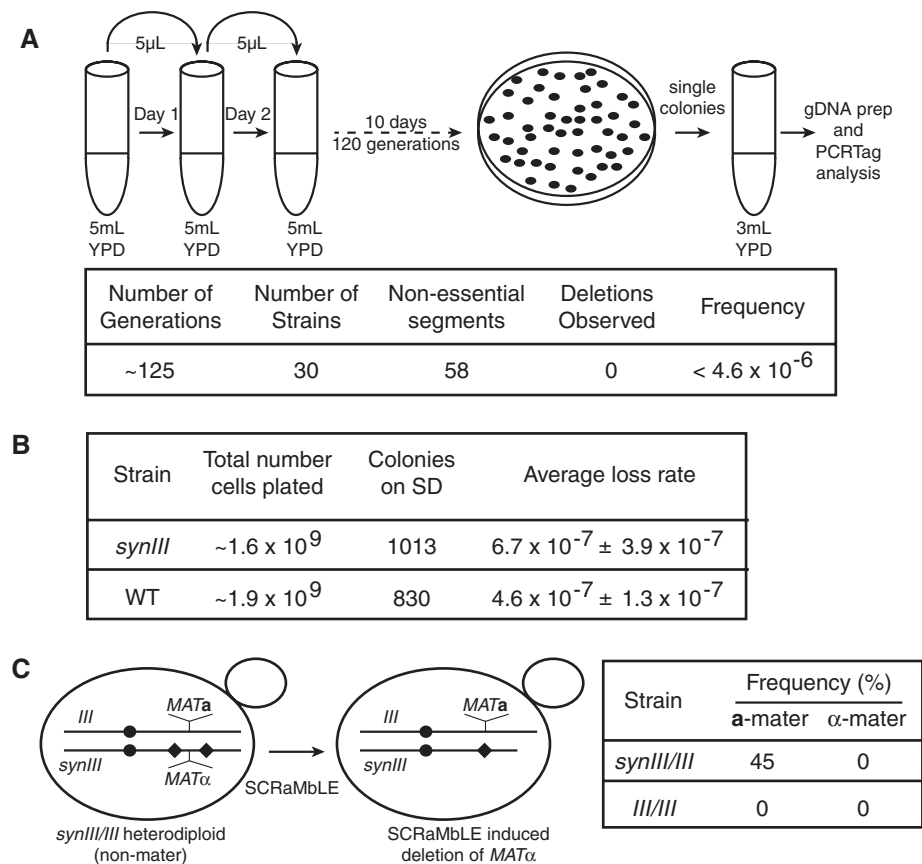
Fig. 4. Genomic stability of the synIII strain. (**A**) PCRTag analysis of synIII strain after ~125 generations. We assayed for the loss of 58 different segments lacking essential genes in the absence of SCRaMbLEing; no losses were observed after over 200,000 segment-generations analyzed; reported frequency is a maximum estimate of segment loss frequency per generation. gDNA, genomic DNA. (**B**) Evaluation of the loss rate of synIII chromosome using a-like faker assay. No significant change in the loss frequency was observed, although the absolute loss rate value is modestly higher in synIII. SD, standard dextrose. (**C**) SCRaMbLE leads to a gain of mating type a behavior in synIII heterozygous diploids. Frequencies are of a-mater and α-mater colonies post-SCRaMbLE (induction with estradiol) in synIII/III and III/III strains. A complete SCRaMbLE analysis is shown in fig. S18. Diamonds represent loxPsym sites, and circles indicate centromeres.

Panel A table:

Number of Generations	Number of Strains	Non-essential segments	Deletions Observed	Frequency
~125	30	58	0	$< 4.6 \times 10^{-6}$

Panel B table:

Strain	Total number cells plated	Colonies on SD	Average loss rate
synIII	~1.6×10^9	1013	$6.7 \times 10^{-7} \pm 3.9 \times 10^{-7}$
WT	~1.9×10^9	830	$4.6 \times 10^{-7} \pm 1.3 \times 10^{-7}$

Panel C table:

Strain	Frequency (%)	
	a-mater	α-mater
synIII/III	45	0
III/III	0	0

WT *MAT*a/α diploids (III/III), and very briefly induced with estradiol. In spite of the minimal level of SCRaMbLEing induced, we observed a massive increase in the frequency of a-mater derivatives in the native III/synIII heterozygous strains (Fig. 4C and fig. S18). Such a-mater derivatives can arise from the loss of the *MAT*α locus, because such *MAT*-less strains express a-specific genes. PCRTag mapping of several such derivatives showed that these variants had indeed lost different sections of synIII, all of which included the *MAT* locus (fig. S18).

The total synthesis of the synIII chromosome represents a major step toward the design and complete synthesis of a novel eukaryotic genome structure using the model *S. cerevisiae* as the basis for a synthetic designer genome, Sc2.0. The many changes made to synIII, including intron deletion, tRNA gene removal, and loxPsym sites and PCRTags introduction, do not appear to significantly decrease the fitness or alter the transcriptome or the replication timing of the synIII strain, supporting the very pliable nature of the yeast genome and potentially allowing for much more aggressively redesigned future genome versions. Sc2.0 represents just one of myriad possible arbitrary genome designs, and we anticipate that synthetic chromosome design will become a new means of posing specific evolutionary and mechanistic questions about genome structure and function. Rapid advances in synthetic biology coupled with ever decreasing costs of DNA synthesis suggest that it will soon become feasible to engineer new eukaryotic genomes, including plant and animal genomes, with synthetic chromosomes encoding desired functions and phenotypic properties based on specific design principles.

References and Notes

1. A. Goffeau *et al.*, *Science* **274**, 546–567 (1996).
2. J. S. Dymond *et al.*, *Nature* **477**, 471–476 (2011).
3. J. Dymond, J. Boeke, *Bioeng. Bugs* **3**, 168–171 (2012).
4. J. Cello, A. V. Paul, E. Wimmer, *Science* **297**, 1016–1018 (2002).
5. L. Y. Chan, S. Kosuri, D. Endy, *Mol. Syst. Biol.* **1**, 0018 (2005).
6. G. Pósfai *et al.*, *Science* **312**, 1044–1046 (2006).
7. D. G. Gibson *et al.*, *Science* **319**, 1215–1220 (2008).
8. C. Lartigue *et al.*, *Science* **317**, 632–638 (2007).
9. H. H. Wang *et al.*, *Nature* **460**, 894–898 (2009).
10. D. G. Gibson *et al.*, *Science* **329**, 52–56 (2010).
11. F. J. Isaacs *et al.*, *Science* **333**, 348–353 (2011).
12. S. G. Oliver *et al.*, *Nature* **357**, 38–46 (1992).
13. S. M. Richardson, S. J. Wheelan, R. M. Yarrington, J. D. Boeke, *Genome Res.* **16**, 550–556 (2006).
14. W. P. Stemmer, A. Crameri, K. D. Ha, T. M. Brennan, H. L. Heyneker, *Gene* **164**, 49–53 (1995).
15. J. S. Dymond *et al.*, *Genetics* **181**, 13–21 (2009).
16. N. Annaluru *et al.*, *Methods Mol. Biol.* **852**, 77–95 (2012).
17. D. G. Gibson *et al.*, *Nat. Methods* **6**, 343–345 (2009).
18. H. Ma, S. Kunes, P. J. Schatz, D. Botstein, *Gene* **58**, 201–216 (1987).
19. V. Larionov *et al.*, *Proc. Natl. Acad. Sci. U.S.A.* **93**, 491–496 (1996).
20. D. G. Gibson *et al.*, *Proc. Natl. Acad. Sci. U.S.A.* **105**, 20404–20409 (2008).
21. H. Muller *et al.*, *Methods Mol. Biol.* **852**, 133–150 (2012).
22. D. C. Schwartz, C. R. Cantor, *Cell* **37**, 67–75 (1984).
23. M. Lynch *et al.*, *Proc. Natl. Acad. Sci. U.S.A.* **105**, 9272–9277 (2008).
24. K. W. Yuen *et al.*, *Proc. Natl. Acad. Sci. U.S.A.* **104**, 3925–3930 (2007).
25. C. D'Ambrosio *et al.*, *Genes Dev.* **22**, 2215–2227 (2008).
26. A. Lengronne *et al.*, *Nature* **430**, 573–578 (2004).

Structure of a Class C GPCR Metabotropic Glutamate Receptor 1 Bound to an Allosteric Modulator

Huixian Wu,[1]* Chong Wang,[1]* Karen J. Gregory,[2,3] Gye Won Han,[1] Hyekyung P. Cho,[2] Yan Xia,[4] Colleen M. Niswender,[2] Vsevolod Katritch,[1] Jens Meiler,[4] Vadim Cherezov,[1] P. Jeffrey Conn,[2] Raymond C. Stevens[1]†

The excitatory neurotransmitter glutamate induces modulatory actions via the metabotropic glutamate receptors (mGlus), which are class C G protein–coupled receptors (GPCRs). We determined the structure of the human mGlu$_1$ receptor seven-transmembrane (7TM) domain bound to a negative allosteric modulator, FITM, at a resolution of 2.8 angstroms. The modulator binding site partially overlaps with the orthosteric binding sites of class A GPCRs but is more restricted than most other GPCRs. We observed a parallel 7TM dimer mediated by cholesterols, which suggests that signaling initiated by glutamate's interaction with the extracellular domain might be mediated via 7TM interactions within the full-length receptor dimer. A combination of crystallography, structure-activity relationships, mutagenesis, and full-length dimer modeling provides insights about the allosteric modulation and activation mechanism of class C GPCRs.

The human G protein–coupled receptor (GPCR) superfamily comprises more than 800 seven-transmembrane (7TM) receptors that can be divided into four classes according to their sequence homology: class A, B, C, and F (Frizzled) (*1*). Class C GPCRs play important roles in many physiological processes such as synaptic transmission, taste sensation, and calcium homeostasis; they include metabotropic glutamate receptors (mGlus), γ-aminobutyric acid B (GABA$_B$) receptors, calcium-sensing (CaS) receptors, and taste 1 (TAS1) receptors, as well as a few orphan receptors. A distinguishing feature of class C GPCRs is constitutive homo- or heterodimerization mediated by a large N-terminal extracellular domain (ECD) (Fig. 1A). The ECDs within homodimeric receptors (mGlu and CaS) are cross-linked via an intermolecular disulfide bond. The heterodimeric receptors (GABA$_B$ and TAS1) are not covalently linked, but their heterodimerization is required for trafficking to the cell surface and signaling (*2*). The ECD of class C

[1]Department of Integrative Structural and Computational Biology, The Scripps Research Institute, 10550 North Torrey Pines Road, La Jolla, CA 92037, USA. [2]Department of Pharmacology and Vanderbilt Center for Neuroscience Drug Discovery, Vanderbilt University Medical Center, Nashville, TN 37232, USA. [3]Drug Discovery Biology, Monash Institute of Pharmaceutical Sciences, Monash University, Parkville, Victoria, Australia. [4]Center for Structural Biology and Department of Chemistry and Institute for Chemical Biology, Vanderbilt University Medical Center, Nashville, TN 37232, USA.

*These authors contributed equally to this work.
†Corresponding author. E-mail: stevens@scripps.edu

GPCRs consists of a Venus flytrap domain (VFD), which contains the orthosteric binding site for native ligands (Fig. 1A), and a cysteine-rich domain (CRD), except for GABA$_B$ receptors. The CRD, which mediates the communication between ECD and 7TM domains, is stabilized by disulfide bridges, one of which connects the CRD and VFD (3).

The mGlu family was the first group of class C GPCRs to be cloned (4, 5). Comprising eight members, the mGlu family can be separated into three subgroups (6)—group I (mGlu$_1$ and mGlu$_5$), group II (mGlu$_2$ and mGlu$_3$), and group III (mGlu$_4$, mGlu$_6$, mGlu$_7$, and mGlu$_8$)—on the basis of sequence homology, G protein–coupling profile, and pharmacology (7). Group I mGlus are predominantly coupled to G$_{q/11}$ and activate phospholipase C$_\beta$, which hydrolyzes phosphoinositides into inositol 1,4,5-trisphosphate (IP$_3$) and diacylglycerol, thereby inducing intracellular calcium mobilization and activating protein kinase C (PKC).

The group I mGlus, mGlu$_1$ and mGlu$_5$, are considered promising therapeutic targets to treat diseases including cancer, chronic pain, schizophrenia, Alzheimer's disease, anxiety, and autism (7, 8). However, the development of subtype-selective small-molecule ligands that might serve as drug candidates for these receptors has been hampered by the conservation of the orthosteric (glutamate) binding site (Fig. 1A). This problem can be overcome by using allosteric modulators that act at alternative binding sites; these compounds bind predominantly within the 7TM domain of the class C receptors. Allosteric modulators can alter the affinity or efficacy of native ligands in positive, negative, and neutral ways, demonstrating a spectrum of activity that cannot be achieved by orthosteric ligands alone.

Here, we report the crystal structure of the human mGlu$_1$ 7TM domain bound to a negative allosteric modulator (NAM), 4-fluoro-N-(4-(6-

(isopropylamino)pyrimidin-4-yl)thiazol-2-yl)-N-methylbenzamide (FITM) (9), at 2.8 Å resolution (table S1) (10). This structure provides a three-dimensional framework for understanding the molecular recognition and facilitating the discovery of allosteric modulators for the mGlu family and other class C GPCRs. It also complements crystallographic studies of the transmembrane domain structures of class A (11, 12), B (13, 14), and F (15) GPCRs and extends the knowledge base upon which to study the diversity and evolution of the GPCR superfamily.

Overall Structure of the mGlu$_1$ 7TM Domain

The human mGlu$_1$ 7TM domain (residues 581 to 860) (fig. S1), complexed with FITM, was crystallized by the lipidic cubic phase method using the thermostabilized apocytochrome b$_{562}$RIL (BRIL) N-terminal fusion strategy (10). A series of in vitro pharmacological studies were performed
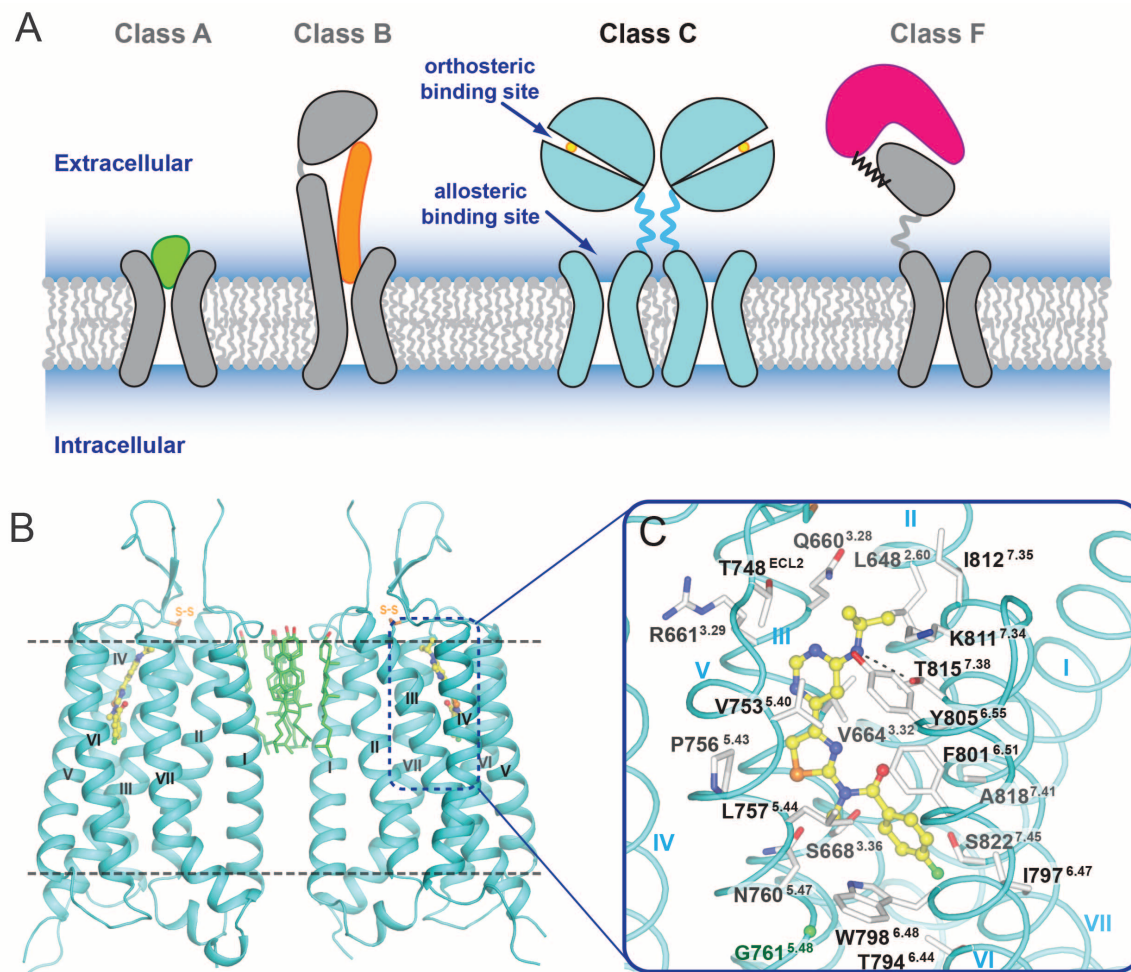
Fig. 1. Overall structure of the mGlu$_1$ TM domain. (A) Cartoon models for structure and endogenous ligand recognition in different GPCR classes. For class A, in most cases, the endogenous ligand (green) is recognized by an orthosteric site in the 7TM domain. For class B, the endogenous peptide ligand (orange) binds to both ECD and 7TM domains. For class C, the endogenous small-molecule ligands (yellow circle) are recognized by orthosteric sites in the VFDs. For class F, lipoprotein WNT (magenta) binds the CRD domain of Frizzled receptors. **(B)** The mGlu$_1$ 7TM domain that crystallized as a parallel dimer is shown in cyan cartoon. Cholesterols mediating the dimer interface are shown as green carbons. **(C)** Side chains of the FITM binding pocket residues are shown as white carbons. Hydrogen bond interaction between the NAM and Thr815$^{7.38}$ is shown as a dashed line. The C$_\alpha$ carbon of Gly761$^{5.48}$ is shown as a green ball. In (B) and (C), the ligand FITM is shown as yellow carbons. Amino acid abbreviations: A, Ala; C, Cys; D, Asp; E, Glu; F, Phe; G, Gly; H, His; I, Ile; K, Lys; L, Leu; M, Met; N, Asn; P, Pro; Q, Gln; R, Arg; S, Ser; T, Thr; V, Val; W, Trp; Y, Tyr.

to verify that this truncated construct binds FITM and is functional in G protein coupling (figs. S2 and S3). The structure was solved using a 4.0 Å single-wavelength anomalous dispersion (SAD) data set collected from a single crystal soaked with tantalum bromide cluster; the resolution was then improved to 2.8 Å by means of native data collected from 14 crystals (table S1 and fig. S4).

The mGlu$_1$ 7TM domain forms a parallel dimer in each asymmetric unit, with a dimer interface mediated mainly through helix I (Fig. 1B; see also figs. S5 and S6). We observed six well-resolved cholesterol molecules packed against hydrophobic residues on the extracellular side of helices I and II, mediating the dimer formation. The extracellular loop (ECL) 2 adopts a β-hairpin conformation, pointing to the extracellular space, which has also been observed in many peptide class A GPCRs (16, 17). This β hairpin is connected to the top of helix III through a disulfide bond (C657-C746) that is conserved through all classes of GPCRs. The mGlu$_1$ NAM, FITM, binds

within a pocket formed by the 7TM bundle close to the extracellular side (Fig. 1, B and C), a region that partially overlaps with the orthosteric binding sites observed for class A GPCRs (11). The intracellular loop (ICL) 1 forms an ordered helical turn; a large part of ICL2 (residues 688 to 695 in molecule A, residues 689 to 693 in molecule B) is missing in the structure because of the long and presumably flexible nature of this loop. ICL3 is well resolved and forms a short link connecting the intracellular ends of helices V and VI. In addition, we did not observe helix VIII, reported in most class A GPCR structures as well as in classes B and F. Instead, electron densities for C-terminal residues (844 to 860 in molecule A, 847 to 860 in molecule B) are missing in the mGlu$_1$ structure, indicating that this region can be disordered.

Major Structural Differences with Other GPCR Classes

Superposition of 7TM domains between mGlu$_1$ and GPCRs of different classes (fig. S7) reveals

that, despite the lack of sequence conservation (<15% identical residues) or common functional motifs (figs. S8 and S9), the overall fold is preserved across the whole GPCR superfamily (root mean square deviation <3.5 Å for 7TM regions). On the basis of structural superposition, we generated a structure-based alignment in the 7TM domain with class A GPCRs and transplanted the class A Ballesteros-Weinstein (B&W) numbering (18) to class C GPCRs (figs. S8 and S9) (19).

Differences, however, were observed in the 7TM helices between class C and other classes, including distinct distribution patterns of proline-induced kinks in the helical backbone. Instead of having conserved prolines in the X.50 position of helices V, VI, and VII (which induce kinks as observed in class A), residues at the 5.50, 6.50, and 7.50 positions in mGlu$_1$ are all nonproline residues (fig. S8). Notably, Pro833$^{7.56}$ (20) at the intracellular end of helix VII in mGlu$_1$ induces a kink, resulting in an outward orientation of the C-terminal part of this helix (fig. S7B). In
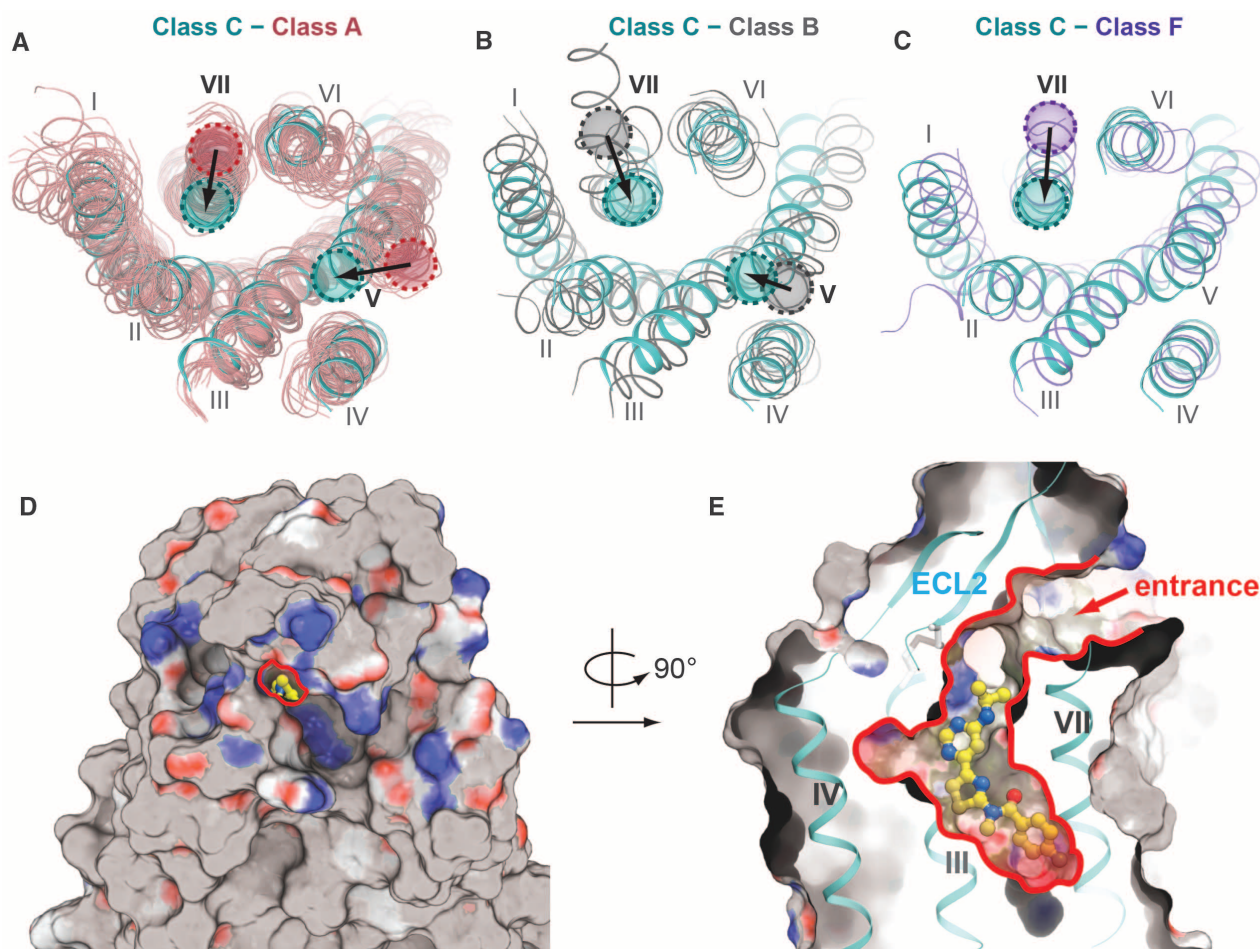
Fig. 2. 7TM domain comparison of mGlu$_1$ with GPCRs of other classes. (**A** to **C**) Extracellular view of superpositions between mGlu$_1$ shown in cyan and (A) class A GPCR shown in salmon, (B) class B GPCR (CRFR1 and glucagon receptor; PDB IDs 4K5Y and 4L6R, respectively) shown in gray, and (C) class F GPCR (smoothened receptor; PDB ID 4JKV) shown in purple. In (A) to (C), shifts of helix V or VII in mGlu$_1$ relative to other classes are indicated by arrows. (**D**) Extracellular view of the surface presentation of the structure, showing the narrow entrance (highlighted by red line) to the allosteric ligand-binding cavity in the center. (**E**) A cut-through surface side view of the ligand-binding cavity. The arrow indicates the extracellular entrance to the allosteric ligand-binding cavity. In the surface presentations in (D) and (E), nonpolar residues are shown in gray, hydrogen bond acceptors are in red, and hydrogen bond donors are in blue. PDB IDs of class A GPCRs structures used in (A): 1U19, 2RH1, 2YCW, 3RZE, 3PBL, 3UON, 4DAJ, 3EML, 3V2W, 3ODU, 4DJH, 4EA3, 4DKL, 4EJ4, 3VW7, and 4GRV.
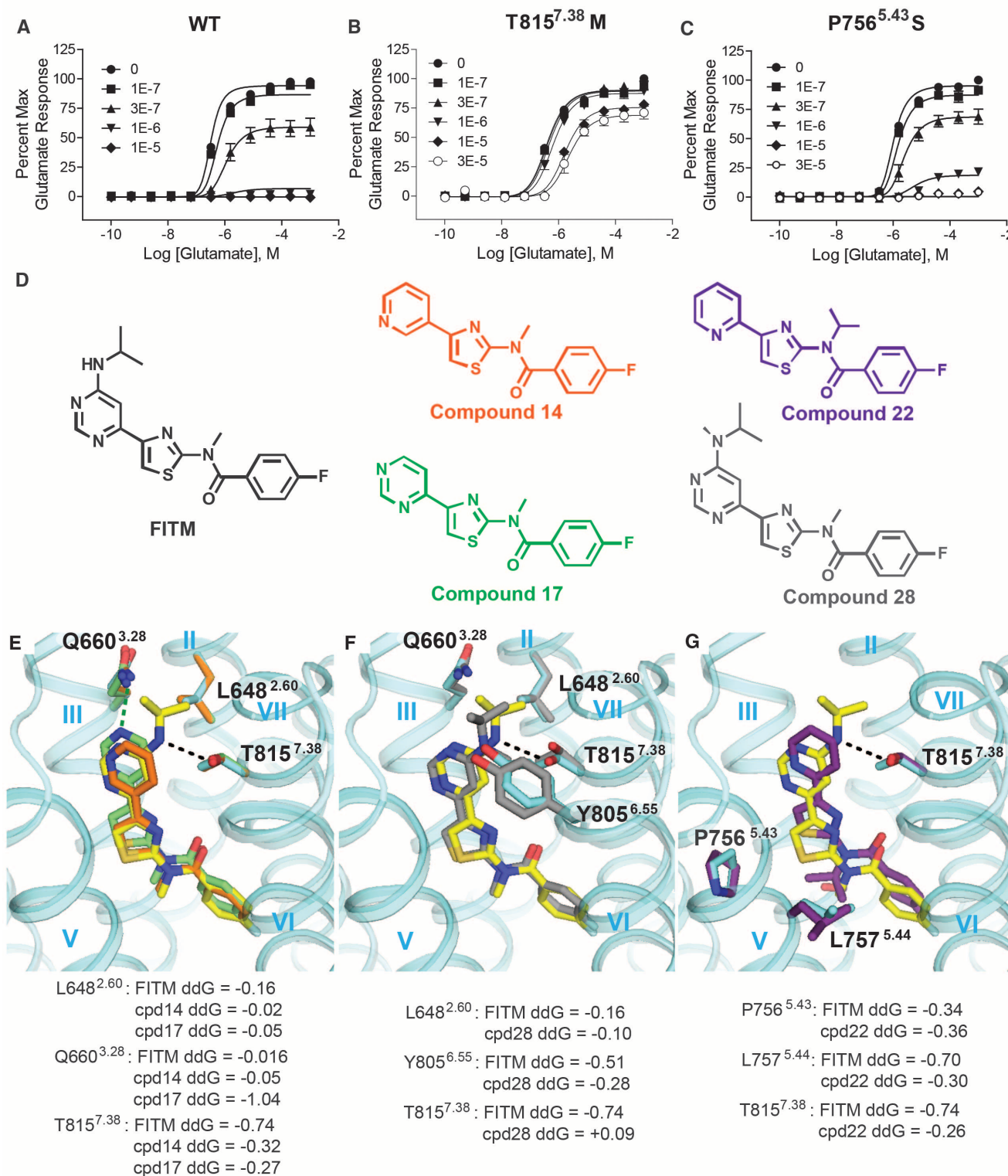
Fig. 3. Critical FITM-receptor interactions are revealed by mutations and structure-activity relationships. (**A** to **C**) FITM is a full NAM of the wild-type (WT) full-length human mGlu$_1$ receptor (A); the affinity of FITM and the degree of negative cooperativity with glutamate are reduced in Thr815[7.38]Met (B) and Pro756[5.43]Ser (C) mutants (table S3). Error bars denote SEM. (**D**) Structures of FITM and FITM-related NAMs used for study. (**E** to **G**) Binding pose of FITM (yellow carbons; mean half-maximal inhibitory concentration IC$_{50}$ = 5 nM) in comparison with lower-potency analogs: (E) compound 17 (green carbons; IC$_{50}$ = 10 nM) and compound 14 (orange carbons; IC$_{50}$ = 230 nM), (F) compound 28 (gray carbons; IC$_{50}$ = 77 nM) and (G) compound 22 (purple carbons; IC$_{50}$ = 2 µM). Per-residue binding energy ddG is predicted by Rosetta and shown as Rosetta Energy Units (REU) (37). In (E) to (G), side-chain rotamers from the top 1% of key amino acids are depicted in sticks and colored corresponding to their respective docked ligand, with the exception of those from the crystal structure shown in cyan; the dashed lines indicate hydrogen bond interactions between the receptor and the ligands.

contrast, the proline conserved in the class A Asn-Pro[7.50]-x-x-Tyr motif is on the opposite side of helix VII and induces an inward kink (fig. S7B).

Helices I to IV of mGlu$_1$ overlay relatively well with other GPCR structures, whereas helices V to VII demonstrate more obvious differences. Relative to class A and B receptors (Fig. 2, A and B), helix V of mGlu$_1$ is shifted inward to the center of the 7TM bundle. Additionally, the extracellular end of helix VII is shifted inward relative to all other classes. These shifted helices, together with ECL2, restrict access to the NAM-binding cavity (Fig. 2, D and E). The recently solved class F smoothened receptor (15) also has a narrow cavity embedded in the extracellular half of its 7TM

bundle, resulting partly from the inward positioning of helix V, but its ECL2 β hairpin is located inside the 7TM bundle and forces an outward shift of helix VII as compared to mGlu$_1$ (Fig. 2C). This more restricted 7TM cavity in class C receptors is consistent with interactions of known native ligands with the ECD rather than the 7TM domain.

The FITM Binding Pocket

Analogous to the orthosteric site for many family A GPCRs, the binding pocket for the ligand FITM is defined by residues on ECL2 and helices II, III, V, VI, and VII (Fig. 1C and fig. S10). ECL2 forms a lid on the top of the ligand-binding cavity, leaving a small opening through which the pocket

is accessible from the extracellular side (Fig. 2, D and E). The ligand, FITM, fits tightly into the long and narrow pocket. Most of the ligand-receptor interactions are hydrophobic, with the exception of the contacts of the pyrimidine-amine group with the Thr815[7.38] side chain. Substitution of Thr815[7.38] with methionine or alanine reduces the affinity and potency of FITM (Fig. 3B, fig. S11F, and table S2) and of other mGlu$_1$ NAMs from different scaffolds (21–23). The p-fluorophenyl moiety of the ligand points to the bottom of the pocket, making contacts with Trp798[6.48], a residue that is conserved among mGlus as well as in many class A receptors. However, unlike the conformation of the Trp[6.48] side chain observed in

Fig. 4. The intracellular crevice in NAM-bound mGlu$_1$ adopts a closed conformation. (**A**) Cartoon demonstrating agonist-triggered opening of the intracellular cavity for G protein binding. (**B** and **C**) Side view (B) and intracellular view (C) of the superposition of mGlu$_1$ (cyan) with inactive state of β$_2$-adrenergic receptor shown in yellow (PDB ID 2RH1) and a fully active G protein–coupled state of β$_2$-adrenergic receptor shown in orange (PDB ID 3SN6). Red arrows in (B) and (C) indicate movement of the intracellular end of helix VI, highlighted in red dashed circle in (B), during activation of β$_2$-adrenergic receptor. (**D** and **E**) Side view (D) and intracellular view (E) of the mGlu$_1$ receptor; side chains of residues involved in a hydrogen bond network that stabilize the receptor in an inactive conformation are shown as white carbons.
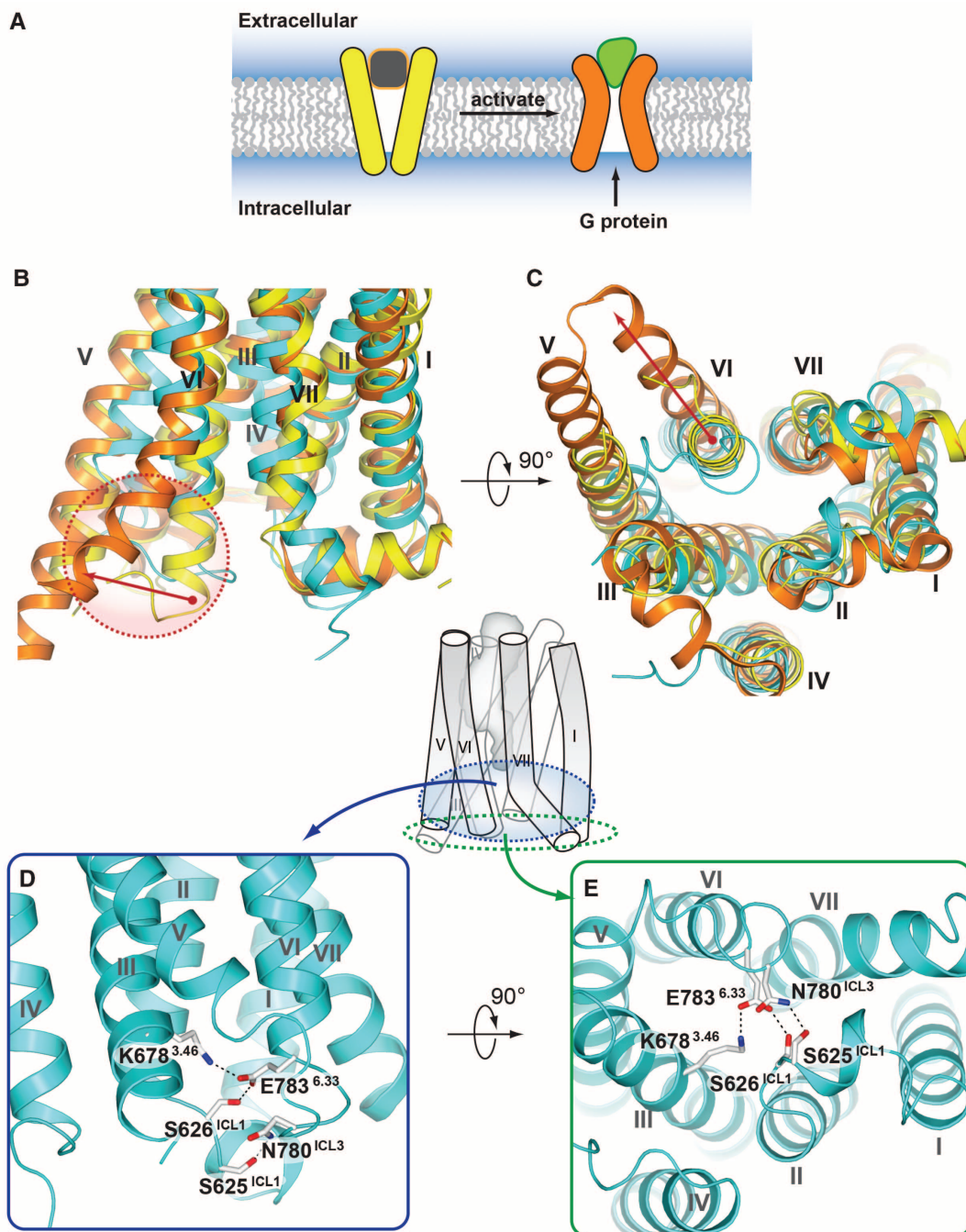
most class A GPCRs, which points into the center of the helical bundle, Trp798[6.48] in the structure of FITM-bound mGlu[1] points outward. This conformation of the bulky indole group is accommodated by Gly761[5.48] on helix V, which has no side chain (Fig. 1C). However, in mGlus other than mGlu[5], residues at position 5.48 have relatively large side chains and Trp[6.48] may adopt a different conformation.

Determinants of Subtype Selectivity Within the Common Allosteric Site

Previous mutagenesis studies have proposed at least one common allosteric site for the mGlu family within the 7TM domain. The mGlu[1] binding pocket for FITM (Fig. 1C) largely corresponds to mutagenic data for the common allosteric site in mGlus and likely extends to other class C GPCRs (see table S3). Despite the evidence that binding of various chemotypes of class C GPCR allosteric modulators involve similar residue positions, many mGlu modulators display a high degree of subtype selectivity, including FITM, which shows high affinity (equilibrium dissociation constant $K_i = 2.5$ nM; fig. S2) and selectivity for mGlu[1] over mGlu[5] (fig. S12) (9). Examination of the contact residues in the binding pocket reveals only four residues of mGlu[1] that differ from mGlu[5]: Val664[3.32], Ser668[3.36], Thr815[7.38], and Ala818[7.41], all of which have previously been implicated in subtype selectivity by mutagenesis-based studies (24–26). Therefore, we mutated these four residues to their corresponding amino acid in mGlu[5] (fig. S11 and table S2) and compared FITM-mediated antagonism of the mutant receptors to the wild-type full-length human mGlu[1] (Fig. 3A). Methionine substitution of Thr815[7.38] (Fig. 3B) had the most profound effect, reducing FITM affinity by a factor of ~6 and decreasing negative cooperativity with glutamate (table S2). Thus, Thr815[7.38] is a key selectivity determinant for FITM, consistent with the observed polar interaction between Thr815[7.38] and the ligand in the structure.

In addition, we assessed mutations known to influence the allosteric modulation of other mGlu subtypes that had not previously been explored in mGlu[1]. Thr794[6.44]Ala and Ser822[7.45]Ala mutations had no effect on FITM, whereas Pro756[5.43]Ser reduced FITM affinity (by a factor of ~3) as well as negative cooperativity (Fig. 3C and table S2). Location of Pro756[5.43] in the ligand-binding pocket suggests that a Pro756[5.43]Ser mutation may induce conformational changes in the backbone, altering the shape of the binding pocket in relation to the thiazole core of FITM.

Multiple mGlu[5] modulator scaffolds are known to be sensitive to mutations of two nonconserved residues, Ser[6.39] and Ala[7.46] (23, 25, 27–31); neither is observed here as contributing to the FITM-binding pocket. However, both of these residues contribute to a small pocket separated from the FITM pocket by the Tyr672[3.40] side chain. Given that Ser[3.36] in mGlu[1] is replaced by Pro[3.36] in mGlu[5], it is conceivable that the proline-induced kink in helix III particular to mGlu[5] may change the shape of the pocket, making Ser[6.39] and Ala[7.46] of mGlu[5] accessible to ligands.

To further improve our understanding of the critical ligand-receptor interactions for FITM binding within the pocket, we docked a selection of FITM analogs (Fig. 3, D to G, and fig. S13) (9) into the crystal structure. Redocking FITM (fig. S13, A to C) and analyzing the binding energy contribution per residue (fig. S13D) revealed that Thr815[7.38] forms an energetically favorable hydrogen bond with FITM (fig. S13, C and D). Compound 17 lacks not only the hydrogen bond with Thr815[7.38], but also a nonpolar interaction with Leu648[2.60] (Fig. 3, D and E); however, a potential hydrogen bond with Gln660[3.28], which is not observed in FITM binding (fig. S11A and table S2), may compensate for this loss and account for the retained activity at 10 nM. The 3-pyridyl analog (compound 14; Fig. 3, D and E) lacks this potential interaction with Gln660[3.28], accounting for its further decreased potency (230 nM). Compound 28 exhibits lower potency (by a factor of ~10) and differs from FITM by the introduction of a methyl group to the amine on the pyrimidine ring. Docking compound 28 reveals a major energy penalty that arises from the loss of a polar interaction and the introduction of steric clash with Thr815[7.38] (Fig. 3, D and F). Compound 28 also lacks a polar interaction with Gln660[3.28] and requires movement of Thr815[7.38] and Tyr805[6.55] to accommodate the methyl group (Fig. 3F). Compound 22 (Fig. 3, D and G), which contains an isopropyl group on the amide linker, requires movement of two residues in helix V (Pro756[5.43] and Leu757[5.44]) to fit in the pocket, and also lacks hydrogen-bonding capacity with either Thr815[7.38] or Gln660[3.28], accounting for its reduced (micromolar) potency. Collectively, by comparing the binding of FITM with those of other less active or inactive compounds, we attribute the superior potency observed for FITM to the polar interaction between Thr815[7.38] and the amine derivative on the 5' position of the pyrimidine ring, as well as the perfect fit of the ligand shape within the narrow binding pocket.

NAM-Bound mGlu[1] Is in an Inactive State

In the NAM-bound structure of mGlu[1], the intracellular site responsible for G protein interaction is in a conformation similar to the inactive conformation observed in class A GPCRs (Fig. 4, A to C). One of the interactions apparently stabilizing this conformation is a salt bridge between the Lys678[3.46] side chain at the intracellular end of helix III and the Glu783[6.33] side chain at the intracellular end of helix VI (Fig. 4, D and E); both residues are well conserved in all class C receptors. In class A GPCRs, a similar interaction called an "ionic lock" is observed between the conserved Arg[3.50] of the Asp(Glu)-Arg[3.50]-Tyr motif and an acidic residue in the 6.30 position. The "ionic
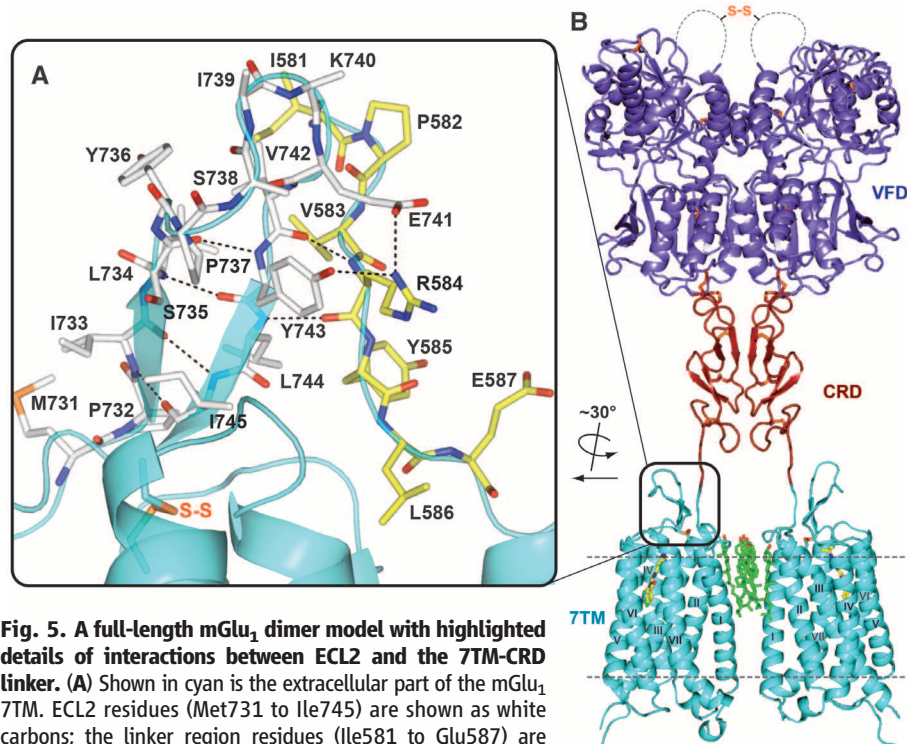
Fig. 5. A full-length mGlu[1] dimer model with highlighted details of interactions between ECL2 and the 7TM-CRD linker. (**A**) Shown in cyan is the extracellular part of the mGlu[1] 7TM. ECL2 residues (Met731 to Ile745) are shown as white carbons; the linker region residues (Ile581 to Glu587) are shown as yellow carbons. Hydrogen bond interactions between ECL2 and the linker region are shown as dashed lines. (**B**) Full-length model of mGlu[1] with the VFD in the Acc (active closed-closed) state. VFD, CRD, and 7TM domains are colored in slate, firebrick, and cyan, respectively. The current model probably does not capture the specific conformation and interaction between the CRD and 7TM domains, and a more tightly packed domain interaction is very likely. This model is presented to generate discussion and to show the general features of the VFD, CRD, and 7TM domains.

lock" plays a role in stabilizing the receptor's inactive state by restricting the activation-related outward movement of helix VI. In addition to the salt bridge between Lys678[3.46] and Glu783[6.33], Ser626[ICL1]—a residue conserved in most class C GPCRs—also participates in this interaction network. Ser625[ICL1] and Asn780[ICL3] form a hydrogen bond, stabilizing the interaction between ICL1 and ICL3 and further occluding the G protein–binding site (Fig. 4, D and E). Thus, polar interactions within the intracellular crevice may be involved in the regulation of G protein binding and receptor activation in both class A and class C GPCRs, although through distinct residue positions.

Communication Between ECD and 7TM Domains

In the mGlu receptor family, as well as in other class C GPCRs, a signal is initiated by the native ligand binding to the ECD, which induces conformational changes in the ECD. In our structure, the linker region (Ile581-Glu592) between the ECD and 7TM domain is resolved. The linker forms strong interactions with the ECL2 β sheet through main-chain and side-chain hydrogen bonds (Fig. 5A). ECL2 is connected by a covalent disulfide bond to the top of helix III, known to be important in triggering activation in class A GPCRs (32). This observation raises the possibility that this interaction network might contribute to the communication between the ECD and the 7TM domain during receptor activation. In addition, part of the linker residues (e.g., Trp588, a residue conserved in all mGlus) insert into the lipid bilayer, where they form extensive contacts with cholesterol molecules that mediate the observed dimerization of the 7TM domain (fig. S6). These interactions suggest a potential role of dimerization and/or lipid components in the coupling between the ECD and 7TM domain during the activation process.

ECDs of class C GPCRs mediate receptor homo- and heterodimerization (2). Several dimeric structures of mGlu receptor VFDs have been solved in different conformations: putative active (A) or resting (R) states defined by the relative orientation between the VFD protomers, as well as closed (c) or open (o) states defined by the conformation of each VFD (33). Comparing different conformations, the distance between the C-terminal ends of the ECDs within a dimer changes markedly (3). In our crystal structure of the 7TM domain, we observed a parallel dimer mediated by interactions of helix I and cholesterols. In this dimer conformation, the distance between the N-terminal linkers that are attached to the C termini of ECDs is ~20 Å. If this is a conformation that can be adopted by the full-length receptor dimer, the CRDs of each protomer should also be in close proximity. Disulfide bond cross-linking experiments suggested that the CRDs of each protomer may form close contact in an activated receptor dimer (34). Although our structure is solved in complex with a NAM and the 7TM domain appears to be in an inactive state, there is evidence supporting the existence of a glutamate-bound but signaling-incapable state in

the full-length mGlu dimer (35). Moreover, there is evidence that cholesterol can positively modulate glutamate responses by recruiting mGlus to lipid rafts (31, 36), consistent with the observation that the close proximity of the N terminus of the 7TM domain results from a dimer conformation mediated by multiple cholesterol molecules.

To test the possibility of fitting the existing ECD structures into our observed 7TM dimer conformation, we created a full-length dimer model in which the VFD adopts an Acc (active closed-closed) conformation, as this conformation has the closest distance (~50 Å) between the C termini of the ECDs (3) (Fig. 5B). A 20° rotation was applied to the CRD, coupled with a conformational change in the Gln513-Val523 loop region that reduces this distance to 20 Å, fulfilling the CRD interface proposed in the cysteine mutant study (34), as well as matching the distance of the 7TM domain N termini observed in the crystallographic dimer. This model might represent a glutamate-bound but signaling-incapable conformation of mGlu₁. Although this model is consistent with the currently available experimental data, we acknowledge that it is only one of several possible explanations for the biological role of the 7TM domain dimer we observed. We further acknowledge that the 7TM domain dimer conformation might vary in different states of the receptor and may be modulated by several factors in biological systems, such as membrane lipid content or other protein-protein interactions.

The mGlu₁ 7TM structure presented here uncovers atomic details of the class C GPCR transmembrane domain, providing a missing link in our structural understanding of the GPCR superfamily. As noted for the recently solved class B and class F GPCR structures, and now for class C, despite a lack of sequence and motif conservation, the architecture of the 7TM bundle is generally preserved. Furthermore, although class C GPCRs are known to form obligate dimers via the ECDs, the observed 7TM dimer suggests additional points of communication between protomers, mediated by multiple cholesterol molecules and direct protein-protein interactions. Moreover, as a robust structural template, the mGlu₁ 7TM domain structure will likely provide insights into pharmacology of small-molecule allosteric modulators for class C GPCRs.

References and Notes

1. M. C. Lagerström, H. B. Schiöth, *Nat. Rev. Drug Discov.* **7**, 339–357 (2008).
2. J. Kniazeff, L. Prézeau, P. Rondard, J. P. Pin, C. Goudet, *Pharmacol. Ther.* **130**, 9–25 (2011).
3. T. Muto, D. Tsuchiya, K. Morikawa, H. Jingami, *Proc. Natl. Acad. Sci. U.S.A.* **104**, 3759–3764 (2007).
4. K. M. Houamed et al., *Science* **252**, 1318–1321 (1991).
5. M. Masu, Y. Tanabe, K. Tsuchida, R. Shigemoto, S. Nakanishi, *Nature* **349**, 760–765 (1991).
6. S. Nakanishi, *Science* **258**, 597–603 (1992).
7. C. M. Niswender, P. J. Conn, *Annu. Rev. Pharmacol. Toxicol.* **50**, 295–322 (2010).
8. G. Dölen, R. L. Carpenter, T. D. Ocain, M. F. Bear, *Pharmacol. Ther.* **127**, 78–93 (2010).
9. A. Satoh et al., *Bioorg. Med. Chem. Lett.* **19**, 5464–5468 (2009).
10. See supplementary materials on *Science* Online.
11. V. Katritch, V. Cherezov, R. C. Stevens, *Annu. Rev. Pharmacol. Toxicol.* **53**, 531–556 (2013).
12. K. Palczewski et al., *Science* **289**, 739–745 (2000).
13. F. Y. Siu et al., *Nature* **499**, 444–449 (2013).
14. K. Hollenstein et al., *Nature* **499**, 438–443 (2013).
15. C. Wang et al., *Nature* **497**, 338–343 (2013).
16. H. Wu et al., *Nature* **485**, 327–332 (2012).
17. B. Wu et al., *Science* **330**, 1066–1071 (2010).
18. J. A. Ballesteros, H. Weinstein, *Methods Neurosci.* **25**, 366–428 (1995).
19. In each helix, the following residues are assigned number 50: T607[1.50], I638[2.50], I682[3.50], I714[4.50], L763[5.50], A800[6.50], and L827[7.50]. The numbering of other residues in each helix is counted relative to the X.50 position according to the B&W numbering scheme.
20. Superscripts refer to the B&W numbering for class A GPCRs and were transplanted to class C GPCRs on the basis of structural superposition.
21. G. Suzuki et al., *J. Pharmacol. Exp. Ther.* **321**, 1144–1153 (2007).
22. J. Fukuda et al., *Neuropharmacology* **57**, 438–445 (2009).
23. P. Malherbe et al., *Mol. Pharmacol.* **64**, 823–832 (2003).
24. S. Litschig et al., *Mol. Pharmacol.* **55**, 453–461 (1999).
25. A. Pagano et al., *J. Biol. Chem.* **275**, 33750–33758 (2000).
26. A. Surin, S. Pshenichkin, E. Grajkowska, E. Surina, J. T. Wroblewski, *Neuropharmacology* **52**, 744–754 (2007).
27. P. Malherbe et al., *J. Neurochem.* **98**, 601–615 (2006).
28. Y. Chen, C. Goudet, J. P. Pin, P. J. Conn, *Mol. Pharmacol.* **73**, 909–918 (2008).
29. C. Mølck et al., *Mol. Pharmacol.* **82**, 929–937 (2012).
30. K. J. Gregory et al., *Mol. Pharmacol.* **82**, 860–875 (2012).
31. K. J. Gregory et al., *Mol. Pharmacol.* **83**, 991–1006 (2013).
32. F. Xu et al., *Science* **332**, 322–327 (2011).
33. N. Kunishima et al., *Nature* **407**, 971–977 (2000).
34. S. Huang et al., *Proc. Natl. Acad. Sci. U.S.A.* **108**, 15480–15485 (2011).
35. E. Doumazane et al., *Proc. Natl. Acad. Sci. U.S.A.* **110**, E1416–E1425 (2013).
36. C. Eroglu, B. Brugger, F. Wieland, I. Sinning, *Proc. Natl. Acad. Sci. U.S.A.* **100**, 10219–10224 (2003).
37. J. Meiler, D. Baker, *Proteins* **65**, 538–548 (2006).

Polyhedra Self-Assembled from DNA Tripods and Characterized with 3D DNA-PAINT

Ryosuke Iinuma,[1]*† Yonggang Ke,[1,2,3]*‡ Ralf Jungmann,[1,4]* Thomas Schlichthaerle,[1] Johannes B. Woehrstein,[1,4] Peng Yin[1,4]§

DNA self-assembly has produced diverse synthetic three-dimensional polyhedra. These structures typically have a molecular weight no greater than 5 megadaltons. We report a simple, general strategy for one-step self-assembly of wireframe DNA polyhedra that are more massive than most previous structures. A stiff three-arm-junction DNA origami tile motif with precisely controlled angles and arm lengths was used for hierarchical assembly of polyhedra. We experimentally constructed a tetrahedron (20 megadaltons), a triangular prism (30 megadaltons), a cube (40 megadaltons), a pentagonal prism (50 megadaltons), and a hexagonal prism (60 megadaltons) with edge widths of 100 nanometers. The structures were visualized by means of transmission electron microscopy and three-dimensional DNA-PAINT super-resolution fluorescent microscopy of single molecules in solution.

DNA nanotechnology has produced a wide range of shape-controlled nanostructures (*1–10*). Hollow polyhedra (*1, 5, 11–26*) are particularly interesting because they resemble natural structures such as viral capsids and promise applications for scaffolding and encapsulating functional materials. Previous work has constructed diverse polyhedra, such as tetrahedra (*13, 16, 20, 24*), cubes (*1, 19, 23*), bipyramids (*15*), truncated octahedra (*11*), octahedra (*12*), dodecahedra (*16, 18*), icosahedra (*17, 21*), nanoprisms (*14, 22, 25, 26*), and buckyballs (*16*), with ≤80-nm sizes and ≤5-MD molecular weights (such as Fig. 1A, structures 1 to 8). Assembly strategies include step-wise synthesis (*1, 11, 21, 22*), folding of a long scaffold (*12, 19, 20, 24, 25*), cooperative assembly of individual strands (*13–15, 18, 26*), and hierarchical assembly of branched DNA tiles (*16, 17, 23*).

A promising route to scaling up polyhedra is the hierarchical assembly of larger monomers. Previous work using small three-arm-junction (80 kD) (*16, 23*) and five-arm-junction (130 kD) (*17*) tiles has produced several ≤5-MD polyhedra (such as Fig. 1A, structures 5 to 7). Additionally, a 15-MD icosahedron (Fig. 1A, structure 9) (*5*) was assembled from three double-triangle–shaped origami monomers. Perhaps because of the lack of precise geometric control of the flexible double-triangle monomers, this icosahedron has low yield

(*5*), and this method has not been generalized to construct more complex polyhedra.

We developed a more general strategy for hierarchical self-assembly of polyhedra from megadalton monomers using a DNA "tripod," a 5-MD three-arm-junction origami tile [60 times more massive than previous three-arm tiles (*16, 23*)]. The tripod motif features inter-arm angles controlled by supporting struts and strengthened by vertex helices. Self-assembly of tripods into wireframe polyhedra is further facilitated by a dynamic connector design. We constructed a tetrahe-

dron (~20 MD), a triangular prism (~30 MD), a cube (~40 MD), a pentagonal prism (~50 MD), and a hexagonal prism (~60 MD) (Fig. 1A and fig. S1) (*27*). With 100-nm edges, these polyhedra have a size comparable with those of bacterial microcompartments such as carboxysomes.

To characterize the three-dimensional (3D) single-molecule morphology of these polyhedra, we used a DNA-based super-resolution fluorescence imaging method (resolution below the diffraction limit) called DNA-PAINT (a variation of point accumulation for imaging in nanoscale topography) (*28–30*). Unlike traditional transmission electron microscopy (TEM), which images the samples in a vacuum under dried and stained conditions, 3D DNA-PAINT introduces minimal distortion to the structures in a "native" hydrated imaging environment.

Design

In one-pot annealing, the scaffold and staple strands first assemble into a tripod origami monomer, and then the tripods (without intermediate purification) assemble into the polyhedron (Fig. 1A). Diverse polyhedra can be constructed by using tripods with different designed inter-arm angles. The tripod has three equal-length (~50 nm) stiff arms connected at the vertex (connection details are available in fig. S2) with controlled inter-arm angles (Fig. 1B). To ensure stiffness, each arm contains 16 parallel double-helices packed on a honeycomb lattice (*5*) with twofold rotational symmetry. A supporting "strut" consisting of two double-helices controls the angle between the

[1]Wyss Institute for Biologically Inspired Engineering, Harvard University, Boston, MA 02115, USA. [2]Department of Cancer Biology, Dana-Farber Cancer Institute, Harvard Medical School, Boston, MA 02115, USA. [3]Department of Biological Chemistry and Molecular Pharmacology, Harvard Medical School, Boston, MA 02115, USA. [4]Department of Systems Biology, Harvard Medical School, Boston, MA 02115, USA.

*These authors contributed equally to this work.
†Present address: JSR Life Sciences Corporation, Ibaraki 305-0841, Japan.
‡Present address: Wallace H. Coulter Department of Biomedical Engineering, Georgia Institute of Technology and Emory University, Atlanta, GA 30322, USA.
§Corresponding author. E-mail: py@hms.harvard.edu

Fig. 1. DNA-origami polyhedra. (**A**) Polyhedra self-assembled from DNA tripods with tunable inter-arm angles, and comparison of their sizes and molecular weights with selected previous polyhedra (structures 1 to 9) (details are provided in fig. S1). (**B**) Design diagram of a tripod. Cylinders represent DNA double helices. Details of the arm connection at the vertex are provided in fig. S2. (**C**) Cylinder model illustrating the connection between two tripod monomers. (**D** and **E**) Connection schemes for assembling (**E**) the tetrahedron and (**D**) other polyhedra (represented here by the cube design).

two arms. We name a tripod according to its three inter-arm angles (for example, the tetrahedron and the cube are respectively assembled from 60°-60°-60° and 90°-90°-90° tripods). To avoid potential unwanted aggregation resulting from blunt-end stacking of DNA helices (4), up to six short DNA double-helices (denoted "vertex helices") are included at the vertex so as to partially conceal its blunt duplex ends (Fig. 1B). The number of helices and their lengths vary for different polyhedra (fig. S2). Additionally, the vertex helices are expected to help maintain inter-arm angles by increasing rigidity of the vertices. Two connection strategies are used to assemble tripods into polyhedra. To facilitate exposition, the three arms are denoted as X-arm, Y-arm, and Z-arm (Fig. 1B). Connecting X-arm to X-arm (Fig. 1C) and Y-arm to Z-arm produces polyhedra (such as a cube) (Fig. 1D)

other than the tetrahedron, which is assembled by connecting X to X, Y to Y, and Z to Z (Fig. 1E).

Results

Tripod Conformation Control with Struts

First, we verified that the inter-arm angle was controlled by the length of the supporting strut. Gel electrophoresis of 60°-60°-60° and 90°-90°-90° tripods revealed a dominant band for each tripod (Fig. 2A), confirming their correct formation. Consistent with its more compact designed conformation, the 60°-60°-60° tripod migrated slightly faster than did the 90°-90°-90° one. The two tripod bands each were purified, were imaged with TEM, and showed designed tripod-like morphologies (Fig. 2B). The measured inter-arm angles were slightly smaller than designed [53 ± 5° (SD, n = 60 tripods) for 60°-60°-60° tripods;

87 ± 4° (SD, n = 60 tripods) for 90°-90°-90° tripods], possibly reflecting a small degree of strut bending.

Connector Designs

The strands connecting the tripods are called "connectors." Connector designs affected the polyhedra assembly yields. Two designs were tested for the cube. In scheme i, each 30-base connector spanned two adjacent tripods, with a 28-base segment anchored on one tripod and another 2-base (sticky end) anchored on the other (Fig. 2C and fig. S3). Gel electrophoresis (shown in Fig. 2C and quantified in Fig. 2E) revealed that the assembly yield was affected by the number of connected helices (n): a product band was only observed for $4 \leq n \leq 12$; for $n < 4$, the dominant bands were monomers, likely reflecting overly
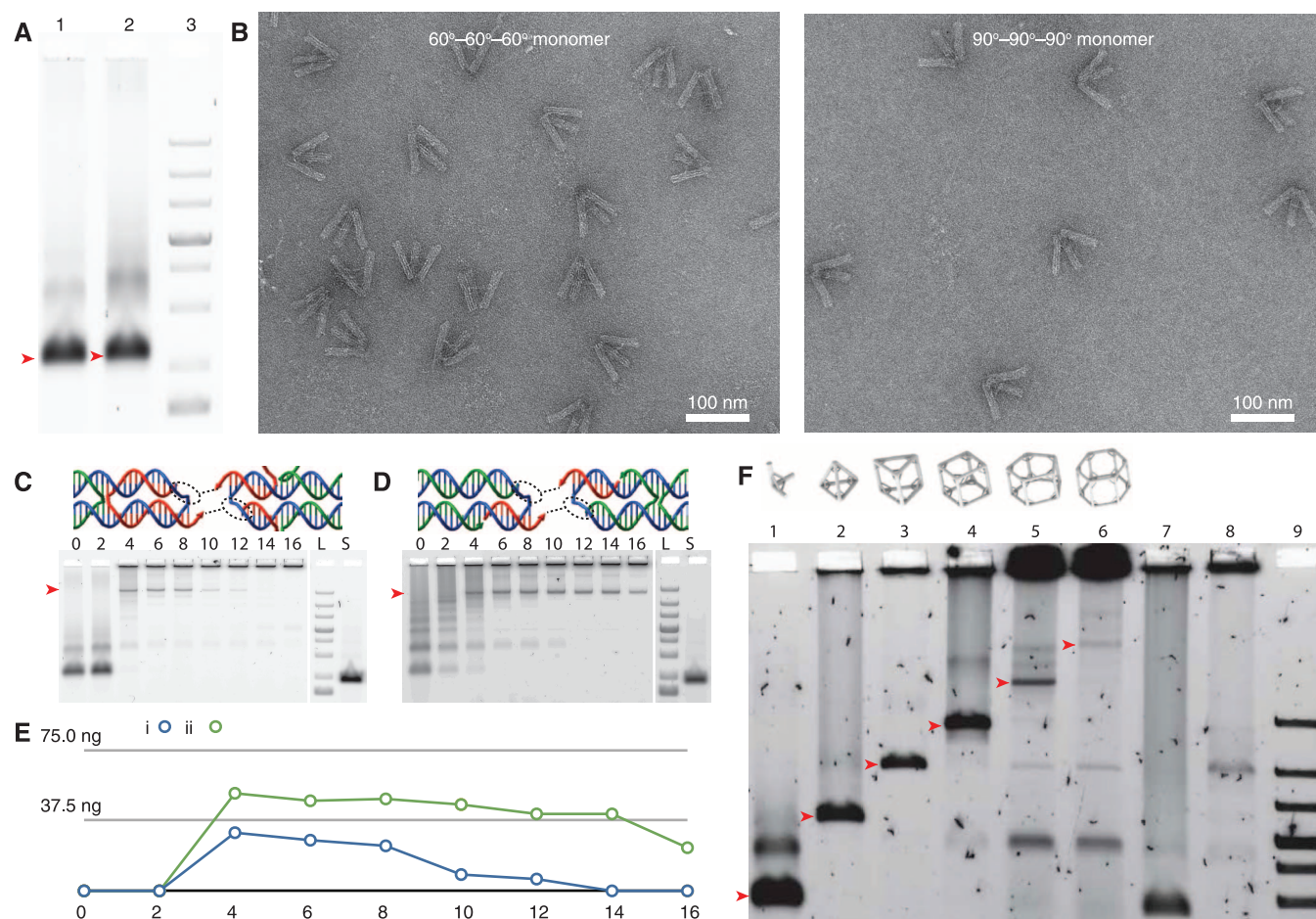
Fig. 2. Self-assembly of DNA tripods and polyhedra. (**A**) Gel electrophoresis and (**B**) TEM images of the 60°-60°-60° (lane 1 in the gel) and 90°-90°-90° (lane 2) tripods. Gel lane 3 is a 1-kb ladder. Gel electrophoresis involves 1.5% native agarose gel and ice water bath. (**C** and **D**) Two schemes of connector designs and corresponding gel electrophoresis results. For each scheme, the strand model depicts the connection between two pairs of DNA duplexes. The number above a gel lane denotes the number of connected helices between two adjacent arms. Lane L is a 1-kb ladder, and lane S is a scaffold. Arrowheads indicate the bands corresponding to assembled cubes. (**C**) Scheme i: long (30 nt) connector (red) including a 2-nt sticky end. The complete 30-nt connector is only shown on the left, with a 28-nt segment

anchored on the left helices and a 2-nt exposed sticky end available for hybridization with the 90°-90°-90° right neighbor (dashed circle depicts hybridization site). (**D**) Scheme ii: short (11 nt) connector including a 2-nt sticky end. (**E**) Assembly yields of the cubes, calculated as intensity ratio between a cube band and the corresponding scaffold band. (**F**) Agarose gel electrophoresis of the polyhedra. Lane 1 is the 90°-90°-90° monomer. Lanes 2 to 6 are polyhedra. Lane 7 is the assembly reaction containing tripods without struts. Lane 8 is the assembly reaction containing 90°-90°-90° tripods without vertex helices. Lane 9 is a 1-kb ladder. Gel bands corresponding to desired products are marked with arrowheads. Gel electrophoresis involves 0.8% native agarose gel and ice water bath.

weak inter-monomer connections; for $n > 12$, aggregations dominated.

In scheme i, the connectors were stably anchored (forming 28 base pairs) on tripods before inter-monomer connection occurred. In scheme ii, the connector was shortened from 30 to 11 bases so that it should only be anchored to two adjacent tripods by 9- and 2-base segments in the assembled cube (Fig. 2D) and only dynamically

binds to a monomeric tripod. Compared with the stably attached connector design, the dynamic connector design could potentially help correct inter-monomer mismatches that occurred during the assembly because such mismatches would be less likely frozen in a kinetic trap. Indeed, scheme ii showed substantially increased assembly yield (Fig. 2E). It was thus used for subsequent polyhedra designs, except for the tetrahedron, in which

scheme i produced sufficient yield for this relatively simple structure. The assembly yields were estimated from the gel (Fig. 2F). The 90°-90°-90° monomer sample (Fig. 2F, lane 1) showed a strong monomer band and a putative dimer band (not studied with TEM, ~27% intensity as compared with the monomer). We define the assembly yield of a polyhedron as the ratio between its product band intensity and the combined intensity of the 90°-90°-90° monomer and dimer bands (lane 1) and obtained yields of 45, 24, 20, 4.2, and 0.11% for the tetrahedron, the triangular prism, the cube, the pentagonal prism, and the hexagonal prism, respectively (Fig. 2F).

Table 1. Strut designs of the polyhedra. All units are nanometers. Entries are the designed length of the strut connecting the (i) Y-arm and Z-arm, (ii) X-arm and Z-arm, or (iii) X-arm and Y-arm or the designed distance from the vertex to the strut attachment point on the (iv) X-, (v) Y-, or (vi) Z-arm.

	i	ii	iii	iv	v	vi
Tetrahedron	28	28	28	29	29	29
Triangular prism	18	26	26	18	18	18
Cube	30	30	30	21	21	21
Pentagonal prism	32	26	26	19	18	18
Hexagonal prism	37	28	28	20	20	20

Polyhedra Assembly

The lengths and the attachment points of the struts varied for each polyhedron (Table 1). The tetrahedron, the triangular prism, the cube, the pentagonal prism, and the hexagonal prism should

Fig. 3. TEM images of polyhedra. The zoomed-in (columns 1 and 2) and zoomed-out (column 3) images are shown for (**A**) the tetrahedron, (**B**) the triangular prism, (**C**) the cube, (**D**) the pentagonal prism, and (**E**) the hexagonal prism. Images of the tetrahedron, the triangular prism, and the cube were acquired from purified samples. Images of the pentagonal prism and the hexagonal prism were collected from crude samples (denoted with an asterisk). Scale bars are 100 nm in the zoomed-in TEM images and 500 nm in the zoomed-out images. Aggregates are clearly visible for unpurified samples [such as in (D), right].
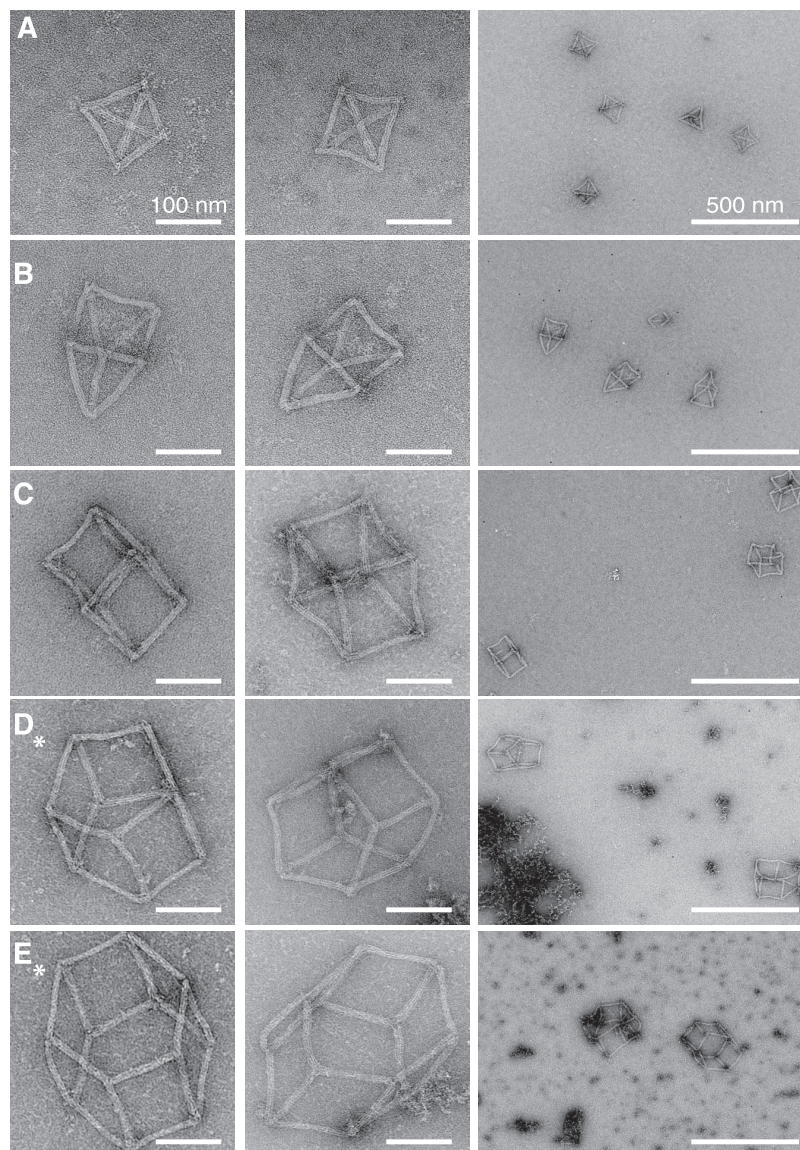
be assembled from monomers with designed 60°-60°-60°, 90°-90°-60°, 90°-90°-90°, 90°-90°-108°, and 90°-90°-120° angles, respectively (Fig. 1A). The first three monomers indeed produced tetrahedra, triangular prisms, and cubes [verified with gel electrophoresis (Fig. 2F) and TEM imaging (Fig. 3, A to C)], suggesting accurate control for angles within 90°. However, the pentagonal prism was assembled from monomers with designed angles of 90°-90°-120° (instead of 90°-90°-108°), and the hexagonal prism from 90°-90°-140° (instead of 90°-90°-120°). Thus, the assembly of these two polyhedra requires monomers with designed Y-Z angles greater than those of the design criteria. This requirement likely reflects slight bending of the relevant struts, which could be compensated by using longer struts.

Effects of Struts and Vertex Helices

We next verified that both the struts and the vertex helices were required for the tripods to assemble into the designed polyhedron. Three samples were prepared for cube assembly by using tripods that contain (i) both the struts and the vertex

helices (Fig. 2F, lane 4), (ii) the vertex helices but not the struts (lane 7), and (iii) the struts but not the vertex helices (lane 8); the latter samples were subjected to gel electrophoresis after annealing. The first sample showed a sharp strong band corresponding to the cube (verified with TEM) (Fig. 3C). The second failed to produce any clear product band. The third produced substantial aggregates and a clear but weak band with mobility comparable with that of the triangular prism. This band may correspond to a hexamer, but its molecular morphology was not investigated. On the basis of the above experiments, we included both the struts and the vertex helices in the tripods for subsequent polyhedra assembly.

TEM Characterization

Product bands were purified and imaged under TEM. For the tetrahedron, the triangular prism, and the cube, most structures appeared as intact polyhedra; a small fraction of broken structures (< 20%) were likely ruptured during the purification and imaging (Fig. 3, A to C). In contrast, few intact structures were observed for the pu-

rified pentagonal and hexagonal prisms. Thus, unpurified samples for these two were directly imaged, and the expected molecular morphologies were observed (Fig. 3, D and E). Additional images are provided in figs. S4 to S13. The struts are clearly visible in many images (a zoomed-in example is provided in fig. S14).

3D DNA-PAINT Super-Resolution Microscopy

Localization-based 3D super-resolution fluorescence microscopy (31–33) offers a minimally invasive way to obtain true single-molecule 3D images of DNA nanostructures in their "native" hydrated environment (distorted and broken tetrahedra, likely caused by the TEM imaging conditions, are shown in figs. S4 and S15). In stochastic reconstruction microscopy (34), most molecules are switched to a fluorescent dark (OFF) state, and only a few emit fluorescence (ON state). Each molecule is localized with nanometer precision by fitting its emission to a 2D Gaussian function. In DNA-PAINT, the "switching" between ON and OFF states is facilitated through the repetitive, transient binding of fluorescently labeled oligonucleotides
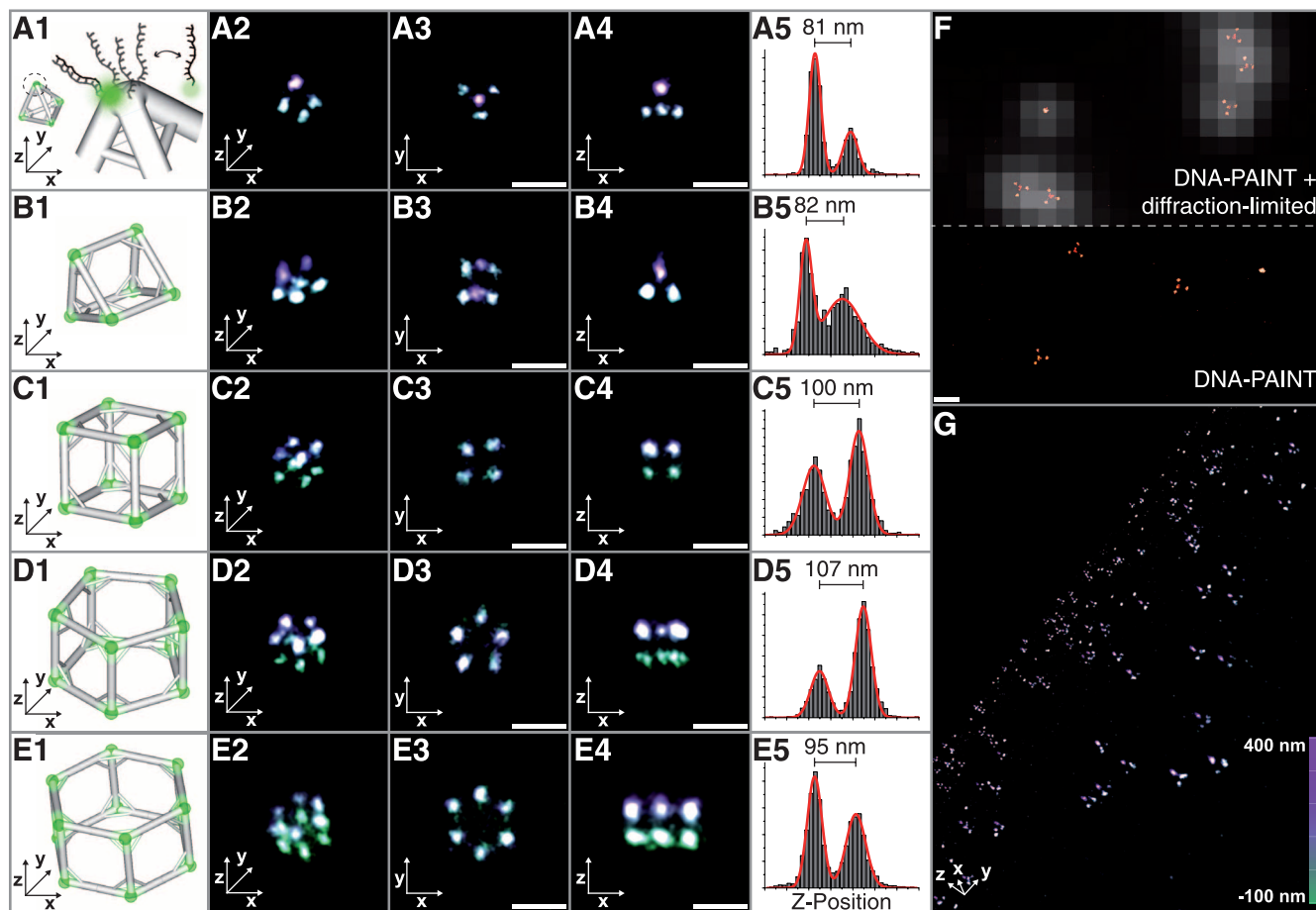
Fig. 4. 3D DNA-PAINT super-resolution fluorescence imaging of polyhedra. (**A1**) Staple strands at the vertices of each polyhedron were extended with single-stranded docking sequences for 3D DNA-PAINT super-resolution imaging. (**A1** to **E1**) Schematics of polyhedra, with DNA-PAINT sites highlighted in green. (**A2** to **E2**) 3D DNA-PAINT super-resolution reconstruction of typical polyhedra shown in the same perspective as depicted in A1 to E1. (**A3** to **E3**) 2D x-y projection. (**A4** to **E4**) 2D x-z projection. (**A5** to **E5**) Height

measurements of the polyhedra obtained from the cross-sectional histograms in the x-z projections. (**F**) A larger 2D super-resolution x-y projection view of tetrahedra and drift markers (bright individual dots). The diffraction-limited image is superimposed on the super-resolution image in the upper half. (**G**) Tilted 3D view of a larger-field-of-view image of the tetrahedron. Drift markers appear as bright individual dots. Scale bars, 200 nm. Color indicates height in the z direction.

("imager" strands) to complementary "docking" strands (*24, 28, 29, 35*).

We extended DNA-PAINT to 3D imaging (*29*) using optical astigmatism (*31, 36*), in which a cylindrical lens used in the imaging path "converts" the spherical point spread function (PSF) of a molecule to an elliptical PSF when imaged out of focus. The degree and orientation of the elliptical PSF depends on the displacement and direction of the point source from the current focal imaging plane and is used to determine its z position (*31, 36*). We applied 3D DNA-PAINT to obtain subdiffraction-resolution single-molecule images of the polyhedra. To ensure all the vertices of a polyhedron will be imaged, each vertex is modified with multiple (~18) 9-nucleotide (nt) docking strands (Fig. 4A1) in a symmetric arrangement (fig. S2). For surface immobilization, a subset of strands along the polyhedron edges were modified with 21-nt extensions, which were hybridized to biotinylated complementary strands attached to a streptavidin covered glass slide [(*27*), DNA sequences].

Using 3D DNA-PAINT microscopy, all five polyhedra showed designed 3D patterns of vertices (Fig. 4, columns 1 to 4) with expected heights (Fig. 4, A5 to E5), suggesting that the solution shape of the structures is maintained during surface immobilization and imaging. We quantified the tetrahedra formation and imaging yields (Fig. 4, F and G, and fig. S16). Out of 285 structures, 253 (89%) contained four spots in the expected tetrahedral geometry. Height measurement yielded 82 ± 15 nm, which is consistent with the designed value (82 nm). Single DNA-PAINT binding events were localized with an accuracy of 5.4 nm in x-y and 9.8 nm in z [(*27*) describes how localization accuracy was determined]. This z localization accuracy almost completely accounts for the 15-nm spread in the height measurement distribution. The calculated localization precisions translate to an obtainable resolution of ~13 nm in x and y, and ~24 nm in z. Movies S1 and S2 are 3D DNA-PAINT videos. Design is provided in figs. S17 to S22, and tables S1 to S7 have sequence details.

Discussion

Previous work demonstrated diverse DNA polyhedra self-assembled from small three-arm-junction tiles (~80 kD) (*16, 23*), which consist of three double-helix arms connected by flexible single-stranded hinges. However, straightforward implementation of megadalton three-arm origami tiles by use of similar flexible inter-arm hinges (tripods with no struts or vertex helices) failed to produce well-formed polyhedra (Fig. 2F, lane 7). An origami tripod contains 50 times more distinct strands than do previous three-arm-junction tiles (formed from three distinct strands) and is 60 times more massive in molecular weight. Apart from the challenges associated with the more error-prone construction of the more complex monomers from individual strands, successful hierarchical assembly of such large monomers into polyhedra also needs to overcome much slower reaction

kinetics, caused by the larger size and lower concentration of the tripod monomers. The stiff DNA tripods, with rationally designed inter-arm angles controlled by supporting struts and vertex helices, lead to successful construction of diverse polyhedra, suggesting that conformation control of branched megadalton monomers can facilitate their successful assembly into higher-order structures.

The design principles of DNA tripods may be extended to stiff megadalton n-arm ($n \geq 4$) branched motifs with controlled inter-arm angles. Self-assembly with such n-arm motifs could be used to construct more sophisticated polyhedra and potentially extended 2D and 3D lattices with ≤100-nm tunable cavities. Such structures could potentially be used to template guest molecules for diverse applications—for example, spatially arranging multiple enzymes into efficient reaction cascades (*37*) or nanoparticles to achieve useful photonic properties (*38, 39*). Furthermore, the DNA polyhedra constructed here, with a size comparable with those of bacterial microcompartments, may potentially be used as skeletons for making compartments with precisely controlled dimensions and shapes by wrapping lipid membranes around their outer surfaces (*40*). Such membrane-enclosed microcompartments could potentially serve as bioreactors for synthesis of useful products or as delivery vehicles for therapeutic cargo (*25*).

For 3D characterization of DNA nanostructures, super-resolution fluorescence microscopy (such as 3D DNA-PAINT) provides complementary capabilities to present electron microscopy [such as cryogenic electron microscopy (cryo-EM) (*12, 16, 17, 23*)]. Whereas cryo-EM offers higher spatial resolution imaging of unlabeled structures, DNA-PAINT is less technically involved to implement, obtains true single-molecule images of individual structures (rather than relying on class averaging), and preserves the multicolor capability of fluorescence microscopy (*29*). Additionally, DNA-PAINT in principle allows for observation of dynamic structural changes of nanostructures in their "native" hydrated environment, which is currently suitable for slow changes on the minutes time scale (such as the locomotion of synthetic DNA walkers) and potentially for faster motions with further development.

References and Notes

1. J. H. Chen, N. C. Seeman, *Nature* **350**, 631–633 (1991).
2. E. Winfree, F. Liu, L. A. Wenzler, N. C. Seeman, *Nature* **394**, 539–544 (1998).
3. P. W. Rothemund, N. Papadakis, E. Winfree, *PLOS Biol.* **2**, e424 (2004).
4. P. W. Rothemund, *Nature* **440**, 297–302 (2006).
5. S. M. Douglas *et al.*, *Nature* **459**, 414–418 (2009).
6. J. Zheng *et al.*, *Nature* **461**, 74–77 (2009).
7. B. Wei, M. Dai, P. Yin, *Nature* **485**, 623–626 (2012).
8. Y. Ke, L. L. Ong, W. M. Shih, P. Yin, *Science* **338**, 1177–1183 (2012).
9. D. Han *et al.*, *Science* **339**, 1412–1415 (2013).
10. V. Linko, H. Dietz, *Curr. Opin. Biotechnol.* **24**, 555–561 (2013).
11. Y. Zhang, N. C. Seeman, *J. Am. Chem. Soc.* **116**, 1661–1669 (1994).
12. W. M. Shih, J. D. Quispe, G. F. Joyce, *Nature* **427**, 618–621 (2004).
13. R. P. Goodman *et al.*, *Science* **310**, 1661–1665 (2005).
14. F. A. Aldaye, H. F. Sleiman, *J. Am. Chem. Soc.* **129**, 13376–13377 (2007).
15. C. M. Erben, R. P. Goodman, A. J. Turberfield, *J. Am. Chem. Soc.* **129**, 6992–6993 (2007).
16. Y. He *et al.*, *Nature* **452**, 198–201 (2008).
17. C. Zhang *et al.*, *Proc. Natl. Acad. Sci. U.S.A.* **105**, 10665–10669 (2008).
18. J. Zimmermann, M. P. Cebulla, S. Mönninghoff, G. von Kiedrowski, *Angew. Chem. Int. Ed. Engl.* **47**, 3626–3630 (2008).
19. E. S. Andersen *et al.*, *Nature* **459**, 73–76 (2009).
20. Y. Ke *et al.*, *Nano Lett.* **9**, 2445–2447 (2009).
21. D. Bhatia *et al.*, *Angew. Chem. Int. Ed. Engl.* **48**, 4134–4137 (2009).
22. H. Yang *et al.*, *Nat. Chem.* **1**, 390–396 (2009).
23. C. Zhang *et al.*, *J. Am. Chem. Soc.* **131**, 1413–1415 (2009).
24. D. M. Smith *et al.*, *J. Nucleic Acids* **2011**, 360954 (2011).
25. S. M. Douglas, I. Bachelet, G. M. Church, *Science* **335**, 831–834 (2012).
26. Z. Nie *et al.*, *Chem. Commun. (Camb.)* **49**, 2807–2809 (2013).
27. Materials and methods are available as supplementary materials on *Science* Online.
28. R. Jungmann *et al.*, *Nano Lett.* **10**, 4756–4761 (2010).
29. R. Jungmann *et al.*, *Nat. Methods* **11**, 313–318 (2014).
30. A. Sharonov, R. M. Hochstrasser, *Proc. Natl. Acad. Sci. U.S.A.* **103**, 18911–18916 (2006).
31. B. Huang, W. Wang, M. Bates, X. Zhuang, *Science* **319**, 810–813 (2008).
32. G. Shtengel *et al.*, *Proc. Natl. Acad. Sci. U.S.A.* **106**, 3125–3130 (2009).
33. J. J. Schmied *et al.*, *Nano Lett.* **13**, 781–785 (2013).
34. S. W. Hell, *Science* **316**, 1153–1158 (2007).
35. C. Lin *et al.*, *Nat. Chem.* **4**, 832–839 (2012).
36. H. P. Kao, A. S. Verkman, *Biophys. J.* **67**, 1291–1300 (1994).
37. J. Fu, M. Liu, Y. Liu, N. W. Woodbury, H. Yan, *J. Am. Chem. Soc.* **134**, 5516–5519 (2012).
38. G. P. Acuna *et al.*, *Science* **338**, 506–510 (2012).
39. A. Kuzyk *et al.*, *Nature* **483**, 311–314 (2012).
40. M. Langecker *et al.*, *Science* **338**, 932–936 (2012).

Soft Microfluidic Assemblies of Sensors, Circuits, and Radios for the Skin

Sheng Xu,[1]* Yihui Zhang,[2,3]* Lin Jia,[1]* Kyle E. Mathewson,[4]* Kyung-In Jang,[1] Jeonghyun Kim,[1,6] Haoran Fu,[2,5] Xian Huang,[1] Pranav Chava,[1] Renhan Wang,[1] Sanat Bhole,[1] Lizhe Wang,[1] Yoon Joo Na,[1] Yue Guan,[1] Matthew Flavin,[1] Zheshen Han,[1] Yonggang Huang,[2]† John A. Rogers[1,4]†

When mounted on the skin, modern sensors, circuits, radios, and power supply systems have the potential to provide clinical-quality health monitoring capabilities for continuous use, beyond the confines of traditional hospital or laboratory facilities. The most well-developed component technologies are, however, broadly available only in hard, planar formats. As a result, existing options in system design are unable to effectively accommodate integration with the soft, textured, curvilinear, and time-dynamic surfaces of the skin. Here, we describe experimental and theoretical approaches for using ideas in soft microfluidics, structured adhesive surfaces, and controlled mechanical buckling to achieve ultralow modulus, highly stretchable systems that incorporate assemblies of high-modulus, rigid, state-of-the-art functional elements. The outcome is a thin, conformable device technology that can softly laminate onto the surface of the skin to enable advanced, multifunctional operation for physiological monitoring in a wireless mode.

Continuous physiological monitoring and intervention are needed for the treatment of many medical conditions. Multimodal, noninvasive access to the body can be accomplished through cutaneous electrical/optical/fluidic interfaces. "Skin-like" devices, sometimes referred to as "epidermal" electronic systems (*1, 2*), offer thicknesses (*3–5*), moduli, levels of elastic stretchability, and other basic physical properties that match those of the skin itself so as to allow a soft, compliant type of integration. Recent work demonstrates that such characteristics can be achieved by exploiting ultrathin geometries (*1, 6, 7*), soft active materials (*3, 4, 8–13*), and/or liquid metals (*14–16*). Here, we demonstrate ideas that expand options beyond these specialized approaches to include commercial, chip-scale components, ranging from integrated circuits, to radio frequency hardware, microelectromechanical structures, physical/chemical sensors, and power sources. The key concept involves microfluidic suspensions of interconnected assemblies of such chips

in thin elastomeric enclosures to enable soft, low-modulus mechanics at the system level. Here, the high-modulus components have little impact on the overall mechanics, even when they are present at high areal coverage. For otherwise similar device layouts, this strategy improves the mechanical compliance and the stretchability by orders of magnitude compared with those possible using previous approaches that incorporate chip-scale components (*17–20*). The resulting systems can laminate softly and noninvasively onto the skin to define highly functional interfaces with the ability to combine unusual elements with standard parts. These concepts enable broad classes of sophisticated bio-integrated electronic devices, as illustrated here through systems that offer wirelessly powered operation and precision measurement of biopotentials, acceleration, and/or temperature, with radio frequency (RF) data transmission.

The layout involves a matrix of microfluidic spaces designed to decouple the mechanics of the constituent devices and associated interconnect network from a thin, elastomeric enclosure that simultaneously provides a supporting surface (substrate) and an encapsulation layer (superstrate). Each component selectively bonds to the bottom surface of this enclosure at small, localized cylindrical features of relief (support posts) molded onto the thin elastomer substrate. Except for these posts, the devices are suspended in the surrounding fluid and, as a result, are mechanically isolated. A free-floating network of serpentine-shaped interconnects with multilayer, neutral mechanical plane layouts joins the devices into circuit architectures that provide system-level function. Presented in Fig. 1A is an exploded view schematic illustra-

tion of an integrated device capable of acquisition, filtering, amplification, and RF transmission of electrophysiological (EP) data, for precision measurement of electrocardiograms (ECGs), electromyograms (EMGs), electrooculograms (EOGs), and electroencephalograms (EEGs).

Bonding the superstrate and substrate at their edges defines a microfluidic structure that is subsequently filled with a dielectric fluid by use of an injection needle (Fig. 1B and fig. S1). Selection criteria for the fluid include (i) wettability toward the electronic components and the substrate/superstrate to facilitate the filling process, (ii) large volume resistivity ($>1 \times 10^{14}$ Ohm $\cdot$ cm) to eliminate electrical crosstalk, (iii) high dielectric strength (>10 kV/mm) to avoid electrical breakdown, (iv) moderate viscosity (~5 Pa $\cdot$ s) to enhance impact resistance, (v) good thermal stability [weight loss $< 0.5\%$ at $100°$C for 4 hours (fig. S2)] to allow reliable long-term operation, (vi) low-loss RF properties and small dielectric constant (<3) to minimize influence on RF operation, (vii) low reactivity and chemical stability to avoid corrosion or other forms of chemical degradation, (viii) hydrophobic character to expel moisture from the package, and (ix) optical transparency to enable rapid inspection of the components. The devices reported here use a soft, silicone elastomer (Ecoflex, Smooth-On, Easton, Pennsylvania) for the substrate/superstrate, and a high-molecular-weight silicone oligomer (Sylgard 184, without curing agent) for the fluid.

The free-floating interconnects can buckle, twist, and deform with little constraint, both in and out of the plane, in response to externally imposed deformations of the entire system. Likewise, the fluid-based strain isolation strategy allows large-range motions of the substrate/superstrate with minimal coupling to the device components. This mechanics are apparent from the three-dimensional (3D) finite element analysis (FEA) results of Fig. 1C. The ability of the interconnects to move freely increases their range of stretchability, relative to designs that involve bonding to or embedding in solid or porous elastomers (*17–23*). For the case of an interconnect shown in Fig. 1C, this increase in stretchability corresponds to a factor of ~10 or ~20 when compared with the case of bonding or embedding, respectively (fig. S3). The maximum principal strain in the interconnect metal (Fig. 1C) is less than ~0.2% for a biaxial stretch of 50% for the entire system. The support posts lead to differences in absolute strains between the hard components and the elastomer immediately below, which can be as large as ~64% for the same level (50%) of biaxial stretch.

A dense array of sharp, pyramidal features molded onto the substrate prevent nonspecific adhesion to the interconnects and the devices, to allow low-friction, lubricated relative motions. The cross-sectional scanning electron microscope (SEM) images of Fig. 1D and fig. S4 show this relief, as well as that associated with a support post to allow strain isolation of component chips

[1]Department of Materials Science and Engineering and Frederick Seitz Materials Research Laboratory, University of Illinois at Urbana-Champaign, Urbana, IL 61801, USA. [2]Department of Mechanical Engineering and Department of Civil and Environmental Engineering, Center for Engineering and Health, and Skin Disease Research Center, Northwestern University, Evanston, IL 60208, USA. [3]Center for Mechanics and Materials, Tsinghua University, Beijing, 100084, P.R. China. [4]Beckman Institute for Advanced Science and Technology, University of Illinois at Urbana-Champaign, Urbana, IL 61801, USA. [5]Department of Civil Engineering and Architecture, Zhejiang University, Hangzhou 310058, P.R. China. [6]Department of Materials Science and Engineering, Department of Energy Engineering, Hanyang University, Seoul 133-791, Republic of Korea.

*These authors contributed equally to this work.
†Corresponding author. E-mail: jrogers@illinois.edu (J.A.R.); y-huang@northwestern.edu (Y.H.)

and a physical barrier to prevent entanglement of adjacent interconnects. The same region after integration of the interconnect network by transfer printing appears in Fig. 1, E and F. The chips [all <1 mm in thickness, achieved with mechanical grinding (fig. S5)] bond electrically and mechanically to this network via a low-temperature solder (figs. S6 and S7 and movie S1). Wide, straight traces (fig. S8) pass through opposite edges of the microfluidic enclosure (microfluidic thickness, ~1 mm; superstrate thickness, ~0.1 mm) and terminate at external contact pads that provide

locations for lamination of epidermal electrodes (fig. S9) as interfaces to the skin. The completed system (Fig. 1G) includes modules for (i) wireless power supply through resonant inductive energy transfer, (ii) low-noise amplification and filtering of EP signals, and (iii) frequency-modulated RF transmission of measured data. The components and the design rationale are summarized in table S1 and fig. S10. The abilities of the device to stretch (shown here to ~30% uniaxial strain) and twist (shown here to ~75°) are evident from images in Fig. 1, H and I, respectively. Details

on the materials and fabrication procedures are available as supplementary materials on *Science* Online.

Mechanical behaviors at the system level are important to overall design. Summarized in Fig. 2 are systematic computational and experimental studies of the device in Fig. 1, without the superstrate membrane to facilitate imaging. 3D-FEA results (Fig. 2A) and experimental pictures (Fig. 2B) reveal the configurations of the chips and interconnects at various levels of equal-biaxial stretch. The good agreement validates the models
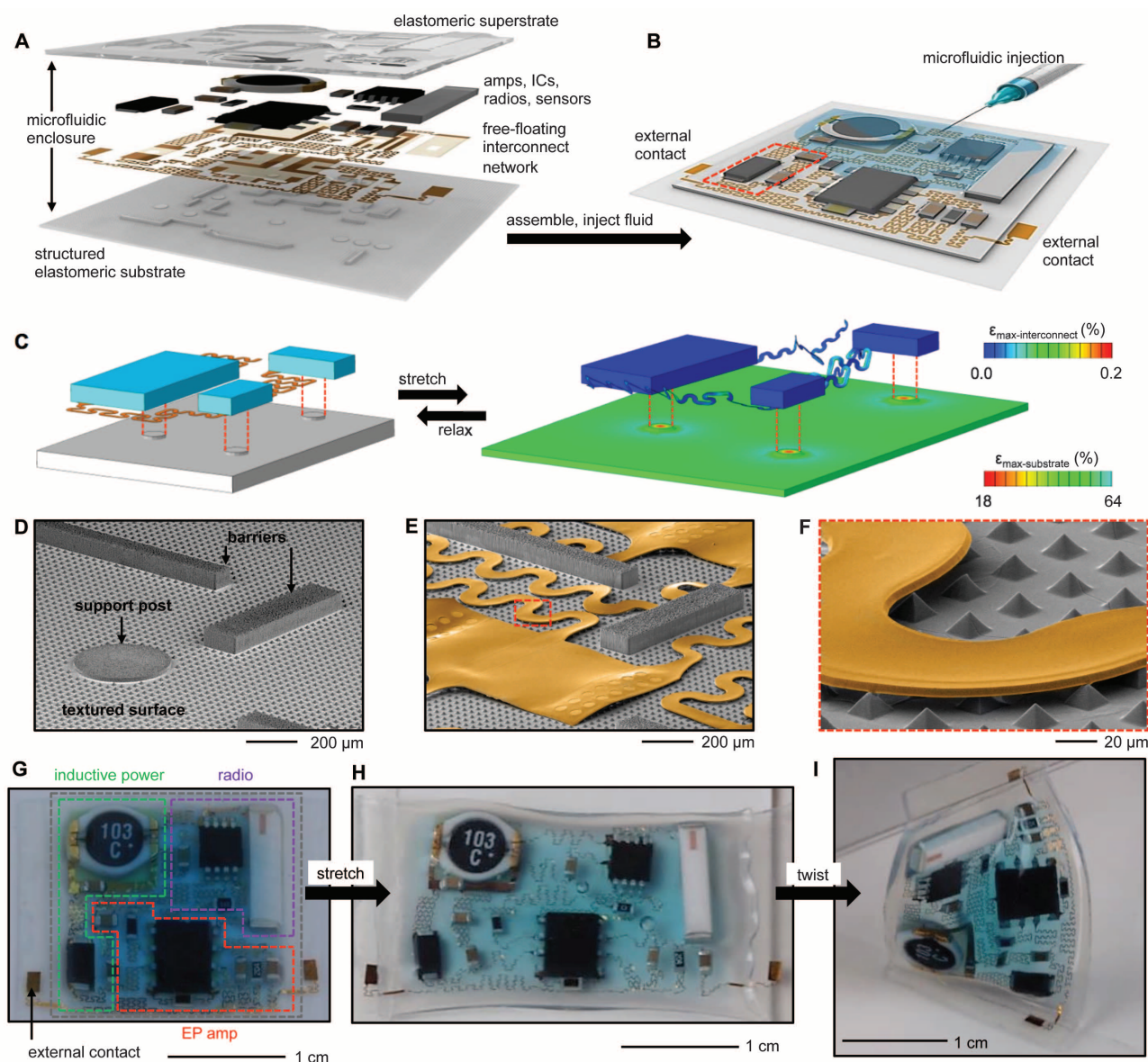
Fig. 1. Schematic illustrations, SEMs, and pictures of a soft, stretchable electronic system that integrates strain-isolated device components and a free-floating interconnect network in a thin elastomeric microfluidic enclosure. (**A**) Exploded-view schematic illustration of the key components of the system. (**B**) Illustration of the system after assembly, during initial stages of microfluidic injection using a syringe. (**C**) 3D-FEA results, in exploded-view format, that show the mechanics associated with equal-biaxial stretching of a small region of this system, as indicated by the red dash box in (B). The colors indicate the maximum principal strains. The buckling physics of the free-floating serpentine interconnects and the strain isolation mechanics of the suspended chips represent the key features. (**D**) Angled-view SEM of a region of the substrate showing a textured surface with different structures labeled. (**E**) Angled-view SEM of the same region in (D), after transfer printing the interconnect network (yellow). (**F**) Angled-view SEM of the region of (E) indicated by the red dashed box. (**G**) Image of a system with the colored dashed boxes and labels to identify the various subsystems. The gray dashed box around the periphery indicates, approximately, the location of bonding of the superstrate. (**H** and **I**) Image of this system in a (H) stretched and (I) twisted configuration.

and establishes their utility as design tools for optimizing the layouts of the chips and the shapes of the interconnects. In particular, for any choice of system geometry the computed results allow rapid identification of locations of (i) high principal strains, (ii) entanglements in the interconnects, and (iii) collisions between the chips. An iterative process that involves coupled considerations in circuit and mechanics design, with 3D-FEA modeling as a guide, allows optimization of all relevant parameters (including positions of molded barriers) for a desired device size, degree of stretchability, and effective modulus. The system shown here results from several iterations in the layouts of the chips and the geometries of the self-similar serpentine shapes that form the aperiodic interconnection network. Attention to the hierarchical mechanics of in- and out-of-plane bending and

twisting in the serpentines and their dependence on geometry is paramount, subject to constraints set by requirements on their electrical properties. The subtle effects that can occur are shown in Fig. 2C and fig. S11. An example of one of the many modifications introduced with guidance from theory is a small bonding site added at the midpoint of the long interconnect at the base edge so as to ensure reversibility in its mechanics and to avoid entanglements (fig. S7). The final design offers an effective modulus, at the system level, that is only slightly larger (by 3 to 5%) than the intrinsic value associated with the bare elastomeric substrate (table S2). Uniaxial testing of substrate with and without the chips, interconnect network, and surrounding fluid reveal almost identical stress/strain responses, as shown in the bottom frame of Fig. 2B. This outcome is notable,

considering the large differences between the moduli of the electronic materials (~100 GPa) and the elastomers (~180 kPa).

In addition to a low modulus, the system offers a large range of stretchability. For example, 100% equal-biaxial strain induces maximum principal strains of only ~2% in the active materials (Cu of the interconnects), as highlighted by a segment of the interconnect network shown in the bottom frame of Fig. 2A. The maximum biaxial stretchability predicted with 3D-FEA is ~125%, limited by localized fracture of the Cu (failure strain ~5%) in the interconnect network, which is consistent with experimental observation (~100%). Reversible, elastic behaviors can be obtained (yield strain of Cu, ~0.3%) for biaxial strains of ~49% (fig. S12), even with the high (~46%) cumulative areal coverage of chips
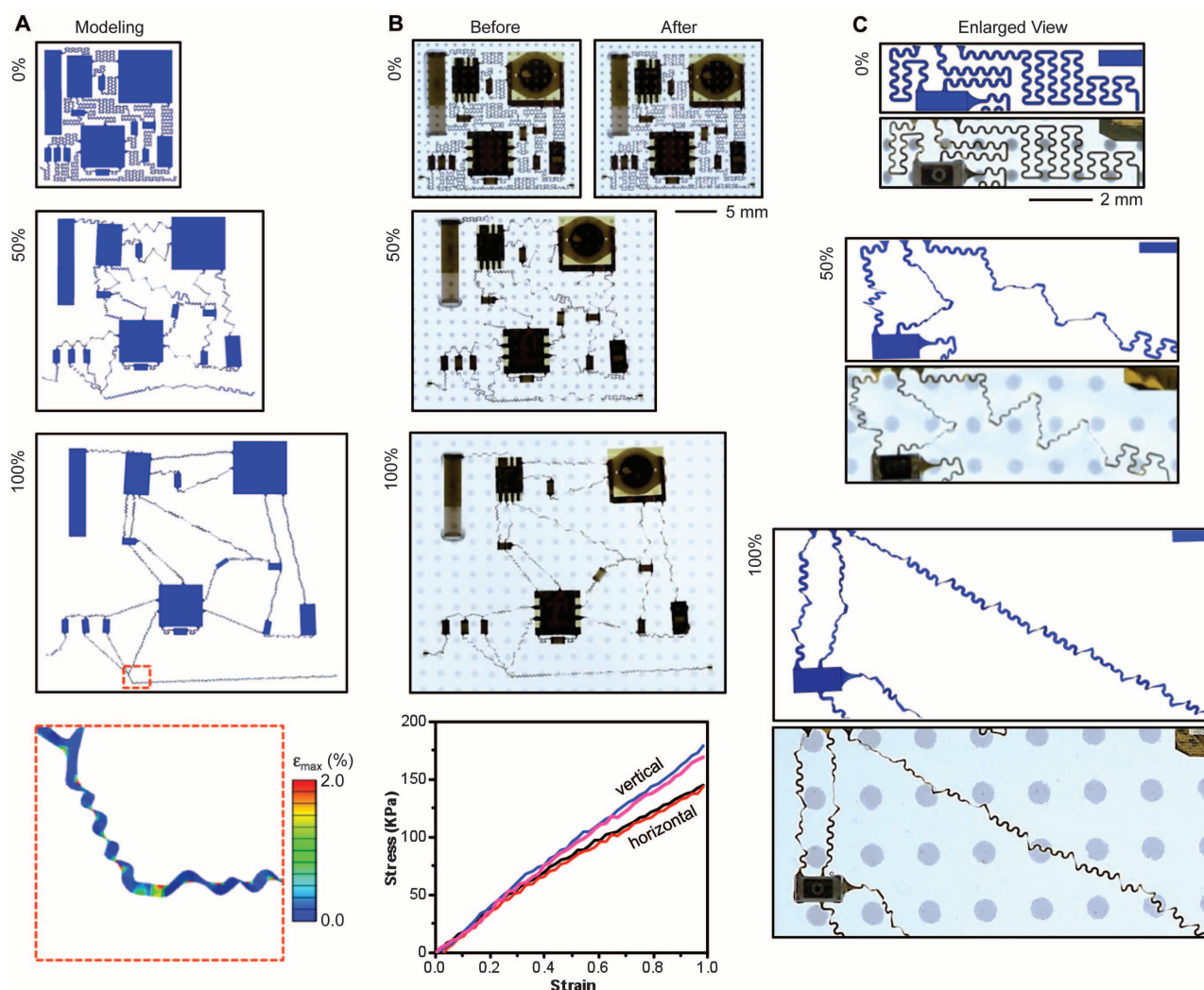
Fig. 2. Computational and experimental studies of the physics of buckling in free-floating interconnect networks and of strain isolation in suspended chips for a wireless EP sensor. (**A**) System-level 3D-FEA results for various magnitudes of equal-biaxial tensile strain. The color shows the maximum principal strains across each part of the system. (Bottom) Illustration of a small region of the interconnect network. (**B**) Optical images of the device at equal-biaxial strains that correspond to those evaluated by

3D-FEA. An additional image shows the system after release of the strain, to illustrate reversibility in the responses. (Bottom) Graph of the stress/strain responses measured by uniaxial testing for the case of a system with (black, in horizontal; blue, in vertical) and without (red, in horizontal; pink, in vertical) the chips and interconnect network. The results indicate nearly complete decoupling of the mechanics of the chips and interconnects from the substrate. (**C**) Images and 3D-FEA results for a local region.

in this device layout. Practical limits in uniaxial stretching are ~40%, defined by collisions of adjacent chips caused by orthogonal contractions that arise from the Poisson effect (figs. S13 and S14). The device can be cycled for more than 6000 times under 30% uniaxial strain at a frequency of 0.6 Hz (fig. S15) without degradation. In all cases, deformations in the substrate show no evidence of constraints in motion associated with the chips or the interconnect network, as illustrated by the uniform separations between fiducial dots (Cr, 100 nm thick) deposited in a square array on the back surface of the substrate, which is visible in the images of Fig. 2. Quantitative analysis is provided in fig. S16. This low-modulus [~180 kPa, as soft as the skin (*1*)],

isotropic stretchable response follows from the microfluidic strain-isolation approaches. Analogous systems that do not exploit selective bonding of the chips to support posts show highly nonuniform deformations in the substrate (fig. S17); those that replace the microfluidics with solid elastomer show an elastic stretchability of only 6% and local effective moduli that vary from values comparable with those of the chips themselves (>100 GPa) to the elastomer constrained by the bonded interconnects (~250 kPa). Such characteristics are poorly matched to requirements for mounting on the skin.

Shown in Fig. 3, A and B, is a completed device (~1.7 × 1.8 cm^2) that includes a pair of epidermal electrodes (each ~0.8 × 1 cm^2, in fila-

mentary, self-similar serpentine mesh designs) (fig. S18) laminated onto the skin of the forearm, in undeformed and deformed states, respectively. Here, low interface stresses associated with the low effective modulus of the device enable robust adhesion to the skin through van der Waals forces alone, facilitated by an ultralow modulus thin elastomer coating on the bottom surface of the substrate. Alternating voltage (150 kHz) applied to a primary coil in proximity (within millimeters) to the device activates it by creating direct current output from the inductive power module. The total power consumption is ~35 mW. Laminating the device across the sternum with the electrodes in bilateral fourth intercostal spaces enables wireless (~2.4 GHz) collection of ECG (movie S2) at distances of up to 1 m (fig. S19). The data show excellent signal-to-noise ratios, with clearly identifiable sequences of Q, R, and S waveforms (Fig. 3C). The fidelity of this system is similar to that of conventional commercial hardware with wired connections (fig. S20). Even weak electrophysiological signals can be captured effectively through EEG measured between electrodes on the forehead (positions Fpz and AF7), as illustrated in Fig. 3D, compared with signals simultaneously collected by using commercial hardware. Here, the subject engaged in mental math (counting backward by 7 from 200) for 1 min, closed his eyes, and remained at rest for another minute. EOG activity from the eyes closing separates the two tasks. The data reveal strong high-frequency activity during mental math and strong low-frequency activity during rest (fig. S21), as expected. Experimental details and many additional examples (fig. S22) appear in the supplementary materials.

The core concepts can also be used in multifunctional systems that allow not only EP sensing but also precision recording of motion with a triaxial accelerometer and with a thermal sensor, switched sequentially by a multiplexer (fig. S23). Such capabilities are important for applications that range from training in sports to tracking in sleep apnea studies, monitoring in neonatal care, and assessing cognitive state and awareness. The device in this case (1.9 × 2.9 cm^2) includes 31 component chips and a complex, multilayer interconnect network. The components and design rationale are summarized in table S3 and fig. S24. At low duty cycle operation (fig. S25), the power consumption (few milliwatts) lies in a range that can be addressed not only with near-field communication, but also with a small coin-cell battery or, potentially, far-field RF power transfer. A pair of contact pads enables integration of these and other options in power supply (Fig. 4A and fig. S26). A combined circuit and mechanics iterative design process, similar to that described for the single-channel device, enables a high level of stretchability and low effective modulus. As a consequence, the system can naturally integrate with the skin and remain adhered through van der Waals forces during twisting, stretching, and pinching (Fig. 4B and fig. S27). An EMG
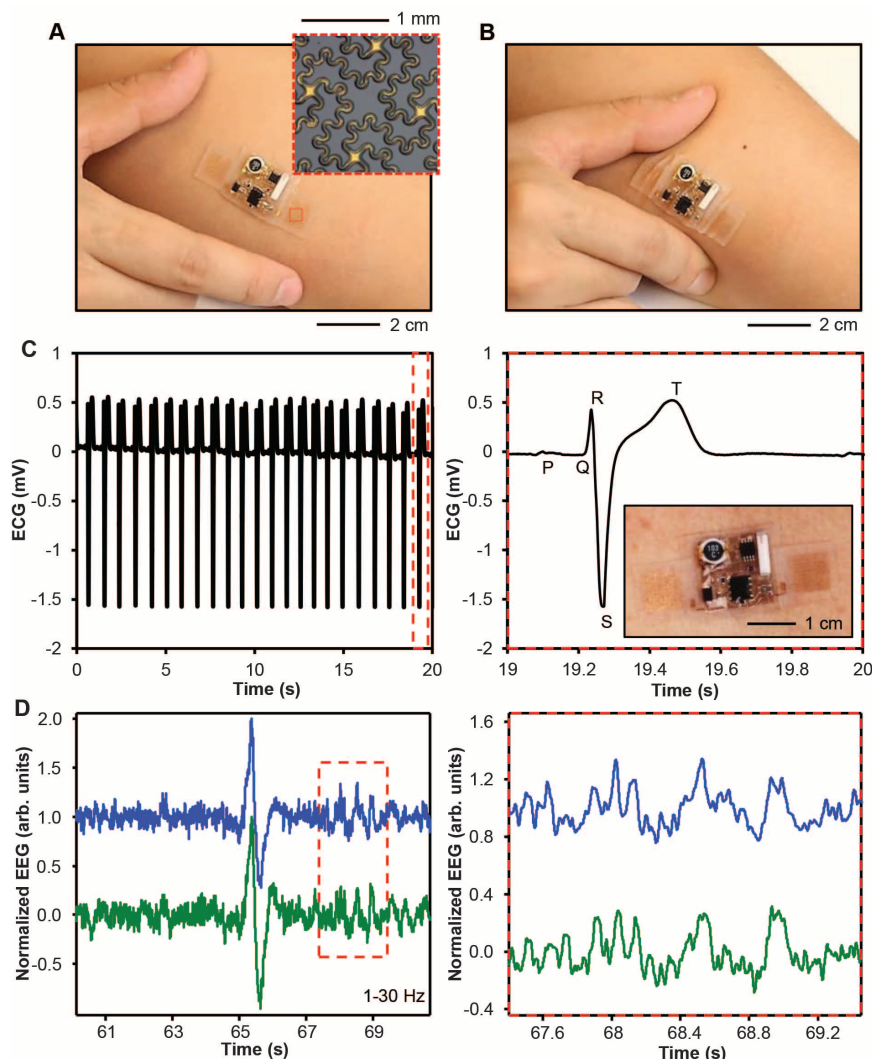
Fig. 3. Images and operational data from a wireless EP sensor. (**A** and **B**) Optical images of the device on the forearm, with a pair of epidermal electrodes in self-similar serpentine mesh layouts (inset optical micrograph) for an (A) undeformed state and (B) compressed and twisted state. (**C**) ECG acquired by using a device mounted on the sternum. The graph on the right provides a detailed view that shows the expected Q, R, and S waveforms. (**D**) EEG acquired from the left forehead during mental math and rest (green), and simultaneous measurement by using a wired commercial device (blue), mounted next to the wireless system. The large deflection represents the eyes closing as the subject shifts from mental math to resting, as shown in detail in the right plot. Data are plotted in arbitrary units, normalized and offset in the vertical direction to facilitate comparisons.

recorded from the forearm during repeated clenching and releasing of the fist is shown in Fig. 4C. The output of the accelerometer during walking and falling appears in Fig. 4D. The temperature responses induced through breathing onto the device (Fig. 4E) and physical exercise are consistent with those observed by using a commercial infrared camera (figs. S28 and S29).

The results presented here establish a general, quantitative experimental and theoretical framework for hard/soft composite systems that exploit (i) microfluidic suspensions to mechanically isolate rigid materials from compliant, elastomeric enclosures, (ii) topographical features and patterned surface chemistries to control interface adhesion, and (iii) self-similar structural designs to provide hierarchical buckling mechanics and large elastic strain range. Multifunctional devices that exploit these ideas allow mounting on the skin in ways that are barely perceptible, in a mechanical sense. Additional possibilities include construction of hybrid systems that incorporate epidermal transistors for amplified, multiplexed addressing of signals from distributed arrays of soft sensors, with collections of strain-isolated, chip-scale components for data storage, processing, and RF transmission. Here, replacing the fluids with ultralow-modulus elastomers may capture some of the favorable mechanics and also eliminate the potential for leakage. Areas of potential use range from physiological status monitoring in neo-natal intensive care units to continuous assessment of responses to pharmaceuticals administered in the home, where existing technologies exert undue stresses and levels of discomfort on the patient. These directions—especially when pursued by using recent advances in power-efficient radios (24–26), wireless energy transfer schemes (27–29) and functional microfluidics (14–16)—have potentially broad implications for the future of body-integrated electronics.

References and Notes

1. D. H. Kim et al., Science 333, 838–843 (2011).
2. J.-W. Jeong et al., Adv. Mater. 25, 6839–6846 (2013).
3. M. Kaltenbrunner et al., Nature 499, 458–463 (2013).
4. M. S. White et al., Nat. Photonics 7, 811–816 (2013).
5. M. S. Mannoor et al., Nat. Commun. 3, 763 (2012).
6. J. A. Rogers, M. G. Lagally, R. G. Nuzzo, Nature 477, 45–53 (2011).
7. C. F. Pan et al., Nat. Photonics 7, 752–758 (2013).
8. C. Wang et al., Nat. Mater. 12, 899–904 (2013).
9. S. C. B. Mannsfeld et al., Nat. Mater. 9, 859–864 (2010).
10. D. J. Lipomi et al., Nat. Nanotechnol. 6, 788–792 (2011).
11. T. Sekitani, T. Someya, MRS Bull. 37, 236–245 (2012).
12. G. Schwartz et al., Nat. Commun. 4, 1859 (2013).
13. C. Keplinger et al., Science 341, 984–987 (2013).
14. M. Kubo et al., Adv. Mater. 22, 2749–2752 (2010).
15. E. Palleau, S. Reece, S. C. Desai, M. E. Smith, M. D. Dickey, Adv. Mater. 25, 1589–1592 (2013).
16. D. M. Vogt, Y. L. Park, R. J. Wood, IEEE Sens. J. 13, 4056–4064 (2013).
17. S. Wagner, S. Bauer, MRS Bull. 37, 207–213 (2012).
18. T. Sterken et al., Conf. Proc. IEEE Eng. Med. Biol. Soc. 2011, 6886–6889 (2011).
19. F. Axisa et al., Conf. Proc. IEEE Eng. Med. Biol. Soc. 2011, 5687–5690 (2007).
20. M. Gonzalez et al., Microelectron. Reliab. 51, 1069–1076 (2011).
21. H. Vandeparre, Q. Liu, I. R. Minev, Z. Suo, S. P. Lacour, Adv. Mater. 25, 3117–3121 (2013).
22. A. Romeo, Q. H. Liu, Z. G. Suo, S. P. Lacour, Appl. Phys. Lett. 102, 131904 (2013).
23. S. P. Lacour, S. Wagner, R. J. Narayan, T. Li, Z. G. Suo, J. Appl. Phys. 100, 014913 (2006).
24. Y. Lee, B. Giridhar, Z. Foo, D. Sylvester, D. B. Blaauw, IEEE J. Solid-State Circuits 48, 2511–2521 (2013).
25. Y. Lee et al., IEEE J. Solid-State Circuits 48, 229–243 (2013).
26. Y. Sun, H. Luo, S. K. Das, IEEE Trans. Depend. Secure Comput. 9, 785–797 (2012).
27. E. Y. Chow, M. M. Morris, P. P. Irazoqui, IEEE Microw. Mag. 14, 64–73 (2013).
28. S. Kim, J. S. Ho, A. S. Y. Poon, Phys. Rev. Lett. 110, 203905 (2013).
29. S. J. Thomas, R. R. Harrison, A. Leonardo, M. S. Reynolds, IEEE Trans. Biomed. Circuit Syst. 6, 424–436 (2012).

Fig. 4. Images and operational data from a multifunctional wireless sensor. (**A**) Optical image with colored dashed boxes and labels to identify the various subsystems. The gray dashed box around the periphery indicates, approximately, the location of bonding of the superstrate. (**B**) Images of the device on the skin in (top) twisted and stretched and (bottom) compressed states. (**C**) EMG acquired from above the left carpi radialis during periodic clenching and relaxing of the fist. (Right) An enlarged view of the EMG for a single clinching motion. (**D**) Acceleration profiles corresponding to walking, with the device mounted on the forearm. The data near the end of this timeframe corresponds to an intentional fall. (**E**) Temperature response to breathing warm air onto the device. The data shown in this figure were collected by use of a small coin cell battery as a source of power.

A Simple Complex on the Verge of Breakdown: Isolation of the Elusive Cyanoformate Ion

Luke J. Murphy,[1] Katherine N. Robertson,[1] Scott G. Harroun,[1] Christa L. Brosseau,[1] Ulrike Werner-Zwanziger,[2] Jani Moilanen,[3] Heikki M. Tuononen,[3]* Jason A. C. Clyburne[1]*

Why does cyanide not react destructively with the proximal iron center at the active site of 1-aminocyclopropane-1-carboxylic acid (ACC) oxidase, an enzyme central to the biosynthesis of ethylene in plants? It has long been postulated that the cyanoformate anion, $[NCCO_2]^-$, forms and then decomposes to carbon dioxide and cyanide during this process. We have now isolated and crystallographically characterized this elusive anion as its tetraphenylphosphonium salt. Theoretical calculations show that cyanoformate has a very weak C–C bond and that it is thermodynamically stable only in low dielectric media. Solution stability studies have substantiated the latter result. We propose that cyanoformate shuttles the potentially toxic cyanide away from the low dielectric active site of ACC oxidase before breaking down in the higher dielectric medium of the cell.

Nature manifests a myriad of efficient strategies to manage and manipulate reactive small molecules—such as water, hydrogen peroxide, carbon dioxide, and oxygen—in the sensitive environs of enzyme active sites. The cyanoformate ion, $[NCCO_2]^-$, a complex of carbon dioxide and cyanide, has been implicated in the biosynthesis of ethylene (1, 2), but because it has eluded detection in condensed media, the details of its decomposition have not been elucidated. Ethylene is an important plant hormone that regulates such essential biological processes as fruit ripening (3, 4). Its production is catalyzed by the enzymes 1-aminocyclopropane-1-carboxylic acid (ACC) synthase, which generates ACC, and ACC oxidase, which converts ACC to ethylene, cyanide, and carbon dioxide. A simplified mechanism of the reaction catalyzed by ACC oxidase is provided in Fig. 1. Mechanistic and structural studies strongly support binding of ACC and oxygen to the iron center located in the active site of ACC oxidase. Sequential single-electron transfer from the cofactor, ascorbate, with elimination of water generates an iron(IV)-oxo species, followed by ring-opening of bound ACC to eliminate ethylene and cyanoformate, which then decomposes to CN^- and CO_2. It is not definitively known whether this decomposition occurs at the active site or elsewhere (5). Bicarbonate has been identified as an essential mediator for proton transfer in the process (6–8).

It remains unclear how the iron-containing active site of ACC oxidase is protected from the cyanide by-product, a known deactivating agent of iron-containing enzymes in general and Fe(III) in particular (9). Although the hydrogen cyanide is ultimately metabolized, primarily by β-cyanoalanine synthase to produce the amino acid β-cyanoalanine (10), coordination to the iron center of ACC oxidase would seem likely beforehand. A recent publication by Dilley et al. (11) revealed that ACC oxidase is activated at cyanide concentrations between 0.1 and 1 mM, whereas above 1 mM the cyanide becomes inhibitory. These authors propose that cyanide is bound as a ligand to Fe(II) in ACC oxidase, which then assists ACC binding. It should be noted, vis-à-vis our later discussion, that in most studies cyanide levels are typically determined from the bulk plant material (12, 13) rather than intra- or extracellularly. How then are the higher levels of cyanide removed from the active site of ACC oxidase for safe metabolization? We believe that the generation of cyanoformate, a simple coordination complex of cyanide and CO_2, plays a vital role in this regard.

Surprisingly, much of the fundamental coordination chemistry of CO_2, particularly with regard to small ligands and their corresponding reactivity, has yet to be explored. For example, little is known of the reactions between carbon dioxide and halides or pseudohalides (e.g., OH^-, CN^-, OCN^-, SCN^-, and N_3^-), although this gap can be attributed, at least partially, to the instability of these donor-acceptor complexes. There are only two well-characterized families of halide/pseudo-halide complexes of CO_2, the more common being bicarbonates, species that form numerous materials stabilized through extensive hydrogen bonding (14). The only other known example is fluorocarbonate, $[FCO_2]^-$. This deceptively simple anion, isoelectronic with $[NO_3]^-$, might superficially be predicted to be stable, but it has only recently been prepared, and the fluoride affinity of carbon dioxide was calculated to be –111 kJ mol^{-1}, which "appears to be the lower limit for a reaction" (15).

We began our investigation into the possibility of isolating cyanoformate with a preliminary computational study. Table S6 of the supplementary materials includes a full list of the calculated energies for the association reaction of CO_2 and CN^-. At all the levels of theory employed, the formation of cyanoformate was found to be thermodynamically favored in vacuo. However, the binding energy of CO_2 was even smaller than that of the aforementioned fluorocarbonate ion. With the computations indicating that a thermodynamically stable, albeit very fragile, species could exist, we set out to try to isolate a derivative. We had recently shown that higher-order zincates could be stabilized and isolated from ion-rich media using tetraphenylphosphonium halide salts (16). Using a similar approach, we exposed a concentrated solution of $[PPh_4]CN$ to an atmosphere of CO_2, and colorless crystals immediately precipitated. The solvent was decanted, and the crystals were isolated and characterized using crystallographic and spectroscopic techniques. Solid-state nuclear magnetic resonance (NMR) of both singly labeled $[PPh_4][NC^{13}CO_2]$ and doubly labeled $[PPh_4][N^{13}C^{13}CO_2]$ isotopologs confirmed formation of the complex, with δ($\underline{C}O_2$) = 144.4 parts per million (ppm), consistent with the chemical shift observed for the fluorocarbonate ion, ~142 ppm (15). The bonding between the cyano and carbonyl groups was also confirmed by direct observation of one bond coupling $[^1J_{13C-13C} = 61(\pm4)$ Hz] between the ^{13}C-labeled carboxyl and ^{13}C-labeled cyano fragments, based on the resolved $^{13}CO_2$
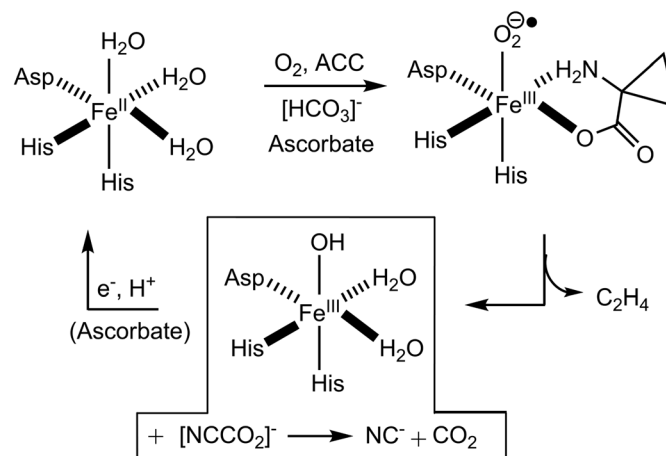
Fig. 1. Simplified reaction scheme for the generation of ethylene, cyanide, and carbon dioxide from ACC, via cyanoformate, at the active site of ACC oxidase.

[1]The Atlantic Centre for Green Chemistry, Department of Chemistry, Saint Mary's University, Halifax, Nova Scotia, B3H 3C3, Canada. [2]Department of Chemistry and Institute for Research in Materials, Dalhousie University, Halifax, Nova Scotia, B3H 4J3, Canada. [3]Department of Chemistry, P.O. Box 35, FI-40014, University of Jyväskylä, Finland.

*Corresponding author. E-mail: jason.clyburne@smu.ca (J.A.C.C.); heikki.m.tuononen@jyu.fi (H.M.T.)

signal in the spectrum of the latter compound (see fig. S19).

Figure 2 shows the structure of [PPh$_4$][NCCO$_2$] as determined by single-crystal x-ray diffraction (see figs. S32 and S33, tables S11 to S17, and the accompanying supplementary discussion for further details). Isolation of the fragile anion in the solid state was likely aided by the crystal lattice stabilization of the salt. The C–C bond in the anion [1.480(9) Å] is equal to that reported by Drück *et al.* (*17*) in the structure of cyanoformamide, NCC(O)NH$_2$. The cyanide C–N bond length [1.056(12) Å] proved to be significantly shorter than that in cyanoformamide [1.141(8) Å]. Investigation of bond lengths reported in the Cambridge Structural Database (CSD) (*18*) showed that the observed cyanide bond length is reasonable, if relatively short, suggesting the presence of a strong CN bond with only a weak C–C interaction to the CO$_2$ portion of the adduct. The strengthening of the CN interaction in the cyanide ligand upon coordination to electron-deficient sites has previously been discussed in the literature (*19*).

The packing of the ions in the structure of [PPh$_4$][NCCO$_2$] in the tetragonal space group $I\bar{4}$ is similar to that observed in many other simple [PPh$_4$]X salts, where X = Br, I, SCN, OCN, N(CN)$_2$, and similar (*20–24*). Viewed down the z axis, the cations and anions form discrete stacked columns. Because of the large size of the cations, the anions can be thought of as occupying the channels formed between the stacked columns of cations. There are few interion interactions in the structure, and those that are present are generally long and presumably weak. Only the interaction

C(2)-H(2)...O(1)' is characterized by a separation of less than 2.5 Å, H(2)…O(1)' = 2.37 Å. The lack of strong interactions between the ions likely results in the relatively free rotation of the anion about the $\bar{4}$ axis in the cavity produced by the parallel stacking of the cations down the z axis.

The theoretically predicted metrical parameters of [NCCO$_2$]$^-$ show very little variation with respect to the employed method and are in good overall agreement with the results from the x-ray structural study, although some small systematic deviations do exist; numeric data are presented in table S4. Heterolytic splitting of the C–C bond in the anion and subsequent analysis of the bonding energy contributions (electrostatic, orbital interactions, and Pauli repulsion) using the Ziegler-Rauk-Morokuma energy-decomposition procedure (*25–27*) show that the linear cyanide and bent carbon dioxide fragments interact predominantly (~90%) through a σ-type donor-acceptor interaction (*28*). Furthermore, the results show that the fragile nature of the adduct arises not so much because of the intrinsic characteristics of the C–C bond but because of the large energy release (~200 kJ mol^{-1}) associated with linearization of the CO$_2$ fragment (*29*). The morphologies of the key frontier orbitals, as well as the results from the analysis of the electron localization function of cyanoformate, are both consistent with the view of cyanide acting as a two-electron donor to carbon dioxide (see figs. S29 and S30 and the accompanying supplementary discussion for full details). Hence, the C–C interaction in [NCCO$_2$]$^-$ is similar to the bonding in adducts of CO$_2$ with N-heterocyclic carbenes (*30–33*), although, to our

knowledge, the latter systems have not been subjected to a thorough theoretical treatment.

Ionic carboxylates exhibit two characteristic C–O stretching bands in their infrared (IR) spectra. The higher-energy asymmetric band ($\nu_{as}CO_2$) typically appears as a very strong and broad band, whereas the lower-energy band (ν_sCO_2) is usually less intense. The spectra collected on samples of [PPh$_4$][NCCO$_2$] (figs. S3 to S5) exhibit both of these expected signals. Consistent with the theoretical predictions for the IR and Raman bands (tables S8 to S10), the cyano stretch (νCN) is not observed in the infrared spectrum but is clearly visible in the Raman (2196 cm^{-1}) (fig. S7). This frequency, when compared with that of other cyano groups, such as in acetonitrile (2253 cm^{-1}) (fig. S6) and [PPh$_4$]CN (2069 cm^{-1}) (fig. S10), supports the notion of a strong CN interaction in [NCCO$_2$]$^-$. We also prepared ^{13}C-labeled samples to confirm our assignments, and these data are included in the supplementary materials.

To visualize the effect of cyanide coordinating to CO$_2$, we have superimposed maps of the electrostatic potential on the total electron density of the reactant and product ions (Fig. 3). These plots aid in the assessment of reactivity, in particular prediction of potential sites of attack for nucleophiles and electrophiles. In CN$^-$, the surface around the carbon atom is electron poor compared with the nitrogen center, but both atoms have electron-rich areas directly on the bond axis, consistent with the two possible coordination modes for this anion. The electrostatic potential of [NCCO$_2$]$^-$ shows that it is now the oxygen centers that are electron rich and therefore the
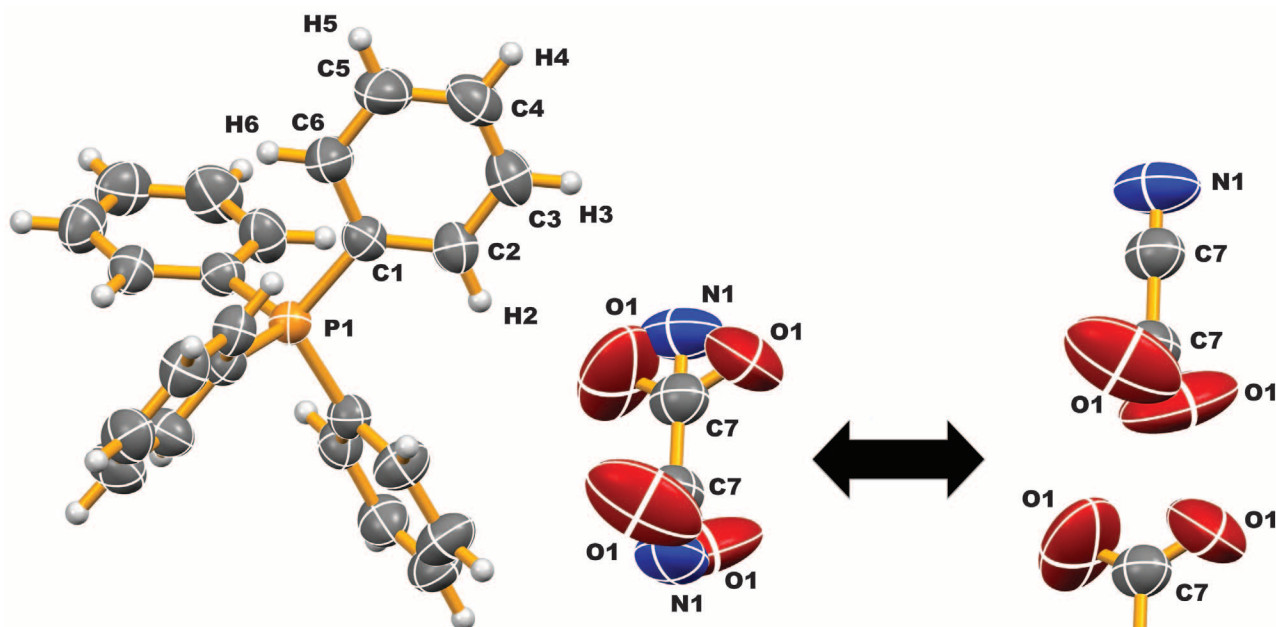
Fig. 2. Solid-state structure of [PPh$_4$][NCCO$_2$]. Thermal ellipsoids are drawn at the 50% probability level. Unique atoms of the cation and all atoms of the anion are labeled. The anion comprises only three unique atoms, carbon and oxygen atoms with site occupancies of 0.50 and nitrogen with a site occupancy of 0.25. The remainder of the anion is generated by symmetry. To the right of the arrow, the anion has been deconvoluted into its two overlapping components, both of which have 50% occupancy in the crystal structure.

most favored sites for electrophilic interactions. This suggests that hydrogen-bond donors and acidic metals will be attracted more favorably to the oxygen atoms rather than to the cyanide portion of the $[NCCO_2]^-$ anion. The delicate interplay of nucleophilic and electrophilic interactions is very important in supporting the many biological reactions involving CO_2 (34), and the chemistry of the cyanoformate anion is no exception in this regard.

We have also calculated the thermodynamics for the formation of cyanoformate as a function of various solvents at different density functional levels of theory (see Fig. 4, fig. S31, table S7, and the accompanying supplementary discussion for full details). The results suggest that $[NCCO_2]^-$ is thermodynamically stable only in nonpolar solvents (toluene); in high-dielectric media, the anion becomes thermodynamically unstable with respect to fragmentation to CN^- and CO_2 (Fig. 4). However, the anion is kinetically stabilized, albeit not by much, in all media because breaking the C–C

bond has an activation barrier of ~40 kJ mol^{-1} at these levels of theory. Although many enzymatic processes occur in bulk water, the local dielectric constant at the active site of an enzyme is typically low (7, 35), in the range of 4 to 20, as compared to 78 for water (36, 37). In the cell, at the low-dielectric active site of the ACC oxidase enzyme, the cyanide ions could remain complexed with CO_2 in the form of $[NCCO_2]^-$, protecting the iron center from attack. However, as the cyanoformate anion migrates out to the bulk aqueous solution of the cytosol, the thermodynamics are modified, and the complex decomposes to the observed products, namely hydrogen cyanide and carbon dioxide.

The pivotal role assigned to the cyanoformate anion, based on its calculated (in)stability in solutions of different dielectric constant, was bolstered by carrying out further decomposition experiments (see the supplementary discussion for full details). Because of the insolubility of $[PPh_4][NCCO_2]$ in many traditional solvents, these studies were

performed on tetrabutylammonium cyanoformate, $[Bu_4N][NCCO_2]$, generated in situ from the cyanide precursor, in the ionic liquid (IL) trihexyl (tetradecyl)phosphonium bis(trifluoromethylsulfonyl)imide, $[P_{66614}][TFSI]$. An aliquot of the $[Bu_4N][NCCO_2]$/IL solution was added to the scrupulously dried solvent being studied, and the disappearance of the $\nu_{as}CO_2$ peak of cyanoformate (1689 cm^{-1}) was monitored using real-time Fourier transform IR (FTIR) spectroscopy. Half-lives were determined from linear regressions of plots of $\ln(P/P_0)$, the ratio of peak height (P) to initial height peak (P_0), versus time (t). Solution half-lives for cyanoformate of 110 min, 55 min, and 17 min were calculated for toluene, tetrahydrofuran, and acetonitrile, respectively. As predicted by theory, the stability of the cyanoformate anion in solution rapidly decreased with increasing dielectric constant of the solution.

Although large-scale experimental studies of the hydrolysis of cyanoformate were not feasible because of the possible release of HCN, the theoretical behavior of the cyanoformate anion in aqueous environments was investigated in more detail by performing geometry optimizations (ωB97X-D/aug-cc-pVTZ level) that included explicit H_2O molecules in addition to the bulk solvent (see the supplementary discussion for full details). In all cases, the calculations minimized to hydrogen-bonded structures (O···H and/or N···H) with no indication of spontaneous hydrolysis. Although a concerted hydrolysis of cyanoformate in water thus seems unlikely, a sequential pathway can be envisioned. As shown computationally, cyanoformate readily dissociates into CN^- and CO_2 in high-dielectric media, and the cyanide anion is an excellent nucleophile that can easily abstract a proton from water (pK_a of HCN = 9.24). The hydroxide ions generated can, in turn, attack the electrophilic carbon of CO_2 to yield the bicarbonate anion. Thus, in an aqueous environment containing dissolved CO_2, the addition of cyanide will lead to the formation of bicarbonate. This is a possible explanation for the observed activation of ACC oxidase by cyanide (11), because bicarbonate is an important participant in the catalytic cycle of the enzyme (6–8).

Our experimental work has clearly shown that cyanoformate is readily converted to bicarbonate (and HCN) in the presence of even a trace of water. Early attempts to isolate the cyanoformate salt often gave crystals of tetraphenylphosphonium bicarbonate, whose structure has been confirmed by crystallographic analysis. In our ^{13}C NMR study, the presence of a peak at 162.3 ppm is certainly attributable to bicarbonate, because the chemical shift correlates well with that reported for other such salts (38). That the bicarbonate originates from the added CO_2 is supported by the large size of this peak relative to others in the same spectrum, because $^{13}CO_2$ was used in the original synthesis. We also probed the decomposition of the synthesized cyanoformate salts in a protic solvent by monitoring the $\nu_{as}CO_2$ stretch of the cyanoformate anion (1689 cm^{-1}) with
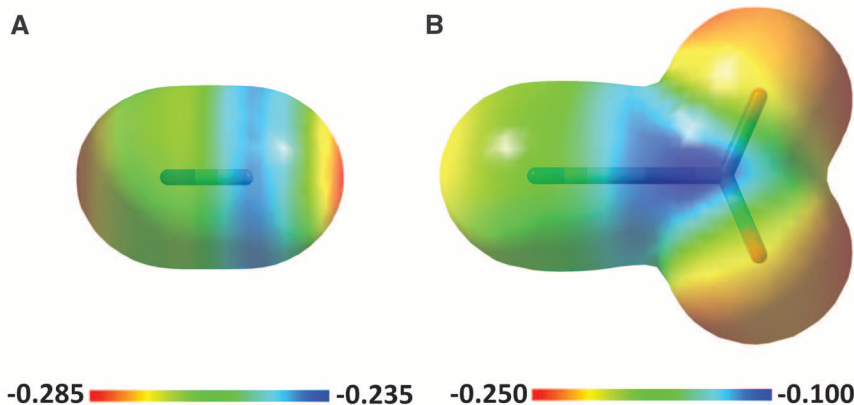
Fig. 3. Electrostatic potentials [atomic units (au)] superimposed on the total electron density isosurface (0.01 au) of (A) CN^- and (B) $[NCCO_2]^-$ at the ωB97X-D/aug-cc-pVTZ level of theory.
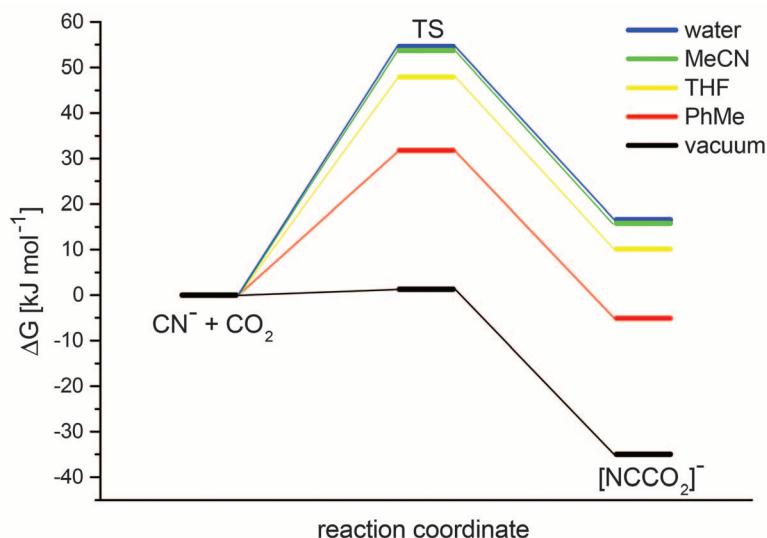
Fig. 4. Calculated reaction profile for the formation of $[NCCO_2]^-$ from CN^- and CO_2 at the ωB97X-D/aug-cc-pVTZ level with different solvent models.

real-time FTIR as 1-propanol was added to a dilute $[Bu_4N][O_2CCN]$/IL solution. This peak rapidly diminished during the addition, while concomitantly a peak corresponding to bicarbonate appeared at 1652 cm^{-1} (39). Over the course of only 2 min, $v_{as}CO_2$ for cyanoformate disappeared completely, while the bicarbonate peak reached a steady absorbance. All of the observed experimental results are entirely consistent with the computationally based proposal of a stepwise process for the decomposition and hydrolysis of the cyanoformate anion.

The stability of cyanoformate, a simple anion of CN$^-$ coordinated to CO_2, has been shown to be dependent on the dielectric constant of its local environment. We propose that this property allows it to shuttle toxic CN$^-$ away from the low-dielectric active site of the enzyme ACC oxidase before its decomposition in higher dielectric media. In broader terms, the ability to manipulate solution stability of otherwise unstable or transient species, through changes to the dielectric constant, should find other important applications.

References and Notes

1. D. Adams, S. F. Yang, *Trends Biochem. Sci.* **6**, 161–164 (1981).
2. G. D. Peiser *et al.*, *Proc. Natl. Acad. Sci. U.S.A.* **81**, 3059–3063 (1984).
3. H. Qiao *et al.*, *Science* **338**, 390–393 (2012).
4. S. P. Burg, E. A. Burg, *Science* **148**, 1190–1196 (1965).
5. N. M. W. Brunhuber, J. L. Mort, R. E. Christoffersen, N. O. Reich, *Biochemistry* **39**, 10730–10738 (2000).
6. M. C. Pirrung, *Acc. Chem. Res.* **32**, 711–718 (1999).
7. A. Bassan, T. Borowski, C. J. Schofield, P. E. M. Siegbahn, *Chem. Eur. J.* **12**, 8835–8846 (2006).
8. L. M. Mirica, J. P. Klinman, *Proc. Natl. Acad. Sci. U.S.A.* **105**, 1814–1819 (2008).
9. S. Shima *et al.*, *Science* **321**, 572–575 (2008).
10. J. M. Miller, E. E. Conn, *Plant Physiol.* **65**, 1199–1202 (1980).
11. D. R. Dilley *et al.*, *AoB Plants* **5**, plt031 (2013).
12. W.-K. Yip, S. F. Yang, *Plant Physiol.* **88**, 473–476 (1988).
13. J. M. Smith, R. N. Arteca, *Physiol. Plant.* **109**, 180–187 (2000).
14. D. Braga *et al.*, *Chem. Eur. J.* **8**, 1173–1180 (2002).
15. X. Zhang, U. Gross, K. Seppelt, *Angew. Chem. Int. Ed. Engl.* **34**, 1858–1860 (1995).
16. I. S. MacIntosh *et al.*, *Organometallics* **29**, 2063–2068 (2010).
17. U. Drück, W. Becker, G. Becker, *Z. Kristallogr.* **167**, 131–134 (1984).
18. F. H. Allen, *Acta Crystallogr. B* **58**, 380–388 (2002).
19. K. F. Purcell, *J. Am. Chem. Soc.* **91**, 3487–3497 (1969).
20. N. W. Alcock, M. Pennington, G. R. Willey, *Acta Crystallogr. C* **41**, 1549–1550 (1985).
21. E. E. Schweizer, C. J. Baldacchini, A. L. Rheingold, *Acta Crystallogr. C* **45**, 1236–1239 (1989).
22. M. Köckerling, J. B. Willems, *Z. Kristallogr., New Cryst. Struct.* **214**, 460 (1999).
23. A. Bernsdorf, M. Köckerling, *Z. Kristallogr., New Cryst. Struct.* **227**, 85–86 (2012).
24. I. Ling, Y. Alias, A. N. Sobolev, C. L. Raston, *Cryst. Eng. Comm.* **12**, 4321–4327 (2010).
25. K. Morokuma, *J. Chem. Phys.* **55**, 1236–1244 (1971).
26. K. Kitaura, K. Morokuma, *Int. J. Quantum Chem.* **10**, 325–340 (1976).
27. T. Ziegler, A. Rauk, *Theor. Chim. Acta* **46**, 1–10 (1977).
28. D. Himmel, I. Krossing, A. Schnepf, *Angew. Chem. Int. Ed.* **53**, 370–374 (2014).
29. I. V. Alabugin, B. Gold, M. Shatruk, K. Kovnir, *Science* **330**, 1047 (2010).
30. H. Zhou, W.-Z. Zhang, C.-H. Liu, J.-P. Qu, X.-B. Lu, *J. Org. Chem.* **73**, 8039–8044 (2008).
31. H. A. Duong, T. N. Tekavec, A. M. Arif, J. Louie, *Chem. Commun.* **2004**, 112–113 (2004).
32. J. D. Holbrey *et al.*, *Chem. Commun.* **2003**, 28–29 (2003).
33. N. Kuhn, M. Steimann, G. Weyers, *Z. Naturforsch. Teil B* **54**, 427–433 (1999).
34. A. M. Appel *et al.*, *Chem. Rev.* **113**, 6621–6658 (2013).
35. M. Shoukry, S. S. Hassan, *Cent. Eur. J. Chem.* **12**, 318–324 (2014).
36. J. J. Dwyer *et al.*, *Biophys. J.* **79**, 1610–1620 (2000).
37. B. E. García-Moreno *et al.*, *Biophys. Chem.* **64**, 211–224 (1997).
38. F. Mani, M. Peruzzini, P. Stoppioni, *Green Chem.* **8**, 995–1000 (2006).
39. F. A. Miller, C. H. Wilkins, *Anal. Chem.* **24**, 1253–1294 (1952).

The Gravity Field and Interior Structure of Enceladus

L. Iess,[1]* D. J. Stevenson,[2] M. Parisi,[1] D. Hemingway,[3] R. A. Jacobson,[4] J. I. Lunine,[5] F. Nimmo,[3] J. W. Armstrong,[4] S. W. Asmar,[4] M. Ducci,[1] P. Tortora[6]

The small and active Saturnian moon Enceladus is one of the primary targets of the Cassini mission. We determined the quadrupole gravity field of Enceladus and its hemispherical asymmetry using Doppler data from three spacecraft flybys. Our results indicate the presence of a negative mass anomaly in the south-polar region, largely compensated by a positive subsurface anomaly compatible with the presence of a regional subsurface sea at depths of 30 to 40 kilometers and extending up to south latitudes of about 50°. The estimated values for the largest quadrupole harmonic coefficients ($10^6 J_2 = 5435.2 \pm 34.9$, $10^6 C_{22} = 1549.8 \pm 15.6$, 1σ) and their ratio ($J_2/C_{22} = 3.51 \pm 0.05$) indicate that the body deviates mildly from hydrostatic equilibrium. The moment of inertia is around $0.335 MR^2$, where M is the mass and R is the radius, suggesting a differentiated body with a low-density core.

After Titan, Enceladus has been the most observed satellite by the Cassini spacecraft during its exploration of the Saturnian system. Images of this small moon (252 km radius) revealed a large plume ejected from the south-polar region, with the source being long fractures from which vapor and ice emerge as discrete jets (1). Concurrent observations of sodium and potassium salts in the plume (2), and the measured temperatures within the fractures (3), strongly argue for the presence of liquid water in the subsurface source region. The plume exhibits a time variability well correlated to the predicted tidal stresses of the body (4).

The endogenic (nonsolar) power emitted from the south-polar region, derived from Cassini Composite Infrared Spectrometer data, is 15.8 GW, with a 20% formal uncertainty (5). This is equivalent to an average surface heat flux of ~20 mW/m^2 and is an order of magnitude larger than conventional estimates of tidal heating if Enceladus' current orbital eccentricity represents a so-called "equilibrium" resonant state with other satellites (6). It indicates time-variability in its internal properties (7), in a resonant state with other nearby moons (8), or in the rate of heat transport. In any or all of these cases, a plausible internal structure is that of a liquid water ocean overlain by a (thermally conductive) crust (5).

The design of the Cassini spacecraft does not allow radio tracking from Earth during remote-sensing observations. Therefore, only 3 of the 19 flybys of Enceladus completed so far have been used for gravity measurements. In these close encounters, the spacecraft was continuously tracked from ground antennas while flying within 100 km of the moon's surface, twice above the southern

[1]Dipartimento di Ingegneria Meccanica e Aerospaziale, Sapienza Università di Roma, via Eudossiana 18, 00184 Rome, Italy. [2]California Institute of Technology, 150-21 Pasadena, CA 91125, USA. [3]Department of Earth and Planetary Sciences, University of California Santa Cruz, 1156 High Street, Santa Cruz, CA 95064, USA. [4]Jet Propulsion Laboratory, California Institute of Technology, 4800 Oak Grove Drive, Pasadena, CA 91109, USA. [5]Department of Astronomy, Cornell University, Ithaca, NY 14850, USA. [6]Dipartimento di Ingegneria Industriale, Università di Bologna, I-47121 Forlì, Italy.

*Corresponding author. E-mail: luciano.iess@uniroma1.it

hemisphere (in the flybys labeled E9 and E19) and once over the northern hemisphere (E12) (9). We determined Enceladus' quadrupole gravity field and degree-3 zonal harmonic coefficient J_3 from measurements of spacecraft range-rate. With a radius ~10 times smaller than that of Titan, and about the same density, the gravitational signature of Enceladus in Doppler measurements is much weaker than that of Saturn's largest moon. However, the small perturbation due to J_3 (about 0.2 to 0.3 mm/s) is still clearly detectable by the Cassini tracking system, whose accuracy is 0.02 to 0.09 mm/s on a time scale of $\tau \approx 60$ s.

Microwave links between the onboard transponder and ground stations of NASA's Deep Space Network enabled precise measurements of the spacecraft range-rate. In addition to gravitational forces, our analysis accounts for the main nongravitational accelerations, most notably neutral particle drag exerted by the substantial gas plume formed by the jets of the south-polar region. Flying by the moon at latitudes below –70°, the spacecraft interacts with the plume at distances of up to 500 km from Enceladus' surface, although most of the effect is localized within 20 s from closest approach. Given the uncertainties in the gas density along the spacecraft flight path, and the short time scale of the interaction, the effect of the drag can be modeled as an unknown, impulsive, vectorial acceleration at closest approach at E9 and E19 (9). The orbital solutions yielded a velocity variation almost parallel to the spacecraft velocity, as expected for a drag force, of magnitude 0.25 mm/s for E9 and 0.26 mm/s for E19, which are comparable with the J_3 signature. The inclusion of the neutral particle drag in the south-polar flybys is therefore essential for obtaining Doppler residuals free of any signatures, which is essential for a faithful gravity solution.

As in previous Cassini gravity analyses (10, 11), the solution for Enceladus' gravity field (labeled as SOL1 in Table 1) was obtained from a multiple-arc analysis in which all data from the three flybys were fitted by using separate initial conditions for the spacecraft state vector at each arc (local parameters). The Enceladus state vector, the five degree-2 harmonic coefficients, and J_3 were considered global parameters common to all arcs. To avoid biased estimates, the a priori uncertainties on the gravity coefficients were at least 30 times larger than were the formal uncertainties obtained from the orbital solution. The nongravitational accelerations due to anisotropic thermal emission from the three radioisotope thermoelectric generators and solar radiation pressure were modeled by using values determined by the spacecraft navigation team from the past 8 years of the Saturn tour. By processing the data into a multiple-arc least-squares filter, we were able to estimate local and global parameters (Table 1). Furthermore, the solution was proven to be stable with respect to perturbations of the dynamical model, such as the estimation of a full degree-3 field (9).

The ratio J_2/C_{22} differs from the value required for hydrostatic equilibrium ($J_2/C_{22} = 10/3$), suggesting that the satellite is not in a fully relaxed shape. The equipotential surface of the tidal, rotational, and gravitational potential (the latter limited to 2,0 and 2,2 harmonics) has semiaxis differences of a-c = 6.00 km and b-c = 2.07 km. The tesseral coefficients C_{21}, S_{21}, and S_{22} are null within 3σ, indicating that the adopted rotational model (9) is correct and that the orientation of the principal axes is that expected for a tidally locked body with a fully damped pole. The estimated value of J_3 implies a 2.5 mGal, negative gravity anomaly at the south pole (Fig. 1).

The interpretation of Enceladus gravity presents a greater difficulty and uncertainty than usual, given the strikingly different appearances of the northern and southern hemisphere and the apparent confinement of endogenic activity to the high southern latitudes. Still, the deviation of J_2/C_{22} from 10/3 (the value for a laterally homogeneous body) is modest (of order 5%) and the non–degree-2 gravity is small (of order 2% relative to J_2), suggesting that there is some prospect of useful inferences.

The topography of Enceladus (12) is not that of a relaxed hydrostatic body under the action of tides and rotation in a synchronous orbit. Comparisons of the geoid heights with actual topography for the largest harmonics show differences of up to 1.2 km (Table 2).
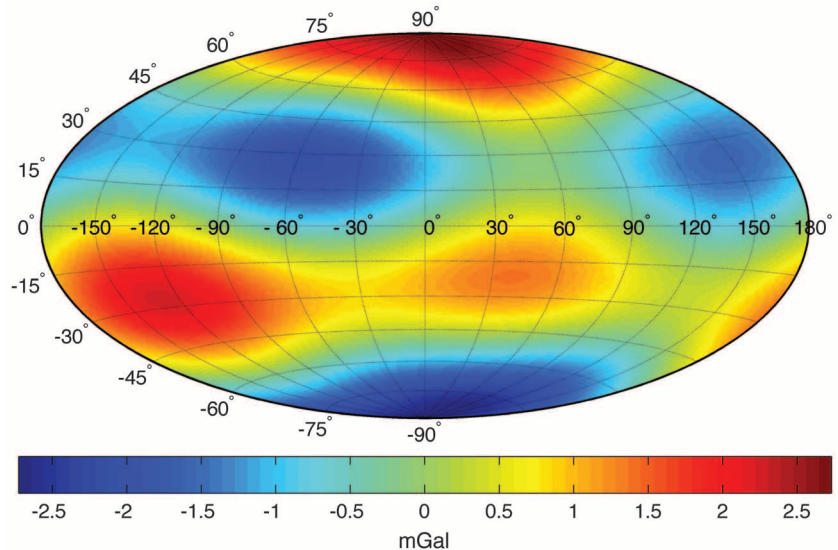
Fig. 1. Enceladus's gravity disturbances. The gravity field due to C21, S21, S22, and J3 (SOL1) is mapped onto the reference ellipsoid. The negative anomaly at the south pole, representing the asymmetry between the two hemispheres, is ~2.5 mGal.

Table 1. Solution for the gravity field of Enceladus. Estimated gravity harmonic coefficients from the multiarc fit of E9, E12, and E19 Doppler data.

Coefficient	SOL 1 Central value ± 1σ
J_2 (×10⁶)	5435.2 ± 34.9
C_{21} (×10⁶)	9.2 ± 11.6
S_{21} (×10⁶)	39.8 ± 22.4
C_{22} (×10⁶)	1549.8 ± 15.6
S_{22} (×10⁶)	22.6 ± 7.4
J_3 (×10⁶)	−115.3 ± 22.9
J_2/C_{22}	3.51 ± 0.05

Table 2. Comparison between Enceladus's geoid heights and actual topography. The existing differences for statistically nonzero harmonic coefficients result in contributions to Enceladus' gravity harmonics.

Harmonic	Topography* (km)	Equipotential height† (km)	Difference Δh (km)	Contribution of difference to gravity harmonics‡ (×10⁶)
$-C_{20}$ (or J_2)	3.85 ± 0.02	2.680 ± 0.010	1.17 ± 0.03	1606 f_{20}
C_{22}	0.92 ± 0.02	0.780 ± 0.007	0.13 ± 0.03	183 f_{22}
$-C_{30}$ (or J_3)	−0.38 ± 0.01	−0.030 ± 0.003	−0.35 ± 0.01	−349 f_{30}

*From (12), 2σ error bars.   †From Table 1, 2σ error bars (9).   ‡The geoid-to-topography ratio (GTR) for uncompensated topographic relief is $3\rho_c/(2l + 1)\bar{\rho}$ for degree l, where ρ_c is the crustal density (~0.93 g/cm³ is assumed) and $\bar{\rho}$ is the mean density (1.61 g/cm³), so GTR ($l = 2$) ≅ 0.35, and GTR ($l = 3$) ≅ 0.25. Here, f is the factor (different for each harmonics) by which the gravity due to the excess topography is compensated by a mass deficit or excess beneath the surface. For Airy compensation, $f = 1 - (1 - d/R)^l$, where d is depth of compensation, R = 252 km, and l is harmonic degree. The entries in the final column are given by Δh *GTR* f/(252km).

Either J_2 and C_{22} are fortuitously close to having ratio 10/3, or the nonhydrostatic contributions are small because of compensation (f is small). The degree-3 gravity, uncontaminated by tides and rotation, provides an estimate: $f_{30} \cong 115.3/349 \cong 0.33$, implying an Airy depth of compensation of ~32 km. This would in turn imply $f_{20} \cong 0.23$ (and f_{22} should equal f_{20} if compensation is isotropic); hence, the part of C_{22} arising from the topographic excess is ~43×10^{-6}. Assuming that the hydrostatic contribution to this harmonic is then the remainder, 1507×10^{-6}, we infer that the most likely moment of inertia (MOI) of Enceladus is $0.336MR^2$, where M is the mass and R is the radius (9). If we choose the value of $f_{20} = f_{22}$ such that the hydrostatic part of J_2 is exactly 10/3 the hydrostatic part of C_{22}, we obtain $f \cong 0.27$, implying a depth of compensation of ~37 km and a moment of inertia of ~$0.335MR^2$.

If we instead use an iterative approach to self-consistently separate the hydrostatic and non-hydrostatic parts of both gravity and topography [(9), section S3.5], we obtain converging estimates of f_{20} and f_{22} (~0.25) when the moment of inertia is $0.335MR^2$, suggesting a compensation depth of ~34 km. The convergent $f_{20} = f_{22}$ is close to the value predicted on the basis of the observed f_{30}, confirming that the assumption of isotropic compensation is reasonable.

When we included elastic flexure as a means of supporting topography in our model, we found that in order to be consistent with the observed gravity-to-topography ratios, the elastic thickness must be less than 0.5 km, a value consistent with other estimates made from flexural analysis (13) and relaxation studies (14).

Results in this MOI range are compatible with a differentiated structure (15). For example, a value of $0.335MR^2$ can arise from a model with a relatively low core density of ~2.4 g/cm^3 and a H$_2$O mantle of density of 1 g/cm^3 and thickness of 60 km (9). The high heat flow and plume activity strongly suggests a differentiated structure, which is compatible with these results.

The data imply a great deal of compensation; if our assumption of Airy isostasy is correct, the inferred compensation depth of 30 to 40 km is most simply explained as the thickness of the ice shell overlying a liquid water layer. The large compensation excludes a very different kind of model, in which the main effect is the tidal and rotational response of a body with a nonradial symmetry of material properties. The tidal and rotational response of a body with a degree-1 variation in properties could introduce topography and gravity at degree 3, an example of mode coupling (16); but if this were responsible for the topographic distortion, then it would predict a much larger gravity distortion than is observed (yielding $f \sim 1$ instead of the observed much smaller values). For the same reason, a frozen-in tidal and rotational bulge from an earlier epoch (17) will not explain the observed gravity if that bulge has persisted in the ice mantle. A frozen-in deformation of the core (18) could in

principle explain the gravity, but the topography would still have to be highly compensated.

The presence of at least a regional south polar subcrustal sea suggests a model in which the mean temperature of the ice beneath the south pole is warmer than elsewhere, perhaps leading to a lower mean density of ~1% (corresponding to 100 K temperature excess and a coefficient of thermal expansion of ~10^{-4} K^{-1}). But to satisfy the observed gravity, it is then necessary to insert a region of higher-density material roughly twice as large as that needed to offset the topographic depression alone and at a depth at least as great as the previous compensation depth estimates. If this material is water and is 8% denser than the surrounding ice, then a layer ~10 km thick is required, diminishing in thickness toward the lower southern latitudes. The total hydrostatic pressure at the base of this region would be in balance with the pressure at the same depth, plausibly at or near the base of the ice shell, in adjacent non–south polar regions that lack water, thus reducing the tendency for this layer to spread laterally. A highly concentrated mass anomaly at the south pole would predict $J_3 = -J_{2,nh}$. The data (Table 2) suggest $J_3 \sim -0.35J_{2,nh}$, and this could be explained by a mass anomaly that extends from the pole to roughly 50° south latitude (9). However, the limitations of the data preclude high confidence in this inference.

Although the gravity data cannot rule out a global ocean, a regional sea is consistent with the gravity, topography, and high local heat fluxes (19) and does not suffer from the thermal problems that a global ocean encounters (19, 20). A global ocean would yield larger and potentially detectable longitudinal librations than are predicted for a solid body (21). The gravity coefficients and inferred MOI of Enceladus are not consistent with a forced 4:1 secondary libration (17, 22) at the 2σ level (9).

References and Notes

1. J. N. Spitale, C. C. Porco, *Nature* **449**, 695–697 (2007).
2. F. Postberg, J. Schmidt, J. Hillier, S. Kempf, R. Srama, *Nature* **474**, 620–622 (2011).
3. J. R. Spencer *et al.*, *Science* **311**, 1401–1405 (2006).
4. M. M. Hedman *et al.*, *Nature* **500**, 182–184 (2013).
5. C. J. A. Howett, J. R. Spencer, J. Pearl, M. Segura, *J. Geophys. Res.* **116**, (E3), E03003 (2011).
6. J. Meyer, J. Wisdom, *Icarus* **188**, 535–539 (2007).
7. G. W. Ojakangas, D. J. Stevenson, *Icarus* **66**, 341–358 (1986).
8. K. Zhang, F. Nimmo, *Icarus* **204**, 597–609 (2009).
9. Materials and methods are available as supplementary materials on *Science* Online.
10. L. Iess *et al.*, *Science* **327**, 1367–1369 (2010).
11. L. Iess *et al.*, *Science* **337**, 457–459 (2012).
12. F. Nimmo, B. G. Bills, P. C. Thomas, *J. Geophys. Res.* **116**, E11001 (2011).
13. B. Giese *et al.*, *Geophys. Res. Lett.* **35**, L24204 (2008).
14. M. T. Bland, K. N. Singer, W. B. McKinnon, P. M. Schenk, *Geophys. Res. Lett.* **39**, L17204 (2012).
15. G. Schubert, J. D. Anderson, B. J. Travis, J. Palguta, *Icarus* **188**, 345–355 (2007).
16. S. Zhong *et al.*, *J. Geophys. Res.* **39**, L15201 (2012).
17. C. C. Porco *et al.*, *Science* **311**, 1393–1401 (2006).
18. W. B. McKinnon, *J. Geophys. Res.* **118**, 1775 (2013).
19. G. Tobie, O. Cadek, C. Sotin, *Icarus* **196**, 642–652 (2008).
20. J. H. Roberts, F. Nimmo, *Icarus* **194**, 675–689 (2008).
21. N. Rambaux, J. C. Castillo-Rogez, J. G. Williams, Ö. Karatekin, *Geophys. Res. Lett.* **37**, L04202 (2010).
22. J. Wisdom, *Astron. J.* **128**, 484–491 (2004).

Geophysical and Geochemical Evidence for Deep Temperature Variations Beneath Mid-Ocean Ridges

Colleen A. Dalton,[1]*† Charles H. Langmuir,[2] Allison Gale[2,3]

The temperature and composition of Earth's mantle control fundamental planetary properties, including the vigor of mantle convection and the depths of the ocean basins. Seismic wave velocities, ocean ridge depths, and the composition of mid-ocean ridge basalts can all be used to determine variations in mantle temperature and composition, yet are typically considered in isolation. We show that correlations among these three data sets are consistent with 250°C variation extending to depths >400 kilometers and are inconsistent with variations in mantle composition at constant temperature. Anomalously hot ridge segments are located near hot spots, confirming a deep mantle-plume origin for hot spot volcanism. Chemical heterogeneity may contribute to scatter about the global trend. The coherent temperature signal provides a thermal calibration scale for interpreting seismic velocities located distant from ridges.

Mantle convection controls the evolution of the planet's interior and results in the motion of tectonic plates. The characteristics of this convection are governed by the density and viscosity of the mantle, which are functions of both temperature and composition.

Two sets of observations that can constrain these properties are the velocity of seismic shear waves (V_S) and the geochemistry of mid-ocean ridge basalts (MORBs). Outstanding controversies about the interpretation of both data sets have historically prevented definitive advances in understanding the relative importance of variations in temperature and composition beneath ridges. V_S can be imaged throughout the entire mantle (1, 2) and is strongly sensitive to temperature (3), poten-

[1]Department of Earth and Environment, Boston University, 685 Commonwealth Avenue, Boston, MA 02215, USA. [2]Department of Earth and Planetary Sciences, Harvard University, 20 Oxford Street, Cambridge, MA 02138, USA. [3]Department of Plant and Earth Science, University of Wisconsin, River Falls, 410 South 3rd Street, River Falls, WI 54022, USA.

*Corresponding author. E-mail: colleen_dalton@brown.edu
†Present address: Department of Geological Sciences, Brown University, 324 Brook Street, Box 1846, Providence, RI 02912, USA.

tially providing critical constraints on global temperature variations. However, factors other than temperature, including composition (4), partial melt (5), volatiles (6), and anelasticity (3), also affect V_S, producing large discrepancies in estimates of upper-mantle temperature (3, 7, 8). Early studies of global variations in the depth of ocean ridges and the major-element composition of MORBs indicated temperature variations of 220° ± 40°C beneath ridges to mantle depths >200 km (9, 10). Yet subsequent studies have emphasized the importance of mantle composition (11, 12) and melt-transfer processes (13, 14) in these data sets and inferred smaller temperature variations (50° to 60°C).

To overcome the limitations associated with each data set, the seismological, petrological, and bathymetric data sets can be jointly analyzed (15). Earlier attempts to compare seismic models and ridge observations, using 34 global locations (16)

or 39 locations along the Mid-Atlantic Ridge (MAR) (17), identified correlations only for mantle depths <200 km and inferred along-ridge temperature variations that were confined to the shallow mantle. The correlations at lithospheric depths, however, must be approached with caution, because the lateral averaging inherent in seismic models introduces an artificial spreading-rate dependence into V_S at shallow depths due to thicker lithosphere near the ridges at slow spreading rates. This issue, when considered together with the lack of correlation at depths >200 km, casts doubt on the conclusion reached by these studies that temperature plays an important role.

We performed a comprehensive global comparison of variations in V_S beneath ridges, axial ridge depth (D_R), and MORB chemistry. To facilitate comparison between the geophysical and geochemical observations, we examined variations at the scale of discrete ridge segments. Individual

Fig. 1. Comparison of ridge observations and V_S. (**A**) Black symbols: D_R and V_S (1) at 300 km depth beneath the ridge for 242 nodes evenly spaced along the six longest ridge systems: the Mid-Atlantic Ridge (MAR), Southwest Indian Ridge (SWIR), Central Indian Ridge (CIR), Southeast Indian Ridge (SEIR), Pacific-Antarctic Ridge (PAR), and East Pacific Rise (EPR). D_R for each node was calculated from a weighted average of the mean depths of nearby segments within a 550-km radius. Colored circles and squares: predictions for variable T_P for Z_{CD} = 300 km and 400 km. V_S was calculated using (3), with grain size = 2 cm. Colored triangles: predictions for variable composition for Z_{CD} = 300 km and 400 km at T_P = 1350°C and 1450°C. Elastic V_S was calculated using Perple_X (21) and the thermodynamic database of (28). (**B**) Correlation coefficient r with V_S. Blue lines: correlation with Na_{90} in 225 segments. Red lines: correlation with 584 raw D_R values. Green lines: correlation with 242 smoothed D_R values. Dashed lines: only D_R values 1 to 4 km or Na_{90} > 1.8 are used. Thin horizontal dashed line: value of r that can be resolved from zero at significance level = 0.001 (196 degrees of freedom). Solid black line: negative correlation between V_S and spreading rate (29). (**C**) Comparison of observed and predicted relationships between Na_{90} and V_S at 300 km depth for temperature variations (colored symbols) and variations in mantle composition at temperatures of 1350°C and 1450°C (black symbols). Na_{90} was predicted using (10). V_S prediction is described in (A).

Fig. 2. Observed D_R and V_S at 300 km. (**A**) Segments located <10° (1100 km) from the Marion and Azores hot spots color-coded by distance from those hot spots. Solid black lines: best-fitting lines. Dashed black lines: best-fitting lines for St. Paul and Iceland from (B). (**B**) As in (A) but for the St. Paul, Iceland, and Bouvet hot spots.

segments at the level of approximately second-order segmentation features (*18*) were identified using multi-resolution bathymetry in GeoMapApp (www.geomapapp.org), yielding 771 ridge segments totaling 60,864 km in length (fig. S1A). Geochemical variations along the ridge were obtained from a global data set of major- and trace-element concentrations for 16,694 MORB samples (*19*) that were corrected for low-pressure fractionation (see the supplementary materials and fig. S1B). Isotropic V_S along the ridges was sampled from the S40RTS model (*1*) at 242 nodes evenly spaced along the six longest ridge systems (fig. S1C).

The data show a strong correlation between D_R and V_S in the mantle beneath the ridge globally (Fig. 1A). The correlation coefficient is >0.6 at depths of 200 to 550 km, with a maximum at 325 km (Fig. 1B). This correlation is not dominated by the end-member points; Fig. 1B provides correlation coefficients calculated using only D_R values of 1 to 4 km. Comparison of V_S and Na_{90}, performed for the entire fractionation-corrected data set excluding back-arc spreading centers, also reveals a statistically significant correlation (Fig. 1C and fig. S23). This correlation is strongest at 225 km and is >0.4 for mantle depths of 150 to 450 km. Other compositional parameters, including Ca_{90}/Al_{90} and Fe_{90}, also co-vary with V_S, D_R, and Na_{90} (figs. S16 to S21). We focus on depths >200 km to avoid artifacts related to the spreading-rate dependence of V_S (Fig. 1B and supplementary text S2).

The robust correlations in Fig. 1 suggest that long-wavelength variations in D_R, V_S, and MORB composition are controlled by a common mech-
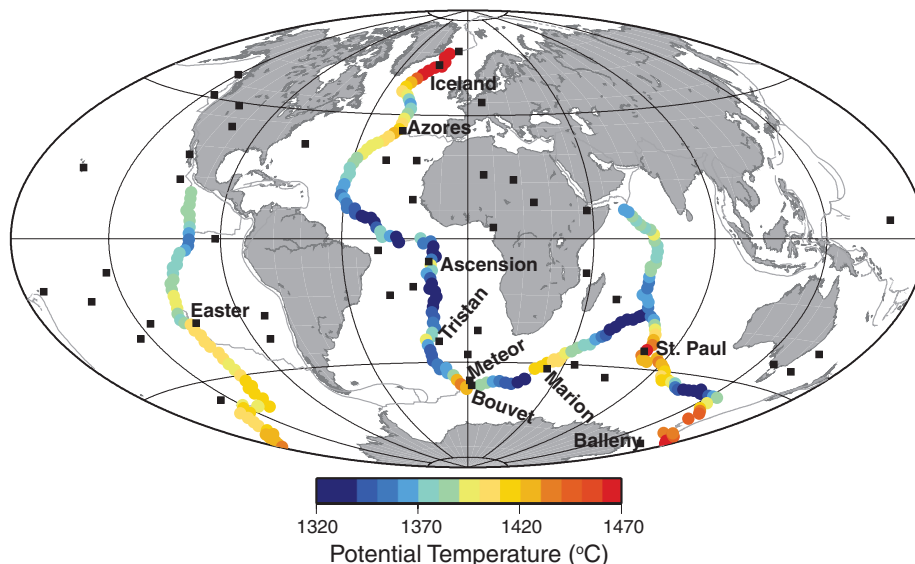
Fig. 3. Along-ridge variation in T_P. Averages of T_P estimated separately from D_R and V_S at 300 km are shown. Temperature differs by <20°C from these averaged T_P values for 82% of locations when estimated from D_R alone and for 93% of locations when estimated from V_S alone. Shallow D_R values near Azores and Marion give the illusion of slightly elevated temperatures, which is inconsistent with the mantle V_S values (Fig. 2A). Black squares: hot spots from (*30*) plus St. Paul/Amsterdam. Hot spots mentioned in the text are labeled.

anism. Furthermore, the depth extent of the correlations (>400 km) is much greater than previously recognized. Earlier studies, for which significant correlations were found only at depths <200 km, suffered from limited sampling [(*16*, *17*) fig. S1B] and the use of low-resolution seismic models. When modern seismic models are used, the correlations at shallow depths identified by (*16*, *17*)

vanish, and strong correlations at depths >200 km emerge (figs. S10 and S11).

We consider two end-member explanations for the new observations: (i) mantle temperature variations at constant composition and (ii) mantle compositional variations at constant temperature. The likely origin of large-scale variations in mantle composition is the extraction of basalt at ocean

ridges and preferential recycling of basalt through subduction; mantle compositional variations are therefore modeled on this basis. For prediction of V_S and D_R, each ridge segment is treated as an isostatically balanced column containing four layers: water, crust, residual mantle, and fertile mantle. Each column is characterized by a mantle potential temperature (T_P) and composition that extend from the Moho to the isostatic compensation depth (Z_{CD}). Overburden pressure at Z_{CD} is assumed to be constant for all columns, allowing water-layer thickness to be determined (supplementary text S4 and figs. S13 and S14). Petrological modeling was performed using MELTS (20) and the approach of (10), and V_S was predicted using (3) for temperature variations and (21) for compositional variations (supplementary text S5 and S6).

We find that the observed global variations in V_S, D_R, and MORB chemistry are consistent with 200° to 250°C variation in mantle T_P, extending to 300 to 400 km (Fig. 1, A and C). Predicted D_R, V_S, and Na_{90} all vary inversely with T_P. Shallow ridges at high temperatures reflect the combined effects of thicker ocean crust and less-dense mantle. Petrological modeling of Fe_{90}, Na_{90}, and Ca_{90}/Al_{90} indicates a temperature range of 1300° to 1550°C, showing a remarkable consistency for temperature estimates from the three independent methods (supplementary text S6 and figs. S16 and S17).

In contrast, mantle compositional variations produced by linear mixing of basalt and peridotite predict flat relationships between V_S and D_R and V_S and Na_{90} that are inconsistent with the positive trend of the observations (Fig. 1), and also predict relationships between Na_{90}-Fe_{90} and Ca_{90}/Al_{90}-Fe_{90} and Fe_{90}-D_R (figs. S16 to S20) that are not consistent with the dominant trend of the observations.

Although the principal component of variation is consistent with mantle temperature variations, compositional variations produce trends orthogonal to the principal correlations and should explain some of the scatter about the global trend. For example, ridge segments near the Azores and Marion hot spots have large variations in D_R at nearly constant V_S (Fig. 2A). This flat relationship between D_R and V_S is consistent with a compositional origin for the Azores and Marion rises (22). Depleted peridotite in the underlying mantle provides a source of buoyancy that elevates the ridge segments. This conclusion is further supported by the distinctly low Fe_{90} of the Azores ridge segments (23), which indicates a depleted source. For other hot spots, such as Iceland, Bouvet, and St. Paul, V_S and D_R increase with distance from the hot spot along lines oriented subparallel to the global trend (Fig. 2B and figs. S24 to S29). The offset of these three trends indicates that a factor in addition to mantle temperature must influence D_R or V_S, but with existing geochemical data it is not clear whether the offsets are produced by changes in mantle composition.

The temperature calibration in Fig. 1A allows T_P along the entire ridge system to be estimated (Fig. 3). Excluding segments with $D_R < 1$ km, the global range of T_P is 1314° to 1464°C, with 1355°C and 1408°C as the first and third quartile. High T_P values in the Atlantic and Indian basins are located near hot spots, especially when considered relative to the regional background value. Locations near the Iceland, Ascension, Tristan, Meteor, Bouvet, St. Paul, and Balleny hot spots are characterized by temperatures 30° to 60°C above the regional background temperature. These are large-scale regional averages; temperatures immediately beneath the hot spots may be much higher. The fact that the warm ridge segments are all located near known hot spots lends strong support to the hypothesis that volcanism at these hot spots is caused by mantle plumes originating in the transition zone or lower mantle (24). Detection of plumes with global tomography suggests that plume material may be deflected horizontally at sublithospheric depths, thus distributing the thermal anomaly over a broad area surrounding the conduit (2). The global range of temperature variations is reduced to 100° to 150°C when only ridge segments located >700 km from hot spots are considered (fig. S8). We find no temperature anomaly associated with the Azores and Marion hot spots, nor with the Easter hot spot in the Pacific basin, where high spreading rates along the East Pacific Rise may readily mix plume and ambient mantle.

Low temperatures are found at 105° to 135°E along the Southeast Indian Ridge (SEIR), overlapping with the Australian-Antarctic Discordance, where seismic studies (25, 26) have imaged high velocities that have been attributed to a convective downwelling in the mantle (27). The two other low-temperature zones identified here—2° to 30°S along the MAR and 55° to 80°E along the Southwest Indian Ridge (SWIR)—are characterized by high V_S values >4.7 km/s at 300 km depth and may indicate additional colder regions occupying the upper mantle.

This study demonstrates that the global long-wavelength variations in the surface expression of mid-ocean ridges—bathymetry and MORB major-element composition—are governed primarily by the temperature of the mantle extending several hundreds of kilometers below the surface. The scatter about the global trend may originate from major-element heterogeneity in the mantle; from imperfections and incompleteness in the petrological and seismological data sets; or from complexities that we have not considered, including volatiles in the mantle, melt-transfer processes, dynamic topography, and buoyancy-driven flow. The principal finding reported here is the consistency of temperatures estimated from V_S, D_R, and MORB compositions, which provides a uniform calibration of mantle temperature that could be applied to V_S worldwide. Although composition or partial melt may influence V_S in certain regions, much of the global seismic-velocity signal in regions distant from ocean ridges probably reflects variations in upper-mantle potential temperature.

References and Notes

1. J. Ritsema, A. Deuss, H. J. van Heijst, J. H. Woodhouse, *Geophys. J. Int.* **184**, 1223–1236 (2011).
2. S. French, V. Lekic, B. Romanowicz, *Science* **342**, 227–230 (2013).
3. U. H. Faul, I. Jackson, *Earth Planet. Sci. Lett.* **234**, 119–134 (2005).
4. C.-T. Lee, *J. Geophys. Res.* **108**, JB002413 (2003).
5. W. C. Hammond, E. D. Humphreys, *J. Geophys. Res.* **105**, 10975–10986 (2000).
6. S. Karato, H. Jung, *Earth Planet. Sci. Lett.* **157**, 193–207 (1998).
7. K. Priestley, D. McKenzie, *Earth Planet. Sci. Lett.* **244**, 285–301 (2006).
8. Y. Yang, D. W. Forsyth, D. S. Weeraratne, *Earth Planet. Sci. Lett.* **258**, 260–268 (2007).
9. E. M. Klein, C. H. Langmuir, *J. Geophys. Res.* **92**, 8089–8115 (1987).
10. C. H. Langmuir, E. M. Klein, T. Plank, in *Mantle Flow and Melt Generation at Mid-Ocean Ridge* (American Geophysical Union, Washington, DC, 1992), pp. 183–280.
11. Y. Shen, D. W. Forsyth, *J. Geophys. Res.* **100**, 2211–2237 (1995).
12. Y. Niu, M. J. O'Hara, *J. Petrol.* **49**, 633–664 (2008).
13. M. L. Collier, P. B. Kelemen, *J. Petrol.* **51**, 1913–1940 (2010).
14. J.-I. Kimura, S. Sano, *J. Petrol.* **53**, 1637–1671 (2012).
15. D. A. Wiens, K. A. Kelley, T. Plank, *Earth Planet. Sci. Lett.* **248**, 30–42 (2006).
16. E. Humler, J. L. Thirot, J. P. Montagner, *Nature* **364**, 225–228 (1993).
17. Y.-S. Zhang, T. Tanimoto, E. M. Stolper, *Phys. Earth Planet. Inter.* **84**, 79–93 (1994).
18. K. C. Macdonald *et al.*, *Nature* **335**, 217–225 (1988).
19. A. Gale, C. A. Dalton, C. H. Langmuir, Y. Su, J.-G. Schilling, *Geochem. Geophys. Geosyst.* **14**, 489–518 (2013).
20. P. D. Asimow, M. S. Ghiorso, *Am. Mineral.* **83**, 1127–1131 (1998).
21. J. A. D. Connolly, *Geochem. Geophys. Geosyst.* **10**, GC002540 (2009).
22. H. Zhou, H. J. B. Dick, *Nature* **494**, 195–200 (2013).
23. A. Gale, S. Escrig, E. J. Gier, C. H. Langmuir, S. L. Goldstein, *Geochem. Geophys. Geosyst.* **12**, GC004334 (2011).
24. W. J. Morgan, *Nature* **230**, 42–43 (1971).
25. D. W. Forsyth, R. L. Ehrenbard, S. Chapin, *Earth Planet. Sci. Lett.* **84**, 471–478 (1987).
26. M. H. Ritzwoller, N. M. Shapiro, G. M. Leahy, *J. Geophys. Res.* **108**, JB002522 (2003).
27. M. Gurnis, R. D. Müller, L. Moresi, *Science* **279**, 1499–1504 (1998).
28. W. C. Xu, C. Lithgow-Bertelloni, L. Stixrude, J. Ritsema, *Earth Planet. Sci. Lett.* **275**, 70–79 (2008).
29. C. DeMets, R. G. Gordon, D. F. Argus, S. Stein, *Geophys. Res. Lett.* **21**, 2191–2194 (1994).
30. V. Courtillot, A. Davaille, J. Besse, J. Stock, *Earth Planet. Sci. Lett.* **205**, 295–308 (2003).

Supplementary Materials

www.sciencemag.org/content/344/6179/80/suppl/DC1
Materials and Methods
Supplementary Text
Figs. S1 to S29
Table S1
References (31–38)

A 12-Million-Year Temperature History of the Tropical Pacific Ocean

Yi Ge Zhang,[1]* Mark Pagani,[1] Zhonghui Liu[2]

The appearance of permanent El Niño–like conditions prior to 3 million years ago is founded on sea-surface temperature (SST) reconstructions that show invariant Pacific warm pool temperatures and negligible equatorial zonal temperature gradients. However, only a few SST records are available, and these are potentially compromised by changes in seawater chemistry, diagenesis, and calibration limitations. For this study, we establish new biomarker-SST records and show that the Pacific warm pool was ~4°C warmer 12 million years ago. Both the warm pool and cold tongue slowly cooled toward modern conditions while maintaining a zonal temperature gradient of ~3°C in the late Miocene, which increased during the Plio-Pleistocene. Our results contrast with previous temperature reconstructions that support the supposition of a permanent El Niño–like state.

Temperatures of the low-latitude Pacific Ocean substantially influence regional and global climates. In particular, the El Niño–Southern Oscillation (ENSO) dominates Earth's interannual climate variability. El Niño is initiated by the eastward propagation of warm western Pacific equatorial waters that deepen thermocline depths and attenuate upwelling rates across the eastern equatorial Pacific (EEP) (1, 2). Regional sea-surface temperature (SST) change associated with El Niño affects the position and vigor of the Walker circulation and Hadley cell, leading to substantially reduced equatorial SST gradients, higher global mean temperatures, extratropical heat export, and regional hydrological impacts (1, 2).

The western equatorial Pacific warm pool is among the warmest surface water on Earth, whereas the EEP, known as the cold tongue, is characterized by cold, nutrient-rich waters that result from a shallow thermocline and intense upwelling rates. The modern SST gradient between the warm pool and cold tongue averages 4° to 5°C (3) and varies in response to ENSO. Accordingly, paleo-SST reconstructions from these regions and the resulting character of the east-west temperature gradient have been used to describe broad climate states over the past 5 million years, particularly during the Pliocene epoch [5.3 to 2.6 million years ago (Ma)], when atmospheric CO_2 concentrations appear similar to today (4, 5) and global temperatures are simulated to be 3° to 4°C warmer than preindustrial conditions (6, 7).

Published temperature records based on magnesium-to-calcium ratios (Mg/Ca) of the planktonic foraminifera *Globoritalia sacculifer*, from Ocean Drilling Program (ODP) site 806 (0°N, 159°E) (Fig. 1) (8), suggest that warm pool temperatures remained relatively constant as Earth cooled over the past 5 million years. Curiously, existing Mg/Ca-based SST records also indicate that the Pacific warm pool of the Pliocene warm period (4.5 to 3 Ma) was ~0.5°C colder than the mean temperature of the late Quaternary (1.5 to 0 Ma), implying that warm pool temperatures were cooler or invariant during periods of global warmth. The appearance of invariant tropical temperatures during periods of global warmth implies a "tropical thermostat" (9) in which tropical warming is limited through evaporation or cloud feedbacks irrespective of the greenhouse gas forcing. However, this phenomenon is not supported by climate simulations (10), and much warmer tropical SSTs are evident during "super greenhouse" climate states in Earth history (e.g., the Cretaceous) (11).

In contrast to the western Pacific warm pool, temperature records from the eastern Pacific sites 847 (0°N, 95°W; based on Mg/Ca and the alkenone unsaturation index U^K_{37}) (8, 12) and 846 (3°S, 91°W; based on U^K_{37}) (13) exhibit cooling for the past 5 million years. Consequently, warm pool and cold tongue SSTs result in a negligible equatorial temperature gradient during the early Pliocene (8, 14) similar to those expressed during brief modern El Niño events (8, 14). A nearly absent equatorial temperature gradient is argued to reflect a permanent El Niño–like state prior to 3 million years ago and has been further interpreted to reflect the establishment of a deep thermocline in the EEP, substantially reduced cold-water upwelling (14), an attenuated Walker circulation (7), and negligible ENSO variability (14). In contrast, high-resolution, coral $\delta^{18}O$ records (15) and isotope records of individual planktonic foraminifera from site 846 (16) indicate that the frequency and intensity of Pliocene ENSO-like oscillations were similar to those of today.

The veracity of the permanent El Niño supposition rests on the accuracy of paleotemperature reconstructions. In particular, *G. sacculifer* Mg/Ca-based SST records used to infer invariant warm pool SSTs assume that foraminifera Mg/Ca compositions are uninfluenced by diagenetic alteration or temporal changes in seawater chemistry [e.g., seawater Mg/Ca ratio (Mg/Ca_{sw})] and/or carbonate ion effect; see supplementary materials). However, $\delta^{18}O$ records on the identical samples (8) fail to capture the modern SST gradient (supplementary materials) and suggest the contribution of diagenetic carbonates. In addition, changes in Mg/Ca_{sw} could have lowered Pliocene

[1]Department of Geology and Geophysics, Yale University, New Haven, CT 06511, USA. [2]Department of Earth Sciences, The University of Hong Kong, Hong Kong SAR, China.

*Corresponding author. E-mail: yige.zhang@yale.edu
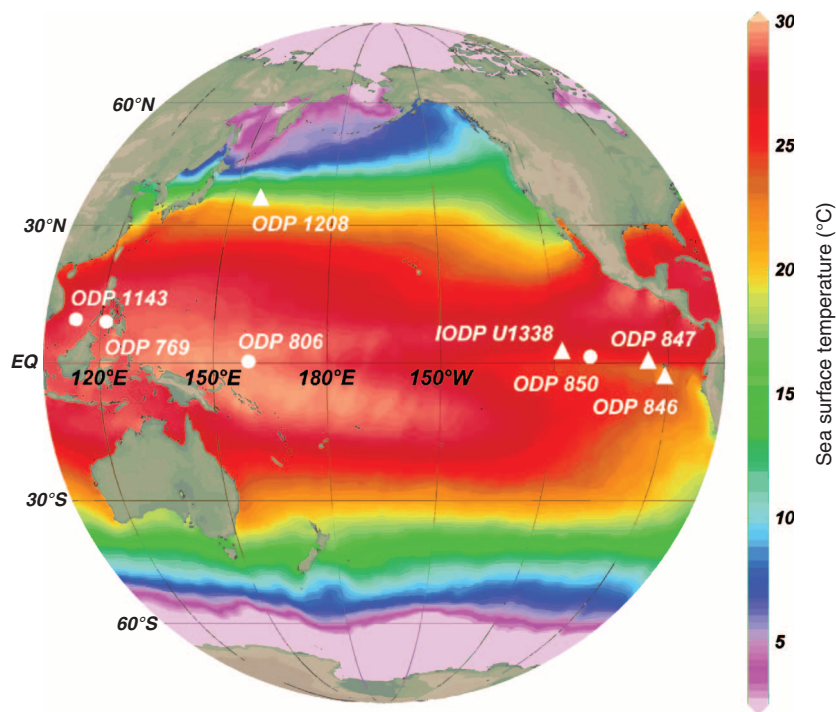
Fig. 1. Pacific sites discussed in this study. Colors represent modern mean annual SSTs. Circles represent sites analyzed in this study: ODP sites 769, 806, 850, and 1143. Triangles represent sites with previously published SSTs: ODP sites 846, 847, and 1208 (36°N, 128°E) and Integrated Ocean Drilling Program (IODP) site U1338 (3°N, 118°W). Map generated by Ocean Data View.

SST estimates because fluid inclusion (*17*) and carbonate veins (*18*) data indicate lower Mg/Ca$_{sw}$ during the Pliocene. Notably, other warm pool temperature records derived from U$_{37}^{K'}$ values (*19*) are limited by the nature of the temperature proxy itself, which reaches a maximum calculable SST value of ~28.5°C (*20*) and thus compromises its capacity to record even higher SSTs (supplementary materials).

In summary, given possible diagenetic overprinting, seawater chemistry changes, and calibration limitations, available SST records likely underestimate maximum warm pool temperatures and potentially distort zonal SST gradient estimates.

For this study, we established new equatorial Pacific SST records using the TEX$_{86}$ temperature proxy. TEX$_{86}$ thermometry is founded on the distribution of the archaeal lipid membranes, glycerol dialkyl glycerol tetraethers, primarily produced by archaea from the phylum *Thaumarchaeota*. *Thaumarchaeota* are aerobic ammonia oxidizers (*21*), raising concerns that the TEX$_{86}$ index can also reflect subsurface temperatures rather than a mixed-layer SST. However, available compound-specific carbon-isotope evidence indicates that the TEX$_{86}$ temperature signal largely derives from the ocean mixed-layer (*22*). Using the current calibration [e.g., (*23*)], TEX$_{86}$ tends to overestimate SSTs in the high latitudes and underestimate temperatures in the low latitudes (*24*). Indeed, TEX$_{86}$ SSTs derived from surface sediments of the tropical Pacific show slightly lower temperature estimates than observed SSTs (see sup-

plementary materials). Nevertheless, the late Pleistocene TEX$_{86}$-derived zonal SST gradient agrees with the modern gradient between sites 806 and 850 (supplementary materials) and broadly captures the temperature characteristics of these distinct regions. Finally, TEX$_{86}$ temperature reconstructions can record much higher SSTs compared to the alkenone proxy (*25*), making it a more suitable proxy to evaluate the evolution of warm pool temperatures.

We reconstruct the history of equatorial Pacific temperature gradients for the past 12 million years using both TEX$_{86}$ and U$_{37}^{K'}$ temperature proxies at ODP sites 769 (9°N, 121°E), 806, and 1143 (9°N, 113°E) in the western warm pool region and site 850 (1°N, 111°W) in the eastern Pacific cold tongue (Fig. 1). Our results illustrate a distinctly different thermal history of the Pacific warm pool compared to previously published records. For example, in contrast to relatively invariant Mg/Ca temperatures from site 806 (Fig. 2), TEX$_{86}$ records from three localities near the center and edge of the modern warm pool unambiguously show ~4°C of cooling since the late Miocene (Fig. 3), with an ~2°C decline since the early Pliocene (Fig. 2). TEX$_{86}$ values from the late Miocene to Pliocene also indicate that warm pool temperatures were almost always higher than the calculable limit of U$_{37}^{K'}$ temperatures until ~3-5 million years ago. Consequently, U$_{37}^{K'}$ temperatures cannot be applied to interpret the temperature history of the warm pool older than ~3 Ma (Figs. 2 and 3).

Cold tongue U$_{37}^{K'}$ temperatures from site 850 in the western portion of the eastern equatorial upwelling region (Fig. 1) compare well with published alkenone records from sites 846 (*13*) and 847 (*12*) over the past 5 million years (Fig. 3). Site U1338 shows comparatively warmer temperatures (*26*), consistent with its location at the edge of the upwelling region (Fig. 1). Both TEX$_{86}$ and U$_{37}^{K'}$ temperature reconstructions in the EEP region indicate that the cold tongue slowly cooled by ~6°C since 12 Ma, with higher cooling rates during the Pliocene and Pleistocene. TEX$_{86}$ and U$_{37}^{K'}$ temperature estimates begin to deviate at about 6 Ma, with TEX$_{86}$ SSTs showing consistently cooler temperatures, readily explained by differential changes in the depth and/or seasonality of production between haptophyte algae (alkenone producers) and archaea (supplementary materials). If changes in production depth are responsible for the temperature offset between these two proxies, production of archaea and haptophytes is still within the top 50 m of the mixed layer given the sharp vertical temperature gradient in the EEP (supplementary materials). Although sites 850 and U1338 represent the warmer edge of the EEP, alkenone values are still below the maximum temperature limit for 12 million years (Fig. 3)—in contrast to U$_{37}^{K'}$ temperatures in the western warm pool—and thus can record the cooling history of the EEP (Fig. 2 and supplementary materials).

We assess the evolution of the east-west equatorial Pacific temperature gradient (ΔT_{zonal}) by interpolating and averaging temperature results using TEX$_{86}$ and U$_{37}^{K'}$ temperature records, and solely using TEX$_{86}$ data (Fig. 4). Integrating all of the available SST data expands the spatial assessment for each region. However, because U$_{37}^{K'}$ is mostly maximized in warm pool samples older than 3 Ma, warm pool temperature reconstructions largely rest on TEX$_{86}$ SST records prior to 3 Ma (Figs. 2 and 3). In contrast, the composite temperature of the cold tongue is dominated by U$_{37}^{K'}$ records (Figs. 2 and 3). At our localities, TEX$_{86}$ values tend to yield lower temperature estimates than U$_{37}^{K'}$ when both are available (Figs. 2 and 3 and supplementary materials). As a result, our SST trends from the integrated data set often yield lower average temperatures in the warm pool, higher temperatures in the cold tongue, and a smaller ΔT_{zonal} relative to estimates that only use our TEX$_{86}$ records (Fig. 4 and supplementary materials). For example, the Pliocene ΔT_{zonal} shows a range of 3.2°C (total data set) to 4.1°C (based solely on TEX$_{86}$ data; see supplementary materials).

Averaging ΔT_{zonal} data over the Quaternary (2.6 to 0 Ma), Pliocene (5.3 to 2.6 Ma), and late Miocene (12 to 5.3 Ma) indicates that about 60 to 70% of the Quaternary ΔT_{zonal} is expressed in the late Miocene, whereas ~80% of the Quaternary ΔT_{zonal} characterizes the Pliocene and thus closely reflects modern oceanographic conditions (supplementary materials). Notably, our records indicate that both the warm pool and the cold tongue were warmer in the past, but that a cold EEP (relative

Fig. 2. SST reconstructions of the Pacific warm pool for the past 5 Ma. Mg/Ca temperatures do not account for changes in seawater Mg/Ca (*8*). Dashed line denotes the maximum calculable temperature (~28.5°C) of the U$_{37}^{K'}$ calibration. Calibration errors for U$_{37}^{K'}$ (*20*) and TEX$_{86}$ (*23*) are 1.1° and 2.5°C, respectively, but vary spatially (*24*). Warm pool temperature trend is calculated with all TEX$_{86}$-derived SSTs and U$_{37}^{K'}$ temperatures after 3 Ma. U$_{37}^{K'}$- SST records from site 806 (5 to 0 Ma) (*4*) and 1143 (4 to 0 Ma) (*34*) are previously published.

to the warm pool) was present. Thus, the oceanographic processes that produce the modern cold tongue, including a shallow EEP thermocline and active upwelling, were likely in play—consistent with high rates of biogenic opal accumulation in the EEP during the late Miocene and Pliocene (27).

A late Miocene–Pliocene climate state characterized by strong temperature asymmetry across the equatorial Pacific provides the necessary conditions for robust ENSO-type interannual climate variability but does not directly prove its existence. Regardless, our temperature reconstructions support other proxy records (15, 16) and climate simulations (28, 29) that indicate ENSO-like behavior during the Pliocene and beyond (30).

Today, waters of the Equatorial Undercurrent that source upwelled waters in the eastern equatorial Pacific derive from the extratropics and higher latitudes, including the Subantarctic mode water (31). Geochemical tracers, drifter experiments, and climate simulations (32) indicate that waters from the eastern, subtropical Pacific subduct and resurface in the EEP thermocline within two decades. Indeed, the linkage between the eastern equatorial Pacific and anomalously warm waters from higher latitudes was used to explain a period of prolonged warming of the EEP in the early 1990s (32). Similarly, during the late Miocene to Pliocene, warmer extratropical waters (7, 33) (Fig. 4) that sourced the EEP likely contributed a reduction in ΔT_{zonal}. As meridional temperature gradients increased during global cooling, colder extratropical water contributed to EEP cooling and an increase in ΔT_{zonal} (Fig. 4).

Given the areal extent of tropical warm pools and their importance in regulating global temperatures, our new warm pool temperature records substantially revise the character and nature of global warming in the recent past.
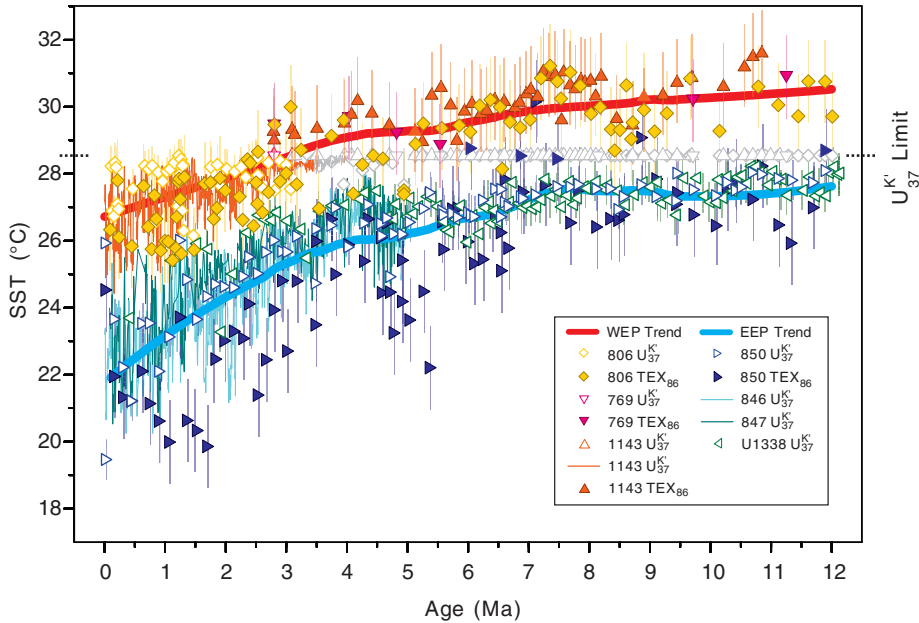
Fig. 3. Temperature evolution of the western and eastern equatorial Pacific since 12 Ma. All published data [$U^{K'}_{37}$ from sites 806 (5 to 0 Ma) (4); 846 (5 to 0 Ma) (13); 847 (5 to 0 Ma) (12); 1143 (4 to 0 Ma) (34); and U1338 (12 to 0 Ma) (26)] are converted to temperature with the calibration of Conte et al. (20) for $U^{K'}_{37}$ and Kim et al. (23) for TEX_{86}. Western equatorial Pacific (WEP) temperature trend is calculated with all TEX_{86} from sites 769, 806, and 1143. $U^{K'}_{37}$ records from ODP sites 806 and 1143 are also applied for the past 3 Ma. $U^{K'}_{37}$ data before 3 Ma, shown in gray, are mostly maximized and are not included in trend calculations. Temperature trend in the eastern equatorial Pacific (EEP) is calculated with $U^{K'}_{37}$ values from sites 846, 847, 850, and U1338 and with TEX_{86} results from site 850.
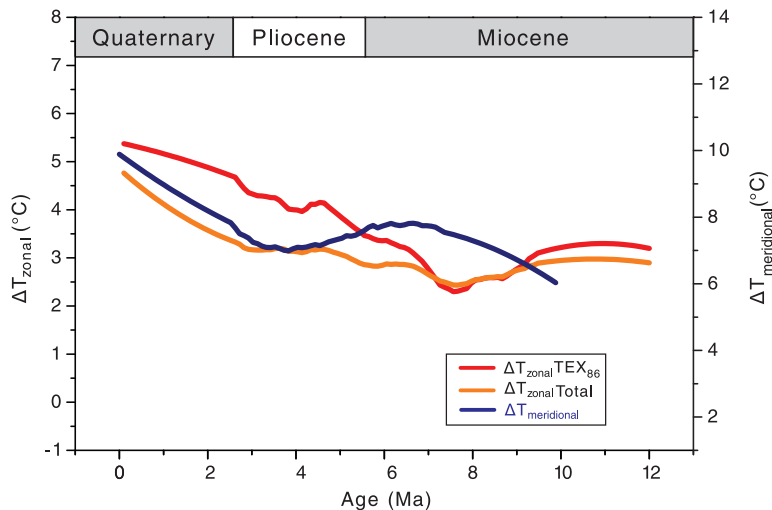
Fig. 4. Zonal (ΔT_{zonal}) and meridional ($\Delta T_{meridional}$) temperature gradients of the Pacific Ocean for the past 12 million years. Zonal gradient is computed with both $U^{K'}_{37}$ and TEX_{86} data, and with TEX_{86} data only. Meridional gradient is calculated between sites 806 and 1208 (33). Fifty-point Savitzky-Golay smoothing has been applied to the raw data. Note the different scales for ΔT_{zonal} and $\Delta T_{meridional}$.

References and Notes

1. M. J. McPhaden, S. E. Zebiak, M. H. Glantz, *Science* **314**, 1740–1745 (2006).
2. P. Molnar, M. A. Cane, *Paleoceanography* **17**, 11-1–11-11 (2002).
3. K. B. Karnauskas, R. Seager, A. Kaplan, Y. Kushnir, M. A. Cane, *J. Clim.* **22**, 4316–4321 (2009).
4. M. Pagani, Z. H. Liu, J. LaRiviere, A. C. Ravelo, *Nat. Geosci.* **3**, 27–30 (2010).
5. O. Seki et al., *Earth Planet. Sci. Lett.* **292**, 201–211 (2010).
6. D. J. Lunt et al., *Nat. Geosci.* **3**, 60–64 (2010).
7. C. M. Brierley et al., *Science* **323**, 1714–1718 (2009).
8. M. W. Wara, A. C. Ravelo, M. L. Delaney, *Science* **309**, 758–761 (2005).
9. V. Ramanathan, W. Collins, *Nature* **351**, 27–32 (1991).
10. I. N. Williams, R. T. Pierrehumbert, M. Huber, *Geophys. Res. Lett.* **36**, L21805 (2009).
11. M. Pagani, M. Huber, B. Sageman, in *Treatise on Geochemistry,* H. D. Holland, K. K. Turekian, Eds. (Elsevier, Oxford, 2014), pp. 281–304.
12. P. S. Dekens, A. C. Ravelo, M. D. McCarthy, *Paleoceanography* **22**, PA3211 (2007).
13. K. T. Lawrence, Z. Liu, T. D. Herbert, *Science* **312**, 79–83 (2006).
14. A. V. Fedorov et al., *Science* **312**, 1485–1489 (2006).
15. T. Watanabe et al., *Nature* **471**, 209–211 (2011).
16. N. Scroxton et al., *Paleoceanography* **26**, PA2215 (2011).
17. T. K. Lowenstein, M. N. Timofeeff, S. T. Brennan, L. A. Hardie, R. V. Demicco, *Science* **294**, 1086–1088 (2001).
18. R. M. Coggon, D. A. H. Teagle, C. E. Smith-Duque, J. C. Alt, M. J. Cooper, *Science* **327**, 1114–1117 (2010).
19. A. V. Fedorov et al., *Nature* **496**, 43–49 (2013).
20. M. Conte et al., *Geochem. Geophys. Geosyst.* **7**, Q02005 (2006).
21. M. Könneke et al., *Nature* **437**, 543–546 (2005).
22. S. G. Wakeham, C. M. Lewis, E. C. Hopmans, S. Schouten, J. S. Sinnighe Damsté, *Geochim. Cosmochim. Acta* **67**, 1359–1374 (2003).
23. J. H. Kim et al., *Geochim. Cosmochim. Acta* **74**, 4639–4654 (2010).
24. J. E. Tierney, M. P. Tingley, *Geochim. Cosmochim. Acta* **127**, 83–106 (2014).
25. S. Schouten, A. Forster, F. E. Panoto, J. S. Sinnighe Damste, *Org. Geochem.* **38**, 1537–1546 (2007).
26. G. Rousselle, C. Beltran, M.-A. Sicre, I. Raffi, M. De Rafelis, *Earth Planet. Sci. Lett.* **361**, 412–421 (2013).
27. J. W. Farrell et al., in *Proceedings of the Ocean Drilling Program, Scientific Results,* N. Pisias, L. Mayer, T. Janecek, A. Palmer-Julson, T. H. van Andel, Eds. (Ocean Drilling Program, College Station, TX, 1995), vol. 138.

28. A. M. Haywood, P. J. Valdes, V. L. Peck, *Paleoceanography* 22, PA1213 (2007).
29. A. S. von der Heydt, A. Nnafie, H. A. Dijkstra, *Clim. Past* 7, 903–915 (2011).
30. S. Galeotti *et al.*, *Geology* 38, 419–422 (2010).
31. J. R. Toggweiler, K. Dixon, W. S. Broecker, *J. Geophys. Res.* 96 (C11), 20467 (1991).
32. D. Gu, S. G. H. Philander, *Science* 275, 805–807 (1997).
33. J. P. LaRiviere *et al.*, *Nature* 486, 97–100 (2012).
34. L. Li *et al.*, *Earth Planet. Sci. Lett.* 309, 10–20 (2011).

Construction of a Vertebrate Embryo from Two Opposing Morphogen Gradients

Peng-Fei Xu,* Nathalie Houssin,* Karine F. Ferri-Lagneau,*† Bernard Thisse, Christine Thisse‡

Development of vertebrate embryos involves tightly regulated molecular and cellular processes that progressively instruct proliferating embryonic cells about their identity and behavior. Whereas numerous gene activities have been found to be essential during early embryogenesis, little is known about the minimal conditions and factors that would be sufficient to instruct pluripotent cells to organize the embryo. Here, we show that opposing gradients of bone morphogenetic protein (BMP) and Nodal, two transforming growth factor family members that act as morphogens, are sufficient to induce molecular and cellular mechanisms required to organize, in vivo or in vitro, uncommitted cells of the zebrafish blastula animal pole into a well-developed embryo.

The formation of vertebrate embryos depends on the activity of an organizing center, corresponding to the dorsal blastopore lip in amphibians and known as the Spemann-Mangold or dorsal organizer (*1*). When grafted ventrally into a host, this organizer results in the formation, at the site of the graft, of a secondary embryonic axis. The molecular nature of the activity carried by this dorsal tissue has been identified (*2*), and its main components are dorsally secreted factors that act as antagonists of ventral morphogens and help to establish a ventral-to-dorsal gradient of their activity (fig. S1A). However, when placed in a neutral environment such as the blastula animal pole, the Spemann organizer has very limited organizing activity, leading only to induction of axial mesendodermal tissues (*3*).

We previously established that, in zebrafish, the organizing activities controlling the development of the embryo are not restricted to the dorsal organizer but are distributed all along the embryonic margin (*3*, *4*) and result from the combined activity of two signaling pathways: bone morphogenetic protein (BMP) and Nodal. We found that the organizing activity of each portion of the embryonic margin varies depending on the BMP/Nodal ratio of activities (fig. S1B): A high BMP/Nodal ratio organizes the tail; a low BMP/Nodal ratio organizes the posterior head, whereas

intermediate ratios of activity induce formation of the trunk (*4*). Based on these observations, we hypothesized that exposing uncommitted embryonic cells to a continuous variation of BMP/Nodal ratios may be sufficient to organize a complete embryonic axis (fig. S1C).

To test this hypothesis, we engineered opposing gradients of BMP and Nodal by injecting their corresponding mRNAs, at the 128-cell stage, into two different animal pole blastomeres that give rise to distinct clones of cells secreting these factors (Fig. 1A). The animal pole of the blastula was chosen as the territory to instruct because it contains all elements necessary to mediate the molecular and cellular responses to BMP and Nodal stimulation (*3*, *4*). Additionally, because the animal pole is distant from the margin, the influence of the primary axis and of maternal determinants is expected to be minimal.

In support of our hypothesis, these two secreting centers organize the animal pole cells (see supplementary materials and methods) into a secondary embryonic axis that forms at the animal pole (Fig. 1, B to E), solely from animal pole cells (fig. S2). These ectopic axes contain tissues and organs present in the primary axis and extend from the forebrain to the tip of the tail (Fig. 1B). In most cases, the primary and secondary axes fuse in the cephalic region, where animal pole cells are recruited by both growing structures. However, in some cases (1.3%; *n* = 1012 embryos), clones are in such a position that the two embryonic axes do not fuse (Fig. 1, C to E), with each displaying a forebrain, eyes, and a beating heart and exhibiting spontaneous myotomal contractions indicative of a functional nervous system (movie S1). Although the antero-posterior (A-P)

axis of the primary embryo always parallels the animal-vegetal (An-Vg) axis of the egg, we found no correlation between the An-Vg axis of the egg and the A-P axis of the secondary embryo, which can be parallel, perpendicular, or even antiparallel to the A-P axis of the primary embryo and, therefore, to the An-Vg axis of the egg (Fig. 1, C to E). This demonstrates that, in zebrafish, there is no intrinsic information present in the egg or in the early embryo determining the orientation of the A-P axis that cannot be reversed by application of appropriate signals.

To understand the relative contribution of the two signaling pathways to the organization of the secondary embryonic axis, we examined the consequence of adding BMP or Nodal individually. At the blastula stage, BMP signaling is already active at the animal pole (*5*); adding more BMP to this region has very little effect (fig. S3). Conversely, at the blastula stage, stimulating the animal pole with Nodal results in a thickening of the animal pole blastoderm (Fig. 2A). At the onset of gastrulation, the central part of the resulting protrusion internalizes (Fig. 2, B and C), forming a blastopore with a circular, radially symmetrical blastopore lip where mesodermal cells involute (movie S2).

At blastula and gastrula stages, epiboly disperses cells of the animal pole over the ectoderm. However, in the presence of a Nodal-expressing clone, the surrounding animal pole cells do not spread but converge toward the center of the Nodal-secreting source (fig. S4). It is known that the guidance cues for convergence movements in the zebrafish gastrula are controlled by janus kinase/signal transducer and activator of transcription 3 (JAK/STAT3) signaling (*6*, *7*). Activation of STAT3 is independent of Nodal signaling but dependent on the maternal β-catenin signaling pathway (*6*). Because ectopic Nodal signaling induces an attracting center at the animal pole, we hypothesized that STAT3 may be activated in that domain. Consistent with this, in STAT3 morphant embryos, ectopic Nodal signaling fails to induce radial convergence movements, whereas internalization of the mesendoderm is not affected (Fig. 2D). Furthermore, Nodal induction of expression of *liv1* (Fig. 2E), a downstream target of STAT3 (*8*), is abolished in STAT3 morphant embryos (Fig. 2F), demonstrating that although Nodal is not required for activation of STAT3 in the dorsal domain of the blastula (*7*), it is sufficient to induce this activation at the animal pole.

In zebrafish, Nodal is known to be essential for inducing the organizing activity carried by the

Department of Cell Biology, University of Virginia, Charlottesville, VA 22908, USA.

*These authors contributed equally to this work.
†Present address: Biomedical/Biotechnology Research Institute, North Carolina Central University, Kannapolis, NC 28081, USA.
‡Corresponding author. E-mail: christhisse@virginia.edu

dorsal gastrula margin (9–11). Accordingly, stimulation of animal pole cells by Nodal induces expression of dorsal and dorso-lateral marginal genes (fig. S5) but never induces markers of lateral or ventral cell identities such as eve1 (Fig. 2G). At the onset of gastrulation, the expression of genes induced at the animal pole by Nodal is organized in concentric circles (fig. S5), reflecting the morphogenic activity of Nodal (12). At late gastrula stage, a notochordal domain expressing ntl extends out of the animal pole as a result of radial convergence and extension movements (Fig. 2G), and the involuted prechordal plate cells expressing frzb

have reached the yolk syncytial layer and spread in all directions in a radially symmetrical manner (Fig. 2H). Thus, engineering a Nodal activity gradient at the animal pole results in the formation of a radially symmetric structure possessing dorsal identity.

Providing a gradient of BMP opposed to the Nodal activity gradient (Fig. 3A) converts the radially symmetrical structure induced by Nodal alone into a bilaterally symmetric embryonic axis. Time-lapse analysis reveals that, at the blastula stage (movie S3), the protrusion induced in the presence of both BMP and Nodal gradients is morphologically identical to the protrusion induced by Nodal alone (Figs. 2A and 3A). However, at gastrulation, we observe a thinning of the

blastopore lip close to the BMP-secreting clone and a simultaneous thickening of the opposite side (Fig. 3B), suggesting that cells are migrating away from the BMP source. This is likely to reflect the repulsive effect of BMP on migrating lateral mesodermal cells (13). In addition, and in accordance with its function in dorso-ventral (D-V) axis formation (14–16), BMP patterns the blastopore lip induced by Nodal, defining a ventral domain close to the BMP-secreting center and progressively more dorsal identities with increasing distance from the BMP source. Consequently, at the gastrula stage, dorsal marginal markers are restricted to the domain of the blastopore lip furthest from the BMP-secreting clone (Fig. 3, C to E), whereas ventral- and lateral-specific genes are induced close to the BMP-secreting center (Fig. 3F and fig. S6).

Whereas D-V patterning requires BMP activity (16), establishment of the A-P polarity has been shown to depend on Nodal (17). Accordingly, the A-P polarity of the secondary axes induced by Nodal or by Nodal and BMP is in the opposite orientation to that of the primary embryonic axis (fig. S7, A and B). This is probably the consequence of the expression, in the induced ectopic blastopore lip, of FGF8a (18) and Wnt8a (19), which act as posteriorizing morphogens (20, 21) (fig. S7, C to F). Although these posteriorizing factors control the initial A-P polarity, the direction of extension of the induced secondary
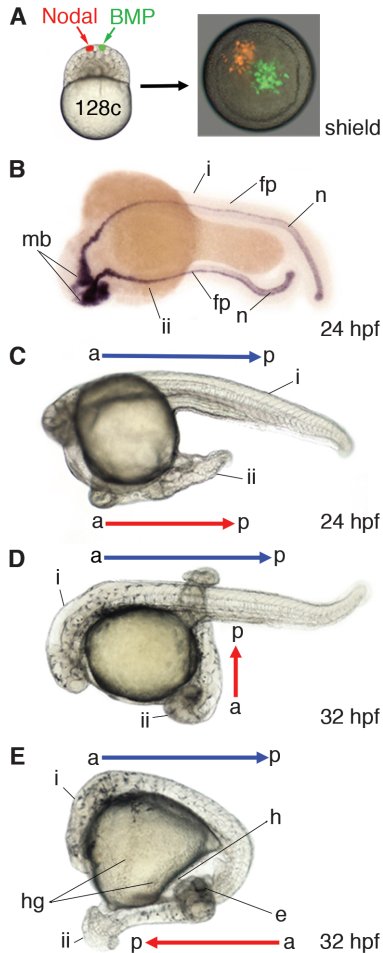
Fig. 1. BMP and Nodal induce a secondary embryonic axis at the animal pole. (**A**) Injection of Nodal and BMP mRNAs in two different animal pole blastomeres at the 128-cell (128c) stage results in (**B**) formation of a secondary embryonic axis (ii) expressing sonic hedgehog a from the midbrain to the tip of the tail. (**C** to **E**) Secondary embryonic axes including anterior head and displaying antero-posterior (a-p) orientation (red arrow) (C) parallel, (D) perpendicular, and (E) antiparallel to a-p orientation (blue arrow) of the primary axis (i). e, eye; fp, floorplate; h, heart; hg, hatching gland; n, notochord; mb, midbrain. Images in (B) to (E) are composite photos from a stack of images made at different planes of focus. hpf, hours postfertilization.
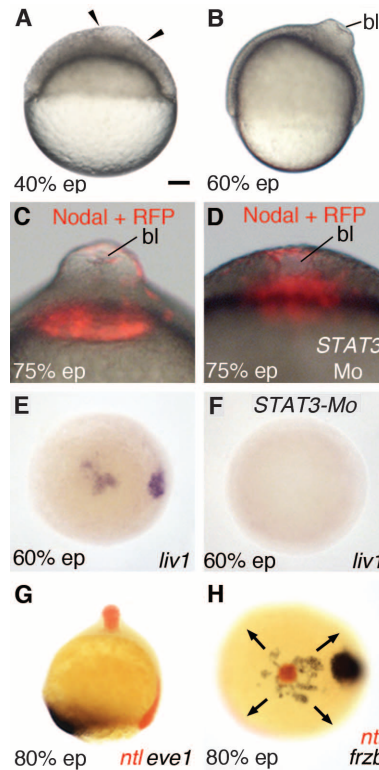
Fig. 2. Nodal induces formation of a blastopore where ectopic gastrulation occurs. (**A**) Thickening of the blastoderm (arrowheads) induced by ectopic Nodal signaling. (**B**) Formation of a blastopore (bl) at gastrulation. (**C**) Internalization of the Nodal-secreting cells [Nodal plus red fluorescent protein (RFP)]. (**D**) Blastopore induced by Nodal after STAT3 depletion by morpholino (STAT3 Mo) injection. (**E** and **F**) Nodal induces expression of liv1 in the wild type (E), but not in STAT3-depleted embryos (F). (**G** and **H**) Expression of genes induced by Nodal at the animal pole revealed by double-color in situ hybridization. Arrows in (H) indicate the spreading of prechordal plate cells expressing frzb. The developmental stage is indicated in the lower left corner of each panel. ep, epiboly. Probes are indicated in the lower right corner in (E) to (H). (A to D and G) Lateral view; (E, F, H) animal pole view. Scale bar in (A) corresponds to 100 μm for (A), (B), (E), and (F) and 40 μm for (C) and (D).
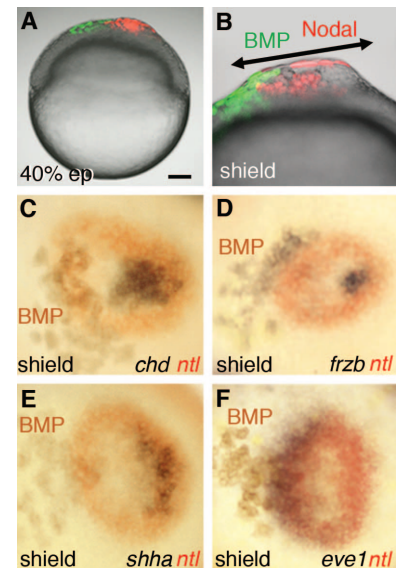
Fig. 3. BMP breaks the radial symmetry and patterns the blastopore lip induced by Nodal. (**A**) BMP- and Nodal-secreting clones induce (**B**) a blastopore with an asymmetrical blastopore lip. (**C** to **F**) Expression of genes induced at the animal pole by Nodal and BMP. The developmental stage is indicated in the lower left corner of each panel; probes are indicated in the lower right corner in (C) to (F). Brown cells in (C) to (F) are cells secreting BMP. (A and B) Lateral view; (C to F) animal pole view. Scale bar in (A) corresponds to 100 μm for (A) and 40 μm for (B) to (F).

axis depends only on the position of the BMP-secreting clone relative to the blastopore lip induced by Nodal and is completely independent of the orientation of the primary embryonic axis (fig. S7, G and H, and fig. S8).

All of these data support the conclusion that formation of the secondary embryonic axis that we generate occurs without any contribution from signals that organize and pattern the primary axis and that it depends only on the clones secreting BMP and Nodal that we engineered. To further demonstrate this, we tested the ability of BMP and Nodal to induce embryonic development from blastula animal pole explants cultured in vitro and, therefore, independent of the primary axis.

Explantation of animal pole cells is performed at the 512-cell stage [midblastula transition (MBT)] (Fig. 4A). At that stage, animal pole cells of the

Fig. 4. In vitro construction of embryonic axes with opposing gradients of BMP and Nodal. (**A**) Animal pole injection and explantation. c, cells. (**B**) Uninjected explants. (**C** to **E**) Explants from embryos injected with both BMP and Nodal mRNAs analyzed at the gastrula stage (C) for the morphology (left) and by in situ hybridization with endoderm (*sox32*), prechordal (*frzb*), notochord (*shha*), and epidermal (*foxi1*) markers or observed at 24 hpf (D and E) and analyzed by in situ hybridization with retina (ret, *vsx2*), spinal cord neurons (ne, *vsx2*), forebrain (fb, *emx1*), hindbrain (hb, *egr2b*), and somite (so, *myoD*) markers. bl, blastopore; n, notochord; nt, neural tube. Scale bar in (A) corresponds to 200 μm for (A), 80 μm for (B) and (C), and 100 μm for (D) and (E).

zebrafish embryo are all pluripotent, undifferentiated, and equivalent (*22*). Notably, nuclei of animal pole cells are completely devoid of β-catenin (*23*), which accumulates in the nuclei of only a small number of dorso-marginal cells (*24*, *25*). This is different from what is observed for amphibian embryos that display a preexistent pattern at the animal pole of the blastula (*26*) that depends on the endogenous D-V gradient of β-catenin (*24*).

The animal pole of uninjected embryos, explanted at the MBT and placed in culture medium, does not differentiate any embryonic tissues or organs (Fig. 4B). Explants become spherical and, after ~1 hour, differentiate a morphologically visible enveloping layer (EVL). Three hours later, an internal cavity appears within the explant, reminiscent of a blastocoel, a fluid-filled central cavity of the blastula, which is observed in most vertebrate species but is absent in zebrafish (*27*).

Our analysis of genes expressed in these explants at time points corresponding to gastrulation in control embryos (fig. S9) reveals that animal pole cells at or before the time of explantation have received no signals induced by maternal dorsal determinants. After 1 day of culture, no morphologically visible structures are present, and we only observed a rupture of the EVL with extrusion of some of the enclosed embryonic cells (Fig. 4B). Stimulation by injection of Nodal mRNA into one animal pole blastomere before explantation later induces gastrulation with formation of a radially symmetrical blastopore lip (movie S4). When secreting centers for both Nodal and BMP are engineered, gastrulating explants display an asymmetrical blastopore lip, contain cells from the three germ layers, and are patterned along clear A-P and D-V axes (Fig. 4C). After 1 day of culture, these explants differentiate into embryoids that display morphologically recognizable structures such as the forebrain, neural tube, notochord, and somites (Fig. 4D). These embryoids express organ-specific molecular markers (Fig. 4E); their neural tubes are patterned along the A-P axis, and they often display bilateral symmetry, as illustrated by *vsx2* expression, which reveals the presence of two eyes (Fig. 4E).

Similar observations have been made after the fusion of two animal pole explants: one uninjected explant and the other explant injected with BMP and Nodal mRNAs (fig. S10). In this condition, all mesendodermal tissues derive from the injected explant, whereas cells of the uninjected explant differentiate anterior ectodermal derivatives. The ability of the BMP and Nodal signals to organize the fused explants (that initially contain two animal poles with An-Vg axes in opposite orientation) into a single embryoid with a clear A-P axis provides proof that a strongly biased preexistent pattern is not present within the animal pole region of the zebrafish blastula.

Our study demonstrates that stimulation of uncommitted cells at the blastula animal pole with opposing gradients of BMP and Nodal is sufficient to initiate the principal molecular and cel-

lular processes necessary to organize a complete embryonic axis. All other signaling pathways required to achieve full embryonic development are induced and regulated in response to the two initial, experimentally engineered signals. Therefore, our findings establish a baseline for the minimal signaling requirements for early embryonic development and provide a framework for future studies in the field of regenerative medicine that are aimed at constructing tissues and organs in vitro from populations of cultured pluripotent cells.

References and Notes
1. H. Spemann, H. Mangold, *Int. J. Dev. Biol.* **45**, 13–38 (2001).
2. E. M. De Robertis, *Nat. Rev. Mol. Cell Biol.* **7**, 296–302 (2006).
3. A. Agathon, C. Thisse, B. Thisse, *Nature* **424**, 448–452 (2003).
4. J. D. Fauny, B. Thisse, C. Thisse, *Development* **136**, 3811–3819 (2009).
5. J. A. Tucker, K. A. Mintzer, M. C. Mullins, *Dev. Cell* **14**, 108–119 (2008).
6. S. Yamashita *et al.*, *Dev. Cell* **2**, 363–375 (2002).
7. C. Miyagi *et al.*, *J. Cell Biol.* **166**, 975–981 (2004).
8. S. Yamashita *et al.*, *Nature* **429**, 298–302 (2004).
9. R. Toyama, M. L. O'Connell, C. V. Wright, M. R. Kuehn, I. B. Dawid, *Development* **121**, 383–391 (1995).
10. B. Feldman *et al.*, *Nature* **395**, 181–185 (1998).
11. A. F. Schier, W. S. Talbot, *Int. J. Dev. Biol.* **45**, 289–297 (2001).
12. Y. Chen, A. F. Schier, *Nature* **411**, 607–610 (2001).
13. S. von der Hardt *et al.*, *Curr. Biol.* **17**, 475–487 (2007).
14. L. Dale, G. Howes, B. M. Price, J. C. Smith, *Development* **115**, 573–585 (1992).
15. Y. Kishimoto, K. H. Lee, L. Zon, M. Hammerschmidt, S. Schulte-Merker, *Development* **124**, 4457–4466 (1997).
16. S. C. Little, M. C. Mullins, *Birth Defects Res. C Embryo Today* **78**, 224–242 (2006).
17. B. Thisse, C. V. Wright, C. Thisse, *Nature* **403**, 425–428 (2000).
18. W. G. Cox, A. Hemmati-Brivanlou, *Development* **121**, 4349–4358 (1995).
19. L. L. McGrew, S. Hoppler, R. T. Moon, *Mech. Dev.* **69**, 105–114 (1997).
20. M. Zecca, K. Basler, G. Struhl, *Cell* **87**, 833–844 (1996).
21. S. Scholpp, M. Brand, *Curr. Biol.* **14**, 1834–1841 (2004).
22. R. K. Ho, C. B. Kimmel, *Science* **261**, 109–111 (1993).
23. F.-I. Lu, C. Thisse, B. Thisse, *Proc. Natl. Acad. Sci. U.S.A.* **108**, 15876–15880 (2011).
24. S. Schneider, H. Steinbeisser, R. M. Warga, P. Hausen, *Mech. Dev.* **57**, 191–198 (1996).
25. S. T. Dougan, R. M. Warga, D. A. Kane, A. F. Schier, W. S. Talbot, *Development* **130**, 1837–1851 (2003).
26. S. Sokol, D. A. Melton, *Nature* **351**, 409–411 (1991).
27. C. B. Kimmel, W. W. Ballard, S. R. Kimmel, B. Ullmann, T. F. Schilling, *Dev. Dyn.* **203**, 253–310 (1995).

Supplementary Materials
www.sciencemag.org/content/344/6179/87/suppl/DC1
Material and Methods
Figs. S1 to S10
References (*28–32*)
Movies S1 to S4

Monolignol Ferulate Transferase Introduces Chemically Labile Linkages into the Lignin Backbone

C. G. Wilkerson,[1,2,3]* S. D. Mansfield,[4]* F. Lu,[5,6]* S. Withers,[1,2]† J.-Y. Park,[4] S. D. Karlen,[6] E. Gonzales-Vigil,[4] D. Padmakshan,[6] F. Unda,[4] J. Rencoret,[5,6]‡ J. Ralph[5,6]§

Redesigning lignin, the aromatic polymer fortifying plant cell walls, to be more amenable to chemical depolymerization can lower the energy required for industrial processing. We have engineered poplar trees to introduce ester linkages into the lignin polymer backbone by augmenting the monomer pool with monolignol ferulate conjugates. Herein, we describe the isolation of a transferase gene capable of forming these conjugates and its xylem-specific introduction into poplar. Enzyme kinetics, in planta expression, lignin structural analysis, and improved cell wall digestibility after mild alkaline pretreatment demonstrate that these trees produce the monolignol ferulate conjugates, export them to the wall, and use them during lignification. Tailoring plants to use such conjugates during cell wall biosynthesis is a promising way to produce plants that are designed for deconstruction.

Lignin is a complex phenolic polymer that is essential for plant growth and development but concurrently acts as a major impediment to industrial processing. Research efforts globally have therefore focused on altering the natural lignification processes to produce plants with cell walls that process more readily, for example, to liberate carbohydrates with minimal inputs (1–5).

The biosynthetic steps to produce the monomers used in the synthesis of lignin have been elucidated (1, 4, 5), although new genes continue to be discovered (6, 7), and several transcription factors integral to controlling the lignin biosynthetic network have been identified (8). It was also empirically discovered that some perturbations led to the synthesis of lignins that incorporated alternative monomers, usually derived from products of incomplete monolignol biosynthesis, spawning the idea that lignins could be designed to encompass substantial structural alterations that would engender unique properties (4, 9, 10).

Studies of natural plant tissues, along with those from mutants and transgenics with mis-

[1]Department of Plant Biology, Michigan State University, East Lansing, MI 48824, USA. [2]Great Lakes Bioenergy Research Center, Michigan State University, East Lansing, MI 48824, USA. [3]Department of Biochemistry and Molecular Biology, Michigan State University, East Lansing, MI 48824, USA. [4]Department of Wood Science, University of British Columbia, Vancouver, British Columbia V6T 1Z4, Canada. [5]Department of Biochemistry, University of Wisconsin–Madison, Madison, WI 53706, USA. [6]U.S. Department of Energy (DOE) Great Lakes Bioenergy Research Center, the Wisconsin Energy Institute, University of Wisconsin–Madison, Madison, WI 53726, USA.

*These authors contributed equally to this work.
†Present address: Department of Plant Pathology, North Carolina State University, Raleigh, NC 27695, USA.
‡Present address: Instituto de Recursos Naturales y Agrobiología de Sevilla, Consejo Superior de Investigaciones Científicas, Post Office Box 1052, E-41080 Seville, Spain.
§Corresponding author. E-mail: jralph@wisc.edu
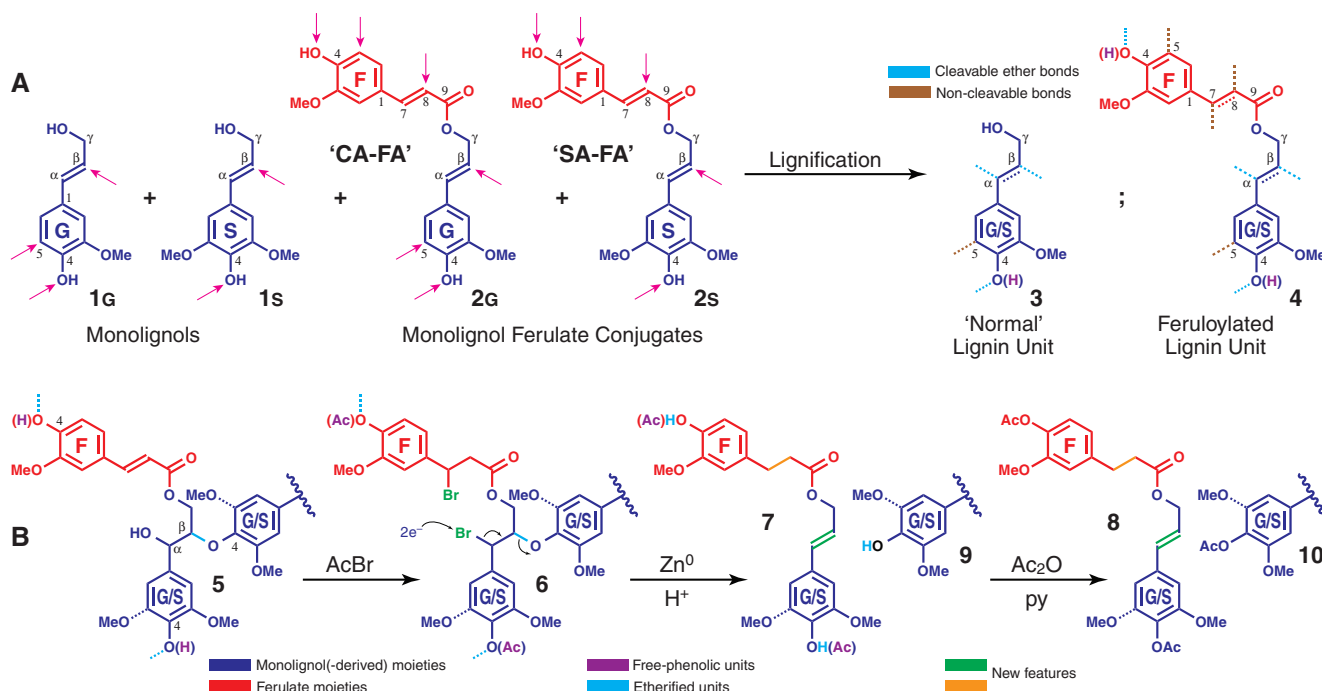
Fig. 1. General schemes for lignification and a method to provide evidence for monolignol ferulate conjugate incorporation into lignins. (**A**) Lignification of monolignols **1** by combinatorial radical cross-coupling reactions produces a lignin in which the units can be represented by generic structure **3**. Analogous lignification of monolignol ferulate conjugates **2** produces structural units **4** in which lignin moieties are γ-acylated by ferulate. Sites of radical coupling for the monolignols **1** and the conjugates **2** are indicated by magenta arrows. In the final lignin units **3** and **4**, cleavable ether bonds are indicated by dotted bonds in cyan; noncleavable bonds, in brown. The complexity with which the conjugates are incorporated is illustrated in fig. S2. Ac, acetyl group; py, pyridine; Me, methyl group; CA-FA, coniferyl ferulate; SA-FA, sinapyl ferulate. (**B**) The DFRC method releases conjugates **8** that diagnostically result from structures **5** within the lignin; the crucial double bond (colored green in **8**) arises only upon cleavage of the signature lignin β-ether bonds, and the ferulate moiety remains attached to its parent unit. Thus, the DFRC method releases an acetylated dihydroferulate analog **8**, of the monolignol ferulate conjugate **2** that was incorporated into the lignin, via reactions that specifically cleave lignin β-ethers but leave the γ-esters intact. Because the initially free-phenolic versus etherified units are acetate-tagged differentially at the stage of intermediate **7**, acetylation with perdeuteroacetic anhydride in the final step can fully reveal the etherification profile of the released units as they were in the cell wall (fig. S8).

regulated monolignol biosynthetic genes, have led to some remarkable discoveries, including plants that produce homopolymers from a range of traditional [e.g., *p*-coumaryl and sinapyl alcohols (*11*, *12*)] as well as nontraditional monomers [e.g., caffeyl and 5-hydroxyconiferyl alcohols and the hydroxycinnamaldehydes (*13–16*)]. These observations illustrate the inherent pliability of the lignification process (*4*, *10*, *17*). Therefore, the formal design of an improved polymer using unconventional monomers seems to be a feasible path to tailor plants with superior processing properties for both paper and biofuels production (*9*, *10*).

To that end, the introduction of monolignol ferulate conjugates **2** (Fig. 1 and fig. S1) into the lignin monomer pool appears to be one of the most promising. These exotic conjugates have been shown, but to date only in in vitro model systems, to be capable of introducing readily cleavable ester bonds into the lignin backbone, per-

mitting easier depolymerization (*10*, *18*). Three lines of independent research precipitated the idea that it would be possible to engineer plants to produce such conjugates for lignification. First, although plants have not been shown to use monolignol ferulate conjugates for lignification, all grasses use analogous monolignol *p*-coumarate conjugates (Fig. 1, *p*-coumarate analogs of **2** without the F-ring methoxyl) (*10*, *19*). However, because of their preference for radical transfer over radical coupling (*10*), *p*-coumarates do not polymerize into growing lignin chains and consequently remain almost entirely as free-phenolic pendent entities. Second, unlike the *p*-coumarate moiety, the ferulate, with an additional methoxyl group, is compatible with normal lignification reactions and can integrally incorporate into the polymer (*10*). Polysaccharide-lignin cross-linking results in grasses where the arabinoxylan-bound ferulates (or the diferulates that derive from them by radical

dehydrodimerization) radically cross-couple with lignin monomers and higher oligomers during lignification (*10*). The full compatibility of ferulate with lignification leads to complex homo- and cross-coupling (fig. S2) that renders its products difficult to detect in the lignin polymer and makes currently impossible the accurate quantification of the extent of its incorporation (*10*). Because the monolignol ferulate conjugate has two phenolic moieties, it incorporates in a manner that produces ester bonds in the lignin backbone (as schematically shown in Fig. 1 and fig. S1). Third, the substantial research characterizing natural plant lignins, a range of monolignol biosynthetic pathway mutants, and transgenic plants with misexpressed biosynthetic genes revealed that the process of lignification is metabolically plastic; various nonmonolignol phenolic monomers have been shown to actively participate in lignification (*3–5*, *9*, *10*, *17*). In fact, because of the combinatorial chemical nature of lignification and the established theory that the polymerization process is not protein- or enzyme-mediated (*17*), a phenolic compound proximal to lignifying tissue may incorporate into lignin subject to its chemical compatibility—its ability to form radicals and to couple and cross-couple with the available phenolics. If a plant could therefore synthesize the monolignol ferulate conjugates **2** with the appropriate temporal and spatial control and had the ability to transport them to the developing wall, the conjugates would ultimately incorporate into the growing lignin polymer (*10*). Recent studies using a corn cell

Table 1. Kinetic data for AsFMT purified from *E. coli*. Michaelis constant (K_m) and specific activity (V_{max}) data are calculated from the mean of at least three replicates ± SE. There was essentially no detectable activity with *p*-coumaroyl-CoA, so data are not given. K_{cat} is the catalysis rate; 1 nkat = 1 nMol product per second.

Varying substrate	Saturating substrate	$K_m \pm$ SE (μM)	$V_{max} \pm$ SE (nkat mg^{-1})	K_{cat} (s^{-1})	K_{cat}/K_m (μM^{-1} s^{-1})
Feruloyl-CoA	Coniferyl alcohol	0.97 ± 0.14	8547 ± 144	426	438.81
Coniferyl alcohol	Feruloyl-CoA	182 ± 20	8060 ± 298	401	2.21
Sinapyl alcohol	Feruloyl-CoA	204 ± 31	2212 ± 118	110	0.54
p-Coumaryl alcohol	Feruloyl-CoA	373 ± 43	14540 ± 721	724	1.94

Fig. 2. Images showing YFP-tagged FMT protein in poplar leaves from transgenics in which the *A. sinensis FMT* gene was driven by the universal 35*S* or the poplar xylem-specific *CesA8* promoter. (**A**) Poplar FMT transgenics growing in the greenhouse do not display any visible phenotypic differences from WT. (**B**) Non-transgenic control line. (**C**) *35S::FMT* showing universal FMT expression. (**D**) *CesA8::FMT* line showing vascular-tissue—specific FMT expression.
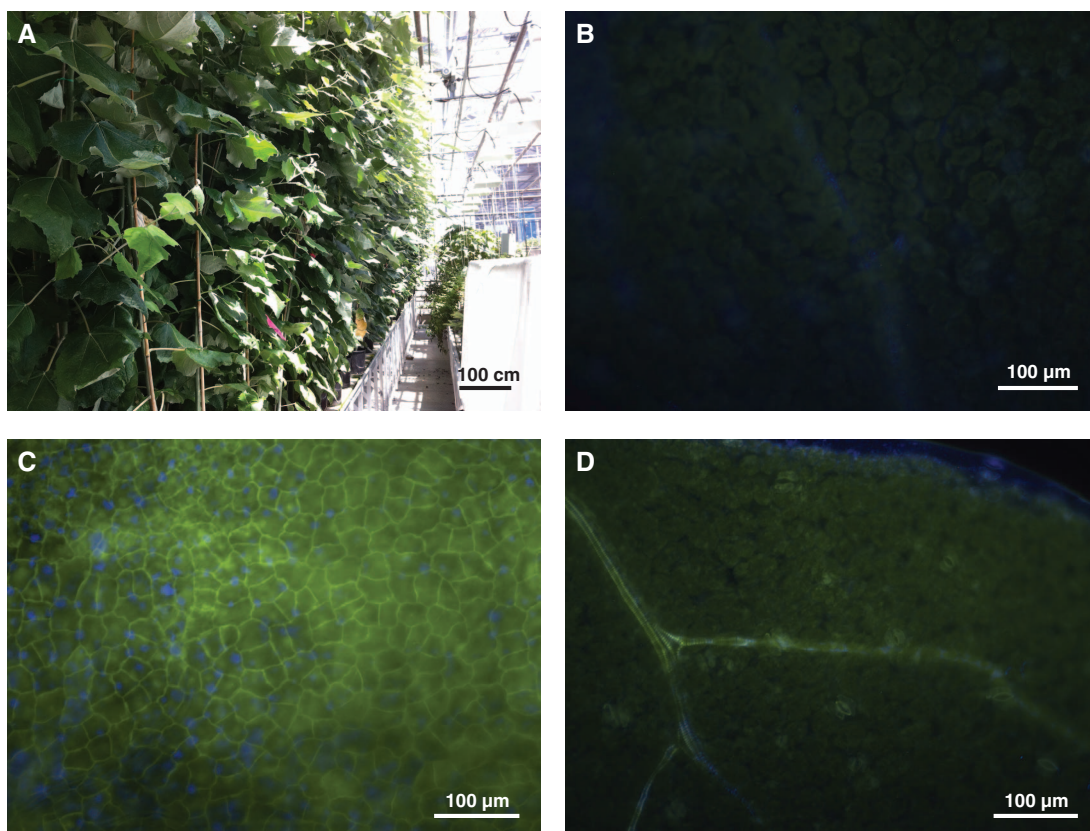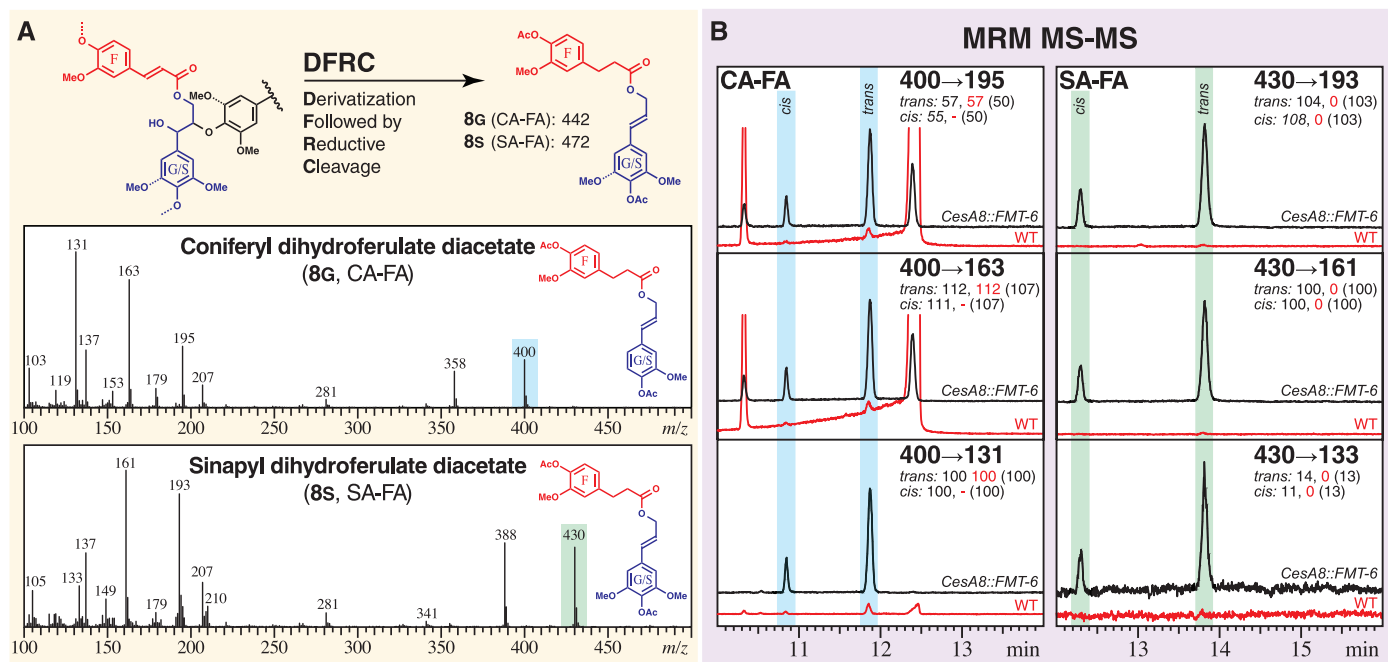
Fig. 3. Mass spectrometric evidence for the incorporation of monolignol ferulate conjugates into transgenic poplar lignins. (**A**) DFRC releasable conjugate **8**; Mass spectra for synthetic compounds **8G** and **8S** are from Q3 scans on a GC–triple-quad MS: molecular ions [mass/charge (m/z) 442, 472] lose ketene ($m/z = 42$) to yield the base peak (fig. S8) ($m/z = 400$, 430). (**B**) Triple-quad multiple reaction–monitoring (MRM) chromatograms of the poplar-derived $m/z = 400$ parent ion to the diagnostic 195, 163, and 131 product ions and $m/z = 430$ parent ion to the 193, 161, and 133 product ions; the numbers for the cis and trans isomers are the MRM intensities for transgenic *CesA8::FMT-6* in black and WT in red (with the corresponding measured intensities from the synthetic standards in parentheses) relative to the 400→131 (CA-FA) and 430→161 (SA-FA) peak for each. All of the data for the poplar-released conjugates match (by retention times, mass spectra, collision-induced fragmentation, and MRM relative intensities of daughter ions), providing evidence for the release of the diagnostic conjugates from the lignin in transgenic poplars. The released DFRC conjugate **8G** derives, in part, from units **5** (Fig. 1) in which the phenolic ends of the CA and the FA moiety are further etherified (fig. S8).

wall synthetic model system demonstrated the feasibility of incorporating such conjugates into lignin and supported the need to implement such a strategy in planta (*18*).

The first requirement was to obtain the gene coding for a protein or enzyme capable of catalyzing the formation of the conjugate, a feruloyl–coenzyme A (CoA) monolignol transferase (FMT). Evidence for the existence of such a gene was found in the Chinese medicinal *dong quai* or Chinese angelica (*Angelica sinensis*) in which the root tissue inherently contained ~2 weight % coniferyl ferulate (*20*). Deep expressed sequence tag sequencing led to identification of many BAHD transferases (table S1). The second most abundant transcript (phylogenetic tree in fig. S3) had only moderate similarity to any putative *Arabidopsis* gene (*Arabidopsis* is not known to make such ferulate conjugates) and ultimately produced a recombinant protein in *Escherichia coli* (fig. S4) with the desired transferase activities, namely high activity with feruloyl-CoA and low activity with *p*-coumaroyl–CoA (Table 1). Such selectivity ensures that the enzyme would not use *p*-coumarate to produce monolignol *p*-coumarate conjugates that, as we know from grasses, do not introduce ester bonds into the lignin backbone. Additionally, the enzyme could use any of the three monolignols as a target substrate (Table 1).

A key additional step consisted of expressing the gene spatially and temporally in the tissues that form lignin. This was successfully achieved in hybrid poplar (*Populus alba × grandidentata*) by using both a universal *35S* promoter and the poplar *CesA8* xylem-specific promoter involved in secondary cell wall cellulose biosynthesis. Fusion with a yellow fluorescent protein (YFP) reporter gene demonstrated that the protein was indeed being produced and facilitated localization for each promoter used. Examination of leaf extracts showed that, unlike in the control plants, FMT protein was being produced in planta in many tissues in the case of the ubiquitous promoter and only in the leaf vasculature (xylem) when the *CesA8* promoter was used (Fig. 2). We subsequently isolated the FMT protein from these plants and demonstrated in vitro that it was able to produce the target conjugates from its substrates, feruloyl-CoA and a monolignol (figs. S5 and S6). In all cases, the plants showed no phenotypic growth abnormalities in the greenhouse (Fig. 2). The total lignin levels generally remained the same as in wild-type (WT) controls and displayed only a very slight consistent increase in the syringyl-to-guaiacyl (S/G) ratio (table S2).

Unequivocally determining that these plants are capable of incorporating monolignol ferulates into the lignin polymer is particularly challenging because ferulate is naturally integrally incorporated into lignins by combinatorial radical coupling, the complexity of which is illustrated in fig. S2. However, derivatization followed by reductive cleavage (DFRC) is capable of cleaving the lignin-signature β-ether bonds while leaving γ-esters intact and has previously been used to analyze *p*-coumaroylated lignins (*21*). With modifications to this method, we were able to show that the novel monolignol ferulates, coniferyl ferulate **2G** and sinapyl ferulate **2S** (Fig. 1), are indeed incorporated into the lignin of the transgenic trees. Thus, a small fraction of the expected structures **5** in the polymer that would result from incorporating monolignol ferulate conjugates into lignins (Fig. 1 and fig. S2) can be cleaved, releasing monolignol (dihydro)ferulate conjugates **8** that are quantifiable by gas chromatography–mass spectrometry (GC-MS) (Figs. 1B and 3). The double bond in the monolignol moiety of **8**, as in the normal DFRC monomers, arises only from reductively cleaving the β-ether bond. Compounds **8** are therefore diagnostic markers indicating that the monolignol ferulate conjugate **2** has incorporated into the polymer by radical coupling. Structures **5** (Fig. 1B) are only a small fraction of the many structures (represented by the generic structure **4**) that can result when the combinatorial radical coupling reactions incorporate monolignol ferulates into lignin (fig. S2), but they are the only com-
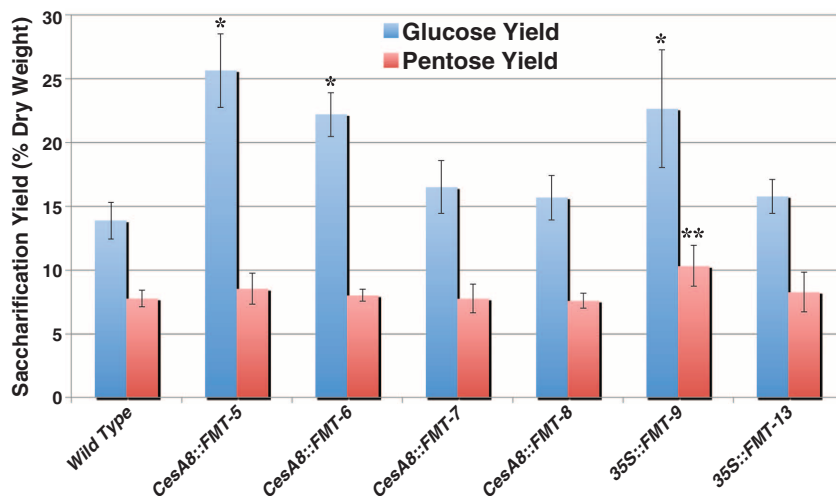
Fig. 4. Digestibility data on various mild alkaline–pretreated transgenic poplar lines compared to WT. Error bars indicate SD from the mean of triplicate determinations; *P < 0.01; **P < 0.005.

ponents that can generate the diagnostic product **8** (Fig. 3). The methodology does, however, permit confirmation that the trees have incorporated monolignol ferulates, at levels markedly above those of WT, into the lignin polymer by the radical coupling reactions that typify lignification (Fig. 1A). It also indicates that, like the natural monolignol *p*-coumarate analogs in grasses, these nonnative monolignol ferulate conjugates are transported intact to the lignifying zone. The GC-MS evidence (Fig. 3) that our transgenic poplars, particularly lines with the *FMT* gene driven by the xylem-specific *CesA8* promoter, are performing all of the biochemistry and chemistry desired is therefore compelling.

A key feature that allows the ensuing modified lignin to be depolymerized under mild conditions is the incorporation of the ferulate unit into the lignin backbone rather than simply existing as a pendant unit. Further insight into how well the conjugates are incorporated was revealed following an isotopically-labeled-reagent modification to the DFRC method (*22*). As delineated in fig. S8, 53% of the ferulate and 53% of the coniferyl alcohol moieties in the releasable conjugates were from phenol-etherified units, and 36% resulted from units that have both ends of the conjugate etherified. Because only a small fraction of units can release the conjugate and because the double bond in the coniferyl alcohol moiety implies that it is derived from a β-etherified unit, an etherified phenolic level comparable to that of guaiacyl monomers released by DFRC, determined in the same runs here at ~50%, confirms that the conjugate is incorporated into the lignin polymer about as well as a conventional monolignol.

Quantifying the level of conjugate incorporation is also a challenge. Currently, no method exists for the analogous quantification of the arabinoxylan-bound ferulates that are incorporated into grass lignins, and it has remained extremely difficult to even detect them, for example, by nuclear magnetic resonance (NMR), decades after their discovery

in part because of the huge range of combinatorial products (illustrated in fig. S2). An estimate (fig. S9 and table S4) can be made by using a model system in which isolated cell walls were ectopically lignified with coniferyl alcohol and 0, 20, 40, and 60% coniferyl ferulate (*18*). By plotting the release of the DFRC conjugate in the model system and those released from the current transgenic lines, we estimate that the *CesA8::FMT* poplar trees are incorporating ~7 to 23% of the ferulate conjugates **2** into their lignins.

The utility of lignins altered in such a fashion is ultimately determined by how well the ensuing cell walls containing these specialized conjugates can be processed industrially. Substantial improvements in saccharification after mild alkaline (6.25 mM NaOH, 90°C, 3 hours) pretreatment (*23*) are evident in the lines determined to contain high levels of transcripts, proteins, and lignified ferulate conjugates (Fig. 4).

The initial concept of inducing plants to use monolignol ferulate conjugates during lignification is realized here; our approach appears to be capable of producing plant materials that are designed for deconstruction. In a fundamental sense, it supports the idea that we can exploit the inherent metabolic plasticity of lignification (*4*) to alter lignins for societal benefit by inducing plants to synthesize novel phenolic monomers that are compatible with inherent plant biochemistry and development. The strategic introduction of ester bonds into the backbone of the lignin polymer is an advance that portends the production of crop plants in which cell wall deconstruction can be realized with reduced energy and/or chemical inputs.

References and Notes
1. X. Li, J. K. Weng, C. Chapple, *Plant J.* **54**, 569–581 (2008).
2. F. Chen, R. A. Dixon, *Nat. Biotechnol.* **25**, 759–761 (2007).
3. R. Vanholme, K. Morreel, J. Ralph, W. Boerjan, *Curr. Opin. Plant Biol.* **11**, 278–285 (2008).
4. J. Ralph *et al.*, *Phytochem. Rev.* **3**, 29 (2004).
5. W. Boerjan, J. Ralph, M. Baucher, *Annu. Rev. Plant Biol.* **54**, 519–546 (2003).
6. R. Vanholme *et al.*, *Science* **341**, 1103 (2013).
7. S. Withers *et al.*, *J. Biol. Chem.* **287**, 8347–8355 (2012).
8. E. Li *et al.*, *New Phytol.* **194**, 102–115 (2012).
9. R. Vanholme *et al.*, *New Phytol.* **196**, 978–1000 (2012).
10. J. Ralph, *Phytochem. Rev.* **9**, 65–83 (2010).
11. J. J. Stewart, T. Akiyama, C. Chapple, J. Ralph, S. D. Mansfield, *Plant Physiol.* **150**, 621–635 (2009).
12. N. D. Bonawitz *et al.*, *Nature*, 10.1038/nature13084 (2014).
13. F. Chen, Y. Tobimatsu, D. Havkin-Frenkel, R. A. Dixon, J. Ralph, *Proc. Natl. Acad. Sci. U.S.A.* **109**, 1772–1777 (2012).
14. R. Vanholme *et al.*, *Plant J.* **64**, 885–897 (2010).
15. J.-K. Weng, H. Mo, C. Chapple, *Plant J.* **64**, 898–911 (2010).
16. Q. Zhao *et al.*, *Proc. Natl. Acad. Sci. U.S.A.* **110**, 13660 (2013).
17. J. Ralph *et al.*, in *Recent Advances in Polyphenol Research*, F. Daayf, A. El Hadrami, L. Adam, G. M. Ballance, Eds. (Wiley-Blackwell, Oxford, 2008), vol. 1, pp. 36–66.
18. J. H. Grabber, R. D. Hatfield, F. Lu, J. Ralph, *Biomacromolecules* **9**, 2510–2516 (2008).
19. D. L. Petrik *et al.*, *Plant J.* **77**, 713–726 (2014).
20. J. J. Xie *et al.*, *Molecules* **14**, 555–565 (2009).
21. F. Lu, J. Ralph, *J. Agric. Food Chem.* **47**, 1988–1992 (1999).
22. P. T. Martone *et al.*, *Curr. Biol.* **19**, 169–175 (2009).
23. N. Santoro *et al.*, *Bioenergy Res.* **3**, 93–102 (2010).
24. Y. Zhu *et al.*, *RSC Adv.* **3**, 21964 (2013).
25. J. Ralph, J. H. Grabber, R. D. Hatfield, F. Lu, U. S. Patent 8,569,465 B2 (2013).
26. C. G. Wilkerson, J. Ralph, S. Withers, U.S. Patent 2013/0219547 (2013).
27. C. G. Wilkerson, J. Ralph, S. Withers, S. D. Mansfield, U.S. Patent 2013/0203973 (2013).

Supplementary Materials
www.sciencemag.org/content/344/6179/90/suppl/DC1
Materials and Methods
Supplementary Text
Figs. S1 to S9
Tables S1 to S4
References (*28–39*)

Optical Control of Muscle Function by Transplantation of Stem Cell–Derived Motor Neurons in Mice

J. Barney Bryson,[1] Carolina Barcellos Machado,[2]* Martin Crossley,[2]* Danielle Stevenson,[2]* Virginie Bros-Facer,[1] Juan Burrone,[2] Linda Greensmith,[1,3]†‡ Ivo Lieberam[2]†‡

Damage to the central nervous system caused by traumatic injury or neurological disorders can lead to permanent loss of voluntary motor function and muscle paralysis. Here, we describe an approach that circumvents central motor circuit pathology to restore specific skeletal muscle function. We generated murine embryonic stem cell–derived motor neurons that express the light-sensitive ion channel channelrhodopsin-2, which we then engrafted into partially denervated branches of the sciatic nerve of adult mice. These engrafted motor neurons not only reinnervated lower hind-limb muscles but also enabled their function to be restored in a controllable manner using optogenetic stimulation. This synthesis of regenerative medicine and optogenetics may be a successful strategy to restore muscle function after traumatic injury or disease.

Electrical stimulation of motor axons within peripheral nerves has been known to induce muscle contraction since Luigi Galvani's early experiments. In more recent times, phrenic nerve pacing has been used clinically to control the function of the diaphragm, the major muscle involved in respiration, in some patients with high-level spinal cord injury (1) or amyotrophic lateral sclerosis (ALS) (2). However, peripheral nerves are composed of efferent motor axons as well as afferent sensory axons (which are unaffected in ALS). Functional electrical stimulation, which stimulates nerves indiscriminately, can thus cause considerable discomfort (3). Furthermore, functional electrical stimulation is ineffective if axon integrity is compromised because of injury or degenerative disease. Other strategies to replace lost motor neurons within the central nervous system include the use of embryonic stem cells (ESCs), but ESC-derived neurons do not always integrate

into adult brain and spinal cord circuitry (4) and have difficulty overcoming molecular inhibitors of neuronal outgrowth (5) and extending axons across the barrier between the central and peripheral nervous system to reach the appropriate muscles (6).

It has previously been shown that motor neurons derived from ESCs can be engrafted into a peripheral nerve environment and successfully reinnervate denervated muscle (7). However, these engrafted cells are not connected to the descending inputs within the central nervous system that normally control motor function; therefore, their neural activity must be regulated by an artificial control system. Such engrafted ESC-derived motor neurons can be electrically stimulated (7), but this approach stimulates endogenous as well as engrafted neurons. In transgenic mice that express the light-sensitive ion channel channelrhodopsin-2 (ChR2) (8, 9) in endogenous motor neurons, it has been shown that the axons of these ChR2 motor neurons can be recruited by optical stimulation in a physiological and graded fashion, resulting in optogenetic control of muscle function (10). It has also been shown that viral expression of ChR2 in motor neurons of adult rats can enable optical stimulation of muscle function (11). In this study, we tested whether expression of ChR2 in ESC-derived motor neurons engrafted into a denervated peripheral nerve (i) confers optically regulated control of muscle function, without interfering with endogenous motor signals or afferent sensory axons, and (ii) enables physiological recruitment of motor units.

We generated genetically modified ESC-derived motor neurons that express both ChR2, to enable

[1]Sobell Department of Motor Neuroscience and Movement Disorders, University College London (UCL) Institute of Neurology, London, UK. [2]Medical Research Council (MRC) Centre for Developmental Neurobiology, King's College London, Guy's Hospital Campus, London, UK. [3]MRC Centre for Neuromuscular Diseases, UCL Institute of Neurology, London, UK.

*These authors contributed equally to this work.
†These authors contributed equally to this work.
‡Corresponding author. E-mail: l.greensmith@ucl.ac.uk (L.G.); ivo.lieberam@kcl.ac.uk (I.L.)

Fig. 1. Expression of Gdnf in ChR2 motor neurons enhances survival and enables them to mature electrically in vitro. (**A**) Embryoid bodies derived from *CAG::ChR2-YFP/Gdnf* transgenic ESCs and parental controls stained for the pan-motor neuron marker Isl1/2. GFP and YFP signals were detected by direct fluorescence. (**B**) Confocal images of MACS-sorted ESC motor neurons derived from *CAG::ChR2-YFP* (MACS, magnetic-activated cell sorting) and *CAG::ChR2-YFP/Gdnf* ESCs immunostained for Gdnf and GFP/YFP. (**C**) Survival analysis of sorted *CAG::ChR2-YFP* and *CAG::ChR2-YFP/Gdnf* ESC motor neurons (MNs) (200 cells per well) plated on ESC astrocytes at indicated time points. *CAG::ChR2-YFP* motor neurons were cultured with (10 ng/ml) or without recombinant Gdnf (two replicates, analysis of variance with Bonferroni correction, *P < 0.25). Error bars indicate SEM. One representative of three separate experiments is shown. Wt, wild type. (**D**) Optogenetic stimulation (blue bars) of *CAG::ChR2-YFP/Gdnf* ESC motor neurons cultured on ESC astrocytes. Scale bars in (A) and (B), 50 μm.

optical stimulation, as well as glial-derived neuro-trophic factor (Gdnf), a neurotrophic factor that promotes long-term motor neuron survival (see supplementary materials and methods). To develop such ESCs suitable for in vivo engraftment of ESC motor neurons, we stably transfected an established mouse ESC clonal cell line that already carried the motor neuron–specific reporter *Hb9::CD14-IRES-GFP* (GFP, green fluorescent protein) (*12*) with a photoreceptor transgene that is expressed regardless of cell type, *CAG::ChR2-YFP* (YFP, yellow fluorescent protein), and with the neurotrophin-expressing *CAG::Gdnf* trans-gene. Embryoid bodies derived from *CAG:ChR2-YFP/Gdnf* ESCs, which express ChR2-YFP in all cells including motor neurons (Fig. 1A), were differentiated in vitro using an established protocol (*13, 14*). *CAG::ChR2-YFP/Gdnf* motor neurons also produce Gdnf (Fig. 1B), which improves their long-term survival in vitro (Fig. 1C). When cultured on an ESC-derived astrocyte feeder layer (fig. S1), ChR2 motor neurons mature electrically over a period of 35 days, until they fire trains of action potentials in response to optical stimulation and closely resemble adult motor neuron activity patterns induced by electrical stimulation (*15*) (Fig. 1D and fig. S2).

After developing these ChR2 motor neurons, we next established an in vivo model to assess the feasibility of restoring muscle function with optical control of the engrafted cells, using the sciatic nerve. Muscle denervation was induced by sciatic nerve ligation in adult mice. This procedure results in a complete initial denervation, followed by limited regeneration of endogenous axons through the ligation site, thereby creating a partially denervated environment resembling the partial muscle denervation of early-stage ALS (fig. S3). Three days postligation, embryoid bodies containing ChR2 motor neurons were engrafted distal to the ligation into the tibial and common peroneal branches of the sciatic nerve. Histological analysis revealed that the engrafted ChR2 motor neurons not only survive for at least 35 days in the peripheral nerve environment (Fig. 2A), but also mature morphologically to resemble adult spinal motor neurons and express the mature motor neuron marker choline acetyltransferase (Fig. 2B). Immunodetection of ChR2-YFP, using an antibody to GFP, demonstrates that ChR2 is localized to the membrane of motor neurons, whereas direct detection of GFP versus YFP fluorescent signals reveals that Hb9-driven GFP expression is virtually absent in ChR2 motor neurons that have matured in vivo for 35 days (figs. S4 and S5). Additionally, ChR2 motor neurons extended large numbers of axons (Fig. 2C) distally toward both anterior [tibialis anterior (TA) and extensor digitorum longus (EDL)] and posterior [triceps surae (TS)] lower hind-limb muscles when grafted into the specific branches of the sciatic nerve that innervate these muscles. Engrafted ChR2 motor neuron axons, which grow alongside regenerating endogenous (YFP-negative) motor axons, are mostly myelinated (Fig. 2D). Histological analysis also revealed robust reinnervation of muscle fibers by ChR2 motor neurons, although the neuromuscular junctions exhibited hallmarks of inactivity, including poly-innervation as well as collateral and terminal axonal sprouting (*16*) (Fig. 2E), most likely because these motor neurons were inactive
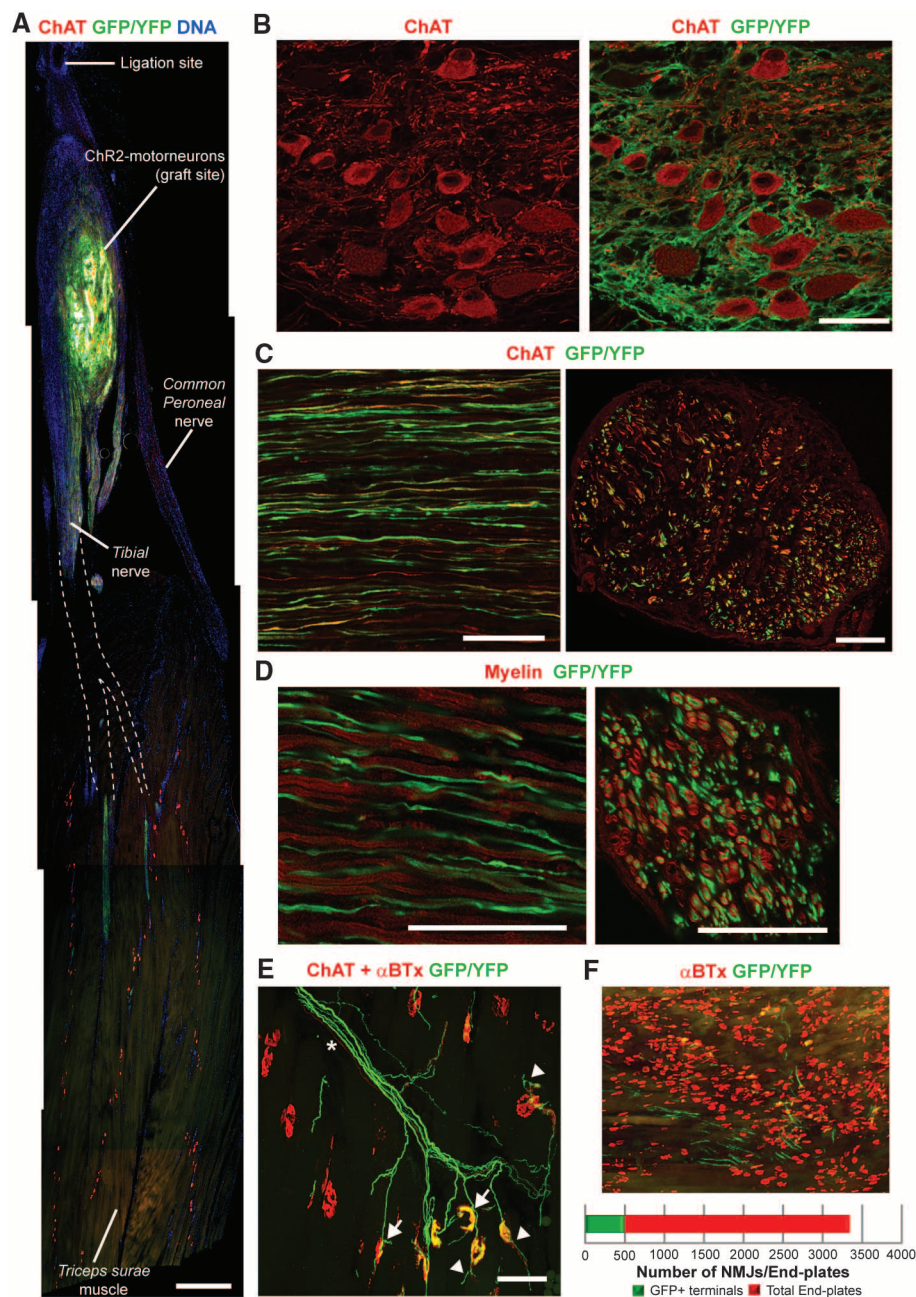
Fig. 2. Robust axonal growth and reinnervation of distal muscles after engraftment of ChR2 motor neurons. (**A**) Image montage of a whole nerve and muscle section showing ChR2 motor neuron cell bodies at the graft site and axon projection (dashed lines indicate approximate trajectory). Scale bar, 500 μm. (**B**) Confocal image of engrafted ChR2 motor neurons immunolabeled for choline acetyl-transferase (ChAT; left image) and GFP and/or YFP (merged image at right). Scale bar, 50 μm. (**C**) Confocal image of longitudinal and transverse common peroneal nerve sections showing both ChR2 motor neurons and endogenous axons. Scale bar, 50 μm. (**D**) Confocal images of engrafted ChR2 motor neuron axons showing myelination. Scale bar, 50 μm. (**E**) Confocal z-stack of ChR2 motor neuron axon terminals innervating multiple neuromuscular junctions within the TS muscle. Arrows indicate preterminal collateral sprouting, arrowheads denote terminal sprouting, and the asterisk indicates an endogenous motor axon. Scale bar, 50 μm. (**F**) Two-dimensional projection image of a TS muscle showing proportion of neuro-muscular junctions (NMJs) innervated by engrafted ChR2 motor neurons, relative to the total number of end plates present [labeled with α-bungarotoxin (αBTx)]. Quantification is shown below. Representative images shown here are compiled from *n* = 4 engrafted nerves from three separate experiments.

in vivo until stimulated by the external optical signal. Nevertheless, quantification of all end plates within a whole TS muscle revealed that 14.7% were innervated by YFP-positive ChR2 motor neurons axons after 35 days (Fig. 2F). Moreover, we observed YFP-positive neuromuscular junctions in both fast-twitch and slow-twitch regions of the TS, indicating that ChR2 motor neurons can innervate different muscle types. Therefore, this time point (35 days) was used in subsequent experiments to establish whether the transplanted ChR2 motor neurons were indeed functional and responsive to optical stimuli in vivo.

In anesthetized animals, we used isometric muscle tension physiology to examine the contractile responses elicited from TA, EDL, and TS (data summarized in table S1) muscles after optical stimulation of the exposed sciatic nerve using finely controlled pulses of 470-nm blue light generated by a light-emitting diode (LED) unit and delivered via a light-guide to the graft site (Fig. 3A and movie S1). Short-duration (14-ms) light pulses were able to induce submaximal twitch contrac-

tions in muscles innervated by transplanted ChR2 motor neurons (Fig. 3B), whereas high-frequency illumination (40 to 80 Hz) induced tetanic muscle contraction (Fig. 3C) that can be repeated in a highly reproducible manner (Fig. 3D). Quantification of these contractile responses demonstrated that the ratio of tetanic to twitch force was 3.09 ± 0.52 and 2.34 ± 0.33 for TA and EDL muscles, respectively (Fig. 3E), similar to normal values in uninjured animals.

Because nerve ligation enables regeneration of some endogenous motor axons, it was possible to directly compare the properties of these endogenous axons with those of the grafted ChR2 motor neurons by electrical nerve stimulation, which activates both populations of axons. This comparison demonstrated that the proportionate increase between twitch and tetanic stimuli after electrical stimulation was similar to that of optical stimulation [3.07 ± 0.5 and 2.96 ± 0.3 for TA and EDL muscles, respectively) (table S1)], although maximal force generation induced by optical stimulation of ChR2 motor neurons was weaker in

comparison with electrical recruitment of both ChR2-expressing and endogenous motor neurons (12.2% of electrically induced force for TA and 12.3% for EDL). It is likely that this reduced force output of muscle fibers innervated by ChR2 motor neurons reflects the 35-day period of inactivity preceding optical stimulation, as indicated by the findings of the histological analysis of these muscles, which showed the presence of axonal sprouting and poly-innervated end plates, characteristic features of inactive muscles (16). Sustained optical stimulation in vivo would probably lead to reinforcement of these neuromuscular junctions and a corresponding increase in force output. Analysis of muscle contractile characteristics also revealed that the latency to peak twitch contraction from initiation of the electrical trigger to the LED unit, or direct stimulation of the nerve, was identical for both optical and electrical stimulation (Fig. 3F). This finding indicates that the nerve conduction velocities were similar for both types of stimulation and supports the histological findings showing that axons of ChR2 motor
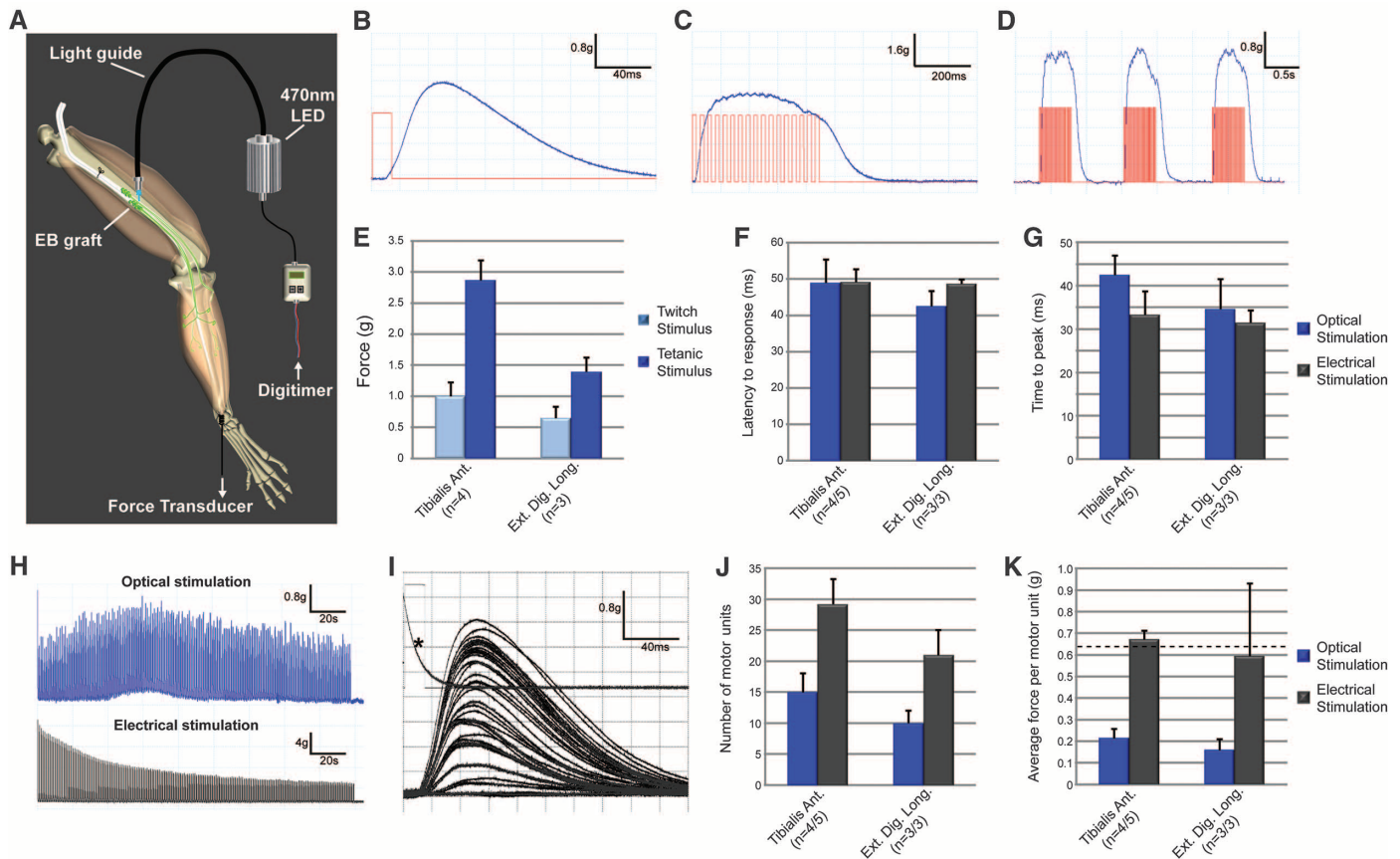
Fig. 3. Restoration of muscle function, in a controlled manner, using optical stimulation of engrafted ChR2 motor neurons in vivo. (**A**) Schematic showing optical stimulation and isometric muscle tension recordings. EB, embryoid body. Representative twitch (**B**), tetanic (**C**), and repetitive tetanic (**D**) contraction traces obtained from the TA muscle, induced by optical stimulation. Blue line, muscle force; red line, electrical trigger signals sent to the LED unit. (**E**) Quantification of twitch and tetanic contraction of TA and EDL muscles. Time to peak contractile force, from initiation of the electrical trigger to the LED unit (**F**) or from the initiation of muscle contraction (**G**), is shown

alongside direct electrical nerve stimulation (n values represent optical/electrical stimulation, respectively, compiled from four separate experiments). (**H**) Representative fatigue traces from TA muscles (different animals) produced by optical (top) or electrical (bottom) stimulation for 180 s. (**I**) Representative TA muscle optical stimulation motor-unit number estimate trace. The asterisk indicates square-wave trigger voltage to the LED unit and oscilloscope trigger. (**J**) Motor-unit number quantification of TA and EDL muscles after optical versus electrical stimulation. (**K**) Analysis of average motor-unit force. The dashed line indicates the normal EDL value. All error bars indicate SEM.

neurons are myelinated (Fig. 2D). Additionally, the contraction rate—that is, the time from initiation of muscle contraction to peak contraction—was also very similar (Fig. 3G) for both forms of stimulation. Repetitive trains of optical or electrical stimuli (40 Hz, 250-ms duration, every 1 s) were delivered for a period of 180 s to investigate the fatigue characteristics of the reinnervated muscles, which normally have a fast-twitch, fatigable phenotype. The results showed that muscle fibers innervated by grafted ChR2 motor neurons were fatigue-resistant, in contrast to muscle fibers activated by electrical stimulation (Fig. 3H). Again, this probably reflects the prolonged period of inactivity of ChR2 motor neurons before optical stimulation.

Simultaneous activation of all motor neurons innervating a specific muscle would result in inefficient spasmodic contraction and muscle fatigue. It is therefore important that motor neurons are recruited physiologically, according to their activation threshold, to generate a graded muscle contraction that is proportionate to the intended force output. Activation threshold is normally determined by motor neuron soma size (17), but in the case of optogenetic activation of motor neurons, axonal diameter and intermodal distance are also important factors (10, 18). With this in mind, it was important to determine whether grafted ChR2 motor neurons could also be recruited in a graded manner by optical stimulation to induce physiological motor-unit recruitment, where smaller motor units are recruited before larger motor units. To test this, the illumination intensity of the LED was varied from 0.8 to 8 mW/mm^2, which resulted in stochastic increases in muscle contractile force, demonstrating that different motor units could be recruited according to their optical activation threshold (Fig. 3I). This technique also enabled us to count the number of individual motor units innervating a given muscle, which for the TA muscle was 15 ± 3.03. Furthermore, by comparing optical and electrical nerve stimulation, we found that grafted ChR2 motor neurons accounted for ~50% of all motor units (Fig. 3J). Moreover, the motor-unit counts enabled us to calculate the average motor-unit force (Fig. 3K), which, after optical stimulation, was found to be 0.21 ± 0.04 g and 0.16 ± 0.05 g for TA and EDL muscles, respectively. Combined recruitment of endogenous and ChR2 motor neuron axons by electrical stimulation resulted in average motor-unit force values of 0.67 ± 0.04 g and 0.59 ± 0.34 g for TA and EDL muscles, respectively, consistent with normal motor-unit force (0.62 g).

In this study, we show that ChR2 motor neurons can be successfully transplanted into a peripheral nerve, where they can survive and extend axons that not only replace lost endogenous motor axons but also reinnervate denervated muscle fibers. Moreover, these transplanted ChR2 motor neurons can be selectively activated by 470-nm light, in a controlled manner to produce graded muscle contractions. Major challenges still remain before this approach can be established as an ef-

fective clinical intervention: These obstacles include the development of an implantable optical stimulator, such as that shown by Towne et al. (11), and a means to encapsulate the grafted cells. Additionally, incorporation of sensitive, red-shifted channelrhodopsin variants, such as ReaChR (19), rather than ChR2 would abrogate potential cellular toxicity associated with short-wavelength light (20).

These results show that through the use of a synthesis of regenerative medicine and optogenetics, it is possible to restore specific motor nerve functions. Although this study is largely a proof-of-principle study, it is possible that with further development this strategy may be of use in conditions where muscle function is lost—for example, after traumatic injury or neurodegenerative disease.

References and Notes

1. W. W. Glenn, M. L. Phelps, *Neurosurgery* 17, 974–984 (1985).
2. R. P. Onders et al., *Surg. Endosc.* 23, 1433–1440 (2009).
3. B. Gernandt, *Acta Physiol. Scand.* 12, 255–260 (1946).
4. S. C. Zhang, *J. Hematother. Stem Cell Res.* 12, 625–634 (2003).
5. M. T. Filbin, *Nat. Rev. Neurosci.* 4, 703–713 (2003).
6. J. M. Harper et al., *Proc. Natl. Acad. Sci. U.S.A.* 101, 7123–7128 (2004).
7. D. C. Yohn, G. B. Miles, V. F. Rafuse, R. M. Brownstone, *J. Neurosci.* 28, 12409–12418 (2008).
8. G. Nagel et al., *Proc. Natl. Acad. Sci. U.S.A.* 100, 13940–13945 (2003).
9. E. S. Boyden, F. Zhang, E. Bamberg, G. Nagel, K. Deisseroth, *Nat. Neurosci.* 8, 1263–1268 (2005).
10. M. E. Llewellyn, K. R. Thompson, K. Deisseroth, S. L. Delp, *Nat. Med.* 16, 1161–1165 (2010).
11. C. Towne, K. L. Montgomery, S. M. Iyer, K. Deisseroth, S. L. Delp, *PLOS ONE* 8, e72691 (2013).
12. C. B. Machado et al., *Development* 141, 784–794 (2014).
13. H. Wichterle, I. Lieberam, J. A. Porter, T. M. Jessell, *Cell* 110, 385–397 (2002).
14. M. Peljto, J. S. Dasen, E. O. Mazzoni, T. M. Jessell, H. Wichterle, *Cell Stem Cell* 7, 355–366 (2010).
15. L. Carrascal, J. L. Nieto-Gonzalez, W. E. Cameron, B. Torres, P. A. Nunez-Abades, *Brain Res. Brain Res. Rev.* 49, 377–387 (2005).
16. W. J. Thompson, *Cell. Mol. Neurobiol.* 5, 167–182 (1985).
17. E. Henneman, *Science* 126, 1345–1347 (1957).
18. J. Tønnesen, *Behav. Brain Res.* 255, 35–43 (2013).
19. J. Y. Lin, P. M. Knutsen, A. Muller, D. Kleinfeld, R. Y. Tsien, *Nat. Neurosci.* 16, 1499–1508 (2013).
20. P. E. Hockberger et al., *Proc. Natl. Acad. Sci. U.S.A.* 96, 6255–6260 (1999).

Neuronal Control of *Drosophila* Walking Direction

Salil S. Bidaye,* Christian Machacek, Yang Wu,† Barry J. Dickson†‡

Most land animals normally walk forward but switch to backward walking upon sensing an obstacle or danger in the path ahead. A change in walking direction is likely to be triggered by descending "command" neurons from the brain that act upon local motor circuits to alter the timing of leg muscle activation. Here we identify descending neurons for backward walking in *Drosophila*—the MDN neurons. MDN activity is required for flies to walk backward when they encounter an impassable barrier and is sufficient to trigger backward walking under conditions in which flies would otherwise walk forward. We also identify ascending neurons, MAN, that promote persistent backward walking, possibly by inhibiting forward walking. These findings provide an initial glimpse into the circuits and logic that control walking direction in *Drosophila*.

Walking relies on the intrinsic rhythmic activity of local motor circuits within the central nervous system, called central pattern generators (CPGs). Such locomotor circuits have been documented in a number of species, including cats (1), rodents (2), crayfish (3), stick insects (4), and cockroaches (5). Proprioceptive feedback from leg mechanosensors

ensures the accurate timing of each joint movement, but walking toward or away from specific targets requires descending signals from the brain. These descending inputs might act on CPGs to adjust the order, timing, or amplitude of individual leg movements (6, 7). The nature and identity of these descending commands are poorly understood.

We designed a thermogenetic screen in *Drosophila* to systematically identify any neurons that, upon activation, would change the fly's walking direction. This screen used a *UAS-trpA1* transgene to target expression of the thermosensitive cation channel TrpA1 (*8*) to arbitrary but stereotyped sets of neurons, as defined by the Vienna Tiles (VT) collection of *GAL4* driver lines. *VT-GAL4 UAS-trpA1* flies were placed in open 10-mm-diameter arenas and visually monitored for aberrant locomotion upon warming to ~30°C, the temperature at which the TrpA1 channel opens. From 3470 GAL4 lines screened, 4 were identified in which

Research Institute of Molecular Pathology (IMP), Dr. Bohrgasse 7, A-1030 Vienna, Austria.

*Present address: Department of Molecular and Cell Biology, University of California, Berkeley, CA 94720, USA.
†Present address: Janelia Farm Research Campus, Howard Hughes Medical Institute, 19700 Helix Drive, Ashburn, VA 20147, USA.
‡Corresponding author. E-mail: dicksonb@janelia.hhmi.org

Fig. 1. Activation and inhibition of backward walking. (**A**) Ring assay for locomotion direction and tracking sample for a fly walking predominantly forward in an anticlockwise direction. The black line indicates the fly's position in the ring (from 0° to 360°), and green and magenta indicate forward and backward walking, respectively. (**B**) Total distance walked in ring chamber during 5-min assay (*n* = 20 flies). Box-and-whisker plots in this and other panels show 10-, 25- 50-, 75-, and 90-percentiles. ***P < 0.0001 in comparison to *UAS-trpA1* controls. (**C** to **E**) Representative tracking data for ring walking assays. Each column shows tracking data for one fly for 5 min. (**F**) Linear walking assay and tracking sample. (**G**) Total distance walked during 10-min assays in linear (top, *n* = 24) and ring (bottom, *n* = 20) chambers. ***P < 0.0001 in comparison to *UAS-TNT* controls. (**H** and **I**) Representative tracking data for linear walking assays. Each column shows tracking data for one fly for 10 min.

flies walked backward in warmed chambers but not at the control temperature of ~24°C. Backward walking was most pronounced with the line *VT50660*, which was selected for further analysis (movie S1). We called this the "moonwalker" line. These flies walk backward by reversing both the order and timing of individual leg movements (fig. S1 and supplementary materials).

To facilitate a quantitative analysis of backward and forward walking, we designed two assay systems. The first uses a ringlike chamber in which flies are confined to a narrow circular groove of 2.5-mm width and 16-mm diameter (Fig. 1A). This chamber restricts the fly's lateral movement but leaves it unconstrained for forward or backward locomotion. We also developed computer software to automatically track the orientation and movement of individual flies (Fig. 1A). In these assays, *VT50660-GAL4 UAS-trpA1* flies predominantly and persistently walked backward at 30°C (Fig. 1, B to E, table S1, and movie S2).

The same flies tested at 22°C, or *UAS-trpA1* control flies tested at either temperature, rarely walked backward.

The second assay system uses a linear groove, 1.5 mm wide and 75 mm long, designed with the objective of inducing flies to walk backward (Fig. 1F). Stick insects walk backward upon mechanical stimulation of their antennae (*9*), suggesting that backward walking is used as a strategy to maneuver out of tight "dead ends." Upon reaching the end of the linear assay chamber, flies are similarly confronted with a dead end, and the chamber is too narrow for them to easily turn around and walk forward again in the opposite direction. We anticipated that, trapped in this way, flies too might walk backward, and if so, we could determine whether backward walking requires the activity of moonwalker neurons.

Control flies indeed walked backward for several millimeters upon reaching the end of the linear chamber (Fig. 1, G and I, table S2, and

VT50660-GAL4 UAS-mCD8-GFP

Anterior

Posterior

MDN (cell type 1)

MAN (cell type 7)

Fig. 2. Stochastic activation reveals moonwalker neurons. (A) Brain (left) and VNC (right) of a *VT50660-GAL4 UAS-mCD8-GFP* male stained with antibodies against GFP (anti-GFP) (yellow) and the synaptic marker monoclonal antibody nc82 (blue). (**B** to **D**) Partial segmentations of single neurons representing each of seven neuronal classes that compose the *VT50660* pattern, following nonrigid registration onto common reference templates. (**E**) Frequency of labeling for each cell type in moonwalker and nonmoonwalker flies. ***P < 0.0001, Fisher's exact test. (**F** and **G**) Single MDN and MAN neurons stained with anti-GFP (yellow), with nc82 counterstain (blue), and registered onto a common reference template. Samples were obtained during stochastic labeling experiments with *UAS>stop>mCD8-GFP*. (**H**) Overlaid registered segmentations of single MDN and MAN cells.

MDN+MAN-1-GAL4 UAS-mCD8-GFP

MDN-1-GAL4 UAS-mCD8-GFP

MAN-1-GAL4 UAS-mCD8-GFP

MDN-1-GAL4 UAS-Syt-GFP UAS-DenMark

MAN-1-GAL4 UAS-Syt-GFP UAS-DenMark
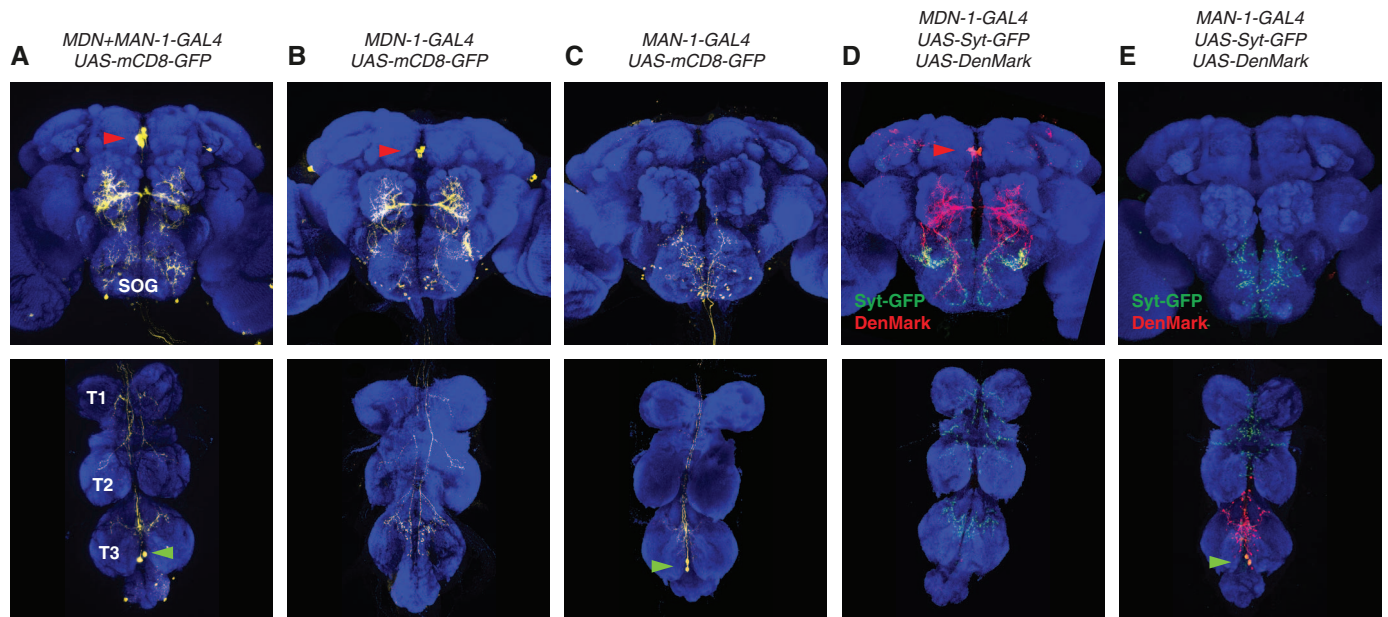
Fig. 3. Split-GAL4 combinations for MDN and MAN. (A to **C)** Brains (top) and ventral nerve cords (VNCs, bottom) of flies carrying the indicated split-GAL4 combination and *UAS-mCD8-GFP*, stained with anti-GFP (yellow) and nc82 (blue). Red and green arrowheads indicate MDN and MAN soma, respectively. SOG, subesophageal ganglion; T1 to T3, leg neuropils. (**D** and **E**) Brains (top) and VNCs (bottom) of flies in which the indicated split-GAL4 combination drives expression of *UAS-syt-GFP* and *UAS-DenMark* reporters, stained with anti-GFP (green, presynaptic), anti-DsRed (DenMark, red, postsynaptic), and nc82 (blue).

movie S3). To test whether moonwalker neurons contribute to this backward walking, we combined *VT50660-GAL4* with a *UAS-TNT* transgene, which encodes an inhibitor of synaptic transmission (*10*). In contrast to control flies, *VT50660-GAL4 UAS-TNT* flies rarely backed up when they reached the end of the chamber (Fig. 1, G and H, table S2, and movie S3). Rather, they typically stalled there, often for several minutes, before eventually squeezing around to walk forward again in the opposite direction. The same behavior was observed upon acute silencing in adult flies (fig. S2). In linear chambers, *VT50660-GAL4 UAS-TNT* flies also walked forward less than control flies (Fig. 1G), but this was due to the extended periods they spent stuck at the ends of the chamber. In circular chambers, in which forward walking is unimpeded, *VT50660-GAL4 UAS-TNT* walked forward at least as much as control flies (Fig. 1G and table S3). Thus, the activity of moonwalker neurons is essential for backward but not forward locomotion.

VT50660-GAL4 reproducibly labels seven distinct cell types in the central nervous system (Fig. 2, A to D, and fig. S3, A to E). We expressed an epitope-tagged TrpA1[c-myc] in random subsets of these cells, tested them for moonwalking at 30°C, and then dissected and stained the central nervous systems of individual flies to determine in which cells TrpA1[c-myc] was expressed (supplementary materials). Two cell types were bilaterally labeled in most of the moonwalkers (33 of 36) and in none of the non-moonwalkers (0 of 34; Fig. 2E and fig. S3F). One of these is a descending neuron, which we refer to as MDN (moonwalker descending neuron; Fig. 2, F and H); the other is an ascending neuron, MAN (moonwalker ascending neuron; Fig. 2, G and H). All other cell types were equally often labeled in both moonwalking and non-moonwalking flies (Fig. 2E). Moreover, of 17 flies in which only MDN or MAN was bilaterally labeled, but not both, only 3 were scored as moonwalkers (fig. S3F). We conclude from these data that sustained backward walking requires the coactivation of both MDN and MAN.

To reproducibly and specifically target transgene expression to these two cell types, we used the split-GAL4 system (*11*, *12*) to derive a set of four drivers that target MDN but not MAN (*MDN-1-4*), four that target MAN but not MDN (*MAN-1-4*), and two that target both (*MDN+MAN-1-2*; Fig. 3 and fig. S4, table S4, and supplementary materials). We first used these split-GAL4 reagents to further characterize the anatomy of MDN and MAN, by driving expression of the membrane marker mCD8-GFP (green fluorescent protein) (*13*), the dendritic marker DenMark (*14*), or the presynaptic marker syt-GFP (*15*). We typically observed two MDN cells per hemisphere, with their soma in the medial posterior protocerebrum, bilateral dendritic arborizations in the medial ventral protocerebrum and subesophageal ganglion (SOG), and axons that extend down to the contralateral thoracic ganglia (Fig. 3D). Presynaptic sites of MDN were observed in the SOG and in each of the leg neuropils. One MAN cell was observed on each side of the midline in the metathoracic (hindleg) ganglion, where its dendrites are also located. MAN sends an axon to the brain, with its predominant presynaptic sites in close proximity to MDN dendrites in the medial SOG (Fig. 3E). Some presynaptic sites for MAN were also observed within the nerve cord, in both the metathoracic ganglion and the wing neuropil.

In functional assays, we found that both of the *MDN+MAN* combinations recapitulated the activation and silencing phenotypes we had previously
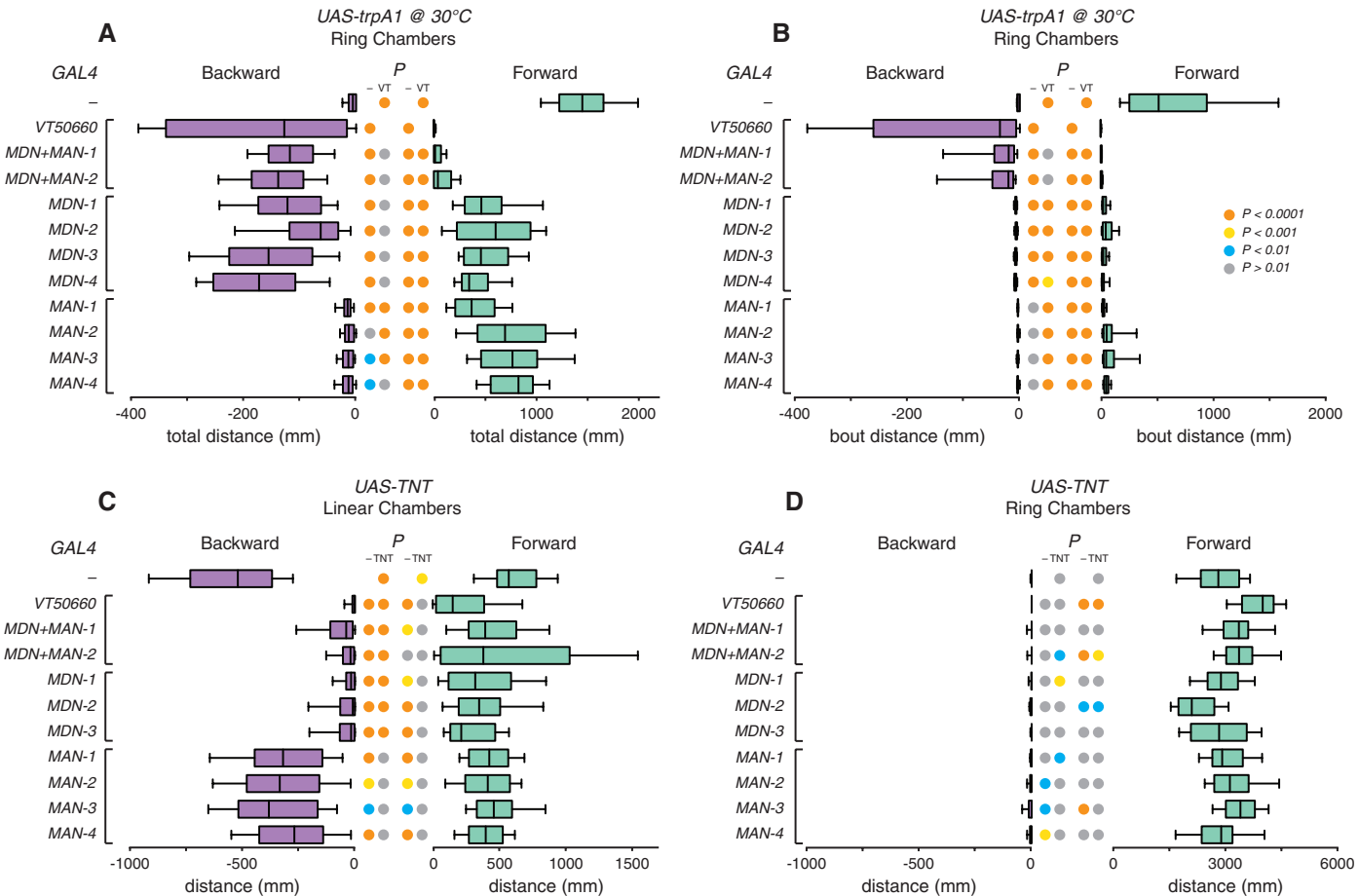
Fig. 4. Distinct functions of MDN and MAN in the control of walking direction. (**A** and **B**) Total walking distance (A) and mean distance per bout (B) in 5-min assays in ring chambers (*n* = 20 to 58). Colored dots show *P* values for comparisons to no *GAL4* (−) and *VT50660-GAL4 UAS-trpA1* (VT) controls. (**C** and **D**) Total walking distance in 10-min assays in linear chambers [(C), *n* = 16 to 60] and 10-min assays in ring chambers [(D), *n* = 18 to 66]. Colored dots show *P* values for comparisons to no *GAL4* (−) and no *UAS-TNT* (TNT) controls.

observed with the original *VT50660* moonwalker line (Fig. 4 and fig. S5, tables S5 to S8, and movies S6 and S7). Moreover, activation of MDN alone was sufficient to induce backward walking (Figs. 4A and fig. S5B, table S5, and movie 6), and synaptic silencing of MDN almost completely blocked backward walking (Fig. 4C and fig. S5E, table S7, and movie S7). Silencing of MDN did not disrupt forward walking (Fig. 4D and table S8). In contrast, activation (Fig. 4A and fig. S5C, table S5, and movie S6) and silencing (Fig. 4C and fig. S5F, table S7, and movie 7) of MAN had little, if any, effect on backward walking. We thus conclude that MDN activity alone is both necessary and sufficient to trigger backward walking.

Nonetheless, our stochastic activation experiments, in which we had selected the most persistent backward walkers, suggested that MAN activation does somehow facilitate sustained backward walking. Indeed, in the ring chambers, although flies in which MDN alone was activated walked backward for total distances similar to those in which both MDN and MAN were activated (Fig. 4A and table S5), backward walking was more sustained when both cell types were activated (Fig. 4B, table S6, and movie S6). Average bout distances for backward walking were <10 mm for MDN activation but >40 mm for MDN+MAN activation. These observations suggest that MAN might promote backward walking, either by inhibiting the natural tendency to walk forward or by maintaining the backward walking state induced upon activation of MDN. To discriminate between these possibilities, we examined the forward-walking behavior of flies in which MAN was either activated or silenced. Silencing MAN had no consistent effect on forward locomotion (Fig. 4D and tables S7 and S8), but activating MAN induced frequent stalling and hence reduced bout lengths (Fig. 4B and fig. S5C, and tables S5 and S6). These data favor a model in which MAN activity inhibits forward locomotion. Accordingly, activation of both MDN and MAN is necessary for the persistent backward walking that characterizes the "moonwalker" phenotype.

In summary, we have identified a descending neuron, MDN, that triggers backward walking in flies. Persistent backward walking is facilitated by MAN, an ascending neuron that appears to inhibit forward walking. MDN resembles the DBNc1-2 or DBNc2-2 neurons in crickets (*16*) and the DMIa-1 neuron in cockroaches (*17*), all of which respond with short latency (<8 ms) to mechanical stimulation of the antennae. MDN might similarly receive direct synaptic input from antennal or other head mechanoreceptors. Analogous circuits mediate backward crawling in *Caenorhabditis elegans*, with the AVA command interneurons receiving input from head mechanosensory neurons as well as upstream interneurons (*18*).

MDN activation reverses both the sequence and phase of leg movements, suggesting that it might flip a critical switch within the premotor circuits of the thoracic ganglia. In stick insects,

backward walking is brought about by a switch in phase of the two muscles that operate the thorax-coxa joint, the protractor and retractor (*19*). In forward walking, loading of the leg during stance phase leads to activation of the retractor, pushing the leg back. Unloading activates the protractor, bringing the leg forward in swing phase. In backward walking, these proprioceptive inputs are reversed: Loading activates the protractor and unloading, the retractor. A descending neuron for backward locomotion could potentially induce this switch, directly or indirectly, by providing presynaptic inhibition onto the excitatory outputs of core CPG interneurons (*20*), thereby reversing the sign of feedback signals from the load sensors on the legs (*21*).

Is there an antagonistic counterpart to MDN that would trigger forward locomotion, as proposed on theoretical grounds (*20*) and analogous to the AVB command interneurons in *C. elegans* (*18*)? Or might the thoracic locomotor circuits instead operate by default in the forward mode, requiring only a single descending signal to discriminate between backward and forward walking? Although its function is presently less clear, we suggest that MAN stabilizes the switch to backward walking by inhibiting a default forward-walking state. The identification of MDN and MAN provides a first glimpse into the nature and logic of the signals that pass between the brain and local motor circuits, steering the animal toward or away from specific targets.

References and Notes

1. T. G. Brown, *Proc. R. Soc. Lond. B Biol. Sci.* **84**, 308–319 (1911).
2. O. Kiehn, *Annu. Rev. Neurosci.* **29**, 279–306 (2006).
3. A. Chrachri, F. Clarac, *Neurosci. Lett.* **77**, 49–54 (1987).
4. A. Büschges, J. Schmitz, U. Bassler, *J. Exp. Biol.* **198**, 435–456 (1995).
5. K. G. Pearson, *J. Exp. Biol.* **56**, 173 (1972).
6. L. Mu, R. E. Ritzmann, *J. Comp. Physiol. A Neuroethol. Sens. Neural Behav. Physiol.* **194**, 283–298 (2008).
7. L. Mu, R. E. Ritzmann, *J. Comp. Physiol. A Neuroethol. Sens. Neural Behav. Physiol.* **194**, 299–312 (2008).
8. F. N. Hamada *et al.*, *Nature* **454**, 217–220 (2008).
9. D. Graham, S. Epstein, *J. Exp. Biol.* **118**, 287 (1985).
10. S. T. Sweeney, K. Broadie, J. Keane, H. Niemann, C. J. O'Kane, *Neuron* **14**, 341–351 (1995).
11. H. Luan, N. C. Peabody, C. R. Vinson, B. H. White, *Neuron* **52**, 425–436 (2006).
12. B. D. Pfeiffer *et al.*, *Genetics* **186**, 735–755 (2010).
13. T. Lee, L. Luo, *Neuron* **22**, 451–461 (1999).
14. L. J. Nicolaï *et al.*, *Proc. Natl. Acad. Sci. U.S.A.* **107**, 20553–20558 (2010).
15. Y. Q. Zhang, C. K. Rodesch, K. Broadie, *Genesis* **34**, 142–145 (2002).
16. S. Schöneich, K. Schildberger, P. A. Stevenson, *J. Comp. Neurol.* **519**, 1677–1690 (2011).
17. J. A. Burdohan, C. M. Comer, *J. Neurosci.* **16**, 5830–5843 (1996).
18. M. Chalfie *et al.*, *J. Neurosci.* **5**, 956–964 (1985).
19. P. Rosenbaum, A. Wosnitza, A. Büschges, M. Gruhn, *J. Neurophysiol.* **104**, 1681–1695 (2010).
20. T. I. Tóth, S. Knops, S. Daun-Gruhn, *J. Neurophysiol.* **107**, 3267–3280 (2012).
21. T. Akay, B. Ch. Ludwar, M. L. Göritz, J. Schmitz, A. Büschges, *J. Neurosci.* **27**, 3285–3294 (2007).

SRP RNA Remodeling by SRP68 Explains Its Role in Protein Translocation

Jan Timo Grotwinkel,* Klemens Wild,* Bernd Segnitz, Irmgard Sinning†

The signal recognition particle (SRP) is central to membrane protein targeting; SRP RNA is essential for SRP assembly, elongation arrest, and activation of SRP guanosine triphosphatases. In eukaryotes, SRP function relies on the SRP68-SRP72 heterodimer. We present the crystal structures of the RNA-binding domain of SRP68 (SRP68-RBD) alone and in complex with SRP RNA and SRP19. SRP68-RBD is a tetratricopeptide-like module that binds to a RNA three-way junction, bends the RNA, and inserts an α-helical arginine-rich motif (ARM) into the major groove. The ARM opens the conserved 5f RNA loop, which in ribosome-bound SRP establishes a contact to ribosomal RNA. Our data provide the structural basis for eukaryote-specific, SRP68-driven RNA remodeling required for protein translocation.

Membrane protein insertion critically depends on the signal recognition particle (SRP) (*1*, *2*). SRP binds to nascent chains emerging from the ribosomal exit tunnel and guides the ribosome–nascent chain complex

(RNC) to the translocation pore by interaction with the membrane-bound SRP receptor (SR; SRαβ in eukaryotes, FtsY in bacteria). Eukaryotic SRP is typically composed of SRP RNA (7SL RNA) and six protein subunits: SRP9, SRP14, SRP19, SRP54,

SRP68, and SRP72 (Fig. 1A). It comprises the Alu domain, responsible for elongation retardation during translation, and the S domain, which binds to the N-terminal signal sequence in newly synthesized proteins via SRP54 (Ffh in bacteria) and regulates the targeting process by SRP-SR interaction (3). The two SRP guanosine triphosphatases (GTPases), SRP54 and SRα, belong to the SIMIBI family of nucleotide triphosphate binding proteins (4) and form a quasi-symmetric heterodimer (the targeting complex) with a composite active center (5–7). For bacterial SRP, the SRP RNA was shown to constitute a molecular switch that promotes targeting complex formation and stimulates GTP hydrolysis (8–11).

SRP68 and SRP72 form a stable heterodimer in solution (12, 13) and are present in the cytosol as well as in the nucleolus (14). Because pre-SRP cannot be exported from the nucleus without SRP68 and SRP72 bound (15), a role in SRP assembly and transport was postulated. Systematic mutagenesis (16, 17) and RNA-protein footprinting (18) showed that human SRP68, SRP72, and SRP

Heidelberg University Biochemistry Center (BZH), INF 328, D-69120 Heidelberg, Germany.

*These authors contributed equally to this work.
†Corresponding author. E-mail: irmi.sinning@bzh.uni-heidelberg.de

RNA interact with each other independently. Specific RNA binding of SRP68 is mediated by the N-terminal domain of about 200 residues (17). SRP reconstituted without the SRP68-SRP72 heterodimer (henceforth SRP68/72) lacks elongation arrest activity and is inactive in translocation (19). In cryo–electron microscopy (cryo-EM) structures of SRP and SR bound to the RNC, extra mass attributed to the SRP68/72 heterodimer locates at the three-way junction linking helices 5, 6, and 8 of the SRP RNA and to the hinge between the Alu and S domains (20, 21). However, these data could not be interpreted because structural information about SRP68/72 was absent.

To understand the role of SRP68 in protein targeting, we determined the structure of the human SRP68 RNA-binding domain (RBD, residues 39 to 246) at 1.7 Å resolution (table S1 and fig. S1) by molecular replacement with a previously determined structure from the thermophilic fungus *Chaetomium thermophilum* (ctSRP68-RBD; residues 1 to 217) (table S2). Despite a sequence homology between the mammalian and fungal proteins of less than 30% (fig. S2), the fold of SRP68-RBD is highly conserved (fig. S3). SRP68-RBD comprises seven antiparallel α helices, α1 to α7, and an extended loop region (the L2 loop) (Fig. 1B and fig. S2). The fold of SRP68-RBD does not resemble any classical RNA-binding domain (22)

and has similarity to a tetratricopeptide repeat (TPR) domain (23) (fig. S4). The kinked helix α7 opens a hydrophobic groove, which could accommodate an extra α helix (fig. S5). Electrostatic surface calculations show a positively charged patch formed by helices α2 to α4 and the L2 loop (Fig. 1C), which is largely preserved (Fig. 1D) and is suitable for RNA binding.

As a next step, we determined the structure of a ternary complex consisting of human SRP19, SRP68-RBD, and 125 nucleotides of S-domain SRP RNA (nucleotides 114 to 238) at 3.5 Å resolution (table S1 and fig. S6A). SRP68-RBD binds to the three-way junction of SRP RNA helices 5, 6, and 8 as a rigid body (Fig. 2A and fig. S6, B and C). The positively charged patch of SRP68-RBD interacts with the SRP RNA (interface of 1175 Å²) and the structure agrees with previous biochemical probing data (18) (Fig. 2B). Binding occurs mainly to the phosphoribose backbone, which implies shape recognition of the RNA rather than specific interactions with nucleotides. The three helices α2 to α4 form a concave surface filling the hollow created by the junction, with helix α2 protruding into the major groove of helix 5 at the 5f loop, central helix α3 bridging over the junction, and helix α4 being accommodated in a so-called T-loop structure (24) (Fig. 2A and fig. S7). Adjacent to the T loop, A176 is bulged out of
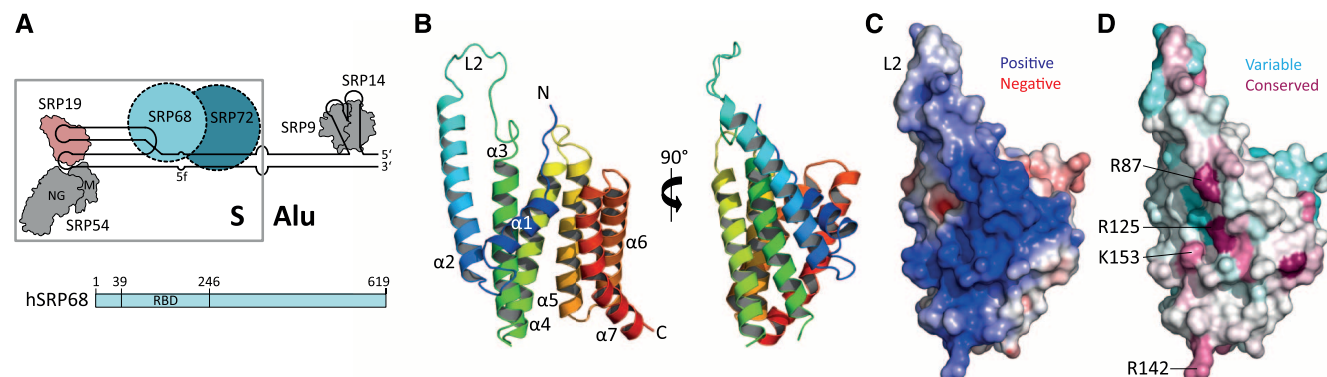
Fig. 1. Structure of SRP68-RBD. (**A**) Scheme of eukaryotic SRP. The human SRP68 RNA-binding domain (RBD) is indicated. (**B**) Overall structure of TPR-like human SRP68-RBD (rainbow). (**C**) Electrostatic surface potential (±5k_BT) highlighting the positively charged patch. (**D**) Sequence conservation within the patch. Amino acid abbreviations: K, Lys; R, Arg.
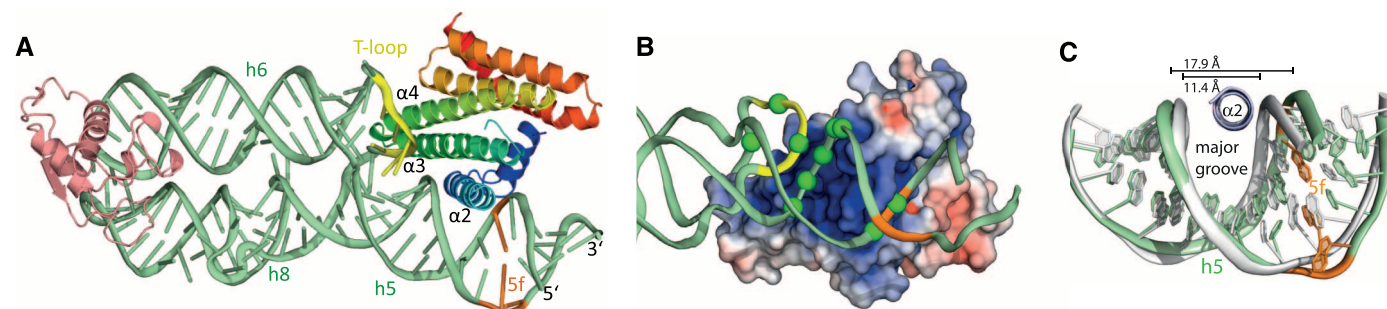
Fig. 2. Structure of the ternary complex. (**A**) Structure of the SRP RNA S domain bound to SRP19 (salmon) and SRP68-RBD (rainbow). SRP RNA helices are denoted h5 to h8; orange, 5f loop; yellow, T loop. (**B**) SRP RNA–SRP68-RBD interface [rotated 90° relative to (A); electrostatics ±5k_BT]. Green spheres indicate phosphate groups protected in chemical probing (18). (**C**) Major groove opening in RNA helix 5 by ARM motif insertion; gray area denotes SRP RNA without SRP68-RBD (28).

helix 8 and fixed by base triple formation with a wobble base pair in helix 6 (U132-G165) and by π-cation stacking interaction with Arg[142] of helix α4 (fig. S7B). Relevant binding determinants were identified by mutational analyses for both SRP68-RBD and the SRP RNA (fig. S8).

The deep and narrow major groove in A-RNA helices is rather inaccessible for recognition (25). Bulge-loops of at least two nucleotides increase the recognizability, enabling the insertion of α helices, as known for arginine-rich motifs (ARMs) (26). The 5f loop of eukaryotic SRP RNA is an asymmetric internal bulge-loop with two conserved purines (human: A231, G232) opposite a single adenine (A119) (27). In a previously solved SRP S-domain structure without SRP68-RBD (28), all bases are hidden in the helical stack. The insertion of 17 residues of SRP68-RBD helix α2 (73 to 89) deeply into the major groove at the 5f loop causes a drastic groove opening by more than 6 Å (50%) (Fig. 2C). Helix α2 contains a cluster of conserved arginine residues matching the determinants of the ARM in the HIV protein Rev, and superposition of the respective inserted helices reveals a striking similarity and the general principle of this interaction (fig. S9). Although a detailed analysis requires higher-resolution data,

it is evident that Arg[84] and Arg[85] penetrate deepest into the groove and likely provide a base-specific readout.

The ARM contact not only opens the major groove of helix 5 but also induces a restructuring of the 5f loop. Despite the limited resolution, density for the 5f loop can only be explained by fitting two alternative backbone conformations (fig. S10), which are both different from the "closed" 5f loop without SRP68-RBD (28) and indicate a successive opening of the bulge (fig. S11). Opening results in exposure of two purines (A231, G232). Notably, in prokaryotes, a single nucleotide is bulged out from the SRP RNA at the "distal interaction site" (loop D, corresponding to the 5f loop) (fig. S12). In *Escherichia coli*, insertion of this nucleotide into the interface of the targeting complex activates GTP hydrolysis (11, 29). If this mechanism is conserved in eukaryotes, the targeting complex should bind to the restructured 5f loop. In the eukaryotic RNC-SRP-SR cryo-EM structure (30), additional density was observed adjacent to SRP68-RBD at the 5f loop (figs. S13 and S14). Binding of the targeting complex to this site would explain inhibition of protein translocation and of SR binding observed upon SRP68/72 alkylation (31).

To further analyze the functional relevance of SRP RNA remodeling by SRP68-RBD, we compared the ternary SRP RNA–SRP19–SRP68-RBD complex with S-domain complexes lacking the SRP68-RBD (28, 32). Comparison reveals not only the local changes described above, but also a different overall shape of the RNA (Fig. 3A). Although the tips of helices 6 and 8 and the closing tetraloops are unchanged, the distal ends of the helices together with helix 5 become restructured. SRP68-RBD causes bending of helix 5 with respect to the coaxially stacked helix 8 by about 20° away from helix 6. The break point locates next to the conserved tertiary RNA-RNA interaction at an internal asymmetric loop of helix 8 that is important for binding the SRP54 M domain (28). Binding of SRP68-RBD results in the stabilization of the three-way junction, as manifested by the decrease of the atomic displacement parameters (fig. S15A).

In the next step, we fitted our x-ray structure into the electron density map of mammalian SRP bound to wheat germ RNC previously obtained by cryo-EM (20, 21) (Fig. 3B). In this complex, SRP wraps around the large ribosomal subunit with the S domain covering the polypeptide exit tunnel and the Alu domain occupying the "factor
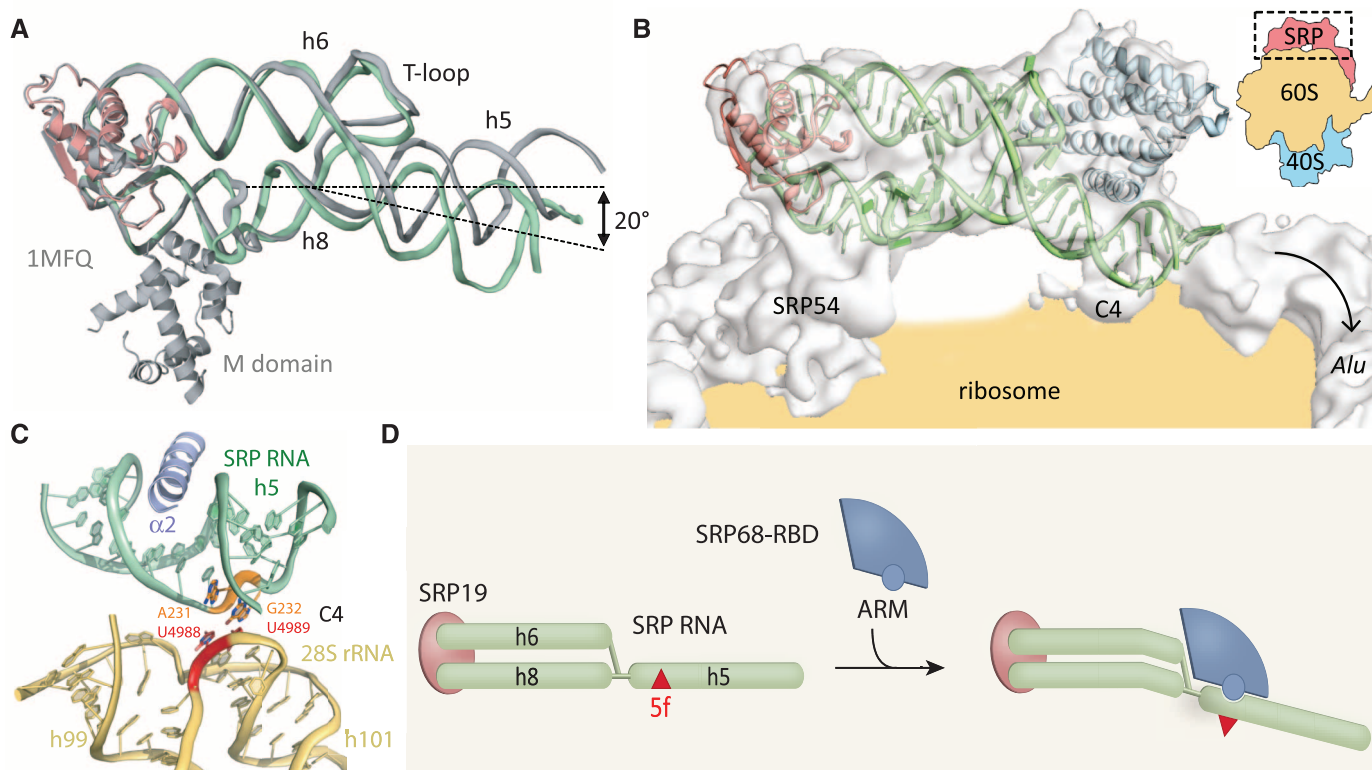
Fig. 3. Consequences of SRP RNA remodeling for RNC binding. (**A**) Superposition of the ternary complex (SRP68-RBD not shown) with the S-domain structure without SRP68 [gray (28)] based on SRP19 (salmon). The dashed lines highlight SRP68-RBD–induced bending of the SRP RNA. (**B**) Structure of the ternary complex (SRP68-RBD, blue) fitted into the cryo-EM density of mammalian SRP-RNC (21). The inset indicates SRP on the ribosome. C4 denotes the only direct contact between SRP RNA and the ribosome (20). (**C**) Model of the C4 contact of human RNC-bound SRP (21, 33). The bulged-out bases of the "open" 5f loop (A231, G232) are in close contact with two unpaired uridines (red) in the 3′-terminal three-way junction of 28S rRNA (yellow). (**D**) Scheme of SRP RNA remodeling by SRP68. Binding of SRP68-RBD (blue) at the three-way junction causes RNA bending, and the 5f loop (red triangle) bulges out upon ARM insertion, enabling the C4 contact observed in the RNC-SRP complex.

binding site" in the 40S-60S interface. Although the EM structure contains the entire SRP68/72 proteins, the bulk of the heterodimer seems flexible and does not give rise to defined electron density. Extra density observed at the SRP RNA three-way junction can be fitted with the rigidly bound SRP68-RBD. Note that the remodeled SRP S domain including SRP68-RBD perfectly fits the EM density (21), whereas the previously docked structure without SRP68-RBD (28) does not fit at helix 5 (fig. S15B). This shows that RNA bending occurs upon binding of SRP68-RBD and not upon RNC-SRP interaction. At long range, bending of SRP RNA allows the Alu domain to touch down at the 40S-60S interface and might explain the previous observation that SRP lacking SRP68/72 has lost its elongation arrest function (19). At short range, bending enables the only contact established between S-domain RNA and the ribosome (C4 connection) (20), which involves the 3′-terminal helices (helices 99 to 101) of 28S ribosomal RNA (rRNA) (Fig. 3C). Notably, within this ribosomal three-way junction, pyrimidine bases are bulged out [U4988 and U4989 in human 28S rRNA (33)] that could be readily involved in forming base pairs with the two purines in the "open" 5f loop of SRP RNA. Intriguingly, SR binding to the RNC-SRP complex (30) induces a 10° rotation of SRP around SRP RNA helix 8, modifying the C4 contact (figs. S14 and S16).

Eukaryotic SRP assembly is a hierarchical process (12, 15) with SRP68/72 being required for export from the nucleus (12), and recruitment of SRP54 as the last component in the cytosol ensures that only complete SRP is ready for productive RNC interaction. SRP68-driven remodeling of the SRP RNA is of key importance for SRP structure and function. SRP68 bends the S-domain RNA and restructures the 5f loop (Fig. 3D), which enables a direct RNA-RNA contact with the ribosome. The presentation of bulged-out nucleotides on a rigid SRP RNA scaffold is conserved, which suggests that the molecular details of their interaction with the targeting complex apply to all kingdoms of life. Although our understanding of SRP-mediated protein translocation is rather advanced, outstanding questions specifically for eukaryotic SRP concern the remaining, flexible part of the SRP68/72 heterodimer, the role of the SRβ GTPase in protein translocation, and the mechanism of SRP GTPase activation. Structural and biochemical studies are likely to bring future surprises.

References and Notes

1. Y. Nyathi, B. M. Wilkinson, M. R. Pool, *Biochim. Biophys. Acta* **1833**, 2392–2402 (2013).
2. D. Akopian, K. Shen, X. Zhang, S. O. Shan, *Annu. Rev. Biochem.* **82**, 693–721 (2013).
3. P. Walter, R. Gilmore, G. Blobel, *Cell* **38**, 5–8 (1984).
4. D. D. Leipe, Y. I. Wolf, E. V. Koonin, L. Aravind, *J. Mol. Biol.* **317**, 41–72 (2002).
5. G. Bange, I. Sinning, *Nat. Struct. Mol. Biol.* **20**, 776–780 (2013).
6. P. F. Egea *et al.*, *Nature* **427**, 215–221 (2004).
7. P. J. Focia, I. V. Shepotinovskaya, J. A. Seidler, D. M. Freymann, *Science* **303**, 373–377 (2004).
8. S. F. Ataide *et al.*, *Science* **331**, 881–886 (2011).
9. K. Shen, X. Zhang, S. O. Shan, *RNA* **17**, 892–902 (2011).
10. N. Bradshaw, S. B. Neher, D. S. Booth, P. Walter, *Science* **323**, 127–130 (2009).
11. F. Voigts-Hoffmann *et al.*, *Mol. Cell* **52**, 643–654 (2013).
12. E. Iakhiaeva, C. S. Hinck, A. P. Hinck, C. Zwieb, *Protein Sci.* **18**, 2183–2195 (2009).
13. E. Scoulica, E. Krause, K. Meese, B. Dobberstein, *Eur. J. Biochem.* **163**, 519–528 (1987).
14. J. C. Politz *et al.*, *Proc. Natl. Acad. Sci. U.S.A.* **97**, 55–60 (2000).
15. H. Grosshans, K. Deinert, E. Hurt, G. Simos, *J. Cell Biol.* **153**, 745–762 (2001).
16. J. Yin, E. Iakhiaeva, E. Menichelli, C. Zwieb, *RNA Biol.* **4**, 154–159 (2007).
17. E. Iakhiaeva, S. H. Bhuiyan, J. Yin, C. Zwieb, *Protein Sci.* **15**, 1290–1302 (2006).
18. E. Menichelli, C. Isel, C. Oubridge, K. Nagai, *J. Mol. Biol.* **367**, 187–203 (2007).
19. V. Siegel, P. Walter, *J. Cell Biol.* **100**, 1913–1921 (1985).
20. M. Halic *et al.*, *Nature* **427**, 808–814 (2004).
21. M. Halic *et al.*, *Nature* **444**, 507–511 (2006).
22. B. M. Lunde, C. Moore, G. Varani, *Nat. Rev. Mol. Cell Biol.* **8**, 479–490 (2007).
23. L. Holm, P. Rosenström, *Nucleic Acids Res.* **38**, W545–W549 (2010).
24. A. S. Krasilnikov, A. Mondragón, *RNA* **9**, 640–643 (2003).
25. K. M. Weeks, D. M. Crothers, *Science* **261**, 1574–1577 (1993).
26. J. L. Battiste *et al.*, *Science* **273**, 1547–1551 (1996).
27. M. A. Rosenblad, N. Larsen, T. Samuelsson, C. Zwieb, *RNA Biol.* **6**, 508–516 (2009).
28. A. Kuglstatter, C. Oubridge, K. Nagai, *Nat. Struct. Biol.* **9**, 740–744 (2002).
29. K. Shen *et al.*, *J. Biol. Chem.* **288**, 36385–36397 (2013).
30. M. Halic *et al.*, *Science* **312**, 745–747 (2006).
31. V. Siegel, P. Walter, *Cell* **52**, 39–49 (1988).
32. K. Wild *et al.*, *Acta Crystallogr. D* **66**, 295–303 (2010).
33. A. M. Anger *et al.*, *Nature* **497**, 80–85 (2013).

Accurate, Fast, Cell Cycle Studies

Made easy using the BD Accuri™ C6 Personal Flow Cytometer.

Arguably, as easy as Cell Cycle is going to get.

The BD Accuri C6 is making it even easier to apply the power of flow cytometry to your research with free software templates and ready-to-go reagent kits that simplify the assessment of cell cycle and DNA status studies involving propidium iodide, 7-amino actinomycin D, and bromodeoxyuridine. You get more insight and easier workflow, whether you're a flow expert or have never used flow cytometry before.

These templates feature predefined workspace that speeds setup and analysis. Applying the power of flow cytometry, the BD Accuri C6 uses less samples and delivers greater accuracy.

Several kits are available including BD Cycletest™ Plus DNA Kit that uses PI and other active agents to obtain precise ploidy and cell cycle measurements using isolated cell nuclei and BD Pharmingen™ BrdU Kits that use 7-AAD and BrdU to provide high resolution cell cycle measurements.

Find out more about how the BD Accuri C6 puts the power of 4-color cell analysis within reach by being easy to use, simple to set up and maintain, transportable, and affordable.

bdbiosciences.com/go/templates

BD Helping all people live healthy lives

Congratulations to the 2014 AAAS Student Poster Competition Winners

The 2014 Student Poster Competition took place at the AAAS Annual Meeting in Chicago, 13–17 February. The student winners' work displayed originality and understanding that set them apart from their peers. The 2015 poster entry site will open in mid-May 2014.

BRAIN AND BEHAVIOR

Winner: Kirollos Bechay, University of California, Irvine
Histone-deactylation is a Critical Mechanism of Auditory Learning and Cortical Plasticity

Honorable Mention: Eric W. Hendricks and Austin J. Tofte, Eastern Illinois University
Estrogen Drastically Increases Mitochondrial Respiration in Alzheimer's Mouse Model

CELLULAR AND MOLECULAR BIOLOGY

Winner: Zoey Adele Prokopiak, Slippery Rock University, and Kevin Houlihan, University of North Carolina, Chapel Hill
Cooperative Effects of Hydrogen Bonds in Protein Structure Prediction

Honorable Mention: Akihito Fukudome, Emre Aksoy, and Krishna Kumar, Texas A&M University
A Plant RNA Polymerase II CTD Phosphatase Regulates Xenobiotic Stress Response

DEVELOPMENTAL BIOLOGY, PHYSIOLOGY, AND IMMUNOLOGY

Winner: Neto Sosa and Yoon Kyung Kim, University of California, Irvine
Production of Immunomodulatory Protein CD200 from E. coli for Coating Biomedical Implants

Honorable Mention: Shannon K. Boi, Joel R. Dennison, and Bailey R. Rhoads, Northern Illinois University
Transcription Factor GLI3 is a Novel Candidate Effector of Toll-like Receptor 4 Signaling

ENVIRONMENT AND ECOLOGY

Winner: Rebeca Flores, University of California, Irvine
Pattern of Resistance and Variability of Tetracycline Resistance Genes in Staphylococcus

Honorable Mention: Daylen T. Isaac, Heritage University
Nutrient Sorption of Biochar

MATH, TECHNOLOGY, AND ENGINEERING

Winner: Muneeb Mohideen, Yale University
Polyplexes Formed from Novel Poly(lactone-ω-hydroxyaminoesters) as Gene Delivery Vehicles

Honorable Mention: Ashwin Chander Ramesh, Rochester Institute of Technology
Power Generation Using Simplified Models of Tethered Airfoils

MEDICINE AND PUBLIC HEALTH

Winner: Stephan Timothy Kudlacek, University of California, Irvine
Asenapine Reverses Efflux Mediated Ciprofloxacin Resistance in Staphylococcus aureus

Honorable Mention: Disa Patel, Northern Illinois University
Assessing Individual Interventions and Need for Policy Interventions to Reduce PM Exposure

PHYSICAL SCIENCES

Winner: Lauren R. Grabstanowicz and Robert M. Rickard, Northern Illinois University
Oxidative Method and Analysis of Self-Doped Black TiO2 for Visible Light Photoactivity

Honorable Mention: Di Liu, Usman Akhter, and Timothy M. Cronin, University of Chicago
Creating Complex Molecular Topologies by Configuring DNA Four-Way Junctions

SCIENCE AND SOCIETY

Winner: Anika Larson, Arizona State University
Choosing Animal Models for Translational Neuroscience

Honorable Mention: Michael A. Bilek, Sunil Thapa, and Erin R. Tuegel, Eastern Illinois University
White-rot Fungi as Biological Pretreatment Agents for Biomass-to-Bioenergy Strategies

SOCIAL SCIENCES

Winner: Christina S. Melki, Indiana University
Evaluation of Clicker Use and Student Success in College Science Classrooms

Honorable Mention: Rebecca Harkness and Will G. Russell, Arizona State University
The Diverse Social Landscape of Prehispanic Southwest New Mexico

AAAS GENERAL POSTER SESSION ATTENDEES' CHOICE

Winner: Gang Chen, Di Liu, and Timothy Cronin, University of Chicago
Programmable Assembly of Colloidal Nanoparticles with Specific Bonding Directionality

DIGITAL REFRIGERATED CIRCULATOR

Compact and easy to use, the Advanced Digital Refrigerating Circulator combines intuitive touchpad operation with automatic or user-adjustable fluid optimization and $\pm 0.01°$C temperature stability to maintain buffer solutions at optimum temperatures even under varying electrophoresis voltages. The Model AD07R-20 features a -20° to +200°C working temperature range, large 3.75" LCD display, and variable speed pressure-suction pump. This versatile circulator also incorporates a wide variety of lab- and operator-friendly features, including a rotating control head that provides a clear view of the temperature display anywhere within a 180° viewing radius, self-storing reservoir cover, and a molded composite top plate that dampens noise and remains cooler at high temperatures. Other standard features include remote temperature sensing capability as well as serial and USB connectivity. The AD07R-20 has a 7 L reservoir; other models, with reservoir sizes as large as 45 L, are also available.
Polyscience
For info: 800-229-7569 | www.polyscience.com

CANCER PANEL

The xGen Acute Myeloid Leukemia Cancer Panel v1.0 consists of 11,743 xGen Lockdown Probes, targeting over 260 clinically relevant genes that were found to be mutated in a study of 200 patients with acute myeloid leukemia (AML), and published by The Cancer Genome Atlas consortium. The AML Cancer Panel is used for enriching the genome for regions of interest before performing next generation sequencing (NGS). It can, therefore, be used to study disease occurrence and progression, and help with the development of better targeted therapies. Target enrichment enables users to focus their sequencing efforts on specific regions of the genome, providing a cost-effective and reliable alternative to whole-genome sequencing, making NGS more accessible to researchers. By including only relevant xGen Lockdown Probes, the AML Cancer Panel enables high coverage of targeted regions, with minimal GC bias.
Integrated DNA Technologies
For info: 800-328-2661 | www.idtdna.com

REACTION VESSEL

The new ReactoMate Pilot jacketed reaction vessel offers precise control of reaction variables, a powerful direct drive overhead stirrer and excellent reaction visibility even with the vacuum jacket option. Optimized for process-scale reactions from 1L to 30 L, the ReactoMate Pilot is available packaged with a Julabo A40 Presto Circulator to ensure superb temperature management and unrivalled performance, a ReactoMate-Pilot Super Support system to support your jacketed reactor, and IKA overhead stirrer to ensure efficient reaction mixing. One of the problematic issues associated with reaction vessel set up is the cumbersome and, often dangerous, scaffolding supporting the unit. Support frames often have bars at the front and sides this can lead to problematic access to reactor and potential fracturing of glassware if exchanging vessels. The new ReactoMate-Pilot Super Support system provides a simple, straightforward and easy way to support your jacketed reactor up to 30 L in size.
Asynt
For info: +44-(0)-1638-781709 | www.asynt.com

STEM CELL FACTORS

A new range of animal-free and endotoxin-free growth factors and cytokines, tailored to stem cell research, is now available. Both expansion and differentiation of stem cells is highly reliant on growth factor and cytokine supplements, with the activity and purity of these recombinants being critical to successful research and clinical applications. Despite recognized limitations, *E. coli* and mammalian cells remain the dominant expression systems for commercial recombinant protein production. Although significant improvements in manufacture have been made, both systems present a risk of unwanted contamination from pathogens and endotoxins. The new range of animal-free and endotoxin-free growth factors and cytokines have been launched to address the growing body of evidence suggesting accepted levels of endotoxin contamination may significantly compromise stem cell maintenance and differentiation. These new recombinant growth factors and cytokines are produced in a plant-based expression system that utilizes barley seed to eliminate the risks and limitations associated with these traditional expression systems.
AMS Biotechnology
For info: +44-(0)-1235-828200 | www.amsbio.com

REFRIGERATOR–READY DESICCATOR

The Scienceware Secador Refrigerator-Ready Desiccator maintains a low-humidity environment inside a refrigerator or -20°C freezer. This new addition to the best-selling Secador desiccator family has extralong depth to maximize refrigerator/freezer space, a slide out shelf for easy access to contents, and a fold-down door with a one-handed locking latch. Desiccant is kept highly visible on a specially designed support at the top of the cabinet, while rugged, clear polycarbonate provides a chemical resistant, see-through body for full visualization of contents. Extrawide rubber feet prevent the desiccator from sliding and easily span any wire shelf spacing in refrigerators/freezers.
Bel-Art Products
For info: 973-694-0500 | www.belart.com

immunogenomics 2014

September 29 - October 1, 2014
HudsonAlpha Biotechnology Campus
Huntsville, Alabama, USA

Bringing together preeminent leaders and thinkers at the intersection of genomics and immunology

Our Keynote Speakers:

Christophe Benoiste
Professor, Department of Microbiology and Immunobiology, *Harvard Medical School*

Mary Ellen Conley
Federal Express Chair of Excellence and Professor, Department of Pediatrics, *University of Tennessee, College of Medicine, Memphis*

Mark Davis
Investigator, Howard Hughes Medical Institute; Professor, Department of Microbiology and Immunology; Director, Institute for Immunity, Transplantation, and Infections, *Stanford University School of Medicine*

Register today at
haig.aaas.org

follow
@immunogenomics
on
twitter

presented by

HudsonAlpha
INSTITUTE FOR BIOTECHNOLOGY

Science
AAAS

Hiring Professors at All Ranks at South University of Science and Technology (SUSTC)Shenzhen, China

The South University of Science and Technology (SUSTC) invites applications and nominations for all ranks of tenured and tenure-track faculty members in the Division of Science, Division of Engineering and Division of Management & Finance.

SUSTC, officially established in April 2012, is a public institution funded by the municipal of Shenzhen, a special economic zone city in southern China. The University is accredited by the Ministry of Education, China and is a pioneer in higher education reform in China. Set on five hundred acres of wooded landscape in the picturesque Nanshan (South Mountain) area, the new campus offers an idyllic environment suitable for learning and scholarship. SUSTC engages in basic and problem-solving research of lasting impact to benefit society and mankind.

The Division of Science, Division of Engineering, and the Division of Management & Finance wish to hire faculty members at all ranks. Key areas include but not limited to: *Neural and Cognitive Sciences, Biology and Gene Engineering, Modern Physics, Control and Modification of Materials, Nanoscience and Nanotechnology, Mathematics and Applied Mathematics, Molecular Chemistry and Catalysis, Large-Scale Computational Research, Robotics and Artificial Intelligence, Information Systems and Electronic Engineering, Modern Cities and Future Developments, Energy Sciences and Technology, Environmental Sciences, Financial Mathematics and Management Sciences.* The Divisions especially encourage research that requires a multi-disciplinary approach. Experienced researchers whose interests do not fall within the above areas are invited to suggest new areas of research. **Cluster hiring is possible, with senior members accompanied by junior members in a group.**

The teaching language at SUSTC is English or Putonghua. The choice is made by the instructor. As we expect an international faculty, the majority of teaching materials and reference books will be in English and many classes will be conducted in English. With a very high faculty-to-student ratio, SUSTC is committed to delivering a student-centered education and encourages students to develop their innovative spirits. Students at junior and senior years are expected to participate in research in the Research Centers.

The University offers competitive salaries, fringe benefits including medical insurance, retirement and housing subsidy. Leading Professors, Chair Professors and Professors will be appointed with tenure. Associate Professors and Assistant Professors will be offered tenure-track contracts.

Please visit our website to apply: http://talent.sustc.edu.cn/en/. All applications should include a CV and a detailed list of publications with Research ID. **Those interested in cluster hiring should send CVs and publication lists with Research ID as a group.** Evaluations will commence immediately and appointments will be made on a continuous basis. Additional information on SUSTC is available on the University homepage **http://www.sustc.edu.cn.**

Qualified applicants are also encouraged to apply for the Recruitment Program of Global Expert ("Thousand Talents Program") through SUSTC. Successful applicants will get extra research fund and living allowance from the government. Additional information is available through email inquiry or **http://talent.sustc.edu.cn/.**

If you have any questions, please feel free to contact us at **hiring@sustc.edu.cn.**

UNIVERSITY OF CALIFORNIA
UC RIVERSIDE

Faculty Opportunities

Position - Associate or Full Professor in Stem Cell Biology

The Division of Biomedical Sciences within the recently accredited School of Medicine at the University of California Riverside is seeking to hire a new faculty member at the tenured rank of Associate or Full Professor. We are looking for an accomplished research scientist with an active research program in stem cell biology able to collaborate and help integrate Stem Cell Research in multiple academic units at UCR including the California Institute for Regenerative Medicine (CIRM) funded Stem Cell Center. Preference will be given to those individuals examining stem cell biology in the context of human disease and/or therapies who are committed to a collaborative approach to research, and who are expert in their specific disease model.

The successful candidate will be appointed in the Division of Biomedical Sciences. The School of Medicine at UCR is the sixth University of California Medical School and serves the rapidly growing and dynamic Inland Southern California region by training a much-needed physician workforce and catalyzing innovations in research, education, and health care delivery to improve the health of medically underserved populations. Laboratory and office space will be in a newly-opened School of Medicine research building. Areas of research within the Division include cancer biology, diseases of ion transport, epithelial biology, signal transduction, integrative immunology, host-pathogen interactions, glial-neuronal interactions, neurodevelopmental disorders and neuroendocrinology. Particular strengths on the campus pertinent to this recruitment include genetics, epigenetics, genomics/bioinformatics, microRNAs, vector biology, bioengineering and nanotechnology, and synthetic and analytical chemistry.

The Division of Biomedical Sciences sponsors an innovative Ph.D. program that integrates the core medical curriculum with biomedical graduate training and research. The successful candidate will be expected to teach in the medical curriculum and actively participate in the Biomedical Sciences Ph.D. program. As such, preference will be given to candidates who are capable of teaching general pharmacology, pathology, physiology (electrophysiology, renal or respiratory), embryology or genetics.

The University of California, Riverside is situated in an historic citrus growing area surrounded by mountain ranges. Riverside is about an hour away from ski slopes, surfing, or hiking in mountain or desert environments, and housing in the area is very affordable. The campus is also located in a prime position to take advantage of the other universities, research institutes, and biotech industries present in Southern California. Applicants must hold a Ph.D., M.D., Pharm D., or equivalent degree and qualify for a tenured faculty appointment at the University of California. Applications will be reviewed beginning **April 28, 2014** and the positions will remain open until filled. UC Riverside is an Equal Opportunity/Affirmative Action Employer.

To Apply: Please submit the following items electronically through the AP Recruit system: **https://aprecruit.ucr.edu/apply/JPF00128**. Curriculum vitae, statement of research accomplishments and goals, statement of teaching expertise and names of four individuals who will be asked to provide letters of reference when a short list of applicants is generated.

UNIVERSITY OF CALIFORNIA
UC RIVERSIDE

Faculty Positions

Two Positions – Assistant, Associate or Full Professor in Biomedical Sciences

The Division of Biomedical Sciences within the recently accredited School of Medicine at the University of California Riverside is seeking to hire two new faculty members at the rank of Assistant, Associate or Full Professor. We are looking for accomplished research scientists with expertise in molecular pharmacology or metabolism and as applied to biomedical research in cancer, the microbiome, toxicology, cardiovascular or renal disease. Preference will be given to those individuals examining the molecular mechanisms of human disease who are committed to a collaborative approach to research, and who are expert in their specific disease model.

The successful candidates will be appointed in the Division of Biomedical Sciences. The School of Medicine at UCR is the sixth University of California Medical School and serves the rapidly growing and dynamic Inland Southern California region by training a much-needed physician workforce and catalyzing innovations in research, education, and health care delivery that will improve the health of medically underserved populations. Laboratory and office space will be in a newly-opened School of Medicine research building. Areas of research within the Division include cancer biology, diseases of ion transport, epithelial biology, signal transduction, integrative immunology, host-pathogen interactions, glial-neuronal interactions, neurodevelopmental disorders and neuroendocrinology. Particular strengths on the campus pertinent to this recruitment include genetics, epigenetics, genomics/bioinformatics, microRNAs, vector biology, bioengineering and nanotechnology, and synthetic and analytical chemistry.

The Division of Biomedical Sciences sponsors an innovative Ph.D. program that integrates the core medical curriculum with biomedical graduate training and research. The successful candidate will be expected to teach in the medical curriculum and actively participate in the Biomedical Sciences Ph.D. program. As such, preference will be given to candidates who are capable of teaching general pharmacology, pathology, physiology (electrophysiology, renal or respiratory), embryology or genetics.

The University of California, Riverside is situated in an historic citrus growing area surrounded by mountain ranges. Riverside is about an hour away from ski slopes, surfing, or hiking in mountain or desert environments, and housing in the area is very affordable. The campus is also located in a prime position to take advantage of the other universities, research institutes, and biotech industries present in Southern California. Applicants must hold a Ph.D., M.D., Pharm D., or equivalent degree and qualify for a tenured faculty appointment at the University of California. Applications will be reviewed beginning **April 28, 2014** and the positions will remain open until filled. UC Riverside is an Equal Opportunity/Affirmative Action Employer.

To Apply: Please submit the following items electronically through the AP Recruit system: Curriculum vitae, statement of research accomplishments and goals, statement of teaching expertise and names of four individuals who will be asked to provide letters of reference when a short list of applicants is generated.

Choose the appropriate link based on qualifications:
Assistant Level: https://aprecruit.ucr.edu/apply/JPF00130
Associate/Full Level: https://aprecruit.ucr.edu/apply/JPF00129

ETH

Eidgenössische Technische Hochschule Zürich
Swiss Federal Institute of Technology Zurich

Assistant Professor of Virus Host Interactions

The Department of Biology (www.biol.ethz.ch) at ETH Zurich invites applications for the above-mentioned position. ETH Zurich is strengthening its involvement in the area of «Life Sciences» which has been fuelled by key advances in systems level analyses being applied to key questions in biology. The new assistant professorship will be part of the Institute of Microbiology and will be placed in the area of organismal microbiology with strong links to microbiology and immunology, to molecular health sciences, to systems biology, to medical and veterinary virology, and to environmental and health sciences. The department and the institute offer outstanding scientific opportunities to participate in interdisciplinary research projects, including close interactions with SystemsX.ch, the Swiss initiative for systems biology, with Life Science Zurich, a well-established platform for teaching and research, and with a network of research laboratories in the areas of microbiology, immunology, virology and related disciplines. The Functional Genomics Center Zurich, the Light Microscopy and Screening Center and the Electron Microscopy Center at ETH Zurich offer an outstanding technological platform for innovative research projects.

Successful candidates demonstrate an outstanding research profile, proven teaching abilities as well as competitive acquisition of third party funding and are expected to entertain a world-class research programme in the area of virus-host interactions. Research areas include, but are not limited to, the impact of virus infections in the homeostasis of host cells or tissues on the organismic or molecular level in animal or plant models or within bacterial consortia, the influence of persistent virus infection on heterologous immune defense, the reciprocal interaction of host endogenous retroviruses/retroelements with commensal bacteria and the identification and exploitation of new viral machineries for potentially new applications in bioengineering. The new assistant professor will be expected to teach undergraduate level courses (German or English) and graduate level courses (English) in the biology teaching program, including an inter-departmental Master's curriculum of Microbiology and Immunology.

This assistant professorship has been established to promote the careers of younger scientists. The initial appointment is for four years with the possibility of renewal for an additional two-year period.

Please apply online at www.facultyaffairs.ethz.ch

Applications should include a curriculum vitae, a list of publications, and a statement of future research and teaching interests. The letter of application should be addressed **to the President of ETH Zurich, Prof. Dr. Ralph Eichler. The closing date for applications is 15 May 2014.** ETH Zurich is an equal opportunity and family friendly employer and is further responsive to the needs of dual career couples. We specifically encourage women to apply.

Unil
UNIL | Université de Lausanne
Faculty of Biology and Medicine

| le savoir vivant |

THE FACULTY OF BIOLOGY AND MEDICINE OF THE UNIVERSITY OF LAUSANNE (UNIL), SWITZERLAND, AND THE LUDWIG CENTRE AT UNIL INVITE APPLICATIONS FOR THE POSITION OF:

TENURE-TRACK ASSISTANT PROFESSOR TOWARDS ASSOCIATE PROFESSOR IN IMMUNE ENGINEERING

The Ludwig Centre (http://www.unil.ch/licr) and the Department of Oncology at UNIL, together with the Federal Institute of Technology of Lausanne (EPFL), have selected Immune Engineering as an area of high priority for cancer research. The three institutions are jointly building a world-class environment in tumor immunology and immune engineering, as part of the new Swiss Cancer Centre.

We are seeking outstanding candidates with experience and interest in molecular cancer immunotherapy, especially molecular vaccines, immune engineering, T cell engineering, antibody engineering and novel technologies that can help mobilize antitumor immunity. Strong candidates with an interest in developing immune therapeutics will be given the highest priority.

The selected candidate will benefit from a start up package, a particularly rich research and translational clinical environment in cancer and immunology, and an array of state-of-the-art core facilities and laboratories within the Ludwig Cancer Centre and EPFL.

Requirements:

- A PhD or MD-PhD degree in cancer immunology.
- An outstanding research track record.
- An interest and expertise in tumour immunology and immune engineering.
- The drive to develop a highly successful and competitive independent research programme.
- The willingness to engage in collaborations with translational research groups and clinicians in one or several of the multidisciplinary research programmes that are being developed in the Cancer Centre.

The job description is available on the Web at the address http://www.unil.ch/fbm/page64812.html. Further information may be obtained from Prof. Dotto (Paolo.Dotto@unil.ch), chairman of the search committee.

Applications must be formulated in English and should include a motivation letter, the curriculum vitae, a list of publications highlighting the five most significant ones, a brief statement of the past and future research programmes, and teaching experience, as well as names and contact information of three references. They should be submitted online by June 4th, 2014 as a single pdf file to www.unil.ch/iafbm/application.

Seeking to promote an equitable representation of women and men among its staff, the University encourages applications from women.

UC RIVERSIDE
UNIVERSITY OF CALIFORNIA

Faculty Opportunities

Position - Associate or Full Professor in Statistics and Biomedical Sciences

The Department of Statistics and the Division of Biomedical Sciences at the University of California Riverside are seeking to hire a new faculty member at the rank of Associate or Full Professor. The successful candidate will be appointed 50% in the Department of Statistics, College of Natural and Agricultural Sciences and 50% in the Division of Biomedical Sciences, School of Medicine.

We are looking for an accomplished research scientist in one or more of a number of specific areas including: Discrete Data Analysis, High Dimensional Data Analysis, Nonparametric Statistics, Survival Analysis, Image Analysis, or Functional Data Analysis. The School of Medicine will initially be involved in community-based research requiring expertise in experimental and quasi-experimental designs, multivariate analysis, sampling, modeling, imputation and novel measurement approaches. Preference will be given to candidates who have demonstrated excellence running an independent Statistics methodology research program, including development of, and participation in, externally funded research as a principal investigator or co-principal investigator, and experience with supporting medical data analyses. A strong teaching record, including doctoral student dissertation mentoring is also desired. Finally, the successful candidate should be committed to a collaborative approach to research within a medical school as well as teaching at both the undergraduate as well as the graduate level.

The new School of Medicine at UCR is the sixth University of California Medical School and serves the rapidly growing and dynamic Inland Southern California region by training a much-needed physician workforce and catalyzing innovations in research, education, and healthcare delivery that improve the health of medically underserved populations. The Department of Statistics was established in 1968 and resides in the College of Natural and Agricultural Sciences. The Department of Statistics has a long tradition of collaborative research in the life sciences, which together with the School of Medicine, provides an exceptional environment for interdisciplinary research on a variety of health-related initiatives. The University of California Riverside is situated in an historic citrus growing area surrounded by mountain ranges. Riverside is about an hour away from ski slopes, surfing, or hiking in mountain or desert environments, and housing in the area is very affordable. The campus is also located in a prime position to take advantage of the other universities, research institutes, and biotech industries present in Southern California.

Qualified candidates must have a Ph.D. in Statistics or Biostatistics or a similar statistically-oriented discipline and qualify for a tenured faculty appointment at the University of California. Applications will be reviewed beginning **April 27, 2014**, and the position will remain open until filled. UC Riverside is an Equal Opportunity/Affirmative Action Employer.

TO APPLY: Interested applicants should upload curriculum vitae, personal research statement, and statement describing teaching and 3-**4 names of individuals who will be asked to provide letters of reference once a short list is developed to https://aprecruit.ucr.edu/apply/JPF00127**

UNIVERSITÄT BASEL

The Faculty of Science (Philosophisch-Naturwissenschaft-liche Fakultät) of the University of Basel invites applications for a position of

Professor of Chemistry (open rank)

We are seeking for candidates with an internationally recognized research program and an outstanding publication record in

Nanomaterials or Sustainable Chemical Science

The selected candidate will actively participate in the recently granted NCCR "Molecular Systems Engineering". He/She is expected to participate to teaching chemistry at all levels of the BSc, MSc and PhD programs. The University of Basel has an established program for career progression allowing promotion to associate and full professor upon successful evaluation.

The Department of Chemistry is located near the centre of Basel, a town which provides a stimulating and supportive environment for interdisciplinary research thanks to the strong presence of science institutes as well as the chemical and pharmaceutical industries. For further information see: http://www.chemie.unibas.ch

The selected candidate is expected to commence the appointment in Spring 2015. Applications received by April 30, 2014 are guaranteed full consideration. The University of Basel is an equal opportunity employer and applications from female candidates are particularly encouraged. Applications, including a curriculum vitae, list of publications, an outline of current and future research plans and names of four referees should be sent by email (as pdf file) to Prof. Dr. Jörg Schibler University of Basel, Dean of the Faculty of Sciences, Klingelbergstrasse 50, 4056 Basel, dekanat-philnat@unibas.ch. For further information, please contact: Prof. Dr. Thomas Ward, Head, Department of Chemistry, E-mail: thomas.ward@unibas.ch

UNI
BASEL

Why not change the world?

Rensselaer Department of Biological Sciences Faculty Search
The Chatter Career Development Chair in Freshwater Ecology
Tenure-Track Assistant or Associate Professor with Tenure

The Department of Biological Sciences at Rensselaer Polytechnic Institute in Troy, NY invites applications for the Chatter Career Development Chair, intended for an Associate or exceptional Assistant Professor in the area of freshwater ecology.

At minimum, applicants must hold a Ph.D. degree, or foreign degree equivalent, in biological sciences or a related field with an outstanding record of research accomplishments, as well as a strong commitment to teaching, commensurate with a faculty appointment at the level of tenure-track Assistant Professor or Associate Professor with tenure.

The department maintains strong interdisciplinary research efforts and is undergoing a broad expansion in environmental sciences. Rensselaer has recently established a strategic partnership with IBM and the FUND for Lake George known as The Jefferson Project at Lake George (see **http://tiny.cc/qn5s1w**). The goal of the multi-million dollar project is to develop a global model for sustained ecosystem understanding and protection focusing on Lake George, a world-class natural resource facing threats of permanent degradation from a range of environmental stressors. An unprecedented array of new tools will fuse monitoring, modeling, experimentation, simulation, forecasting, and protection of Lake George.

Work on the Jefferson Project leverages Rensselaer's Darrin Fresh Water Institute (DFWI) in Bolton Landing, NY (**http://www.rpi.edu/dept/DFWI/index.html**), a multidisciplinary environmental research center dedicated to understanding the structure and function of aquatic, terrestrial, and atmospheric systems. The primary research focus is on the ecological consequences of environmental perturbations due to human activities in the Northeastern United States. The successful candidate is expected to be an active contributor to the Department of Biological Sciences, The Jefferson Project, and DFWI.

Applications should be sent as a single PDF document containing curriculum vitae, statement of research accomplishments, and a brief description of teaching interests to **biology-chair@rpi.edu**.

Applicants must also arrange for the submission of three letters of reference. Questions about this position may be directed to Dr. Susan P. Gilbert, Department Head (**sgilbert@rpi.edu**) or Dr. Sandra Nierzwicki-Bauer, Director of the Darrin Fresh Water Institute (**nierzs@rpi.edu**). Application review will begin on May 1, 2014 and continue until the position is filled.

Successful candidates will have duties that include teaching at the undergraduate and graduate level in the department, development and maintenance of robust programs of research and scholarship, as well as service to the department, the School of Science, and Rensselaer.

Rensselaer

AAAS is here – helping scientists achieve career success.

Every month, over 400,000 students and scientists visit ScienceCareers.org in search of the information, advice, and opportunities they need to take the next step in their careers.

A complete career resource, free to the public, *Science* Careers offers a suite of tools and services developed specifically for scientists. With hundreds of career development articles, webinars and downloadable booklets filled with practical advice, a community forum providing answers to career questions, and thousands of job listings in academia, government, and industry, *Science* Careers has helped countless individuals prepare themselves for successful careers.

As a AAAS member, your dues help AAAS make this service freely available to the scientific community. If you're not a member, join us. Together we can make a difference.

To learn more, visit **aaas.org/plusyou/sciencecareers**

COURSE

PRINCETON Neuroscience INSTITUTE

Neurotechnologies for Analysis of Neural Dynamics

Course Directors: David W. Tank and Michael Berry, Princeton University
Laboratory Director: Alan Gelperin, Princeton University
Course Dates: June 15 – July 12, 2014
Online Application Form and Course Schedule:
NAND.princeton.edu
Application Deadline: May 1, 2014

This intensive new course, Neurotechnologies for Analysis of Neural Dynamics (NAND), is designed to emphasize the major ways that scientists trained in the physical and information sciences contribute to the advance of neuroscience. This course will introduce students with quantitative training in the physical sciences, mathematics or engineering to the concepts and research methodologies of modern neuroscience. Topics covered will range from cellular biophysics to systems neuroscience, including particularly imaging methods for the study of single neurons, networks of neurons and human brain dynamics during execution of behavioral computations. The course will be unique in its focus on neural dynamics at several scales of complexity – cells, circuits, intact brains – and the combination of didactic lectures and laboratory exercises, including cellular biophysics, synaptic interactions and plasticity in neuronal networks, and fMRI imaging of targeted brain regions in human subjects. The course includes substantive instruction in neurotechnology, ranging from large scale electrode and optical recording (and optogenetic stimulation) to mathematical analysis of neural dynamics within the datasets produced by these methods. The capstone of this course will be one-week student-designed research projects integrating concepts and methodologies encountered during the initial formal lectures and laboratory exercises. Course work will include morning lectures and tutorials and laboratory exercises selected to complement and extend the themes presented in morning lectures.